Nuclear Orientation Studies of Isotopes Far from Stability

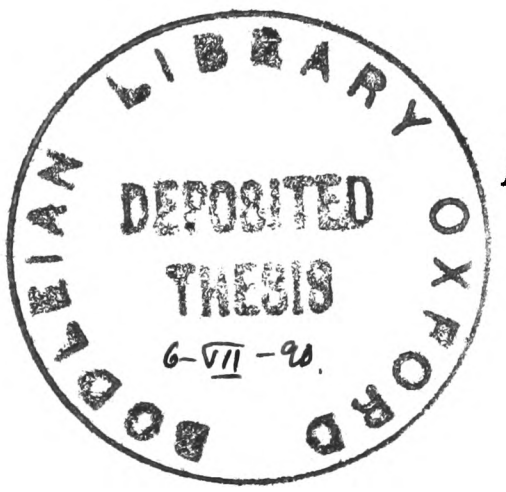

Austyn Glyn Griffiths

Hertford College

A thesis submitted in partial fulfillment of the requirements
for the degree of Doctor of Philosophy
in the University of Oxford

Michaelmas term 1989

Nuclear Orientation Studies of Isotopes Far from Stability

Austyn Glyn Griffiths
Hertford College

A thesis submitted in partial fulfillment of the requirements
for the degree of Doctor of Philosophy
in the University of Oxford

Michaelmas term 1989

Abstract

Low Temperature Nuclear Orientation (LTNO) is an important technique in the study of nuclei far from stability. The theory of LTNO and its applications to the measurement of static nuclear moments and other quantities of spectroscopic interest are reviewed.

Among the nuclei off the line of stability those in the A $\sim$ 75 region are of considerable interest, exhibiting large quadrupole deformations, triaxiality and shape coexistence. LTNO measurements performed on neutron deficient bromine isotopes have yielded the static magnetic dipole moments of the nuclei ^{72g,72m,74m,75,76,77}Br, spectroscopic information on $^{72-77}$Se and also identified the ground state spin of ^{73}Br as $1/2^-$.

Existing odd A and odd-odd particle-rotor computer codes have been extended in order to include a Variable Moment of Inertia (VMI) asymmetric rotational core. The formalism necessary for this modification is developed.

The measured magnetic moments are interpreted within the framework of this particle - VMI rotor model. It is shown that the systematic reduction in the moments of the odd A nuclei $^{75-81}$Br characterizes the transformation of the *prolate* ground state configuration from largely $\pi[301]3/2$ in ^{79,81}Br to almost pure $\pi[312]3/2$ in ^{75,77}Br. This trend is fully consistent with the increase in deformation towards the lower masses suggested by the known electric quadrupole moments. In contrast, the ground state spin of ^{73}Br can only be interpreted in terms of an *oblate* nuclear shape. This is the first evidence for the predicted prolate-oblate shape transition in the bromine nuclei. In addition the magnetic moment of ^{74}Br^m, by identifying a $\pi[431]3/2\nu[422]5/2$ configuration, strongly suggests a positive parity assignment for the isomeric state.

Finally, an experiment to search for possible T-violation effects in nuclear gamma decay is described. Using coincidence techniques, a measurement of the T-odd P-even quantity $(\mathbf{I}\cdot\mathbf{k}\times\mathbf{e})(\mathbf{I}\cdot\mathbf{k})(\mathbf{I}\cdot\mathbf{e})$ has lead to a limit on the T-violating phase angle between the E2 and M1 matrix elements associated with the 604 keV gamma transition in ^{192}Pt of $\sin\eta = \pm 11(12)\times 10^{-3}$.

ACKNOWLEDGEMENTS

Now that it's all over bar the shouting (but not in the viva I trust!), it gives me great pleasure to express my thanks to those individuals without whose efforts this thesis could never have been written.

Firstly, I would like to thank Professors K.W. Allen, R.A. Cowley and D.H. Perkins for making available the excellent facilities of the Clarendon and Nuclear Physics Laboratories. Also due for a mention are the kind people at the Science and Engineering Research Council who kept me in the lap of luxury and sent me to exotic places.

In particular, I am greatly indebted to my supervisors, Nick and Jirina Stone, for initiating my research program and providing considerable guidance and encouragement during its progress. Thanks are also due to Ingemar Ragnarsson and Paul Semmes for their hospitality during my visit to Lund.

Not being a great one for experiments, I would like to acknowledge those who showed me where to stick my BNC cable when I had a loose end. These include Ian Grant, Chris Leyland, Barry Singleton, Phil Walker and all of the staff of the Daresbury Laboratory. Of those unfortunates who were unable to escape to Manchester or Surrey: Jeremy White, Chris Ashworth and Phil Back deserve a special mention. Without their unselfish help I would have been up 'elium Creek without a photon.

On a more personal note I would like to thank all my friends who have contributed so much to my time at Oxford. Naturally this includes all past and present members of NOG: Danny, Jerry, Tim, Chris, Phil and Peter. I have also enjoyed the company of many people in the Department of Nuclear Physics: particularly, Danny (again $\cdots$ the only double he's likely to see this year!), Mark, Chris Chantler, Phil, Andy, Will, Stephan, Martin, Chris Pass and of course Arthur.

Most of all I would like to thank my mother for her love and support during the course of my education. Also a great big thank you to my surrogate mother Ruby for her lukewarm tea and tomato soup.

Austyn Griffiths
Oxford
2.10 am Nov 1 1989

Contents

List Of Figures

page

List Of Tables

Chapter 1

Low Temperature Nuclear Orientation

1.1 Introduction

The probability of emission of electromagnetic radiation depends, in general, on the angle θ between the expectation value $\langle \mathbf{J} \rangle$ of the angular momentum vector of the radiating system and the direction $\mathbf{k}$ in which the photons are observed with sharp linear momentum $\mathbf{p} = \omega \mathbf{k}$ and helicity τ.

For a source of radiation consisting of an ensemble of many radiating systems with their $\mathbf{J}$ vectors randomly oriented, $\langle \mathbf{J} \rangle = 0$ and the radiation is isotropic in space. In order to observe an anisotropic radiation pattern the spatial distribution of the angular momentum vectors must favour a definite direction, so that $\langle \mathbf{J} \rangle \neq 0$. The intensity and polarization properties of the emitted radiation are then a function of the angles between the orientation axes and the directions of observation $\mathbf{k}$ and the polarization $\mathbf{P}$ of the radiation.

If the polarization of radiation is not observed then by definition the *directional distribution* $W(\mathbf{k})$ of the radiation is measured. If the radiation is observed with a detector which is sensitive to the polarization properties $\mathbf{P}$ of the radiation then the *polarization distribution* $W(\mathbf{k}, \mathbf{P})$ is measured. The term *angular distribution* is used to refer to both.

Oriented ensembles of nuclei may be prepared by three different methods:

1. Extranuclear static and dynamic orientation. (Low temperature orientation, optical pumping, radiofrequency methods).
2. Orientation by absorption of nuclear radiation of well defined direction and polarization. (Nuclear reactions, Coulomb excitation).
3. Orientation by observing a preceeding emitted radiation in a well defined direction and with well defined properties. (Angular correlations, nuclear cascade radiation).

In Low Temperature Nuclear Orientation (LTNO), which forms the main subject of this work, orientation is achieved through the interaction of external fields with either the static magnetic dipole moment or the static electric quadrupole moment of the nucleus. At very low

temperatures the energetically lower states, m-states in the case of magnetic interactions, become preferentially populated according to the Boltzmann distribution. Thus in thermodynamic equilibrium various degrees of orientation are obtained depending on the relative magnitudes of the energy splitting of the nuclear substates and the randomizing thermal energy, kT.

The following sections will deal with how the angular distribution of gamma radiation is related to the various nuclear properties of interest and to the orienting interaction.

1.2 The angular distribution of radiation from an oriented source

1.2.1 The description of mixed quantum states by density matrices

A physical system is in a *pure state* if every value of a complete set of commuting observables has been measured. There is then maximum information known about the state under consideration which can thus be described uniquely by a complete set of quantum numbers.

An angular distribution measurement does not result in a complete knowledge of the individual nuclei nor the individual quanta, only ensemble averages are observed. The statistical nature of the the ensemble is involved and maximum information is not available. The quantum mechanical description of such *mixed states* requires *incoherent superpositions* of pure quantum states. Thus an ensemble cannot be described by state vectors, but is instead described by a *density matrix* [1].

Consider a pure state $|\Psi\rangle$, which by selecting a coordinate system in Hilbert space can be described by its projections onto all coordinate axes. Choosing the complete orthonormal set $|\phi\rangle$ for this purpose, then

$$|\Psi\rangle = \sum_{\phi} |\phi\rangle\langle\phi|\Psi\rangle \tag{1.1}$$

where the transformation brackets $\langle\phi|\Psi\rangle$ are of course unitary. The expectation value of any operator a in the state $|\Psi\rangle$ is therefore

$$\langle\Psi|a|\Psi\rangle = \sum_{\phi\phi'}\langle\Psi|\phi'\rangle\langle\phi'|a|\phi\rangle\langle\phi|\Psi\rangle. \tag{1.2}$$

A mixed state consisting of an ensemble of several independent nuclei must then be described by an *incoherent* superposition of the possible pure states $|\Psi_n\rangle$, weighted according to the proportion of nuclei $g(n)$ in those pure states. The expectation value of the operator a in such a mixed state is therefore given by the weighted average of the expectation values $\langle\Psi|a|\Psi\rangle$

$$\langle a\rangle = \sum_{n=1}^{N} g(n)\langle\Psi_n|a|\Psi_n\rangle \Big/ \sum_{n=1}^{N} g(n). \tag{1.3}$$

It is convenient to normalize the weights $g(n)$ to unity

$$\sum_{n=1}^{N} g(n) = 1. \tag{1.4}$$

Substituting (1.2) into (1.3) and using (1.4) one can write

$$\langle a\rangle = \sum_{n\phi\phi'} \langle\phi|\Psi_n\rangle g(n)\langle\Psi_n|\phi'\rangle\langle\phi'|a|\phi\rangle \tag{1.5}$$

or alternatively

$$\langle a\rangle = \sum_{\phi\phi'} \langle\phi|\rho|\phi'\rangle\langle\phi'|a|\phi\rangle \tag{1.6}$$

where

$$\langle\phi|\rho|\phi'\rangle = \sum_{n=1}^{N} \langle\phi|\Psi_n\rangle g(n)\langle\Psi_n|\phi'\rangle. \tag{1.7}$$

The state of the ensemble is thus completely characterized by the *density matrix* ρ whereas the matrix A, with elements $\langle\phi'|a|\phi\rangle$, depends only upon the operator a and the representation $|\phi\rangle$. With these definitions (1.6) may be rewritten in the form

$$\langle a\rangle = Tr(\rho A). \tag{1.8}$$

The density matrix can be considered as a representation of the density operator

$$\rho_{op} = \sum_{n=1}^{N} |\Psi_n\rangle g(n)\langle\Psi_n| \tag{1.9}$$

in the basis $|\phi\rangle$. The density operator completely describes the state of the ensemble, be it mixed (at least two $g(n) > 0$) or pure (only one non-zero $g(n)$).

1.2.2 The statistical tensors

In angular distribution problems the symmetries of the ensemble with respect to rotations are of interest and so it is natural to choose the basis states $|\phi\rangle$ to be the eigenstates $|\varrho jm\rangle$ of the angular momentum operator $\mathbf{J^2}$ and its projection onto the z-axis, J_z. The symbol ϱ represents the other quantum numbers needed to specify the states uniquely. The matrix elements of the density operator in this representation are

$$\rho(\varrho_1 j_1 \varrho_2 j_2) = \langle \varrho_1 j_1 m_1 | \rho | \varrho_2 j_2 m_2 \rangle = \sum_n \langle \varrho_1 j_1 m_1 | \Psi_n \rangle g(n) \langle \Psi_n | \varrho_2 j_2 m_2 \rangle. \tag{1.10}$$

The *grand density matrix* $\rho(\eta)$ which describes an ensemble of nuclei η in all their possible states is a square matrix with $(2j_1+1)+(2j_2+1)+\cdots$ rows and columns, where the j_i are the angular momenta of the different nuclear levels or of the different daughter nuclei and radiation fields into which the nuclei η might decay. The density matrix $\rho(j_1 j_2)$ is just a $(2j_1+1)\times(2j_2+1)$ submatrix of this grand matrix.

The angular momentum states $|jm\rangle$ transform under a rotation of the quantization axis from $S(xyz)$ to $S(\overline{x}\,\overline{y}\,\overline{z})$ according to

$$|j\overline{m}\rangle_{\overline{S}} = \sum_m |jm\rangle_S D^{j*}_{m\overline{m}}(S \to \overline{S}) \tag{1.11}$$

where the D-matrices are defined in Brink and Satchler [2]. The elements of the density matrix transform under the same rotation according to

$$\langle j_1 \overline{m}_1 | \rho | j_2 \overline{m}_2 \rangle_{\overline{S}} = \sum_{m_1 m_2} D^{j_1}_{m_1 \overline{m}_1}(S \to \overline{S}) \langle j_1 m_1 | \rho | j_2 m_2 \rangle_S D^{j_2 *}_{m_2 \overline{m}_2}(S \to \overline{S}). \tag{1.12}$$

Making use of the Clebsh-Gordqn series of D-matrices [2] then

$$\begin{aligned} \langle j_1 \overline{m}_1 | \rho | j_2 \overline{m}_2 \rangle_{\overline{S}} = \sum_{m_1 m_2 \lambda} & \langle j_1 m_1 | \rho | j_2 m_2 \rangle_S (-1)^{m_2 - \overline{m}_2} (2\lambda+1) \begin{pmatrix} j_1 & j_2 & \lambda \\ m_1 & -m_2 & q \end{pmatrix} \\ & \times \begin{pmatrix} j_1 & j_2 & \lambda \\ \overline{m}_1 & -\overline{m}_2 & \overline{q} \end{pmatrix} D^{\lambda *}_{q\overline{q}}(S \to \overline{S}). \end{aligned} \tag{1.13}$$

After multiplying both sides of this equation by the factor

$$(-1)^{j_2 + \overline{m}_2} (2\lambda+1)^{\frac{1}{2}} \begin{pmatrix} j_1 & j_2 & \lambda \\ \overline{m}_1 & -\overline{m}_2 & \overline{q} \end{pmatrix}$$

and summing over $\overline{m}_1$ and $\overline{m}_2$ (keeping $\overline{q}$ fixed) one obtains, because of the orthogonality relations of the 3-j symbols,

$$\left\{\sum_{\overline{m}_1}\langle j_1\overline{m}_1|\rho|j_2\overline{m}_2\rangle_{\overline{S}}(-1)^{j_2+\overline{m}_2}(2\lambda+1)^{\frac{1}{2}}\begin{pmatrix} j_2 & j_1 & \lambda \\ -\overline{m}_2 & \overline{m}_1 & \overline{q}\end{pmatrix}\right\} =$$
$$\sum_q\left\{\sum_{m_1}\langle j_1 m_1|\rho|j_2 m_2\rangle_S(-1)^{j_2+m_2}(2\lambda+1)^{\frac{1}{2}}\begin{pmatrix} j_1 & j_2 & \lambda \\ -m_2 & m_1 & q\end{pmatrix}\right\} D^{\lambda *}_{q\overline{q}}(S\rightarrow\overline{S}). \tag{1.14}$$

The linear combinations of the elements of $\rho(j_1 j_2)$ enclosed in braces transform like spherical tensors of rank λ. Due to this simple transformation property it is more convenient to use these linear combinations than the matrix elements themselves. Thus it is possible to define the *statistical tensors* $\rho^\lambda_q(j_1 j_2)$ to be

$$\rho^\lambda_q(j_1 j_2)=\sum_{m_1}\langle j_1 m_1|\rho|j_2 m_2\rangle(-1)^{j_2+m_2}(2\lambda+1)^{\frac{1}{2}}\begin{pmatrix} j_2 & j_1 & \lambda \\ -m_2 & m_1 & q\end{pmatrix}. \tag{1.15}$$

This represents the vector relationship $\lambda = \mathbf{J_2} - \mathbf{J_1}$ and so the rank of the statistical tensor is an integer in the range $|j_2 - j_1|$ to $j_2 + j_1$.

1.2.3 Oriented nuclear states

If the interacting fields that cause the orientation of the ensemble have an axis of cylindrical symmetry, which in the case of LTNO is that defined by the direction of the external field, then the density operator (1.9) may be expressed in the form

$$\rho_{op}=\sum_{m=-I}^{+I}|Im\rangle g(n)\langle Im| \tag{1.16}$$

where the eigenstates $|Im\rangle$ of the nuclear spin operator I_z are defined with respect to the symmetry z-axis. The corresponding density matrix $\rho(I)$ in the angular momentum representation $|I\overline{m}\rangle$ chosen with respect to some representation-coordinate system $\overline{S}$ is

$$\langle I\overline{m}|\rho|I\overline{m}'\rangle=\sum_m\langle I\overline{m}|Im\rangle g(m)\langle Im|I\overline{m}'\rangle. \tag{1.17}$$

If one chooses $\overline{S}$ to be the symmetry frame defined by the external field then the density matrix becomes diagonal

$$\langle Im|\rho|Im'\rangle = g(m)\delta_{mm'} \tag{1.18}$$

and the weighting factors $g(m)$ are then simply the relative populations of the states $|Im\rangle$ in the ensemble.

An ordinary ensemble of nuclei with spin I at room temperature has in general no fixed orientation axis in space, hence it must be invariant with respect to three dimensional rotations. Thus the statistical tensors describing such an random ensemble must satisfy the relation

$$\rho^{\lambda}_{\overline{q}}(I)_{\overline{S}} = \sum_{q} \rho^{\lambda}_{q}(I)_{S} D^{\lambda *}_{q\overline{q}}(S \rightarrow \overline{S}) = \rho^{\lambda}_{\overline{q}}(I)_{S} \tag{1.19}$$

for any rotation $S \rightarrow \overline{S}$. This is only possible if D^{λ} is the unit matrix ($q = \overline{q} = \lambda = 0$) or if $\rho^{\lambda}_{q}(I)$ vanishes. Hence the statistical tensor in this case is

$$\rho^{0}_{0}(I) = (2I+1)^{-\frac{1}{2}} \tag{1.20}$$

with corresponding density matrix

$$\rho(I) = (2I+1)^{-1}\mathbf{1} \tag{1.21}$$

expressing the fact that the population is uniformly distributed amongst the various $|Im\rangle$ states.

When orientation is achieved, unequal populations of the $|Im\rangle$ states occur giving rise to statistical tensors $\rho^{\lambda}_{q}(I)$ with $\lambda \neq 0$. With the axis of cylindrical symmetry, the z-axis, defined by the applied field it is required that the statistical tensors be invariant with respect to rotations through an arbitary angle α about this axis. This rotation is represented by

$$D^{\lambda *}_{q\overline{q}}(\alpha, 0, 0) = \mathrm{e}^{-iq\alpha}\delta_{q\overline{q}} \tag{1.22}$$

and leads to the condition

$$\rho^{\lambda}_{\overline{q}}(I) = \sum_{q} \rho^{\lambda}_{q}(I) D^{\lambda *}_{q\overline{q}}(\alpha, 0, 0) = \rho^{\lambda}_{q}(I)\mathrm{e}^{-iq\alpha} = \rho^{\lambda}_{q}(I). \tag{1.23}$$

Since α is arbitary this equation implies that $q = \overline{q} = 0$. Thus with cylindrical symmetry the statistical tensors can be uniquely described by the series of parameters, the *orientation parameters* $B_{\lambda}(I)$ [3], where

$$B_{\lambda}(I) = (2I+1)^{\frac{1}{2}}\rho^{\lambda}_{0}(I) = \sum_{m}(-1)^{I+m}[(2I+1)(2\lambda+1)]^{\frac{1}{2}} \begin{pmatrix} I & I & \lambda \\ -m & m & 0 \end{pmatrix} g(m). \tag{1.24}$$

The orientation parameters are normalized to unity: $B_{0}(I) = 1$.

The form of the interaction used in LTNO is now introduced explicitly. In principle this could be either the interaction of the nuclear static quadrupole moment with an applied electric field gradient or that of the static nuclear magnetic dipole moment with an applied magnetic

field. In this thesis only the latter interaction is considered. Using the direction of the **B**-field as the representation axis, the magnetic energy of the nuclear m-levels is

$$E(m) = -\frac{\mu B}{I} m \tag{1.25}$$

where μ is the nuclear magnetic dipole moment. In accordance with the Boltzmann distribution the populations in thermodynamic equilibrium are

$$g(m) = \langle m|\rho|m\rangle = \mathrm{e}^{m\beta} \Big/ \sum_m \mathrm{e}^{m\beta} \tag{1.26}$$

with

$$\beta = \frac{\mu B}{IkT}. \tag{1.27}$$

Hence the statistical tensors for this magnetically oriented ensemble are given by

$$\rho_0^\lambda(I) = (2I+1)^{-\frac{1}{2}} B_\lambda(I) = \left\{ \sum_m \mathrm{e}^{m\beta} \right\}^{-1} \sum_m (-1)^{I+m} (2\lambda+1)^{\frac{1}{2}} \begin{pmatrix} I & I & \lambda \\ -m & m & 0 \end{pmatrix} \mathrm{e}^{m\beta}. \tag{1.28}$$

Figure 1.1 illustrates the temperature dependence of the orientation parameters.

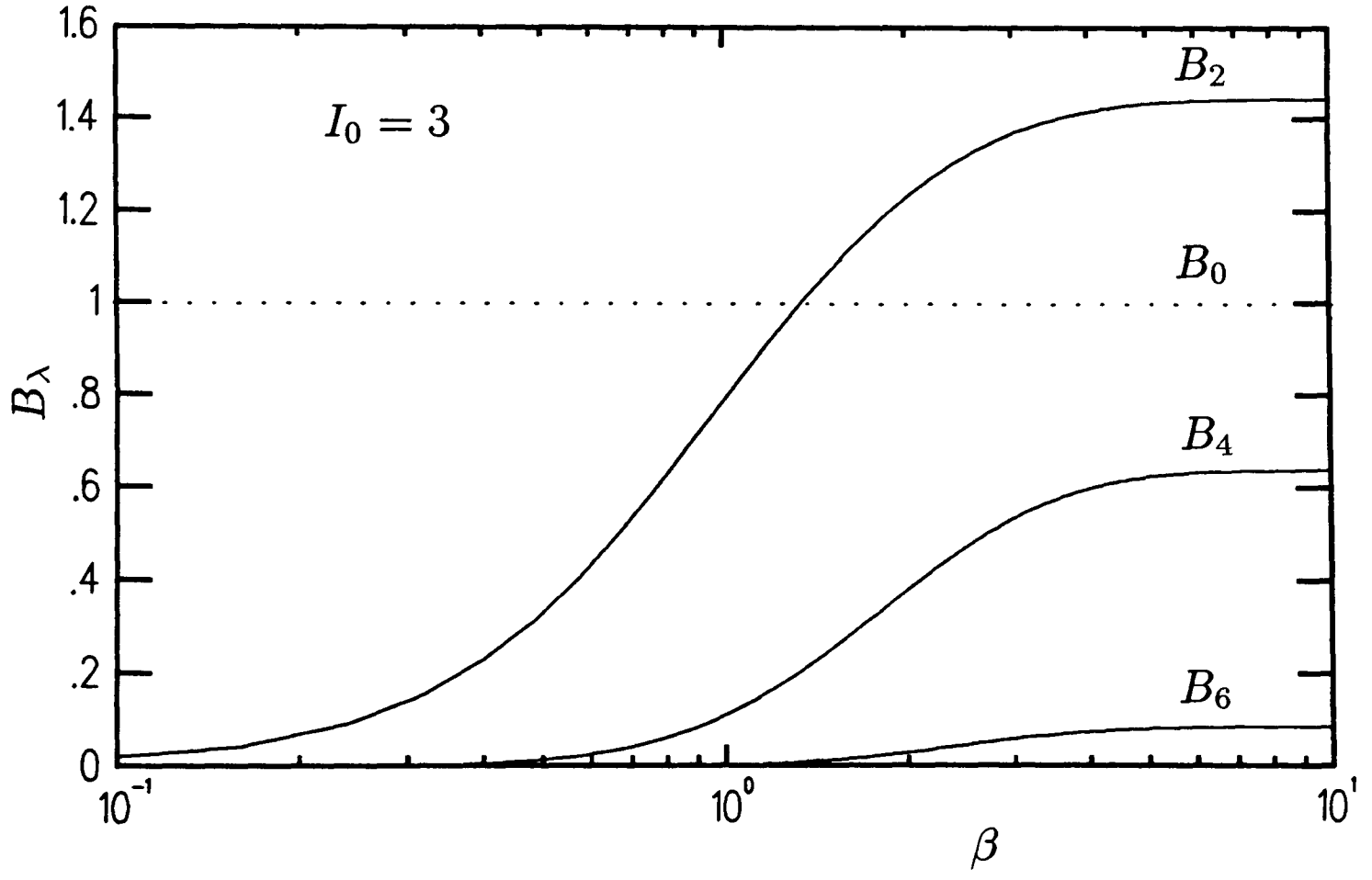

Figure 1.1. The non-zero orientation parameters, B_λ, for a magnetically orientated state of spin 3 as a function of $\beta = \mu B/IkT$.

1.2.4 The efficiency matrices and tensors

The probability of finding a system described by the density matrix ρ in the state $|\phi_n\rangle$ is seen from (1.6) to be given by

$$P(\phi_n) = \langle\phi_n|\rho|\phi_n\rangle. \tag{1.29}$$

Generally it is necessary to calculate this probability when the ensemble is observed by a measuring device which responds to the different pure states with different efficiencies. In direct analogy with the density matrix of the ensemble, such a detector must be described by a weighted *incoherent* superposition of the pure state response characteristics. If the efficiency for detecting the pure state $|\phi_n\rangle$ is denoted by ϵ_n then the result of a measurement with the ensemble in an arbitary state is

$$W = \sum_n \epsilon_n P(\phi_n) = \sum_n \epsilon_n \langle\phi_n|\rho|\phi_n\rangle \tag{1.30}$$

or

$$W = Tr(\epsilon\rho) \tag{1.31}$$

where ϵ is the diagonal matrix with elements ϵ_n. By defining the efficiency operator

$$\epsilon_{op} = \sum_n |\phi_n\rangle\epsilon(n)\langle\phi_n| \tag{1.32}$$

so that the efficiency matrix is the efficiency operator represented in some convenient basis $|m\rangle$

$$\langle m|\epsilon|m'\rangle = \sum_n \langle m|\phi_n\rangle\epsilon(n)\langle\phi_n|m'\rangle \tag{1.33}$$

then it is possible to construct the efficiency tensor according to (1.15)

$$\epsilon_q^\lambda(j_1 j_2) = \sum_{m_1} \langle j_1 m_1|\epsilon|j_2 m_2\rangle(-1)^{j_2+m_2}(2\lambda+1)^{\frac{1}{2}} \begin{pmatrix} j_2 & j_1 & \lambda \\ -m_2 & m_1 & q \end{pmatrix}. \tag{1.34}$$

With these definitions it can be shown [4] that the result of a measurement with a measuring device characterized by efficiency tensor $\epsilon_q^\lambda(j_1 j_2)$ on an ensemble represented by the statistical tensor $\rho_q^\lambda(j_1 j_2)$ is given by

$$W = \sum_{j_1 j_2 \lambda q} \epsilon_q^{\lambda\dagger}(j_2 j_1)\rho_q^\lambda(j_2 j_1). \tag{1.35}$$

Often, as in the case of LTNO, measurements are only made on the emitted radiation implying the existence of, but giving no information on, a final nuclear state. In such cases a summation over the final unobserved states is performed and the measurement is represented by the unit efficiency matrix. If these states have angular momentum j_i then by analogy with (1.20) the corresponding efficiency tensor is

$$\epsilon_q^\lambda(j_1 j_2) = (2j_1+1)^{\frac{1}{2}}\delta_{j_1 j_2}\delta_{\lambda 0}\delta_{q0}. \tag{1.36}$$

Finally, the efficiency matrix for the detection of emitted electromagnetic radiation in helicity states $|\mathbf{p}\tau\rangle$ is considered. Clearly the efficiency operator should be defined in the representation $|\mathbf{p}\kappa\rangle$. Thus

$$\epsilon_{op} = \sum_\kappa |\mathbf{p}\kappa\rangle Q(\kappa)\langle\mathbf{p}\kappa| \tag{1.37}$$

where $Q(\kappa)$ is the response of the detector to the plane wave state of pure polarization $\kappa = \pm 1$. The efficiency matrix is therefore

$$\langle\mathbf{p}\tau|\epsilon|\mathbf{p}\tau'\rangle = \sum_\kappa \langle\mathbf{p}\tau|\mathbf{p}\kappa\rangle Q(\kappa)\langle\mathbf{p}\kappa|\mathbf{p}\tau'\rangle \tag{1.38}$$

and so for a detector which responds only to either positive or negative helicity states

$$\epsilon(+) = \begin{pmatrix} 1 & 0 \\ 0 & 0 \end{pmatrix} \qquad \text{or} \qquad \epsilon(-) = \begin{pmatrix} 0 & 0 \\ 0 & 1 \end{pmatrix}. \tag{1.39}$$

1.2.5 The time evolution of the final state density matrix

An ensemble of nuclei η, which at the time $t = 0$ is described by the density matrix $\langle I_i m_i|\rho|I_i m_i'\rangle$, will ultimately decay into a final nuclear state I_f by the emission of radiation with a definite momentum $\mathbf{p}$. This final state is represented by the final state density matrix $\langle\mathbf{p}\tau I_f m_f|\rho|I_f m_f'\mathbf{p}\tau'\rangle$. This subsection will deal briefly with the derivation of this final state matrix. Starting with the time dependent Schrödinger equation

$$i\frac{\partial}{\partial t}|\Psi\rangle = H|\Psi\rangle \tag{1.40}$$

whose general solution may be written

$$|\Psi(t)\rangle = U(t,t_0)|\Psi(t_0)\rangle \tag{1.41}$$

where $U(t,t_0)$ is the unitary time-evolution operator, then the time behaviour of the density operator is given by

$$\rho_{op}(t) = \sum_n U(t,t_0)|\Psi_n(t_0)\rangle g(n)\langle\Psi_n(t_0)|U^\dagger(t,t_0) = U(t,t_0)\rho_{op}(t_0)U^\dagger(t,t_o). \tag{1.42}$$

From (1.40) and (1.41) it is clear that $U(t,t_0)$ must also satisfy the Schrödinger equation

$$i\frac{\partial}{\partial t}U(t,t_0) = HU(t,t_0). \tag{1.43}$$

The total Hamiltonian of the system is

$$H = H_0 + H_{int} \tag{1.44}$$

where H_0 is that part of the Hamiltonian which gives rise to the stationary states and H_{int} induces transitions between the eigenstates of H_0. Explicitly, for the case of electromagnetic radiation [5]

$$H_{int} = -\int \mathbf{j}(\mathbf{r}')\mathbf{A}(\mathbf{r}',t)dv'. \tag{1.45}$$

Performing the unitary transformation to the Heisenberg representation leads to the operators

$$H_H(t) = \mathrm{e}^{(\frac{iH_0t}{\hbar})}H_{int}\mathrm{e}^{(-\frac{iH_0t}{\hbar})} \tag{1.46}$$

and

$$U_H(t,t_0) = \mathrm{e}^{(\frac{iH_0t}{\hbar})}U(t,t_0)\mathrm{e}^{(-\frac{iH_0t}{\hbar})}. \tag{1.47}$$

The expression corresponding to (1.43) in this representation may be solved to give to first order

$$U_H(t,t_0) = 1 - i\int_{t_0}^{t} H_H(t')dt' + \cdots. \tag{1.48}$$

Combining the second term in this expansion with the transformed analogue of (1.42) and using first-order perturbation theory leads to

$$\begin{aligned}\langle \mathbf{p}\tau I_f m_f|\rho(t)|I_f m_f' \mathbf{p}\tau'\rangle =& \langle \mathbf{p}\tau I_f m_f|\mathrm{e}^{(-\frac{iH_0t}{\hbar})}\left\{\int_0^t \mathrm{e}^{(\frac{iH_0t'}{\hbar})}H_{int}\mathrm{e}^{(-\frac{iH_0t'}{\hbar})}dt'\right\} \\ &\times \rho(0)\left\{\int_0^t \mathrm{e}^{(\frac{iH_0t'}{\hbar})}H_{int}^\dagger\mathrm{e}^{(-\frac{iH_0t'}{\hbar})}dt'\right\}\mathrm{e}^{(\frac{iH_0t}{\hbar})}|I_f m_f' \mathbf{p}\tau'\rangle.\end{aligned} \tag{1.49}$$

The statevector

$$e^{(\frac{iH_0t}{\hbar})}|I_f m'_f \mathbf{p}\tau'\rangle = |I_f m'_f \mathbf{p}\tau'\rangle_H \tag{1.50}$$

is the time independent eigenvector of H_0 in the Heisenberg representation. Since the initial grand density matrix $\rho(0)$ has only the elements $\langle I_i m_i|\rho(0)|I_i m'_i\rangle$, then (1.49) can be written

$$\begin{aligned}\langle \mathbf{p}\tau I_f m_f|\rho(t)|I_f m'_f \mathbf{p}\tau'\rangle =& \langle \mathbf{p}\tau I_f m_f|H_{int}|I_i m_i\rangle\langle I_i m_i|\rho(0)|I_i m'_i\rangle \\ &\times \langle I_i m'_i|H^{\dagger}_{int}|I_f m'_f \mathbf{p}\tau'\rangle \left|\int_0^t e^{i(\omega+\frac{E_f-E_i}{\hbar})t'}dt'\right|^2\end{aligned} \tag{1.51}$$

where the arguments of the exponential arise from the action of $e^{(\frac{iH_0t}{\hbar})}$ on $\langle \mathbf{p}\tau|$ and $\langle I_f m_f|$ and of $e^{(-\frac{iH_0t}{\hbar})}$ on $|I_i m_i\rangle$ respectively. In accordance with the conservation of energy the integral is only appreciably different from zero if $\hbar\omega = \hbar\omega_0 = E_i - E_f$. In the Heisenberg representation the transition matrix elements of (1.51) are time independent

$$\begin{aligned}\langle \mathbf{p}\tau I_f m_f|H_{int}|I_i m_i\rangle &= \int \langle I_f m_f|\mathbf{j}(\mathbf{r}')|I_i m_i\rangle \mathbf{A}_{\mathbf{p}\tau}(\mathbf{r}')dv' \\ &= \sqrt{\frac{2\pi}{L^3\omega}}\langle I_f m_f|\int \mathbf{j}(\mathbf{r}')\mathbf{e}^*_\tau e^{-i\frac{pr'}{\hbar}}dv'|I_i m_i\rangle\end{aligned} \tag{1.52}$$

since the time dependence of $\mathbf{j}(\mathbf{r}', \mathbf{t})$, namely $e^{\frac{i(E_f-E_i)}{\hbar}t}$, is exactly compensated by that of $\mathbf{A}(\mathbf{r}, \mathbf{t})$, namely $e^{i\omega t}$. By integrating over ω and multiplying by the density of states, the last term in (1.51) results in a factor $L^3\omega_0^2 t d\Omega/(2\pi)^2$. This is correct for values of t much smaller than the mean life time $1/\lambda_\gamma$, where λ_γ is the total transition probability. For times larger than this, t should be replaced by the radioactive decay factor $(1 - e^{-\lambda_\gamma t})/\lambda_\gamma$. Thus the elements of the final state density matrix are

$$\begin{aligned}\langle \mathbf{p}\tau I_f m_f|\rho(t)|I_f m'_f \mathbf{p}\tau'\rangle =& \frac{d\Omega}{2\pi}\omega\frac{(1-e^{-\lambda_\gamma t})}{\lambda_\gamma}\langle I_f m_f|\int \mathbf{j}(\mathbf{r}')\mathbf{e}^*_\tau e^{-\frac{ipr'}{\hbar}}dv'|I_i m_i\rangle \\ &\times \langle I_i m_i|\rho(0)|I_i m'_i\rangle\langle I_i m'_i|\int \mathbf{j}(\mathbf{r}')\mathbf{e}_\tau e^{\frac{ipr'}{\hbar}}dv'|I_f m'_f\rangle.\end{aligned} \tag{1.53}$$

Introducing the absolute transition amplitudes $\gamma(\pi L, I_i \rightarrow I_f)$ [4] which are proportional to the multipole expansions of (1.52) and again using the Clebsh-Gordan series for the product of two D-matrices gives

$$\begin{aligned}\langle \mathbf{p}\tau I_f m_f|\rho(\infty)|I_f m_f' \mathbf{p}\tau'\rangle =& \frac{d\Omega}{8\pi\lambda_\gamma}\sum_{m_i m_i'}(2I_i+1)\sum_{LL'\lambda}[(2L+1)(2L'+1)]^{\frac{1}{2}} \\ &\times(2\lambda+1)\begin{pmatrix} I_f & L & I_i \\ m_f & M & -m_i\end{pmatrix}\begin{pmatrix} I_f & L' & I_i \\ m_f' & M' & -m_i'\end{pmatrix} \\ &\times\begin{pmatrix} L & L' & \lambda \\ M & -M' & q\end{pmatrix}\begin{pmatrix} L & L' & \lambda \\ \tau & -\tau' & \mu\end{pmatrix}\langle I_i m_i|\rho(0)|I_i m_i'\rangle \\ &\times[\gamma(EL)+\tau\gamma(ML)][\gamma^*(EL')+\tau'\gamma^*(ML')]D^{\lambda *}_{q\mu}(\mathbf{e_z}\rightarrow\mathbf{k})\end{aligned} \tag{1.54}$$

for times $\lambda_\gamma t \sim \infty$. The diagonal elements of this final state density matrix expression give the absolute probability that a photon with helicity τ is emitted into the solid angle $d\Omega$ in the direction $\mathbf{p}$ from the initial state $\rho(0)$ to form the final nuclear state $|I_f m_f\rangle$.

From this expression the final state statistical tensor $\rho^{\lambda_f}_{q_f}(I_f,\mathbf{p})$ may be constructed in accordance with (1.15). This is a 2×2 matrix in the helicity space τ, whose four elements in $|Im\rangle$ space are

$$\begin{aligned}\langle\tau|\rho^{\lambda_f}_{q_f}(I_f,\mathbf{p})|\tau'\rangle =& \frac{d\Omega}{8\pi\lambda_\gamma}\sum_{\lambda_i\lambda q_i q LL'}(-1)^{\lambda_i-q_i}(2\lambda+1)^{\frac{1}{2}}\left(\frac{2I_i+1}{2I_f+1}\right)^{\frac{1}{2}} \\ &\times\begin{pmatrix}\lambda_f & \lambda & \lambda_i \\ q_f & q & -q_i\end{pmatrix}\rho^{\lambda_i}_{q_i}(I_i)D^{\lambda *}_{q\mu}(\mathbf{e_z}\rightarrow\mathbf{k})[\gamma(EL)+\tau\gamma(ML)] \\ &\times[\gamma^*(EL')+\tau'\gamma^*(ML')]\frac{\begin{pmatrix} L & L' & \lambda \\ \tau & -\tau' & \mu\end{pmatrix}}{\begin{pmatrix} L & L' & \lambda \\ 1 & -1 & 0\end{pmatrix}}F^{\lambda_f\lambda_i}_\lambda(LL'I_fI_i)\end{aligned} \tag{1.55}$$

where the $F^{\lambda_f\lambda_i}_\lambda(LL'I_fI_i)$ are the generalized F-coefficients defined by

$$\begin{aligned}F^{\lambda_f\lambda_i}_\lambda(LL'I_1I_0) =& (-1)^{L'+\lambda_1+\lambda_0+1}[(2I_0+1)(2I_1+1)(2L+1)(2L'+1) \\ &\times(2\lambda_0+1)(2\lambda_1+1)(2\lambda+1)]^{\frac{1}{2}}\begin{pmatrix} L & L' & \lambda \\ 1 & -1 & 0\end{pmatrix}\begin{Bmatrix} I_1 & L & I_0 \\ I_1 & L' & I_0 \\ \lambda_1 & \lambda & \lambda_0\end{Bmatrix}.\end{aligned} \tag{1.56}$$

If one of the oriented states I_0 or I_1 is random, so that either λ_0 or λ_1 is zero, then the generalized F-coefficients reduce to the ordinary F-coefficients $F_\lambda(LL'I_1I_0)$.

1.2.6 The angular distribution of gamma radiation from LTNO sources

Into (1.55), which is perfectly general being derived only from the assumption of the invariance of interactions under three dimensional rotations, the conditions specific to nuclear orientation problems are now introduced. Firstly, the statistical tensor of the initial state can be replaced by the orientation parameters (1.24). Secondly, the final nuclear state is *not* observed and so its efficiency tensor is given by (1.36). Only the radiation quanta are observed, in the direction **k** using a detector described by the efficiency matrix ϵ. Again it will be assumed that the observed quanta are of electromagnetic origin, although the formalism applies also to alpha and beta radiation. Thus using (1.35) the probability of detecting the photon is

$$W(\mathbf{k}) = \sum_{\tau\tau'} \langle \tau | \rho_0^0(I_f) | \tau' \rangle \langle \tau' | \epsilon | \tau \rangle (2I_f + 1)^{\frac{1}{2}} \tag{1.57}$$

where $\langle \tau | \rho_0^0(I_f) | \tau' \rangle$ is given by (1.55).

Considering the detection of circularly polarized radiation with helicity τ by an ideal detector with efficiency matrix (1.39), then $\tau = \tau'$ and so

$$\begin{aligned} W(\theta, \tau) = & \frac{d\Omega}{8\pi\lambda_\gamma} \sum_{\lambda q L L'} \tau^\lambda \tau^{L+L'} B_\lambda(I_i) F_\lambda(LL' I_f I_i) \\ & \times [\gamma(EL) + \tau\gamma(ML)][\gamma^*(EL') + \tau\gamma^*(ML')] P_\lambda(\cos\theta) \end{aligned} \tag{1.58}$$

where use has been made of the fact that [2]

$$D_{00}^{\lambda *}(\phi, \theta, 0) = P_\lambda(\cos\theta). \tag{1.59}$$

The angles ϕ, θ are the polar angles of the observation direction **k** with respect to coordinate system xyz in which the initial state statistical tensor is represented. With the inclusion of the parity selection rules for electromagnetic transitions: $L + L'$ even (odd) if both components are electric or magnetic (one component electric while the other magnetic), the *circular polarization distribution* is obtained as

$$W(\theta, \tau) = \frac{d\Omega}{8\pi} \sum_\lambda \tau^\lambda B_\lambda(I_i) A_\lambda P_\lambda(\cos\theta) \tag{1.60}$$

where the *angular distribution coefficients*, A_λ, are given by

$$A_\lambda = \sum_{L\pi L'\pi'} F_\lambda(LL' I_f I_i) \gamma(\pi L) \gamma^*(\pi' L') \Big/ \sum_{L\pi} |\gamma(\pi L)|^2 \tag{1.61}$$

with the normalization $A_0 = 1$; and by definition

$$\lambda_\gamma = \sum_{L\pi} |\gamma(\pi L)|^2. \tag{1.62}$$

For two mixed multipoles L and $L' = L + 1$ with amplitude mixing ratio $\delta = \gamma(\pi' L + 1)/\gamma(\pi L)$ the angular distribution coefficients can be written in the form

$$A_\lambda = \left\{ F_\lambda(LLI_f I_i) + 2\delta F_\lambda(LL+1 I_f I_i) + \delta^2 F_\lambda(L+1 L+1 I_f I_i) \right\} \Big/ \left\{ 1 + \delta^2 \right\}. \tag{1.63}$$

Figure 1.2 shows an example of the δ dependence of the angular distribution coefficients.

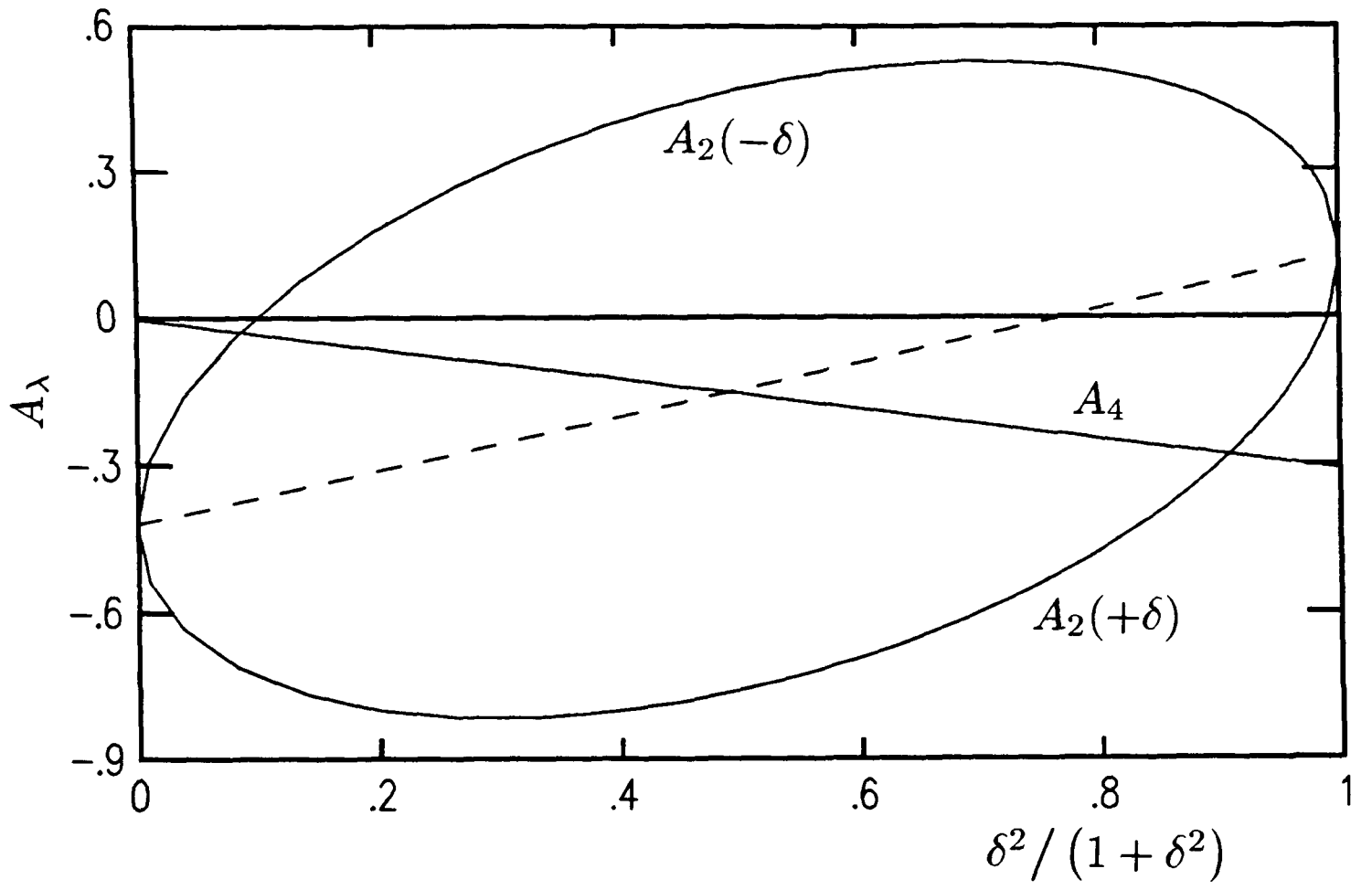

Figure 1.2. The non-zero angular distribution coefficients, A_λ, as a function of δ for gamma radiation in a mixed $2 \rightarrow 2$ transition.

The *directional distribution* of gamma radiation is now obtained by summing (1.60) over both helicity states which yields a factor of 2(0) if λ is even (odd). Thus

$$W(\theta) = \frac{d\Omega}{4\pi} \sum_{\lambda=even} B_\lambda(I_i) A_\lambda P_\lambda(\cos\theta). \tag{1.64}$$

1.2.7 Unobserved intermediate radiations

Generally in LTNO measurements the detected gamma radiation quantum will be preceeded by a cascade of unobserved intermediate radiation. In order to construct the final state statistical tensor, the procedure outlined in subsection 1.2.5 must be performed in turn for each emitted photon. Since only the last of these is observed it is necessary to integrate the final state statistical tensor over solid angle for each unobserved quantum. In this way it can be shown [4] that the final state statistical tensor $\rho_{q_n}^{\lambda_n}(I_n)$ that describes the ensemble after the emission of an unobserved gamma radiation γ_n from an initial state $\rho_{q_{n-1}}^{\lambda_{n-1}}(I_{n-1})$ is obtained from the relation

$$\rho_{q_n}^{\lambda_n}(I_n) = U_{\lambda_n}(\gamma_n)\rho_{q_{n-1}}^{\lambda_{n-1}}(I_{n-1})\delta_{\lambda_n\lambda_{n-1}}\delta_{q_nq_{n-1}} \tag{1.65}$$

where the *de-orientation coefficients*, U_λ, have been introduced which are given by

$$U_\lambda = \sum_{L\pi} U_\lambda(I_iI_fL)|\gamma(\pi L)|^2 \Big/ \sum_{L\pi} |\gamma(\pi L)|^2 \tag{1.66}$$

or in terms of δ

$$U_\lambda = \{U_\lambda(I_iI_fL) + \delta^2 U_\lambda(I_iI_fL+1)\} \Big/ \{1+\delta^2\} \tag{1.67}$$

with the *de-orientation factor* defined by

$$U_\lambda(I_iI_fL) = (-1)^{I_i+I_f+\lambda+L}[(2I_i+1)(2I_f+1)]^{\frac{1}{2}} \begin{Bmatrix} I_i & I_i & \lambda \\ I_f & I_f & L \end{Bmatrix}. \tag{1.68}$$

The de-orientation factors are normalized to unity: $U_0 = 1$. Hence, for a cascade of n unobserved photons the final state statistical tensor is

$$\rho_q^\lambda(I) = U_\lambda(\gamma_n)U_\lambda(\gamma_{n-1})\cdots U_\lambda(\gamma_1)\rho_q^\lambda(I_0). \tag{1.69}$$

In particular, the directional distribution of a gamma radiation γ_{n+1} that is emitted from a state I_n, formed by the emission of n unobserved quanta from an axially oriented state I_0, is

$$\begin{aligned} W(\theta) &= \sum_{\lambda=even} B_\lambda(I_0)U_\lambda(\gamma_1)U_\lambda(\gamma_2)\cdots U_\lambda(\gamma_n)A_\lambda(\gamma_{n+1})P_\lambda(\cos\theta) \\ &= \sum_{\lambda=even} B_\lambda(I_0)U_\lambda^{cascade}A_\lambda P_\lambda(\cos\theta). \end{aligned} \tag{1.70}$$

where the solid angle factor has been dropped for simplicity. If several different cascades are possible between the oriented level and the observed radiation then an effective de-orientation

coefficient is obtained as the average of the $U_\lambda^{cascade}$, weighted by the appropriate branching intensity (which should be normalized to unity).

The formalism of this subsection also applies without modification to alpha, beta and electron capture decay. In the LTNO experiments to be described in this thesis, the gamma cascade resulting in the observed photon is preceeded by the lepton quantum which initiates the nuclear decay. In this case the term $U_\lambda(\gamma_1)$ in (1.70) refers to the lepton field rather than to the electromagnetic field. The appropriate leptonic de-orientation factor is calculated from (1.66) with $\gamma(L)$ understood to be the amplitude of the L^{th} multipole component in the lepton field and L the total angular momentum carried away by both the electron and neutrino.

In as much as the observed directional distribution in LTNO is dependent upon nuclear factors alone, (1.70) represents the final expression for its angular dependence and in principle is an infinite series. However the tensor nature of its coefficients, manifest in their dependance upon the n-j symbols [2], imposes limitations upon its maximum rank λ. By inspection these can be seen to be:

$$\begin{aligned} B_\lambda(I_0) &\equiv 0 \quad \text{if} \quad \lambda > 2I_0 \\ U_\lambda(LI_iI_f) &\equiv 0 \quad \text{if} \quad \lambda > 2I_i \quad \text{or} \quad \lambda > 2I_f \\ A_\lambda(LL'I_iI_f) &\equiv 0 \quad \text{if} \quad \lambda > L + L' \quad \text{or} \quad \lambda > 2I_i. \end{aligned} \tag{1.71}$$

Since the gamma transition probability greatly reduces as the multipole order increments, transitions with $L > 2$ are experimentally rare. Thus in the majority of cases and in the absence of further selection rules the directional distribution series may be truncated to

$$W(\theta) = 1 + B_2U_2A_2P_2(\cos\theta) + B_4U_4A_4P_4(\cos\theta) \tag{1.72}$$

where use has been made of the fact that the zero rank coefficients are normalized to unity.

1.3 Non-nuclear contributions to the angular distribution in LTNO

In the derivations of the previous section only the "nuclear" contributions to the angular distribution have been considered explicitly. Attention will now be given to those aspects of the LTNO system which might be termed "non-nuclear" in origin.

1.3.1 The solid angle correction factors

The directional distribution of (1.70) applies only to detection of nuclear radiation at a single angle θ. Owing to the finite solid angle subtended by the detector, the observed angular distribution will differ somewhat from this ideal distribution expected for "point" detectors. The proper interpretation of precision angular distribution measurements thus depends on the accurate knowledge of this difference.

To perform this correction it is necessary to integrate (1.70), weighted by the detector efficiency, over the subtended solid angle. Consider, therefore, the case of an axially symmetric detector centered along the radius vector with polar angle θ_0. Using this radius vector as the initial line the polar angles β, such that $\theta = \theta_0 + \beta$ and $\Delta\beta$, such that the detector subtends a right cone of semi-angle $\Delta\beta$ at the origin, may be defined. In this co-ordinate system the useful absorption of gamma radiation incident onto the detector is proportional to

$$\left\{1 - e^{-\tau(\gamma)x(\beta)}\right\} \tag{1.73}$$

where $\tau(\gamma)$ is the full energy absorption coefficient and $x(\beta)$ is the path length through the active volume of the detector.

The measured directional distribution will therefore be given by

$$\overline{W(\theta)} = \frac{\int W(\theta)\left\{1 - e^{-\tau(\gamma)x(\beta)}\right\} d\Omega}{\int \left\{1 - e^{-\tau(\gamma)x(\beta)}\right\} d\Omega}. \tag{1.74}$$

Separating out the angular terms from this expression it is seen that the quantities of interest are the integrals

$$I_\lambda = \int P_\lambda(\cos(\theta_0 + \beta))\left\{1 - e^{-\tau(\gamma)x(\beta)}\right\} \sin\beta d\beta d\phi. \tag{1.75}$$

Following the method of Rose [6] the spherical harmonic addition theorem

$$P_\lambda(\cos(\theta_0 + \beta)) = P_\lambda(\cos\theta_0)P_\lambda(\cos\beta) + \cdots \tag{1.76}$$

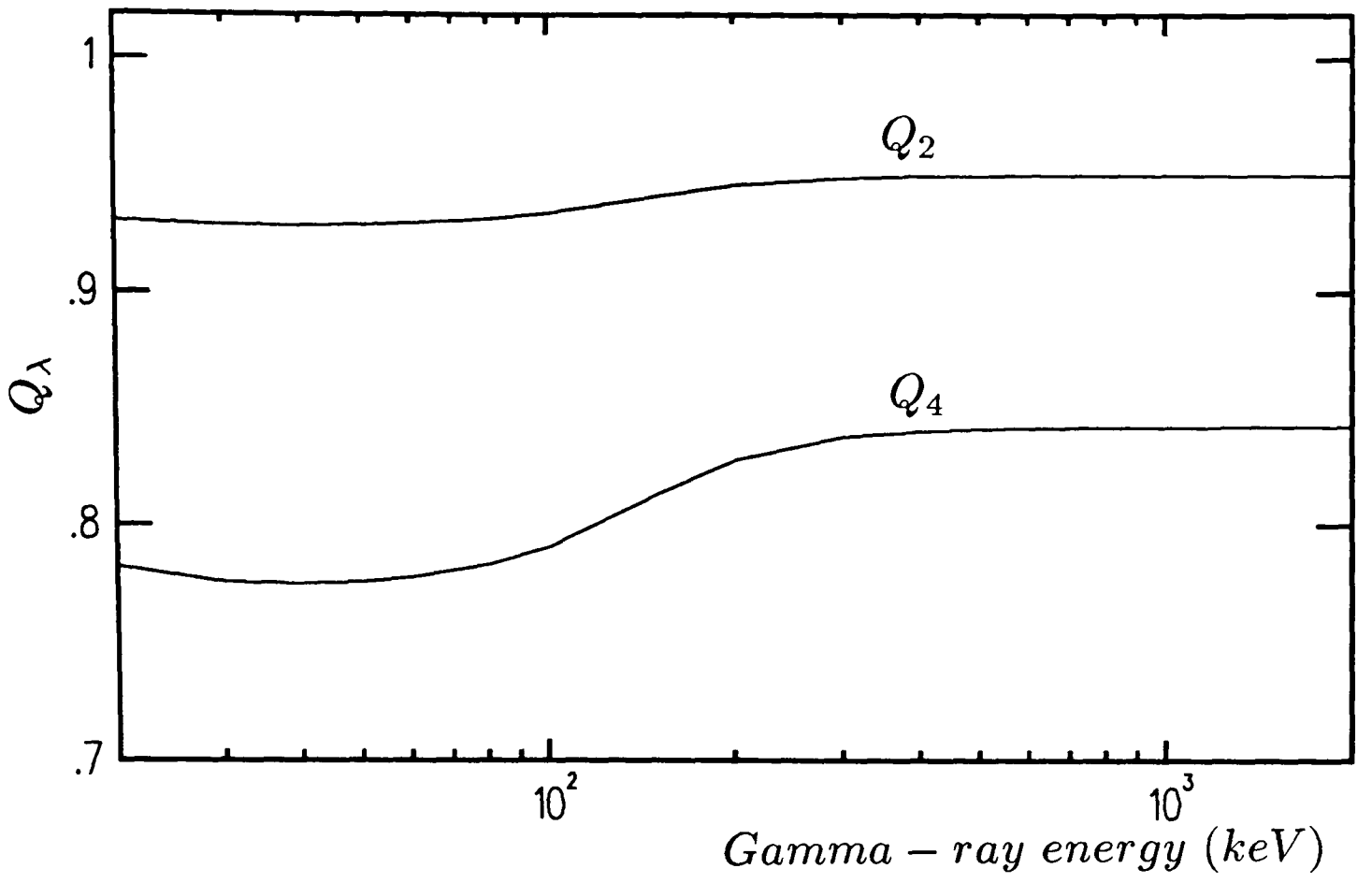

Figure 1.3. The dependence of the solid angle correction factors, Q_λ, on gamma ray energy for a Ge(Li) detector of typical dimensions at 8 cm from the source.

is applied, where the ellipses indicate azimuthal terms. These do not contribute to the integration over ϕ and so (1.75) reduces to

$$I_\lambda = 2\pi P_\lambda(\cos\theta_0) \int_0^{\Delta\beta} P_\lambda(\cos\beta) \left\{1 - e^{-\tau(\gamma)x(\beta)}\right\} \sin\beta d\beta. \tag{1.77}$$

Introducing the *solid angle correction factors*, Q_λ, defined by

$$Q_\lambda P_\lambda(\cos\theta_0) = \frac{I_\lambda}{I_0} \tag{1.78}$$

enables the corrected directional distribution (1.74) to be written in the form

$$\overline{W(\theta)} = \sum_\lambda B_\lambda U_\lambda A_\lambda Q_\lambda P_\lambda(\cos\theta_0). \tag{1.79}$$

The evaluation of the integrals I_λ requires a knowledge of both the detector geometry and the functional form of absorption coefficients $\tau(\gamma)$. These are calculated from the theoretical photoelectric, Compton and pair production cross sections of the detecting material using Monte Carlo simulations [7]. By this method, correction factors have been calculated by Yates [8] for Na(I) detectors and by Camp and Van Lehn [9] and Krane [10] for Ge(Li) detectors. The correction factors used in the present work are calculated using the method of Krane.

Typical dependences of the solid angle correction factors on gamma ray energy and detector to source distance are illustrated in figures 1.3 and 1.4.

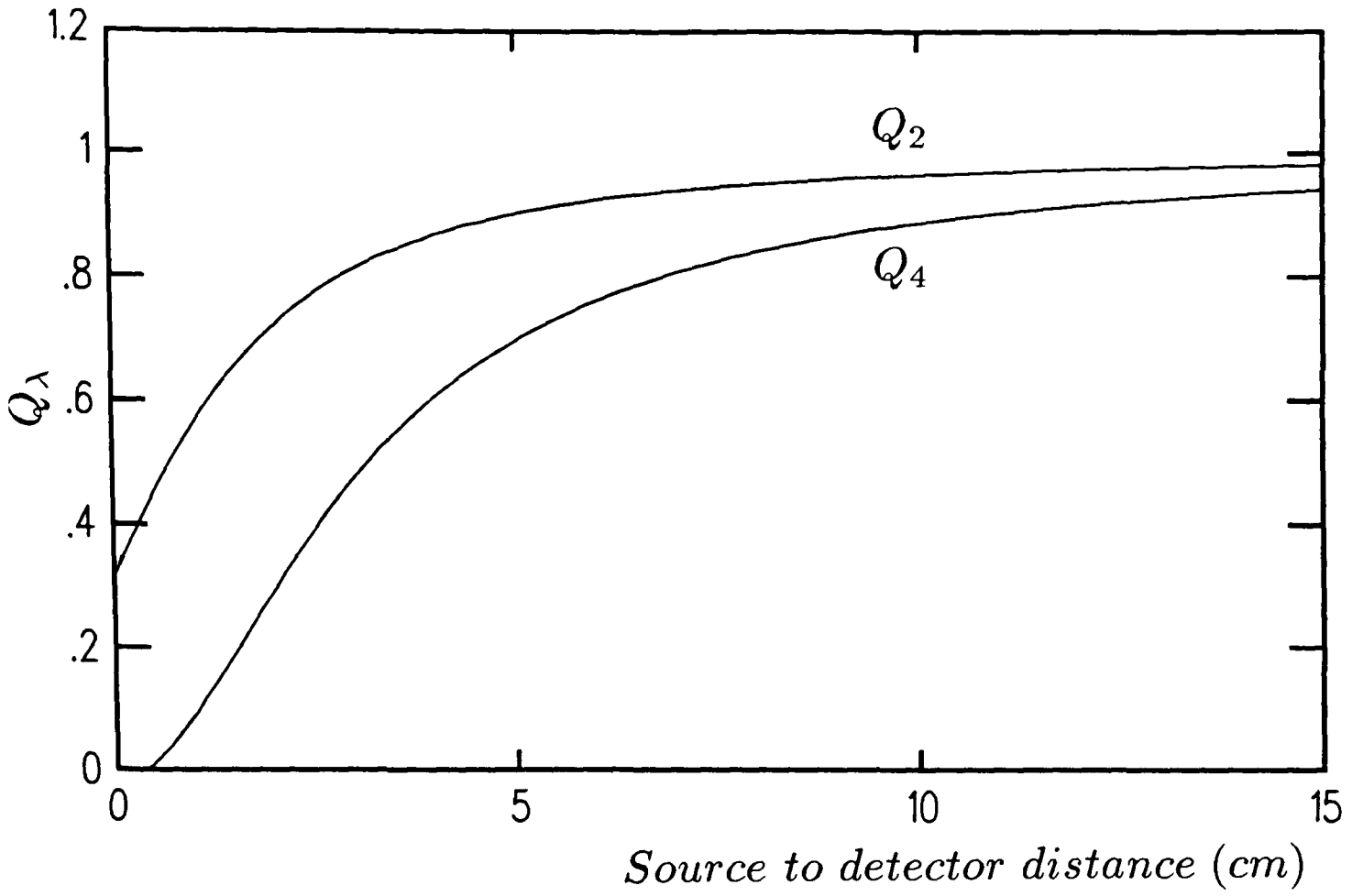

Figure 1.4. The dependence of the solid angle correction factors, Q_λ, on source to detector distance for a Ge(Li) detector of typical dimensions at a gamma ray energy of 500 keV.

1.3.2 The magnetic hyperfine interaction

In subsection 1.2.3 the orienting interaction was considered to be that between the static nuclear magnetic (electric) moment with an externally applied magnetic field (electric field gradient). In the magnetic case, the degree of nuclear orientation is determined largely by the parameter β of (1.27). From (1.26) it can be seen that an appreciable alignment is characterized by $\beta \sim 1$. For a nucleus with a gyromagnetic ratio of unity and taking 5 mK as a lower limit to the continuously attainable temperature of the present generation of ^{3}He - ^{4}He dilution refrigerators, then a magnetic field of at least 15 T would be required for successful orientation. The attainment of such a high field whilst simultaneously maintaining low temperatures is not readily achieved. Thus the "brute force" method, although simple in principle and applicable to all types of nuclei, is not always practical.

Most of the successful orientation experiments have made use of the hyperfine interaction in solids to avoid the need for such high values of B_{app}/T. All experiments described in this thesis have been performed on atomic nuclei implanted into a polycrystalline iron host. The origins of the magnetic hyperfine field [11] will now be briefly discussed.

Considering first the case of a free atom, an electronic current density $\mathbf{J}_e dr$ at a point $\mathbf{r}$ in a coordinate system centered at the nucleus will produce a magnetic field at the nucleus

$$\mathbf{B} = \frac{\mu_0}{4\pi}\frac{\mathbf{r}\times\mathbf{J}_e}{r^3}d\tau. \tag{1.80}$$

Writing $\mathbf{J}_e d\tau = \mathbf{v}dq$, where $\mathbf{v}$ is the velocity of the charge element dq and noting that the electronic angular momentum is $\mathbf{l} = m_e\mathbf{r}\times\mathbf{v}$, then for each electron i

$$\mathbf{B}_{l_i} = -\frac{\mu_0}{4\pi}2\mu_B\mathbf{l}_i\langle r_{l_i}^{-3}\rangle. \tag{1.81}$$

Performing the summation over i, the contributions from closed subshells disappear and in the LS coupling limit

$$\mathbf{B}_L = -\frac{\mu_0}{4\pi}2\mu_B\mathbf{L}\langle r_l^{-3}\rangle. \tag{1.82}$$

Similarly the electron spin will also give rise to a magnetic field, but since there is now a finite probability of electrons with non-zero spin existing at the nucleus it is necessary to consider separately the contributions from electrons "inside" and "outside" of the nucleus. Electrons outside the nucleus give rise to a simple dipole sum field

$$\mathbf{B}_s = -\frac{\mu_0}{4\pi}g_s\mu_B\sum_i\left[3(\mathbf{s_i}\cdot\hat{\mathbf{r}})\hat{\mathbf{r}} - \mathbf{s_i}\right]\langle r_{si}^{-3}\rangle \tag{1.83}$$

while those inside give rise to the Fermi contact term, which can be written in the LS coupling limit as

$$\mathbf{B}_F = -\frac{\mu_0}{4\pi}\frac{8\pi}{3}g_s\mu_B|\psi_s(0)|^2\mathbf{S}. \tag{1.84}$$

In the solid state there are two mechanisms which give rise to such a contact field. In a ferromagnet the *s-d* exchange interaction between the magnetic $3d$-electrons and the *s*-like conduction electrons removes the degeneracy of the $s^\uparrow$ and $s^\downarrow$ conduction bands. This leads to a net surplus of spin-up electrons and consequently a "conduction electron polarization" Fermi contact term of the form

$$\mathbf{B}_F = -\frac{\mu_0}{4\pi}\frac{8\pi}{3}g_s\mu_B\left\{|\psi_s^\uparrow(0)|^2 - |\psi_s^\downarrow(0)|^2\right\}\mathbf{S}. \tag{1.85}$$

Secondly, due to the overlap between the polarized conduction electrons of the magnetic host with the inner *s*-electrons of the non-magnetic impurity, it is possible for filled orbitals with spin parallel to the net spin to have a different density distribution from those same orbitals with antiparallel spin. The result of such exchange correlation effects, which for example can

be incorporated into Hartree-Fock calculations by relaxing the condition that the radial wavefunction is independent of the spin orientation, is that a closed s-subshell can exhibit a net spin without losing its spherical symmetry. These core s-electrons then contribute to the hyperfine field via an "exchange core polarization" contact term of the form (1.85). Such contact terms are important for all systems with non-zero resultant spin. However their significance is greatest for d-electron atoms for which in many cases the strong ligand field present in the lattice serves to quench the orbital contribution. Further, in a system of cubic symmetry such as iron the "outside" spin term vanishes.

These mechanisms give rise to the large magnetic fields, typically $10-1000$ T for impurities in an iron host, required at the nucleus. It only remains to apply a modest external field B_{app} to polarize the host lattice and produce the axis of quantization. Fields of only ~ 0.7 T are sufficient to almost completely ($> 99\%$) align the domains in iron. B_{app} is subject to both the Knight shift and demagnetizing corrections. The former is usually small ($\sim 1\%$), while the latter is also small for a thin foil magnetized in its plane. Since also $B_{hyp} \gg B_{app}$, it is usually adequate to neglect these effects and take the effective magnetic field at the nucleus to be simply $|\mathbf{B}_{hyp} + \mathbf{B}_{app}|$.

The hyperfine interaction experienced by an impurity atom is of course highly sensitive to the nature of the surrounding lattice. It is not necessarily the case that the sites occupied by impurity atoms in the host lattice are unique and so they will be subject to a range of different hyperfine fields. An NMR experiment on oriented nuclei (NMR/ON) would in principle detect separately all of these different interactions. A static LTNO experiment on the other hand detects only the average hyperfine interaction for the system. If all the possible implantation lattice sites are labelled i, with associated magnetic hyperfine fields B^i_{hyp} and population probabilities f_i, then the observed directional distribution of gamma radiation in a static LTNO experiment will be

$$W(\theta) = \sum_{\lambda i} f_i B_\lambda(B^i_{hyp}) U_\lambda A_\lambda Q_\lambda P_\lambda(\cos\theta) \tag{1.86}$$

or in its truncated form

$$W(\theta) = 1 + \sum_i f_i \Big\{ B_2(B^i_{hyp}) U_2 A_2 Q_2 P_2(\cos\theta) + B_4(B^i_{hyp}) U_4 A_4 Q_4 P_4(\cos\theta) \Big\} \tag{1.87}$$

where use has been made of the fact that $\sum_i f_i = 1$. These are the final forms of the directional distribution expressions and will be used throughout this thesis.

Finally the magnetic hyperfine anomaly is discussed. This does not influence the form of the angular distribution formula, but is included here for the sake of completeness.

Once determined for one isotopic implant of a given element, the hyperfine field being atomic in its nature should be the same for all other members of that isotopic chain which are implanted under similar conditions. However, implicit in the Fermi contact term (1.84) and the lack of an "inside" orbital contribution is the assumption of a point nucleus. In reality the nucleus is an extended body implying that (1.84) should be integrated over the nuclear volume and that an "inside" orbital contribution should also be considered since electrons of non-zero orbital angular momentum exist within the nucleus. This provides a nucleus dependent perturbation to the hyperfine interaction energy $-\mu \cdot \mathbf{B}$, which can be considered as a nucleus dependent correction to an otherwise atomic hyperfine field. The hyperfine anomaly is related to the fractional change in the hyperfine interaction when the nuclear perturbation is "switched on" and typically being only $\sim 1\%$ is neglected in this thesis. Therefore in chapter 4 it is assumed that the magnetic hyperfine field as determined for one nucleus may be applied without correction to all other nuclei in the same isotopic chain.

1.3.3 The nature of the lattice site occupation

Clearly, the interpretation of static LTNO data can only proceed once the parameters B^i_{hyp} and f_i of (1.86) are known. In the bromine experiments described in chapter 4 samples were prepared by implanting the radioactive nuclei emerging from an isotope separator at energies of ~ 60 keV into the iron host matrix. Monte Carlo simulations [12] show that the entrant nucleus produces a series of primary lattice recoils which can go on to initiate independent subcascades. The resulting vacancies and interstitials typically cover a volume of order (100lattice spacing)^3. The local temperatures produced in these cascades can reach 5000 K and last for about 10 ps [13] during which time a degree of self-annealing can occur. Frequently this leaves the implant in an undamaged area of the lattice, with residual vacancies and interstitials several atomic spacings away. Thus, provided that the implanted dose is not so great that the entire lattice is significantly damaged, it can be expected that a fair proportion of the implanted nuclei will come to rest in undamaged substitutional sites. This critical dose may be taken to be $\sim 10^{14}$ ions cm^{-2} or ~ 1 atomic percent. By comparison a typical LTNO dose is only $\sim 0.001 - 0.1$ atomic percent.

The actual fraction of nuclei which occupy substitutional sites and also the nature of any alternative sites depends on their "solubility" in the host lattice. For "soluble" implants it is

reasonable to make the simple assumption that the system contains only two sites, the substitutional site with magnetic hyperfine field B_{sub} and associated population f and a second site with zero field and population $1-f$, corresponding to incompletely implanted activity on the surface of the lattice. Experimentally this is generally found to be a satisfactory assumption with values of f approaching 100%, especially where the lattice has been annealed after implantation. In this regime the truncated directional distribution is simply

$$W(\theta) = 1 + f\Big\{B_2(B_{sub})U_2A_2Q_2P_2(\cos\theta) + B_4(B_{sub})U_4A_4Q_4P_4(\cos\theta)\Big\}. \qquad (1.88)$$

For "insoluble" implants the situation is potentially very different. If the implanted ion is much smaller than the host then the lattice will contract locally and will therefore trap interstitials. In the reverse situation, implants will tend to accumulate vacancies. Thus, provided that the enthalpy of solution is sufficient to bind the interstitials or vacancies, the favoured sites will not necessarily be substitutional. This will be especially the case if the temperature is above 140 K or 200 K, the temperatures at which interstitials and vacancies respectively achieve full mobility in iron [14]. Thus it is expected that the proportion of insoluble implants in substitutional sites will be larger for cold implantation (< 4 K) than for room temperature implantation. In general therefore, insoluble implantations will exhibit a substitutional site and one or more sites associated with interstitials or vacancies, together with sites experiencing small or zero net hyperfine fields. In this complicated regime it is necessary to retain the general directional distribution expression (1.87).

This subject will be discussed further, with specific reference to bromine ions, in chapter 4.

1.4 Electric quadrupole orientation

In addition to the magnetic hyperfine field it is also possible to exploit the large electric field gradients in solids to achieve orientation and hence a measurement of the nuclear electric quadrupole moment [15]. This can only be done in a host lattice of non-cubic symmetry where the quadrupole interaction is non-vanishing. Also the requirement of a uniquely defined direction for the electric field gradient necessitates the use of a single crystal host.

Since iron is a cubic lattice the electric interaction disappears for implants occupying substitutional sites. For non-substitutional sites this symmetry is destroyed and a composite magnetic

and electric interaction must be considered. In a polycrystalline lattice the contribution to the total orientation arising from the electric quadrupole interaction is greatly reduced since the principal axis of each microcrystal is randomly directed in space. Nevertheless, the integrated effect of the individual electric interactions leads to an attenuation of the observed orientation when compared to that expected from the magnetic interaction alone. The magnitude of this attenuation depends upon the relative strengths of the magnetic and electric interactions as well as the temperature and oriented spin [16].

With regard to the experiments described in this thesis, all were performed on nuclei implanted into polycrystalline iron foils. In the case of the bromine isotopes studied in chapter 4 this resulted in a significant proportion of nuclei ($\sim 30\%$) coming to rest in non-substitutional lattice sites. However, the resulting electric quadrupole attenuations are expected to be small, typically a few per cent. On the other hand, the iridium sample used in the time reversal experiment discussed in chapter 8 was melted with iron leading to an almost complete occupation of substitutional sites. With full cubic symmetry thus maintained, the electric quadrupole interaction vanishes completely.

Since the role of the electric quadrupole interaction is either small or non existent it is not considered in this work.

1.5 Nuclear spin-lattice relaxation

To conclude this brief survey of the principles of LTNO the situation that arises when the assumption of thermodynamic equilibrium fails will be considered. In such cases it is necessary to include the time dependence of the approach to equilibrium into the calculation of the orientation parameters [17]. It will be assumed that the spin system is highly dilute so that impurities are coupled only to the host lattice and mutual interactions within the nuclear spin system are negligible. In this limit the nuclei relax independently and so cannot be described by a temperature. If this relaxation proceeds via an exchange of energy with the degenerate Fermi gas formed by the conduction electrons of the (metallic) host lattice then the spin-lattice interaction is given by the Hamiltonian

$$H_{S-L} = A\mathbf{I}\cdot\mathbf{S} = AI_zS_z + \frac{1}{2}(S_+I_- + S_-I_+) \tag{1.89}$$

where **I** is the nuclear spin operator and **S** the effective lattice spin operator which is related to the orbital and spin operators of the conduction electrons. Transitions induced by the non-diagonal elements link states differing by one unit in the magnetic quantum number. The corresponding transition probabilities, derived from Fermi's golden rule, are

$$W_{m,m+1} = \frac{\Delta E}{2kC_k} \frac{[I(I+1) - m(m+1)]}{e^{\Delta E/kT} - 1} \tag{1.90}$$

and

$$W_{m+1,m} = W_{m,m+1} + \frac{\Delta E}{2kC_k} [I(I+1) - m(m+1)]\,. \tag{1.91}$$

Here ΔE is the magnetic substate energy splitting and C_k, the Korringa constant, is a system dependent constant arising from the integral over electron states. Under the conditions that the nuclear spin system is weakly coupled to the lattice and has a much smaller heat capacity, it can be shown that the spin density matrix remains diagonal at all times [18]. These diagonal elements, which correspond to the sublevel populations p_m, obey a gain-loss equation of the form

$$\frac{dp_m}{dt} = \sum_n (W_{nm}p_n - W_{mn}p_m) \tag{1.92}$$

or in matrix notation

$$\frac{d\mathbf{p}}{dt} = \mathbf{R}\mathbf{p} \tag{1.93}$$

where $\mathbf{p}$ is a $(2I+1)$ dimensional column vector and $\mathbf{R}$ is the time dependent relaxation matrix. Under the equivalence transformation $\mathbf{D}$, where $D_{mn} = \delta_{mn}e^{-E_m/2kT}$, the matrix $\mathbf{R^S} = \mathbf{D^{-1}RD}$ becomes symmetric. Hence (1.93) is solved by the diagonalization of $\mathbf{R^S}$ which leads to

$$\mathbf{p}(t) = \mathbf{D}\mathbf{U}e^{\mathbf{K}t}\mathbf{U^{-1}}\mathbf{D^{-1}}\mathbf{p}(0) \tag{1.94}$$

where $\mathbf{U}$ and $\mathbf{K}$ are the matrices of the eigenvectors and eigenvalues of $\mathbf{R^S}$ respectively. Thus the time evolution of the populations is a multi-exponential function which is completely determined by the Korringa constant and the initial populations, $p_m(0)$.

Experimentally it is convenient to define a single effective time constant τ_{slr} to approximate the time dependence of (1.94) such that

$$\ln\left[\frac{B_2(t=\infty)-B_2(0)}{B_2(\infty)-B_2(\tau_{slr})}\right]=1. \tag{1.95}$$

The initial populations $B_2(0)$ could be either semi-oriented, if they were produced by decay from an oriented precursor, or random. For the case of interest to the present work (see subsection 4.4.4) the parent state is produced directly by on-line implantation so that the latter assumption is appropriate and $B_2(0)=0$. A simple empirical estimate for τ_{slr} can then be made from

$$\tau_{emp}=\min(\tau_{htl},\tau_{ltl}) \tag{1.96}$$

where

$$\tau_{htl}=\frac{4}{3}\frac{C_k}{T} \quad \text{and} \quad \tau_{ltl}=\frac{3.3}{(I+\frac{1}{2})}\frac{C_k}{\beta T}. \tag{1.97}$$

The labels *htl* and *ltl* refer to the high and low temperature limits, as determined by the conditions $\beta \ll 1$ and $\beta \gg 1$ respectively. Apart from the region where the two limits overlap, i.e. where $\beta \sim 5/(2I+1)$, the agreement with τ_{slr} as deduced from an exact calculation of (1.94) is good. This is illustrated in figure 1.5 for the case of spin 5.

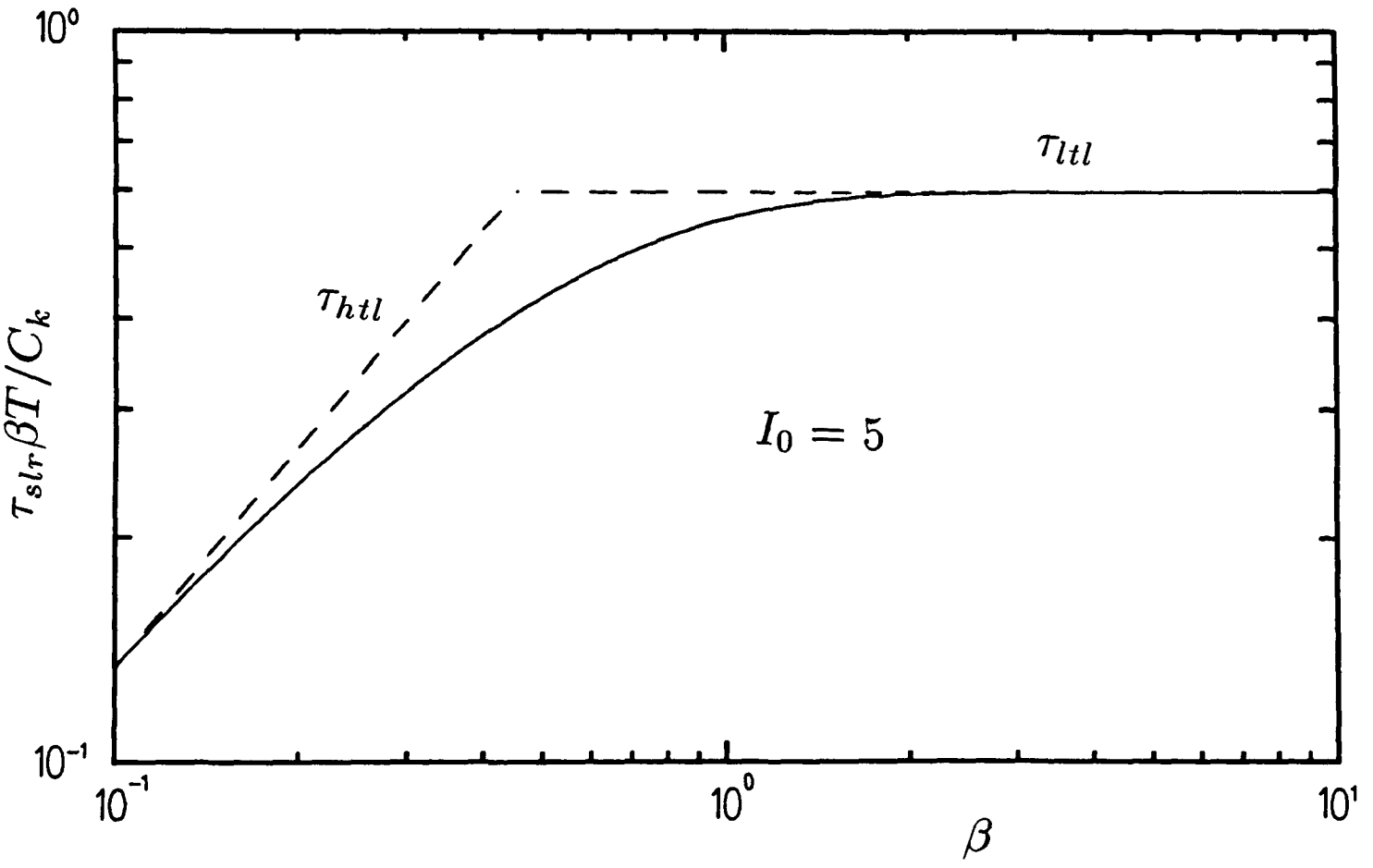

Figure 1.5. The ratio $\tau_{slr}\beta T/C_k$ as a function of β for an oriented state of spin 5. The dashed line represents τ_{emp}.

Provided that the relaxation proceeds via electron-hole pair excitations and magnetic dipole interactions (neglecting hyperfine anomalies) then it is possible to derive the scaling property

$$\left(\frac{\mu}{I}\right)^2 C_k = \text{constant} \tag{1.98}$$

for different isotopes of a given element in the same host. Thus C_k values and hence relaxation times may be estimated for a whole range of isotopes provided that at least one nucleus of the same element has been measured.

The significance of relaxation in LTNO comes when the radioactive decay is considered. If τ_{slr}, which can vary from 10^{-3} to 10^4 s for impurities in iron, is significant in comparison with the nuclear lifetime then an appreciable number of nuclei decay from incompletely oriented states. This results in a temperature dependent reduction of the observed angular distribution anisotropy via an attenuation in the orientation parameters.

In the case of on-line LTNO the situation is further complicated by the steady stream of incoming warm nuclei. Sublevel populations representing the relaxing and populating states and allowances for the radioactive decay of the relaxing sublevels must then be included into (1.93). On the assumption that N nuclei are implanted per second and that these are equally distributed among the relaxing sublevels then the modified analogue of (1.92) may be written as

$$\frac{dp_m}{dt} = \sum_n (W_{nm}p_n - W_{mn}p_m) - \frac{\ln 2}{t_{\frac{1}{2}}} p_m + \frac{N}{(2I+1)}. \tag{1.99}$$

The sublevel populations will then attain secular equilibrium, given by the condition $d\mathrm{p}/dt = 0$. From this the sublevel populations and hence the orientation parameters may be deduced.

Figure 1.6 shows the ratio $B_2(\text{secular})/B_2(\text{equilibrium})$ as a function of β for a range of $t_{\frac{1}{2}}\beta T/\ln 2C_k$ values. The latter expression is essentially a measure of the ratio of the nuclear lifetime to the relaxation time. It is clear that for $t_{\frac{1}{2}}\beta T/\ln 2C_k \ll 1$, $B_2/B_2(\text{eq}) \rightarrow 0$ since the nuclei decay from the unrelaxed warm state, while for $t_{\frac{1}{2}}\beta T/\ln 2C_k \gg 1$, $B_2/B_2(\text{eq}) \rightarrow 1$ full relaxation having occurred before decay.

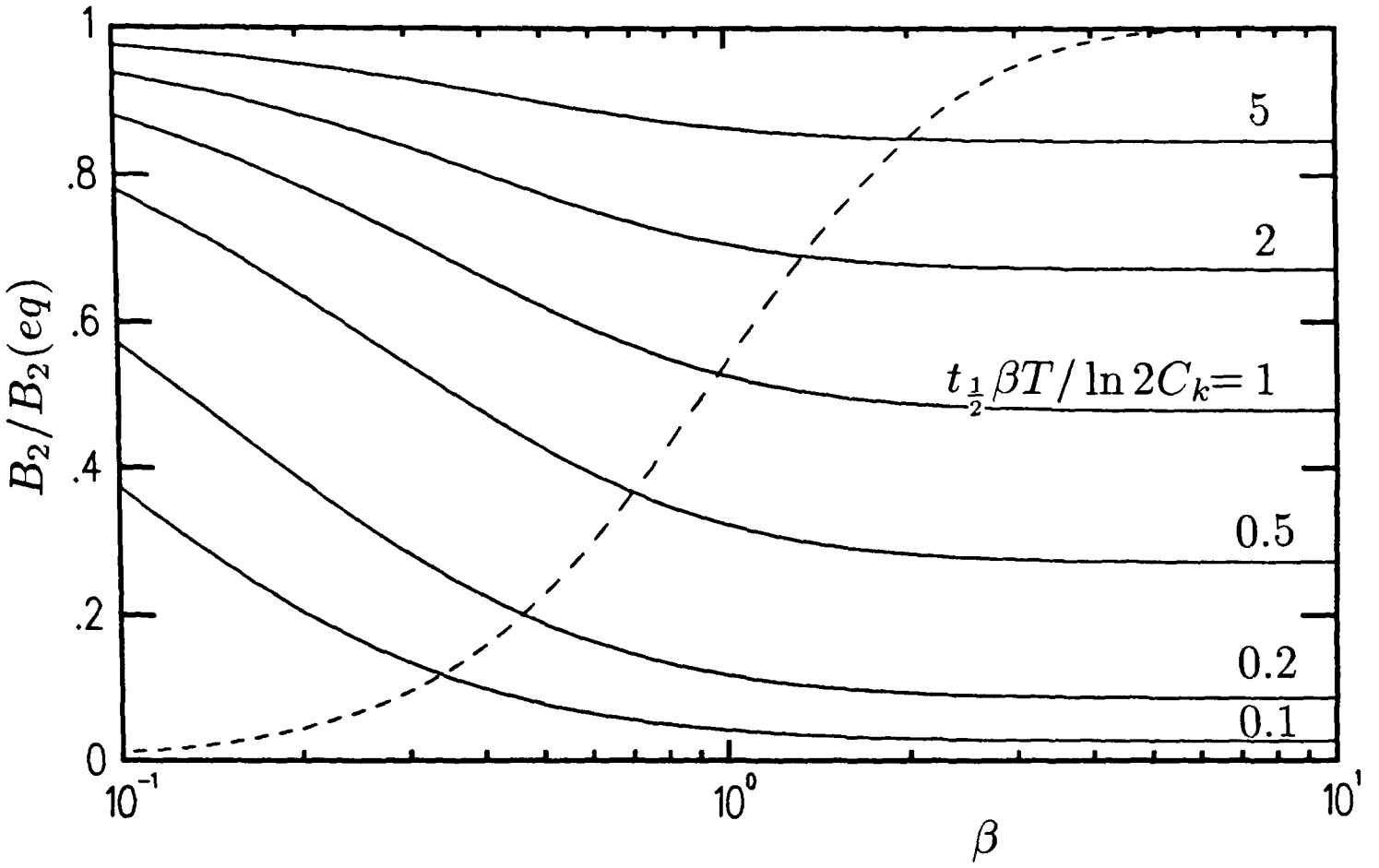

Figure 1.6. The ratio $B_2/B_2(\mathrm{eq})$ for a magnetically oriented state of spin 3 as a function of β for a range of values of $t_{\frac{1}{2}}\beta T/\ln 2C_k$. The dashed line represents $B_2(\mathrm{eq})$, normalized to its saturation value.

References

[1] . U. Fano, Phys. Rev. **90** (1953) 577

[2] . D.M. Brink and G.R. Satchler, Angular Momentum (Oxford, 1968)

[3] . R.J. Blin-Stoyle and M.A. Grace, in Encycl. of Phys. Vol. XLII (Springer-Verlag, 1957)

[4] . R.M. Steffen and K. Alder, in The Electromagnetic Interaction in Nuclear Spectroscopy, ed. W.D. Hamilton (North Holland, 1975)

[5] . A. Messiah, Quantum Mechanics (North Holland, 1961)

[6] . M.E. Rose, Phys. Rev. **C91** (1953) 610

[7] . E. Storm and H.I. Israel, Los Alamos Scientific Laboratory Report LA-3753 (1967)

[8] . M.J.L. Yates, in Alpha-, Beta- and Gamma-Ray Spectroscopy, ed. K. Siegbahn (North Holland, 1965)

[9] . D.C. Camp and A.L. Van Lehn, Nucl. Instr. and Meth. **76** (1969) 192

[10] . K.S. Krane, Nucl. Instr. and Meth. **98** (1972) 205

[11] . N.J. Stone, in Low Temperature Nuclear Orientation, eds. N.J. Stone and H. Postma (North Holland, 1987)

[12] . J.R. Beeler and M.F. Beeler, in Fundamental Aspects of Radiation Damage in Metals, CONF-751006-P1 (1976) 28

[13] . R.S. Averback *et al.*, Nucl. Instr. and Meth. **B33** (1988) 693

[14] . A. Turos *et al.*, Nucl. Instr. and Meth. **B19** (1987) 123

[15] . E. Hagn, in Low Temperature Nuclear Orientation, eds. N.J. Stone and H. Postma (North Holland, 1987)

[16] . R. Haroutunian and M. Meyer, Phys. Rev. **C17** (1978) 292

[17] . E. Klein, in Low Temperature Nuclear Orientation, eds. N.J. Stone and H. Postma (North Holland, 1987)

[18] . A. Sher and H. Primakoff, Phys. Rev. **119** (1960) 178

Chapter 2

Experimental apparatus and techniques

2.1 Introduction

The experiments described in this thesis have been performed either off-line, at the Oxford ^{3}He -^{4}He dilution refrigerator used in conjunction with a $PrNi_5$ demagnetization stage, or at the Daresbury On-Line Isotope Separator-Cryogenic On-Line Device (DOLIS-COLD). The design and performance of these systems will now be outlined.

2.2 The ^{3}He -^{4}He dilution refrigerator

For cooling significantly below 0.3 K the only practical method available until the early 1970's was adiabatic demagnetization of a suitable paramagnetic salt. This technique, however, is basically a single cycle method of cooling; after demagnetization the cryostat begins to warm up owing to the presence of heat leaks. For this reason the method is unsuitable for experiments requiring reasonably continuous low temperature operation in the presence of power sources.

After 1965 the first prototypes of the ^{3}He -^{4}He dilution refrigerator were made operational following the principles originally suggested by London *et al.* [1]. These allowed the continuous cooling denied to the demagnetization techniques.

2.2.1 The ^{3}He -^{4}He cooling process

The operation of the ^{3}He -^{4}He dilution refrigerator relies on the special properties of the ^{3}He -^{4}He mixture at low temperatures. At temperatures below the tricritical point (0.86 K) this mixture separates into two phases. One, the *concentrated* phase, is rich in ^{3}He (99.997 % pure at 0.1 K) while the other, the *dilute* phase, is rich in ^{4}He (7.0 % ^{3}He at 0.1 K). The principal of the dilution refrigerator depends on the fact that the proportion of ^{3}He in the dilute phase remains finite and rather large (6.4 %) even at absolute zero. Through the act of pumping on the dilute phase, ^{3}He is preferentially removed by virtue of its higher vapour pressure. In order to maintain the ^{3}He -^{4}He equilibrium concentration, ^{3}He is drawn across the phase boundary from the concentrated phase. At temperatures below 0.5 K, ^{4}He is effectively a Bose-Einstein condensate and is both thermally and hydrodynamically inert, while ^{3}He can be regarded as a normal Fermi-Dirac liquid. This process can therefore be considered as the "evaporation" of ^{3}He atoms from the concentrated phase into the "vacuum" provided by the dilute phase, thus leading to cooling.

A full discussion of the properties of ^{3}He -^{4}He mixtures is given by Lounasmaa [2].

2.2.2 The dilution refrigerator design

A schematic view of the main features of a conventional ^{3}He -^{4}He *dilution unit* is shown in figure 2.1. In stable operation, the concentrated-dilute phase boundary lies in the *mixing chamber* which is the coldest part of the refrigerator. The lower half of the mixing chamber, which contains the dilute phase, is connected to the *still* via a series of heat exchangers. The still is pumped by a large diffusion pump backed by a sealed rotary pump, preferentially removing ^{3}He ($\sim$ 95%) despite its low ($\sim$ 7%) concentration in the dilute phase. As has already been noted, this leads to the migration of ^{3}He across the phase boundary and consequently cooling. For optimal circulation rates an electric heater maintains the still at $\sim$ 0.8 K. The ^{3}He emerging from the rotary pump exhaust re-enters the cryostat via liquid nitrogen *cold traps* which remove any air that may have leaked into the system. Once inside the cryostat, the ^{3}He is pre-cooled to 1.2 K by contact with the pumped ^{4}He *pot* and then liquefied in the *condenser*. A flow impedance keeps the pressure of the ^{3}He sufficiently high for condensation to occur. The ^{3}He is further cooled to 0.8 K by contact with a wrap around heat exchanger on the still and then returns to the mixing chamber via a concentric tube continuous heat exchanger and four sintered silver step heat exchangers, where cooling takes place by contact with the out-going ^{3}He from

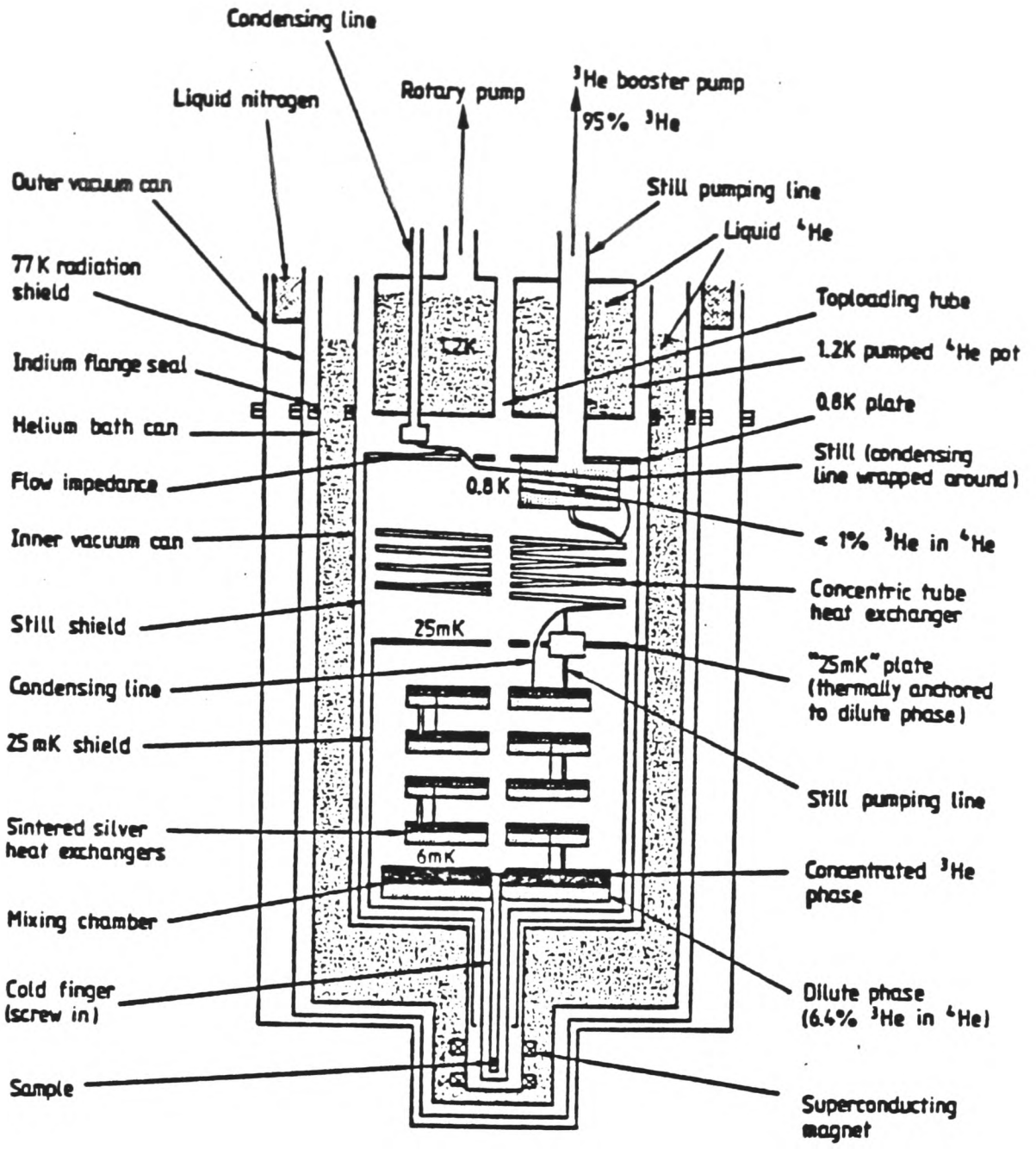

Figure 2.1. A schematic view of a conventional continuous operation ^{3}He -^{4}He dilution refrigerator.

the pumped dilute phase. The efficiency with which the pre-cooling process is performed is one of the limitations on the minimum attainable temperature.

The conventional cryostat design external to the dilution unit consists of the Inner and Outer Vacuum Chambers (IVC and OVC; both evacuated to pressures of $< 10^{-6}\tau$) which enclose the main ^{4}He bath. Within the OVC lies a radiation shield maintained at 77 K by a liquid nitrogen cooled jacket. The IVC contains the dilution unit, the main helium bath on its outer face acting as a 4.2 K heat shield. Finally, in thermal contact with the dilution unit there is the 1.2 K ^{4}He *pot* (fed either continuously or intermittently by the main bath), the 0.8 K heat shield (attached to the still) and the 25 mK heat shield.

The experimental samples and thermometers are soldered to a copper cold finger screwed into the base of the mixing chamber.

2.2.3 The operation of the dilution unit

In attaining the base temperature in this continuous mode, a balance must be struck between the extra cooling induced by increasing the rate at which ^{3}He crosses the phase boundary and the consequent additional heating caused by the greater volume of returning gas and lower heat exchange efficiency at higher circulation rates. For the DOLIS-COLD refrigerator the optimum ^{3}He circulation rate is $\sim 400\mu$moles s^{-1}. With the 4 K baffle of the side access tube shut (see subsection 2.5.1) this can lead to a base temperature of $\sim$ 8 mK.

Experimentally in LTNO it is important to be able to vary the temperature of the refrigerator in some manner. In principal this can be done by adjusting the power output of the still heater, thus changing the circulation rate. However this is a rather uncertain and unreliable method. Greater control is achieved by adding known quantities of heat directly into the mixing chamber via a thermally attached resistor. If this power input is denoted by Q then it can be shown [2] that

$$Q = C\left(T_{mc}^2 - T_{base}^2\right) \tag{2.1}$$

where T_{mc} is the actual temperature of the mixing chamber and T_{base} the temperature which would be achieved in the absence of Q. From a knowledge of the parameters C and T_{base} it is possible to select the required temperature by supplying the appropriate current to the mixing chamber resistor. For the DOLIS-COLD refrigerator typical values for these parameters are

$$C = 0.019\mu\text{W mK}^{-2} \quad \text{and} \quad T_{base} = 8\text{mK}.$$

The Oxford refrigerator is built to a similar specification, but not having to work against the additional heat load provided by the side access tube can achieve base temperatures of 5 mK.

2.3 Sample preparation and polarization

In this work the host lattices have all been polycrystalline iron foils of at least 99.998% purity. These are prepared by cold-rolling an iron sheet down to a thickness of $\sim 10\mu$m and then annealing under an atmosphere of dry hydrogen at a temperature of $\sim 800°$ C for 24 hours. Finally, just before use, the foil is chemically etched in a solution of 54 vol % H_3PO_4 (80%), 36 vol % H_2O_2 (30%), 8.5 vol % distilled water and 1.5 vol % butoxyethanol [3].

The nuclear orientation thermometers used in this work, namely ^{57}Co<u>Fe</u>, ^{60}Co<u>Co</u>(hcp) and ^{60}Co<u>Ni</u>, were all prepared by the high temperature ($900 - 1000°$ C) diffusion of cobalt chloride into the appropriate foil [4]. After etching, 100% of nuclei in full substitutional lattice sites can be consistently achieved owing to the high solubility of cobalt in iron and nickel.

The host foil and thermometer are soldered onto a solid, high purity, copper cold finger which screws into a copper adaptor attached to the mixing chamber of the dilution unit. Both the Oxford and DOLIS refrigerators have a top loading facility which enables the cold finger to be changed whilst the refrigerator is running. This process, which typical takes $\sim$ 3 hours, is often of vital importance to an on-line experiment where the target foil may need to be changed to remove unwanted longer lived activities built up in the sample during implantation.

The loaded sample and thermometer lie at the center of a 1.5 T superconducting split coil magnet which is used to polarize the magnetic domains in the foils. Typically a field of $\sim$ 0.7 T is applied, which provides not only magnetic saturation but also ensures that the solder is not superconducting and hence that a good thermal contact to the cold finger is achieved. The field produced by the magnet has a homogeneity of 1% over the sample volume.

2.4 The demagnetization stage

As has already been pointed out, adiabatic demagnetization is an important technique in the attainment of low temperatures. Such a $PrNi_5$ demagnetization stage has been employed for several years in conjunction with the Oxford dilution refrigerator [5]. This has enabled temperatures of as low as 1 mK to be attained for several hours (rising to about 12 mK during periods of remagnetization) and thus has enhanced the study of nuclei with relatively small hyperfine interactions. The demagnetization stage, having similar dimensions to the cold fingers, is fully top-loadable.

2.4.1 Enhanced nuclear magnetism

In the field of cryomagnetics the traditional type of paramagnetic working substance has been one whose susceptibility closely follows Curies law.

A different class of paramagnets comprise those where the electronic ground state is a singlet, with electronic Zeeman matrix elements linking it to one or more low lying excited singlet states. The ground state singlet can have no permanent magnetic moment, but when a magnetic field is applied these excited states are mixed in, leading to a large Van Vleck paramagnetic susceptibility. This induced moment then interacts with the nuclear magnetic moment through the magnetic hyperfine interaction and leads to a pseudo-Zeeman nuclear interaction which may be orders of magnitude larger than the true Zeeman interaction. Such an class of ions are the odd Z lanthanide nuclei in the tripositive electronic state, including Pr^{3+}. The effect can be illustrated by using the Hamiltonian [6]

$$H = H_x + g_J\mu_B(\mathbf{B}\cdot\mathbf{J}) + A_J(\mathbf{J}\cdot\mathbf{I}) - g_I\mu_B(\mathbf{B}\cdot\mathbf{I}) + H_Q \tag{2.2}$$

where H_x denotes the interaction with the ligand field and the next term the Zeeman interaction for an ion with electronic spin J. The last three terms represent the magnetic hyperfine interaction for a nucleus of spin I, the nuclear Zeeman interaction ($g_I \sim 10^{-3}$ in Bohr magnetons) and the nuclear electric quadrupole interaction respectively. Assuming that H_x produces a singlet ground state $|G\rangle$ and a singlet excited state $|E\rangle$ with energies $\pm\frac{1}{2}\Delta$, then, neglecting H_Q, the Hamiltonian matrix may be written as

$$\begin{pmatrix} +\frac{1}{2}\Delta - g_I\mu_B B_z I_z & \langle E|J_z|G\rangle(g_J\mu_B B_z + A_J I_z) \\ \langle E|J_z|G\rangle(g_J\mu_B B_z + A_J I_z) & -\frac{1}{2}\Delta - g_I\mu_B B_z I_z \end{pmatrix} \tag{2.3}$$

where B_z is the external magnetic field applied along the z-axis. The ground state energy is then

$$W^G = -g_I\mu_B B_z I_z - \frac{1}{2}\Delta\sec\theta \tag{2.4}$$

with

$$\tan\theta = 2\langle E|J_z|G\rangle(g_J\mu_B B_z + A_J I_z)/\Delta. \tag{2.5}$$

The energies of the nuclear magnetic substates may be separated out to give

$$W^N = -g_I\mu_B(B_z + B_E)I_z \tag{2.6}$$

where B_E is the magnetic field at the nucleus generated by the electrons. In the weak field limit, $\langle E|J_z|G\rangle g_J \mu_B B_z \ll \Delta$, this energy may be written

$$W^N = -g_I \mu_B B_z (1 + K_z) I_z \tag{2.7}$$

so that $B_E = K_z B_z$. The enhancement factor K_z is given by

$$K_z = 2\{\langle E|J_z|G\rangle\}^2 g_J A_J / g_I \Delta. \tag{2.8}$$

Effectively, the component of the nuclear moment on the z-axis becomes

$$\mu_z^N = -\frac{\partial W^N}{\partial B_z} = g_I \mu_B (1 + K_z) I_z. \tag{2.9}$$

In Pr^{3+}, where the enhancement factor is $K_z = 145$, the effective nuclear moment is therefore raised to the level of almost one Bohr magneton [6].

In the strong field limit, $\langle E|J_z|G\rangle g_J \mu_B B_z \gg \Delta$, the nuclear Zeeman energy levels of the ground state become

$$W^N = -g_I \mu_B B_z I_z - \langle E|J_z|G\rangle A_J I_z. \tag{2.10}$$

Hence B_E reaches a limiting value equal to that given by the hyperfine interaction when the full electronic magnetic moment of the ground state is achieved, i.e. when $\langle E|J_z|G\rangle = J$. This is enormous compared to the applied field B_z, which may thus be ignored. The splitting between successive nuclear levels is then just JA_J. For Pr^{3+} ions, B_E is 337 T and (in thermal units) JA_J is 210 mK. With such enhanced nuclear Zeeman splittings these ions are particularly suited to cooling by adiabatic demagnetization.

2.4.2 Enhanced nuclear cooling

To achieve cooling by adiabatic demagnetization, the $PrNi_5$ salt is allowed to thermally equilibrate in an applied field of $\sim$ 2.5 T while in thermal contact with the mixing chamber of the dilution unit. In this field the nuclear Zeeman splittings roughly correspond to the strong field limit (2.10) so that, for example, by magnetizing at 50 mK as much as 96% of the Pr^{3+} nuclear entropy may be removed [6]. The demagnetization stage is then thermally decoupled from the dilution unit by allowing an indium heat switch separating the two to become superconducting. The magnetic field is then removed slowly to avoid eddy current heating. In this isentropic process the Boltzmann populations of the Zeeman levels are conserved and so the temperature decreases monotonically with the applied field. The temperature reached on demagnetization to zero field is of the same order as that where the nuclear susceptibility departs from Curies law. Since the mutual interactions within the nuclear spin system are also enhanced, this limiting temperature is of the order of a mK. However, in practice the applied field is not removed completely since the nuclear specific heat capacity of $PrNi_5$ is then reduced [7] leading to greater warm up rates.

2.5 The DOLIS-COLD facility

The Daresbury On-Line Isotope Separator - Cryogenic On-Line Device (DOLIS-COLD) makes use of light and medium heavy ion beams from the Nuclear Structure Facility (NSF) Van der Graff generator at the SERC Daresbury laboratory. The NSF is a conventional vertical tandem accelerator which currently operates at terminal voltages of up to 20 MV.

A schematic view of DOLIS is shown in figure 2.2. The beam from the vertical tandem is deflected through $\pi/2$ and focussed by a single magnetic quadrupole doublet onto the target of the DOLIS on-line ion source (both FEBIAD and Thermal Ion Source). The outgoing secondary beam then passes through an extractor electrode, a cylindrical Einzel lens and an accelerating gap. The 30 kV extractor backs off the 100 kV accelerating supply so that the secondary beam energy does not depend on the extractor voltage. In practice, the ions are usually accelerated by only 60 kV. Vertical focussing i provided by a magnetic quadrupole triplet before mass separation occurs in the 60° sector dipole analyzing magnet. The dispersion and resolution is sufficient to separate nuclei with mass numbers up to A $\sim$ 250. Following the collection chamber an electrostatic switchyard distributes the beam into one of three lines. The central line leads via

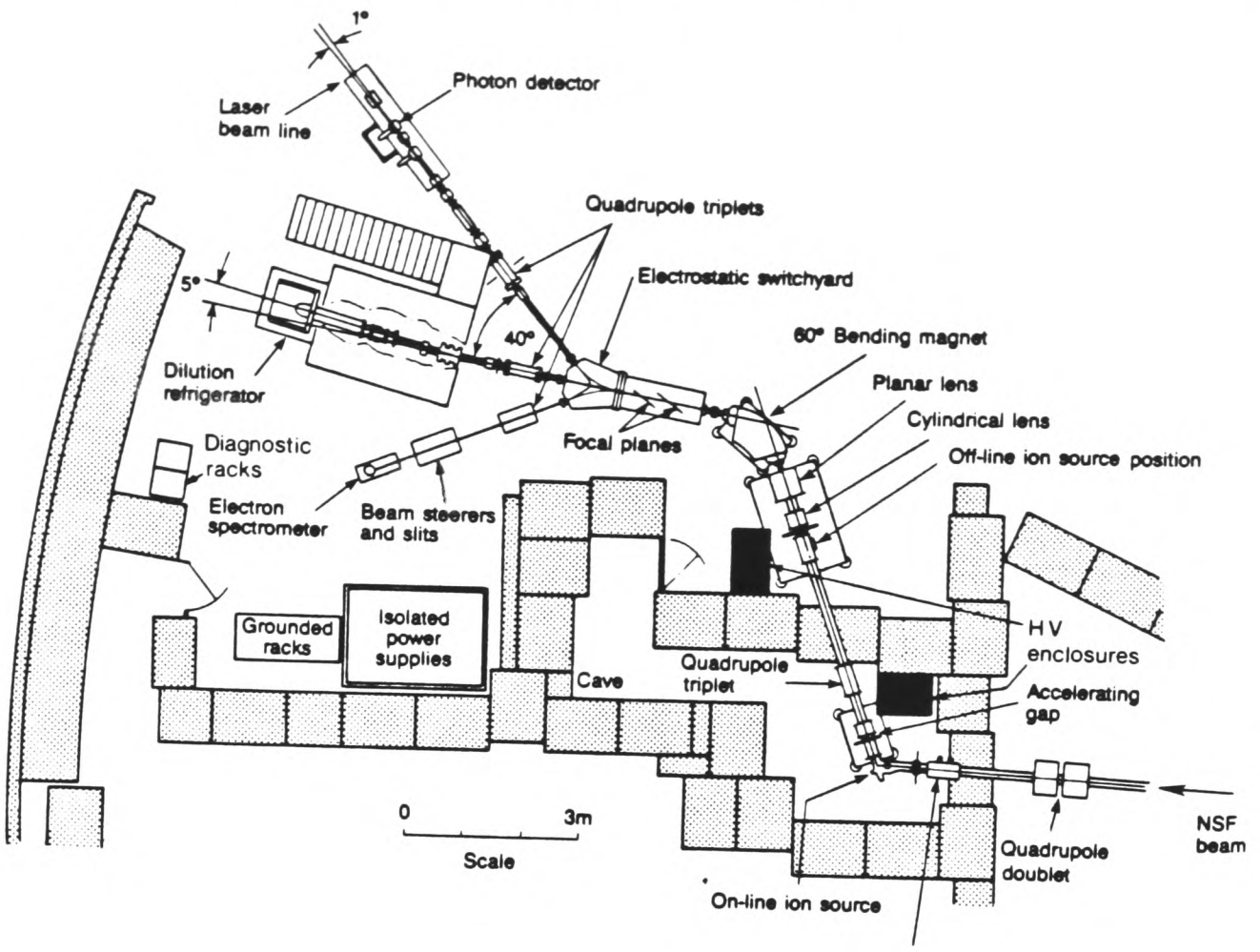

Figure 2.2. A schematic view of the DOLIS facility.

a cooled side access tube to the dilution refrigerator. This incorporates a 5° bend which allows the cold finger of the refrigerator to face a plate cooled to 77 K. The general purpose Mini-Beam Line is at 40° to the central line and in this work has been used for conversion electron studies. The final beam line is used for laser spectroscopy. A full description of the operation of DOLIS has been given by Grant *et al.* [8].

2.5.1 The cooled side access

In an on-line experiment the dilution refrigerator has two extra heat loads placed upon it in addition to the usual heat leaks. These are caused by both the thermal radiation from the incoming beam line and the 60 keV mass separated beam itself. This heat load must be kept at the μW level if temperatures of $\sim$ 10 mK are to be maintained. To this end the refrigerator is supplied with a one metre long side access tube, the inner copper wall of which is cooled to 4 K by thermal contact with the refrigerator's main helium bath. The side access tube and refrigerator are illustrated in figure 2.3 .

One metre from the cold finger there is a variable diameter iris at 77 K and at 40 cm a fixed aperture lead plug, maintained at 4 K by contact with the wall of the side access tube. These not only act as radiation baffles, but also prevent scattered beam from striking the target.

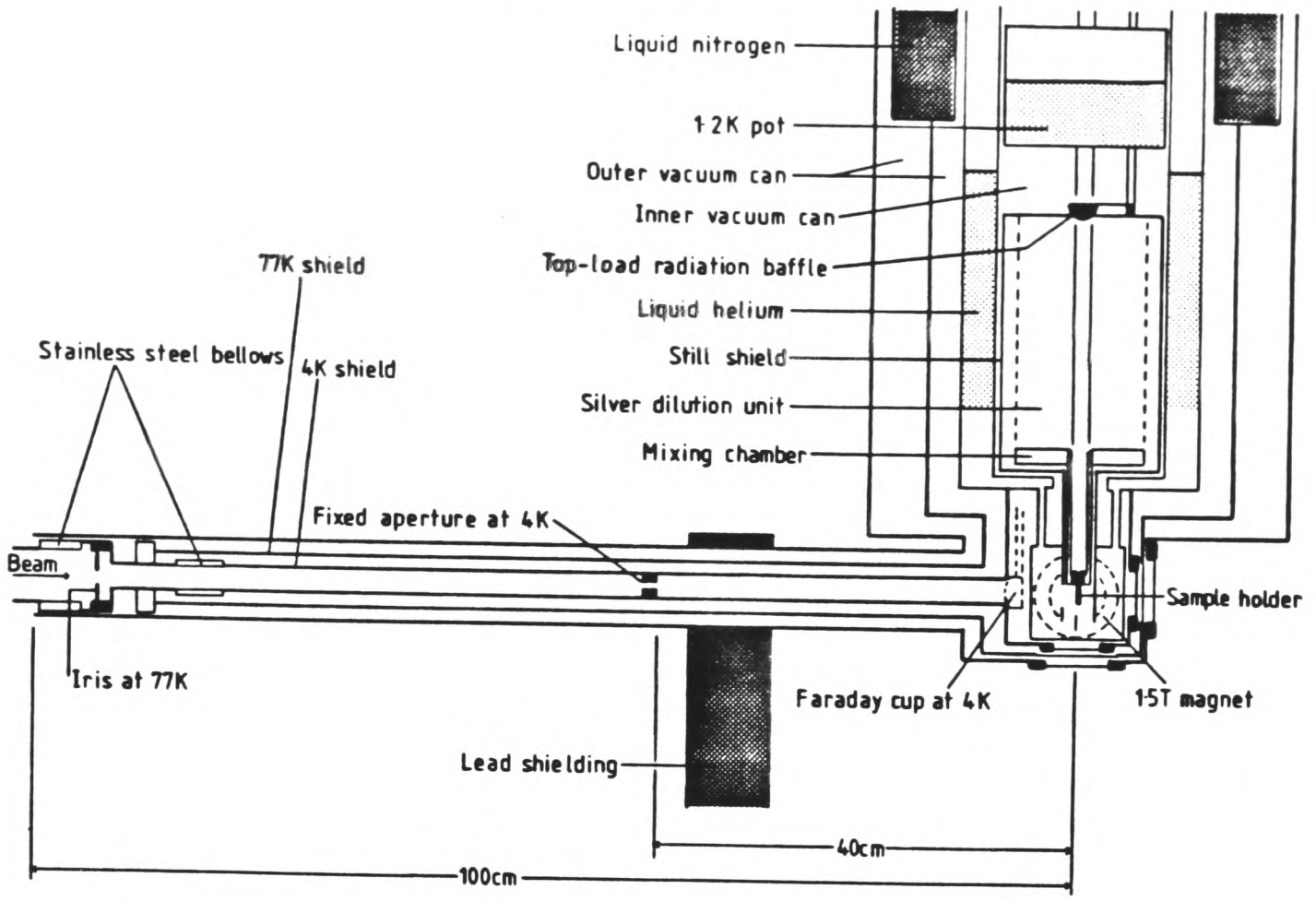

Figure 2.3. The Daresbury dilution refrigerator and side access tube.

Finally, at 7 cm from the sample position, there is a closeable 4 K radiation baffle which has been modified to allow ion current measurements. This can be fully closed for off-line work or for beam diagnostics. The detectors around the refrigerator are shielded against any activity accumulated on the lead plug by an 8 cm wall of lead bricks. As beam transmission rates of $> 90\%$ are consistently achieved, this level of background radiation is never very great.

2.5.2 The Mini-Beam line

The Mini-Beam Line is a general purpose line which in the past has mainly been used for electron conversion studies, allowing the measurement of gamma ray multipolarities and facilitating the search for E0 transitions.

The beam line terminates in two cubes. The separated beam enters the upper cube directly and is collected on a movable 6.4 mm wide cassette tape. Activity may thus be transported down to the lower cube. In this way longer lived isotopes can be studied in the absence of shorter lived varieties and vice versa. Both cubes have re-entrant covers to allow the detectors to be positioned as close to the tape as possible for coincidence measurements. Electron spectroscopy is carried out using a mini-orange magnetic filter in conjunction with a cooled Si(Li) detector. The electrons are focussed onto the face of the Si(Li) detector (which is shielded from direct

gamma rays by a lead plug in the axis of the magnet) while positrons are defocussed and therefore not detected.

Spectroscopic studies which can be performed on the mini-beam line include:

1. $\gamma - \gamma$ coincidence
2. $\gamma - \beta^-$ coincidence
3. conversion electron spectroscopy
4. half-life measurements.

2.6 Data acquisition

For all the work to be described, gamma rays have been observed using Ge(Li) detectors which combine reasonable photopeak efficiency (typically $\sim$ 25% relative to a 3″× 3″ NaI detector at 25 cm from the source) with adequate resolution (typically $\sim$ 2.5 keV at 1333 keV). For directional distribution measurements these are positioned axially ($\theta = 0$) and equatorially ($\theta = \pi/2$) with respect to the polarization axis and detect gamma events in *singles* mode. The Daresbury configuration allows for two axial and two equatorial detectors while at Oxford only one axial and one equatorial detector is used. The detector to source distance is usually $\sim$ 8 cm. A block diagram illustrating singles mode data aquisition is shown in figure 2.4 .

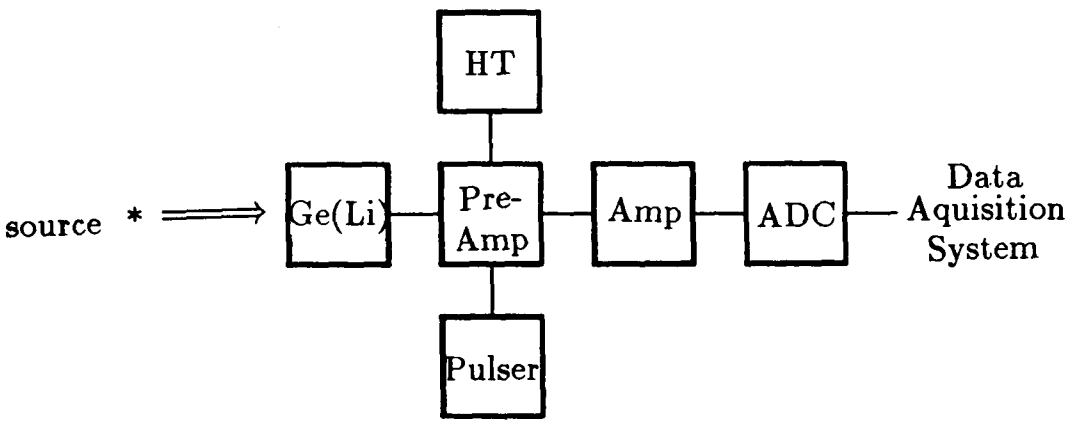

Figure 2.4. A typical singles mode data acquisition arrangement.

In order to correct for dead-time losses in the system (see subsection 3.3) a pulse generator is connected to the test input of the detector pre-amplifier. The pulser frequency is normally set to $\sim$ 10 Hz and has an amplitude such that it is placed at a convenient position at the top

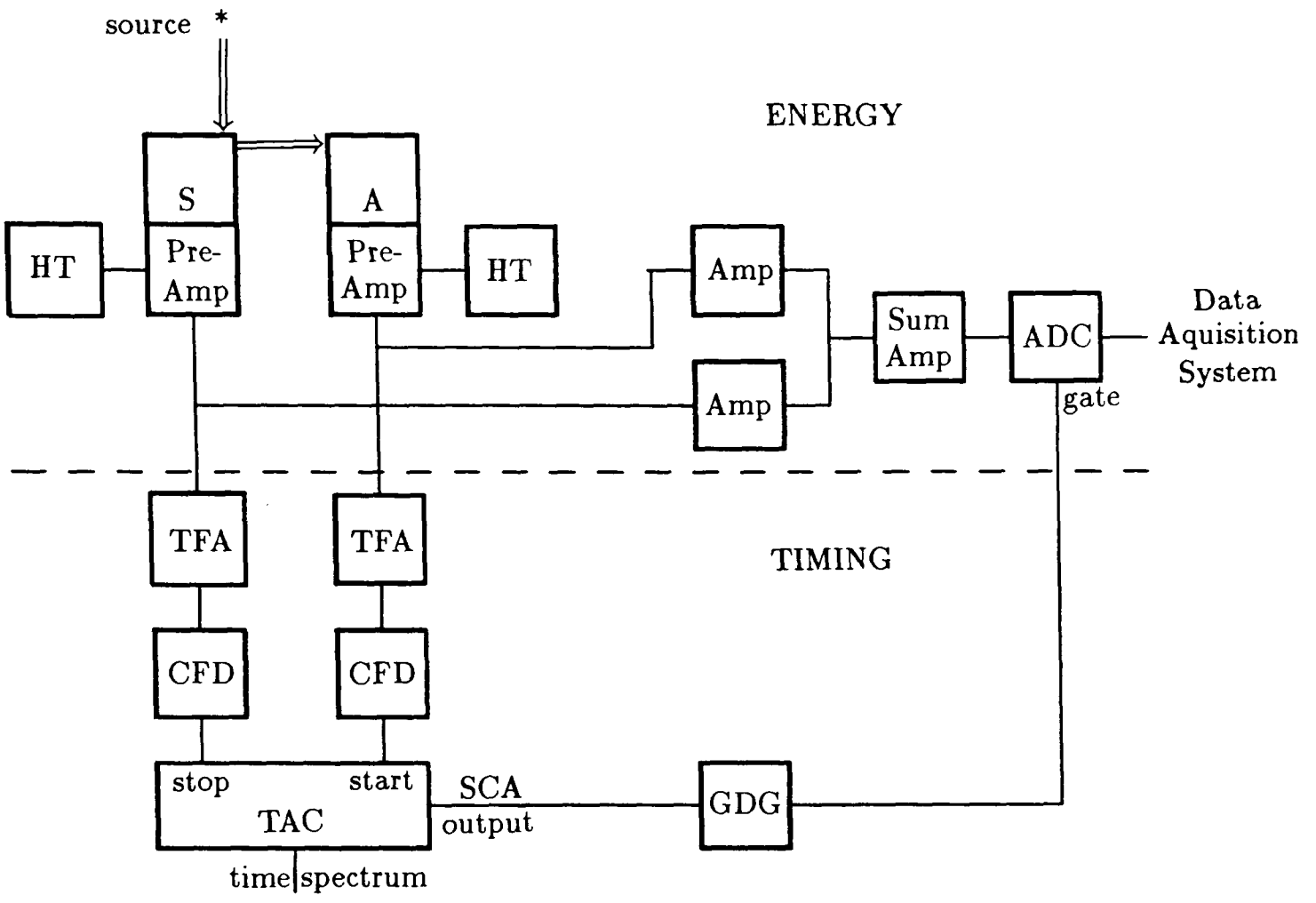

Figure 2.5. A coincidence mode data acquisition system. Energy and timing signals are separated by the dashed line.

of the gamma ray spectrum. The pre-amplifier signals are amplified and directed into standard Analogue to Digital Converters.

In addition to simple directional distribution measurements, polarization measurements can also be performed. Here *coincidence* is required between partially detected gamma ray events in a central detector placed in the polarimeter axis and the subsequent detection of the scattered gamma ray events in one of the onlooking polarimeter detectors. The energies of the two partial gamma ray events are then summed, thereby reconstructing the energy of the original gamma ray. Figure 2.5 shows the main features of such a coincidence data collection system. The scattering detector (also used for directional distribution measurements in singles mode) and one of the analyzing polarimeter detectors are labelled S and A respectively. The circuitry is divided into energy handling and timing, both taking signals from the same pre-amplifier outputs. The two energy signals are amplified, summed and the passed on to a *gated* ADC. The two timing signals are shaped and digitized by passage through Timing Filter Amplifiers and Constant Fraction Discriminators before entry into the Time to Amplitude Converter as the start/stop pulses. Since the analyser A, which in principle only detects previously scattered events from the scatterer S, has by far the smaller count rate, it is prudent to use its timing signals as the TAC start pulse and those of the scatterer for the stop pulse. This of course reverses the

true time ordering of the two signals necessitating the addition of appropriate electronic delays. The TAC produces an output whose amplitude is proportional to the time delay between the start/stop signals. This "time spectrum" is characterized by a constant background of events due to random coincidences, together with a peak corresponding to the time delay between true coincidences. The time spectrum is then "cut" so that the Single Channel Analyzer output of the TAC only produces a signal if the start/stop time differential lies with this true coincidence window. The SCA output, after passage through a Gate and Delay Generator, is used to provide the gating pulse for the ADC. In this way true coincidence events are selected for post ADC processing and data storage.

2.7 Thermometry

In any nuclear orientation experiment accurate measurement of the low temperature is of the utmost importance. The natural approach for such measurements is to capitalize upon the LTNO effect itself. An experimentally viable LTNO thermometer needs to satisfy several important conditions, namely:

1. the hyperfine interaction is well known and a 100% occupation of full substitutional sites in the host lattice can be relied upon,
2. the decay scheme is simple with accurately known $U_\lambda A_\lambda$ coefficients,
3. the nuclear spin-lattice relaxation time is short.

Further experimental considerations of less thermometric importance include long half lives and small radioactive heating.

The useful temperature range of a thermometer can be defined in terms of the sensitivity function $T\partial W(\theta,T)/\partial T$. The maximum of the sensitivity function (for axial measurements) is denoted T_{max}. The upper and lower limits of the useful temperature range, T_u and T_l, define the region where the sensitivity function is greater than 5%. These properties for some of the most frequently used LTNO thermometers are shown in table 2.1 [4]. Not surprisingly, there is little difference between T_{max} and that temperature for which the Boltzmann parameter β (1.27) is unity.

Table 2.1. The useful temperature ranges of the more commonly used LTNO thermometers.

Thermometer	E_γ (keV)	βT (mK)	T_l (mK)	T_{max} (mK)	T_u (mK)
^{54}MnFe	834.8	− 9.2	1.8	7.2	51
^{54}MnNi	834.8	−13.1	2.6	10.4	74
^{57}CoFe	122.1	−14.2	6.5	16.3	40
	136.5		2.9	12.4	90
^{57}CoNi	122.1	− 5.9	2.8	6.8	17
	136.5		1.2	5.2	37
^{60}CoCo(hcp)	1173.2/1332.5	− 6.1	1.3	6.9	50
^{60}CoFe	1173.2/1332.5	− 8.0	1.8	9.0	66
^{60}CoNi	1173.2/1332.5	− 3.3	0.8	3.7	27
^{166}Ho^{m}Ho(hcp)	711.7	137	57	300	1250
	810.3		32	137	750

The experiments described in this thesis were performed in two temperature ranges. Those which employed the dilution refrigerator alone lead to temperatures of 8 – 40 mK, for which ^{57}CoFe and ^{60}CoCo(hcp) thermometers are appropriate. Where the demagnetization stage was used in conjunction with the dilution refrigerator, leading to temperatures of 2 – 12 mK, a ^{60}CoNi thermometer was employed. The sensitivity functions and decay schemes for ^{57}Co and ^{60}Co are shown in figures 2.6 and 2.7 respectively [4].

The accuracy of this method of thermometry has previously been put to the test by a direct comparison of a ^{60}CoCo(hcp) thermometer against a Josephson junction noise thermometer [9]. In the temperature range 10 – 50 mK, the results show only a 0.5% difference in the implied temperatures from the two devices. Thus the measurement of temperature by the LTNO method with accuracies in the region of 1 – 2% is relatively straightforward and unambiguous.

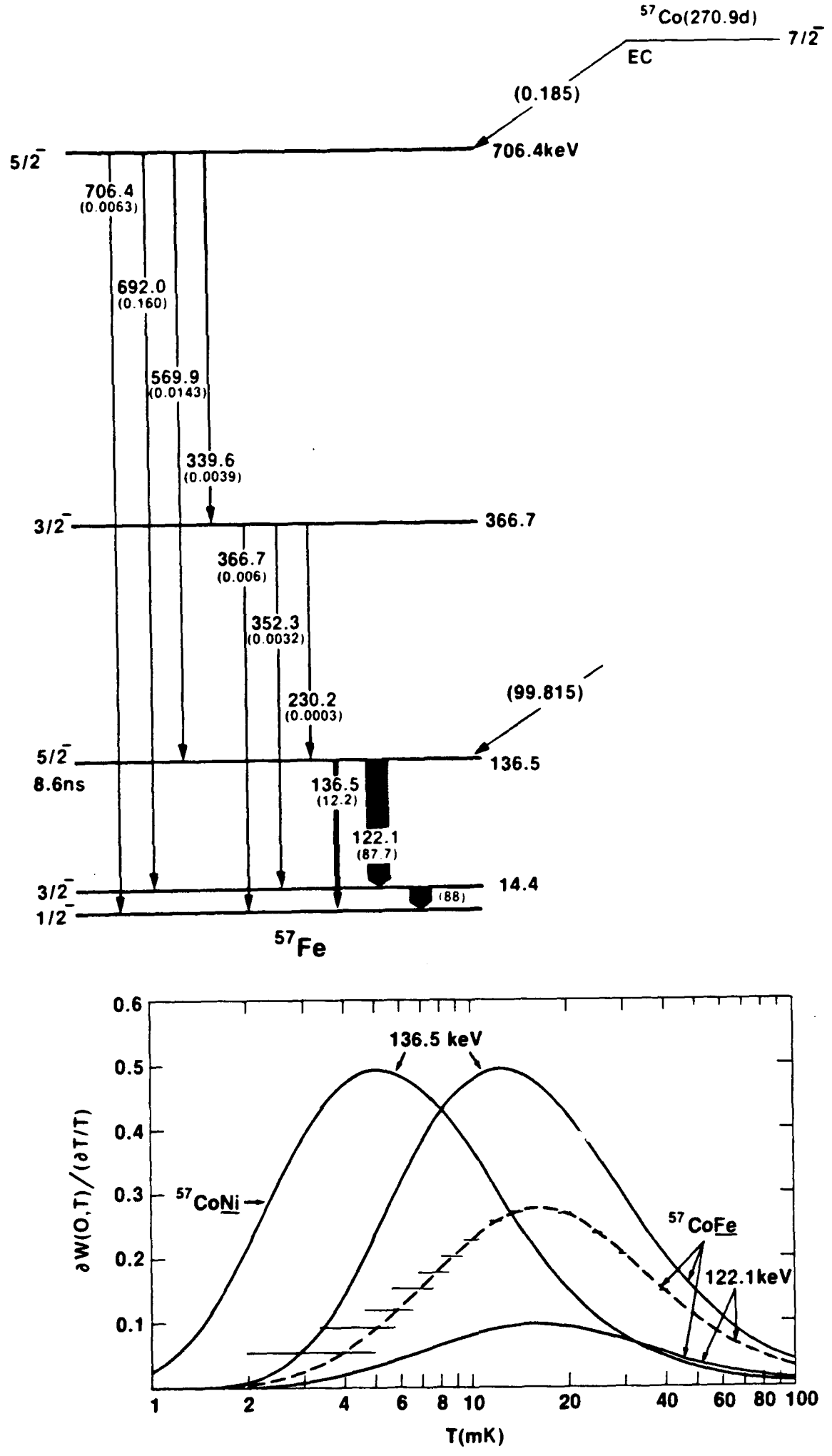

Figure 2.6. The decay scheme and sensitivity functions of ^{57}Co in Fe and Ni. The dashed line represents the effective, intensity normalized, sensitivity function of the 122.1 keV transition while the horizontal bars represent the effects of uncertainties in its mixing ratio.

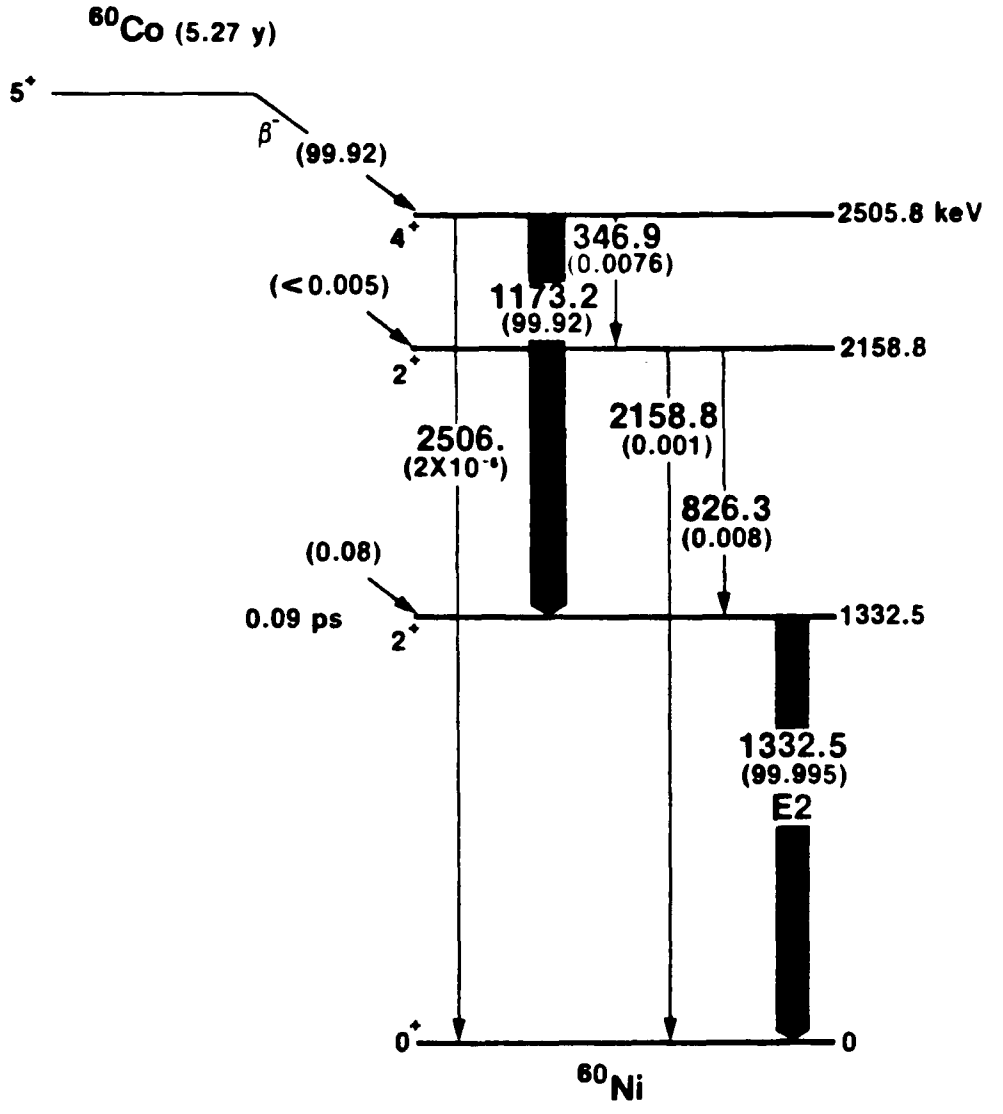

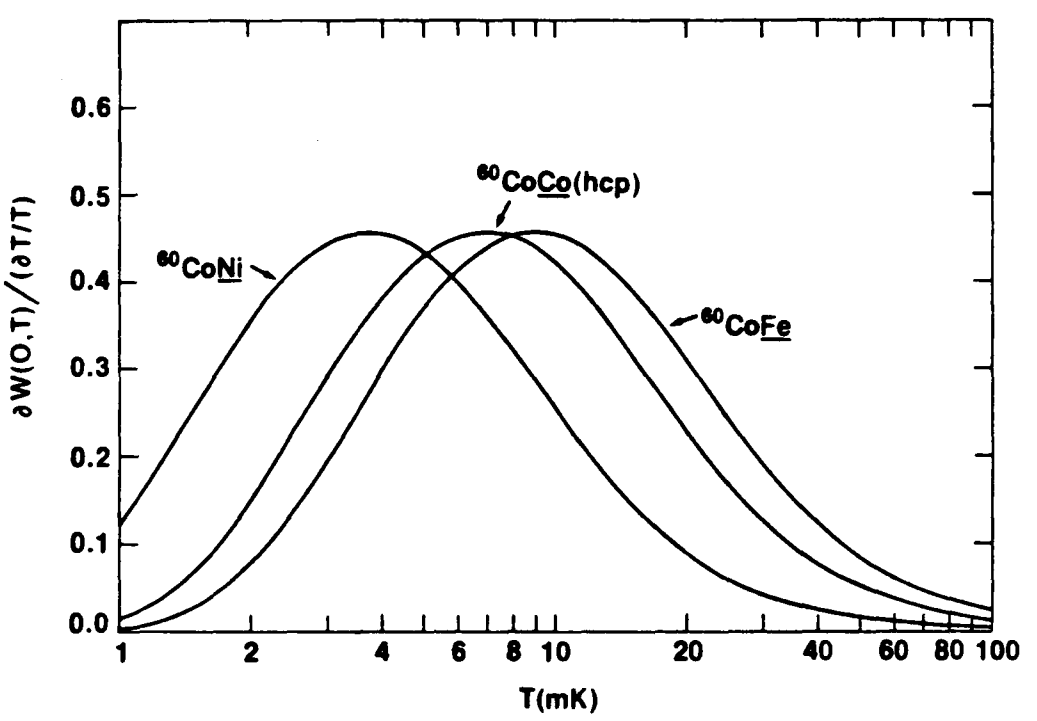

Figure 2.7. The decay scheme and sensitivity functions of ^{60}Co in Co, Fe and Ni.

References

[1] . H. London *et al.*, Phys. Rev. **128** (1962) 1992

[2] . O.V. Lounasmaa, Experimental Principles and Methods Below 1 K (Academic Press, 1974)

[3] . D. Visser, Ph.D. Thesis (University of Groningen, 1981)

[4] . H. Marshak, in Low Temperature Nuclear Orientation, eds. N.J. Stone and H. Postma (North Holland, 1987)

[5] . D.I. Bradley *et al.*, Hyp. Int. **35** (1987) 1033

[6] . B. Bleaney, Physica **69** (1973) 317

[7] . M. Kubota *et al.*, Phys. Rev. Lett. **45** (1980) 1812

[8] . I.S. Grant *et al.*, Nucl. Instr. and Meth. **26B** (1987) 95

[9] . R.J. Soulen and H. Marshak, Cryogenics **7** (1980) 408

Chapter 3

Data Analysis

3.1 Introduction

As has been shown in chapter 1, the angular distribution of gamma radiation from an oriented source is the combined effect of a great many properties of the nuclear system. This chapter will deal with the methods by which these nuclear properties (hyperfine interaction, oriented spin, daughter spins and multipole mixing ratios) are extracted from experimental measurements.

3.2 Spectrum analysis

Once acquired, the gamma ray spectra are analyzed using the Oxford GENeral DATa analysis program, GENDAT †. This package offers two methods of extracting the gamma ray peak areas from these spectra. The first of these, CEN, integrates the counts in the region of interest and subtracts a background linearly interpolated between lower and upper background regions. An example of such a CEN peak fit, with its associated region defining markers, is shown in figure 3.1 . Markers $0 \rightarrow 1$ define the lower background region, $2 \rightarrow 3$ the region of interest and $4 \rightarrow 5$ the upper background region.

The second method, FIT, performs a multiple Gaussian peak fit, allowing unresolved multiplets to be analyzed. FIT invokes a least squares fit to the function

$$y(x) = b_0 + b_1 x + b_2 x^2 + \sum_{p=1}^{N} A_p \exp\left\{-\frac{1}{2}\left(\frac{x - c_p}{\sigma_p}\right)^2\right\} \tag{3.1}$$

where x is the spectrum channel number. The parameters $b_{0,1,2}$ define the background, while c_p and σ_p are the centroids and Full Width Half Maxima of the N peaks labelled by p. Initial

† D. Sinclair and T. Fox, Nuclear Physics Laboratory, Oxford (1983)

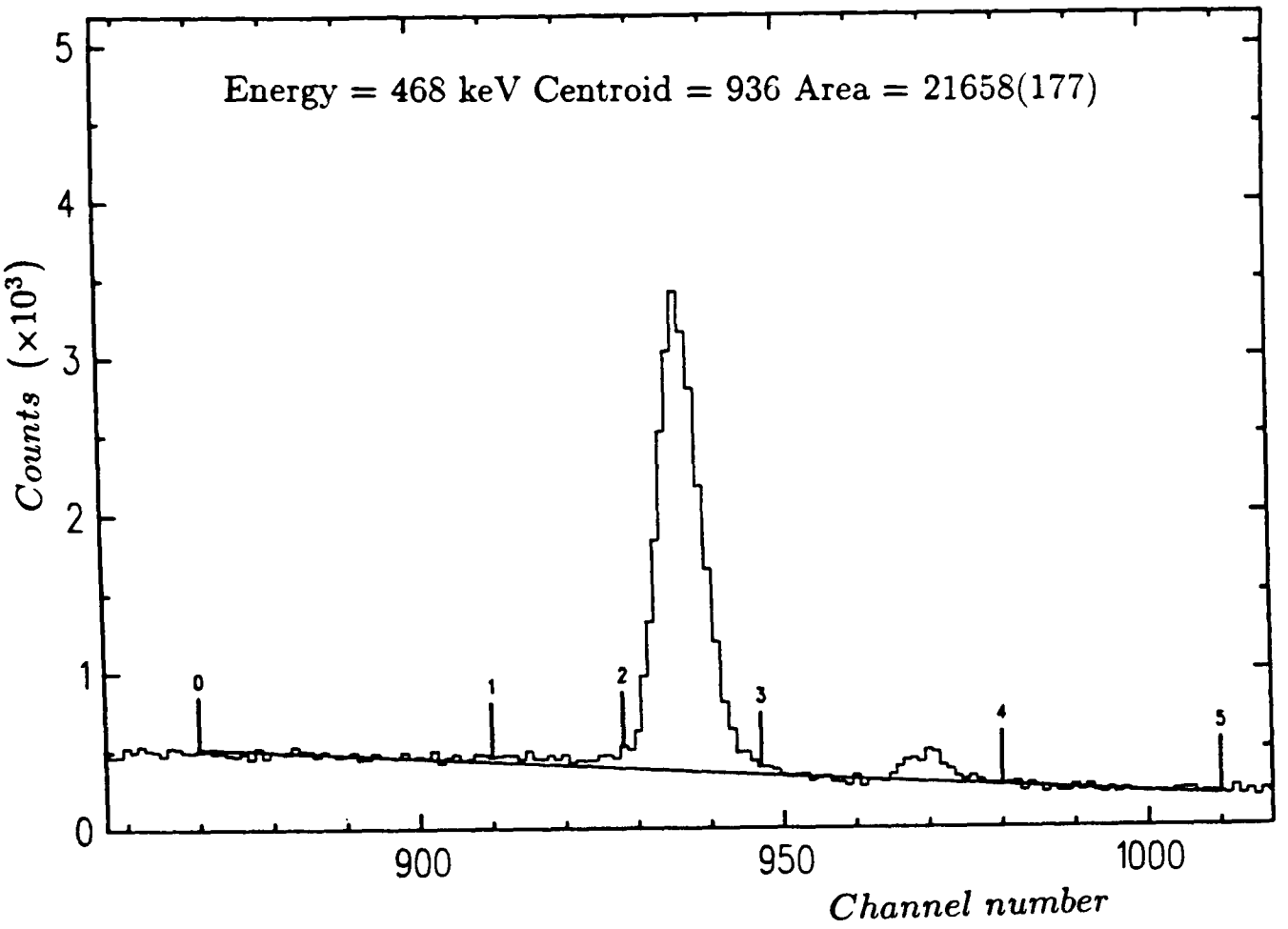

Figure 3.1. The region defining markers appropriate for a CEN peak area fit. The interpolated background is also shown.

guesses for both c_p and σ_p are required. The former is provided by the placement of markers $1 \rightarrow N$, the markers 0 and $N+1$ being used to define the beginning and end of the region to be fitted. These are illustrated for the case of a triplet in figure 3.2 . Initial values for the σ_p are obtained on the assumption that the FWHM is linearly dependent on the gamma ray energy, or more appropriately the centroid c_p. The parameters of this linear function are determined from the fitted centroids and FWHM of two single peaks, one near the beginning and one near the end of the spectrum.

Since the peak shapes need not necessarily be truly Gaussian, the non-peak fitting CEN procedure is used in preference to FIT, unless the use of FIT is forced by the inadequate resolution of multiplet peaks.

Frequently, the background under the peak of interest is discontinuous. In these cases, the 122 keV peak of ^{57}Co being a good example, the behavior of the background under the peak is not clearly defined. GENDAT allows for this by enabling peak markers to be "shifted" from one energy calibration to another. In this way it is possible to apply the *same* markers to *all* spectra, including those of different detectors. Thus although both CEN and FIT may subtract a discontinuous background in a non-unique manner, this is to a large extent compensated by the fact that each peak and its associated background is treated consistently in all spectra.

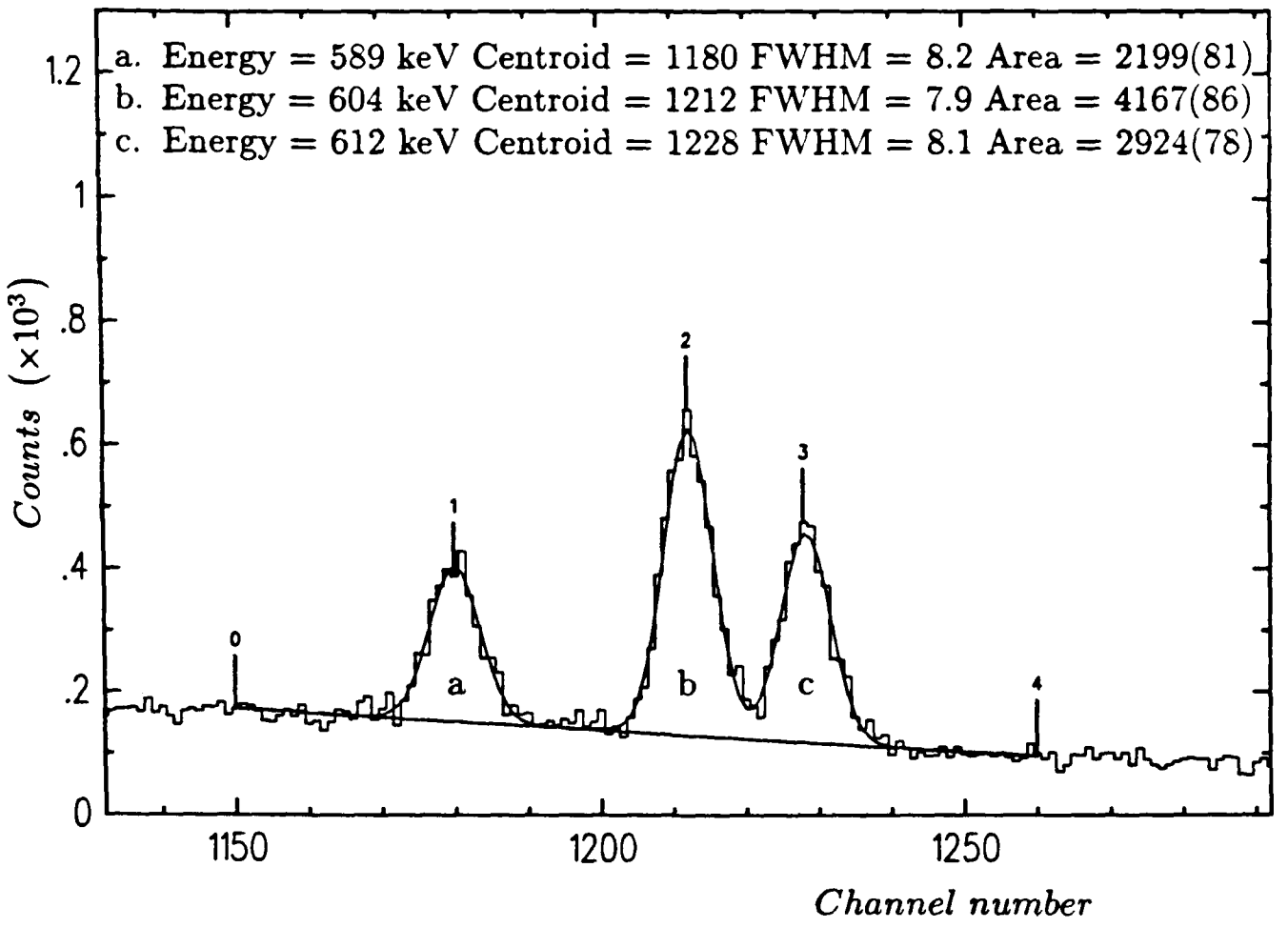

Figure 3.2. The region defining markers appropriate for FIT. The fitted triple Gaussian and the interpolated background are both shown.

In the same vein it is possible to gain shift entire spectra to one control calibration. This is of great use where the detection system suffers from changes in amplification and allows spectra to be added (for improved statistics and hence peak shapes) without fear of a reduction in resolution.

3.3 Experimental determination of $W(\theta)$

In chapter 1 the directional distribution $W(\theta)$ of gamma rays from a LTNO source (1.86) was derived. For a particular gamma ray this can be related to the observed peak area $N_\gamma(\theta)$ by the expression

$$N_\gamma(\theta) = W_\gamma(\theta) I_\gamma \epsilon_\gamma \Omega D \tag{3.2}$$

where I_γ is the gamma ray intensity per parent decay and D denotes the number of parent decays during the counting period. The detector is assumed to have a gamma ray detection efficiency ϵ_γ and to subtend a solid angle Ω at the source.

To clarify the arguments which follow in this section, D will now be evaluated explicitly for the case where the sample decays according to the usual exponential decay law, with decay

constant λ. Thus, for a spectrum whose counting period is of length t_{real} and commences at the time t_{start}

$$\begin{aligned} D &= \int_{t_{start}}^{t_{start}+t_{real}} \mathrm{e}^{-\lambda t} dt \\ &= \mathrm{e}^{-\lambda t_{start}} \left\{1 - \mathrm{e}^{-\lambda t_{real}}\right\} \end{aligned} \tag{3.3}$$

where constant coefficients have been neglected for simplicity. It is clear that the factors D depend on the counting period of the spectrum. However, it is necessary to distinguish between the period for which the ADC was actually available for the processing of signals, t_{live}, and the total counting period, t_{real}. Since in the course of registering a signal the ADC is unable to receive further data, these two times will differ by an amount equal to the dead time, t_{dead}. Typically this constitutes $5 - 25\%$ of the counting time, depending on the count rate. This can be accounted for by introducing a corrective factor, t_{live}/t_{real}. Thus

$$D = t_{live} R \tag{3.4}$$

where the rate R is given by

$$R = \frac{\mathrm{e}^{-\lambda t_{start}}}{t_{real}} \left\{1 - \mathrm{e}^{-\lambda t_{real}}\right\}. \tag{3.5}$$

Experimentally it is necessary to have some means of determining the live time, the real time being pre-defined by the ADC. This is achieved by the pulser method [1], in which an artificial peak is introduced into the measured gamma ray spectrum by a stable pulse generator whose signals are fed into the pre-amplifier of the detector (see section 2.6). These undergo the same pulse processing as the nuclear events and are subject to almost the same counting losses. Therefore the area of the pulser peak divided by the constant repetition rate yields the live time.

However, there is a systematic error associated with such a correction. Namely the fact that the pulser signals come more or less evenly spaced in time and thus they are able to interact with the gamma ray signals, which are randomly distributed in time, but not with themselves. As a result the pulser signals can only correct for the partial gamma ray deadtime, not the total dead time to which they themselves contribute. For the most part these errors can be avoided if the pulser frequency is sufficiently low that the ratio of its dead time to that of the gamma rays is kept below 10% [2].

If p denotes the pulser peak area and f its repetition rate, then from (3.4) one obtains

$$D = \frac{p}{f} R. \tag{3.6}$$

Generally peak areas from several spectra j acquired under similar conditions are summed. Thus

$$\sum_j \{N/p\}_{j,\gamma}(\theta) = \frac{1}{f} W_\gamma(\theta) I_\gamma \epsilon_\gamma \Omega \sum_j R_j. \tag{3.7}$$

In order to eliminate the pulser repetition rate, relative intensity, efficiency and solid angle terms, "warm" counts are taken at a sufficiently high temperature, usually $\sim$ 1 K, so that the directional distribution becomes isotropic ($W(\theta) = 1$). Therefore by taking the "cold" to "warm" ratio and rearranging

$$\begin{aligned} W(\theta) &= \frac{\sum_j \{N/p\}_j(\theta)}{\sum_j R_j} \times \frac{\sum_k R_k}{\sum_k \{N/p\}_k(\theta)} \\ &= \sum_{\lambda i} f_i B_\lambda(B^i_{hyp}) U_\lambda A_\lambda Q_\lambda P_\lambda(\cos\theta) \end{aligned} \tag{3.8}$$

where the subscript γ has been dropped for simplicity and the labels j and k are understood to refer to summation over "cold" and "warm" spectra respectively. From this expression, the fundamental measurement in LTNO, the *anisotropy*, can be defined to be $(W(\theta) - 1)\,\%$.

Thus far only one specific mode of source decay has been considered. If the source is fed by one or more decaying parent nuclei, then D can be derived from (3.3) in an identical manner using instead a multi-exponential integrand. Where the source is produced continuously on-line, then the explicit time dependence of the integrand is unknown as a result of the variable production rate. However, the arguments leading to (3.4), (3.6), (3.7) and (3.8) are still valid, even though R is unknown.

LTNO experiments generally detect the gamma radiation directional distribution at two angles, axial ($\theta = 0$) and equatorial ($\theta = \pi/2$). The data acquisition procedure is such that the counting period begins and ends simultaneously in all detectors. Corresponding axial and equatorial spectra will therefore have common values of R. Applying (3.8) to the ratio of axial and equatorial directional distributions, with the proviso that the summations over the two directions are identical, yields

$$\begin{aligned} \frac{W(0)}{W(\frac{\pi}{2})} &= \frac{\sum_j \{N/p\}_j(0)}{\sum_k \{N/p\}_k(0)} \times \frac{\sum_k \{N/p\}_k(\frac{\pi}{2})}{\sum_j \{N/p\}_j(\frac{\pi}{2})} \\ &= \frac{\sum_{\lambda i} f_i B_\lambda(B^i_{hyp}) U_\lambda A_\lambda Q_\lambda P_\lambda(1)}{\sum_{\lambda i} f_i B_\lambda(B^i_{hyp}) U_\lambda A_\lambda Q_\lambda P_\lambda(0)}. \end{aligned} \tag{3.9}$$

In this way the observed gamma ray peak areas (with pulser normalization) can be directly related to the theoretical angular distribution without making any assumptions as to the nature of the source decay.

The terms on the right hand sides of (3.8) and (3.9) are, in the absence of *a priori* knowledge, multiparameter expressions. Assuming the truncated directional distribution (1.87) leads to just two unknown parameters, $\sum_i f_i B_2 U_2 A_2$ and $\sum_i f_i B_4 U_4 A_4$. In order to calculate these separately it is necessary to retain the two independent axial and equatorial anisotropies (3.8), thus allowing the separation of the two terms by Gaussian elimination. In this way and in the case where the axial and equatorial solid angle correction factors are identical one obtains

$$\sum_i f_i B_2(B^i_{hyp}) U_2 A_2 Q_2 = \frac{1}{7}\left\{3(W(0)-1) - 8(W(\frac{\pi}{2})-1)\right\} \tag{3.10}$$

and

$$\sum_i f_i B_4(B^i_{hyp}) U_4 A_4 Q_4 = \frac{4}{7}\left\{(W(0)-1) + 2(W(\frac{\pi}{2})-1)\right\}. \tag{3.11}$$

Where the series is confined to $\lambda = 2$ by any of the conditions of (1.71), or if *a priori* knowledge allows the two parameters to be related, then there is no loss of information incurred by considering only axial/equatorial ratios.

Finally, it should be noted that the R factors can be removed from (3.8) without calculation by normalizing to a gamma ray peak that is known to exhibit no anisotropy. Presumably this would be by virtue of it having arisen from a level of spin zero or one half and, needless to say, it must belong to the nucleus under consideration in order to achieve the decay correction. In this way separate axial and equatorial anisotropies may be obtained even in the case of on-line sources. However, since a suitable transition may either not be available or may be statistically poor, this is not universally applicable *unlike* the axial/equatorial method.

3.4 Temperature determination

The temperature is determined from the anisotropy of an isotope whose gamma rays have well known orientation coefficients. Since these thermometers are invariably off-line sources, for which the R are always calculable, the temperatures can be extracted from either axial, equatorial or axial/equatorial anisotropies. A more complete discussion of thermometry sources is given in section 2.7.

3.5 Experimental determination of the LTNO parameters

3.5.1 The hyperfine interaction

The extraction of the hyperfine interaction generally proceeds from a least squares fit to the temperature dependence of the experimental anisotropies. Let these anisotropies be denoted by E_l with errors σ_l and correspond to the inverse temperature $1/T_l$. If the appropriate angular distribution function (axial, equatorial or axial/equatorial) to be fitted to these data is $E(1/T_l, \alpha_m)$ which depends on the parameters α_m, then the reduced χ^2 quality of fit is defined as

$$\chi^2 = \sum_l \frac{1}{\sigma_l^2} \{E(1/T_l, \alpha_m) - E_l\}^2 . \tag{3.12}$$

Optimum values for the parameters α_m are then found such that χ^2 is minimized in the parameter space. The error σ_{α_n} on the parameter α_n is determined from the condition [3]

$$\chi^2(\alpha_n \pm \sigma_{\alpha_n}) = \chi^2_{min} + 1 \tag{3.13}$$

where the term on the left hand side is minimized with respect to the remaining parameters $\alpha_{m \neq n}$, while the first term on the right hand side is the absolute minimum of χ^2 with respect to all parameters. This procedure is accomplished by means of the minimizing package MINUIT [4] from the CERN library.

In the case of directional distributions, the parameters α_m refer to the f_i, the hyperfine interaction (electric and magnetic), the U_λ and the A_λ (or the multipole mixing ratio δ). Thus by performing a fit to the temperature dependent data the hyperfine interaction may be deduced. In principle, since the orientation parameters depend on both the Boltzmann parameter β and the oriented parent spin I_0, it is also possible to deduce I_0 in the fitting procedure. In practice the presence of more than one lattice site with non-zero hyperfine interaction, or even the relative effects of the second and fourth rank terms, often have a greater influence on the shape of the temperature dependence and so the more subtle shape differences due to I_0 may be lost.

3.5.2 The angular distribution and de-orientation coefficients

Once the hyperfine interaction and hence the orientation parameters are known, then the U_λ and A_λ coefficients can be calculated from (3.10) and (3.11) (and also from (3.9) if only second rank terms are present). They are also obtained, if sometimes less reliably where both second and fourth rank terms occur, as by-products of the above fitting procedure. In fact if only axial/equatorial ratios are available then this latter method is the only way in which the second and fourth rank terms can be separated if both are present.

Since neither the U_λ nor the A_λ coefficients are temperature dependent they cannot be distinguished experimentally. In the case where the source is "soluble" in the host matrix (1.88) the same is also true of f and so experimentally it is only possible to determine the product $fU_\lambda A_\lambda$. The $U_\lambda A_\lambda$ can only be calculated separately if the factor f can be determined from a gamma ray with known $U_\lambda A_\lambda$ coefficients. If the source is "insoluble" then the more general directional distribution formula (1.87) must be invoked. Here the f_i, by virtue of their association with the $B_\lambda(B^i_{hyp})$ coefficients, scale not only the magnitude of the anisotropy but also its temperature dependence. Thus the parameters f_i are determined directly in the fitting process and the $U_\lambda A_\lambda$ can be obtained immediately.

Further analysis depends on the knowledge of certain details in the decay scheme of the daughter:

1. If the U_λ coefficients can be calculated theoretically for a certain level according to (1.67) and (1.69), then the A_λ coefficients can be deduced for all gamma rays arising from this level. From these it is possible to calculate any one of the properties δ, I_i and I_f using (1.63), provided that the other two are known. Occasionally, if the A_λ coefficients are consistent with a transition of pure multipolarity, then it is possible to deduce either one of the initial or final level spins knowing only the other.

2. If the U_λ coefficients of a level are not calculable, then in order to deduce them experimentally one relies on the knowledge of the A_λ coefficients for one of the daughter transitions. The U_λ coefficients thus derived can, if sufficient information is known *a priori*, be used to determine any one of Δ_β, δ_γ, I_i, I_f and the relative intensities of the feeding transitions (see subsection 1.2.7). Further analysis then proceeds using the method outlined in 1.

In this way it is possible to extract a great deal of useful spectroscopic information about the daughter nucleus, provided that certain details of the decay scheme are known *a priori*. Without being privy to such details, however, the analysis of LTNO data frequently proceeds little further than the extraction of the hyperfine interaction.

References

[1] . H.H. Bolotin *et al.*, Nucl. Instr. and Meth. **83** (1970) 1

[2] . M. Wiernik, Nucl. Instr. and Meth. **96** (1971) 325

[3] . D.W.O. Rogers, Nucl. Instr. and Meth. **127** (1975) 253

[4] . F. James and M. Roos, Comp. Phys. Comm. **10** (1975) 343

Chapter 4

The magnetic moments of the light bromine isotopes

4.1 Introduction

Among the nuclei off the line of stability those in the Z $\sim$ N $\sim$ 40 region are of particular interest, exhibiting large quadrupole deformations, triaxiality and shape coexistence [1-5]. The nuclear ground state spins of the odd A bromine nuclides $^{75-87}$Br with Z=35 are all $3/2^-$. Nilsson orbital calculations show that the last odd proton occupies the [301]3/2 orbital for deformations $\epsilon < 0.22$ and the [312]3/2 orbital at larger prolate deformations. The magnetic dipole moments of these two configurations differ by a factor of three and thus clearly identify the single particle configuration and hence the approximate deformation of the ground state.

With this aim static LTNO measurements have been performed on the light bromine isotopes ^{72g,72m,73,74m,75,76,77}Br. For clarity, the analysis of these experiments will be separated into three chapters. This chapter will describe the experimental details and the measured magnetic dipole moments. Chapter 5 will be concerned with $U_\lambda A_\lambda$ coefficients and the spectroscopy of the daughter Se isotopes, while the theoretical interpretation of the magnetic moments will be given in chapter 7.

4.2 Experimental details and data analysis

Sources of ^{76}Br (16 hrs) and ^{77}Br (57 hrs) implanted at room temperature into polycrystalline iron foils were prepared at the ISOLDE facility, CERN, using the reaction of 600 MeV protons on a target of niobium powder. These were subsequently studied in Oxford at temperatures down to 2 mK using the ^{3}He -^{4}He dilution refrigerator in conjunction with the $PrNi_5$ demagnetization stage. Data was recorded by two Ge(Li) detectors positioned axially and equatorially relative to the axis of orientation, defined by a 1.0 T polarizing field. The source to detector distance was 12 cm.

The isotopes $^{72}Br^{g,m}$ (1.3 m, 10.1 s), ^{73}Br (3.4 m), $^{74}Br^{m}$ (46 m) and ^{75}Br (97 m) were produced on-line using the reaction of 150 MeV ^{28}Si on a ^{54}Fe target which formed part of the FEBIAD ion source of DOLIS. After acceleration to 60 keV, the selected bromine ions were implanted into a polycrystalline iron foil soldered to the cold finger of the dilution refrigerator at temperatures down to 8 mK. Production rates were low for the lighter isotopes, but well resolved gamma spectra were recorded in four Ge(Li) detectors, two in both the axial and equatorial positions. The detector to source distance was 8 cm. The iron foil was polarized by a 0.7 T magnetic field in a direction parallel to its surface and perpendicular to the implanted beam direction.

With regard to data analysis, two different models describing the lattice site occupation of the bromine nuclei in the iron matrix will be assumed. The first model, henceforth known as model 1, is that applicable to "soluble" implants (1.88) where a fraction f of nuclei experience the full substitutional hyperfine field B_{sub}, while the remaining $1-f$ occupy lattice sites with zero hyperfine field. As an alternative, hereafter referred to as model 2, a simplified form of the model applicable to "insoluble" implants (1.87) is taken. Here, as before, a fraction f of nuclei experience the full substitutional hyperfine field B_{sub}, but now it is assumed that the remaining $1-f$ occupy a second lattice site subject to a single non-zero hyperfine field, B_{low}.

Herzog *et al.* [6], using NMR/ON techniques in ^{82}Br, have measured the substitutional magnetic hyperfine field of Br<u>Fe</u> to be B_{sub}=+81.38(6)T. Using this field it was found that the magnetic moment extracted from a model 1 fit to the integral LTNO data, as obtained from a low temperature implanted sample, differed by 10% from the known moment. A satisfactory fit could, however, be made using model 2 with $B_{low} = \pm 26(2)$T. A subsequent work [7] on both room and low temperature implanted samples over a wide range of doses showed that it was generally necessary to invoke model 2 in order to reproduce the magnetic moment. The variation in the value of B_{low} extracted from the various runs was no greater than would be expected from the statistical error of the value quoted above. No further complexity of site distribution can be meaningfully tested by the integral LTNO method. Extensive channelling studies by Alexander *et al.* [8] in the Br<u>Fe</u> system at room temperature and relatively high implantation dose support this multiple site picture. They concluded that there was indeed a second, well defined, non-substitutional site and that this location was independent of the local bromine concentration over a wide range. Building upon this work, Callaghan *et al.* [9] performed an integral LTNO experiment on ^{82}Br<u>Fe</u> in order to evaluate the two hyperfine fields. On the reasoned assumption that the second field contributed little to the experimental anisotropy and could therefore be neglected, they determined the substitutional hyperfine field to be ±84(12)

T with an associated population of 36(5)%. Thus even using the crude model 1 they were able to predict the substitutional hyperfine field to within 15%.

On the basis of these results it can be expected that the model uncertainties will only influence the extracted moments at the level of 10 – 15%. Fitted moments obtained from both of the above models will be quoted in this chapter. The values ultimately adopted, however, will be those of model 2 after assigning errors which reflect the model site distribution uncertainties as well as the statistical errors.

4.3 The isotopes ^{76,77}Br

Both of these nuclei were studied prior to the publication of references [6,7] and so it was not anticipated that the shortcomings of model 1 would be significant. Since the magnetic moment of ^{76}Br 1^- had already been measured ($\pm 0.5482(1)\mu_N$ [10]), the experimental effort on the decay of this isotope was concentrated on the extraction of U_2A_2 coefficients and hence spectroscopic information on ^{76}Se. To this end the $PrNi_5$ demagnetization stage was used to cool the nuclei to 2 mK, as measured by a ^{60}CoNi thermometer, which resulted in the saturation of the gamma ray anisotropies. Unfortunately, these anisotropies were generally rather small, even close to saturation. Of the strongest lines, the 559 and 657 keV transitions showed anisotropies of only +3.8(3)% and −0.6(4)% at 3 mK (see table 5.2). Only the 1130, 1854 and 2951 keV transitions gave anisotropies with sufficiently favourable proportional errors to produce reasonable temperature dependences. These are illustrated in figure 4.1 .

The decay scheme of ^{76}Br is shown in figure 5.2 [11]. Due to a combination of uncertain spin assignments and complicated level feedings by a proliferation of weak gamma rays, no U_2A_2 coefficients can be calculated *a priori*. Therefore within the framework of model 1 it is necessary to perform a fit to the experimental axial/equatorial anisotropies with both μB_{sub} and fU_2A_2 as variable parameters. The fitted hyperfine interaction parameters are listed in the second column of table 4.1 . From this data the average hyperfine interaction is calculated to be $\mu B_{sub} = 35.0(25)\mu_N$T. This is to be compared with the expected value (corrected for applied field) of $\mu B_{sub} = 45.16(3)\mu_N$T.

This 25(6)% difference highlights once again the failure of model 1 to adequately describe the BrFe system as first noted by Herzog *et al.* Following their lead therefore, the more realistic model 2 is invoked. Here, with μ required to reproduce the known value, U_2A_2, f and B_{low} remain as variable parameters. In order to reduce the number of unknowns, B_{low} was taken

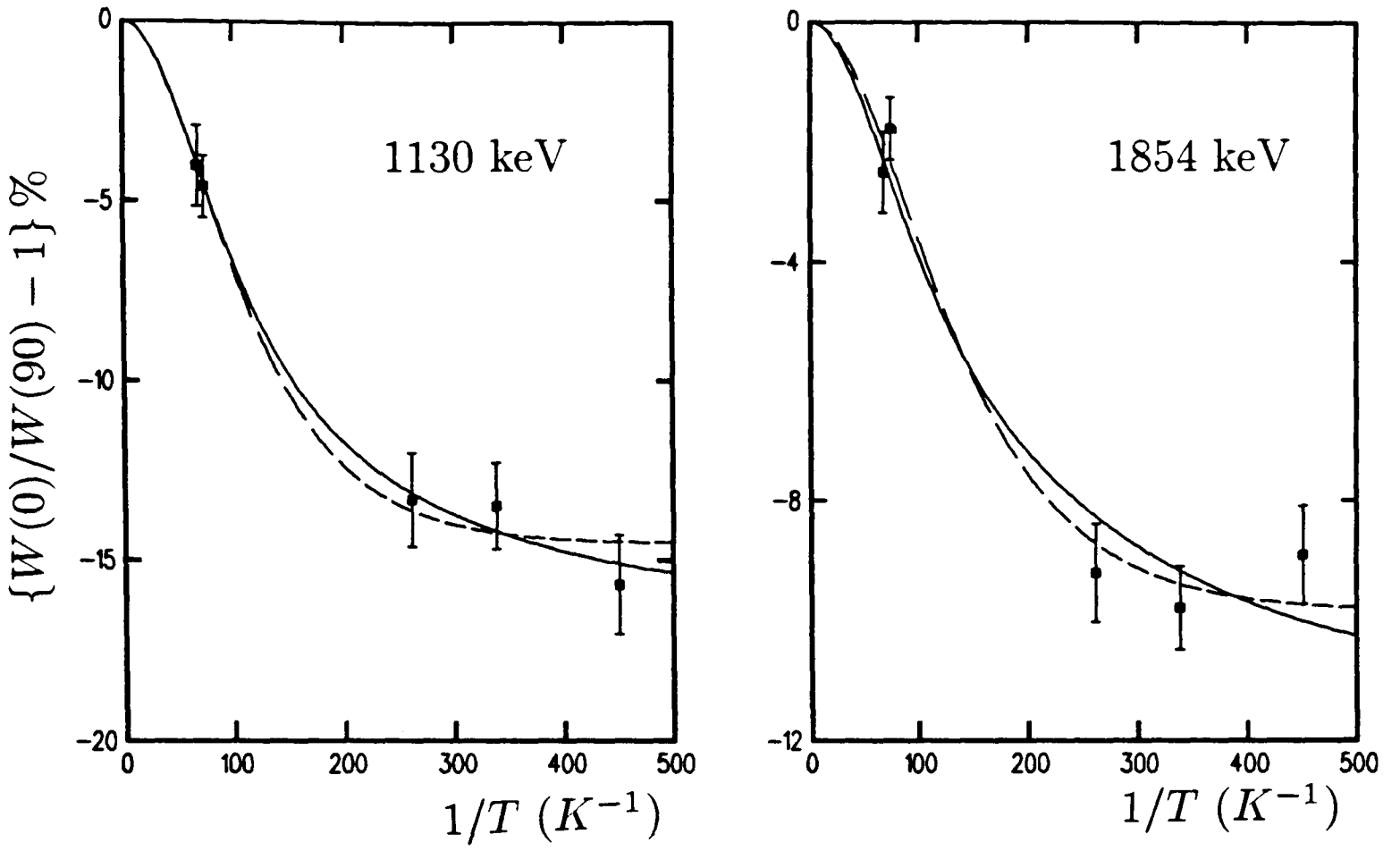

Figure 4.1. The temperature dependences of the 1130, 1854 and 2951 keV transitions in the decay of ^{76}Br. The 2591 double escape peak is also shown. Both the model 1 (dashed) and model 2 (solid) fitted curves are shown for comparison.

Table 4.1. The fitted model parameters for ^{76}Br. The single and double escape peaks of the 2951 keV transition are denoted s.e. and d.e. respectively.

E_γ (keV)	Model 1 fitted μB (μ_NT)	χ^2	Model 2 fitted f (%)	χ^2
1130	39.9(5.1)	0.4	69.2(17.3)	0.2
1854	33.4(4.5)	1.1	56.8(16.9)	1.5
2951	33.3(4.3)	0.3	51.2(15.5)	0.7
2951 s.e.	34.7(10.9)	0.4	61.6(38.3)	0.6
2951 d.e.	33.2(9.3)	0.1	53.5(32.9)	0.3

to be 26(2)T as discussed in section 4.2. In this way the fitted site distribution parameters f given in the third column of table 4.1 are obtained. The weighted average of this data yields $f = 58(9)\%$.

In order to understand how model 2 is able to correctly reproduce the substitutional hyperfine interaction it is instructive to consider the individual contributions from the various lattice sites. These are illustrated in figure 4.2 . The anisotropy data from the 1130, 1854 and 2951 keV transitions (including escape peaks) has been inverted to yield $\sum_i f_i B_2 U_2 A_2$ and then normalized to the 14 mK temperature points, which for this purpose have been combined, and finally summed. The resulting data therefore represents the relative orientation of the ^{76}Br nuclei as a function of temperature. The orientation predicted by model 1, shown dashed, arises solely from the hyperfine interaction of nuclei in substitutional sites. It is clear that the true substitutional hyperfine interaction, $\mu B_{sub} = 45.2\mu_N$T, increasingly underestimates the experimental orientation as the temperature reduces. This gap between the observed orientation and that due to the fully substitutional lattice site may be bridged by introducing a second lattice site which experiences a non-zero hyperfine interaction. The individual contributions of the substitutional and low field sites, weighted by their relative populations, to the total model 2 orientation are illustrated by the solid lines. The discrepancy between the magnetic moments extracted using the two models may be attributed to the proportion of the total orientation arising from this second non-substitutional hyperfine interaction. In the present case this proportion is as high as 35% at the lowest temperature datum, which results in the large disparity between the two extracted moments. The magnetic moments of the other nuclei studied in this work have all been extracted from data taken at temperatures above 6 mK, where the relative contribution from the second field site is greatly reduced. The model differences and hence the ambiguity in the extracted moment will therefore be correspondingly smaller.

Having determined the site distribution parameter $f = 58(9)\%$ of ^{76}Br<u>Fe</u> it is assumed that the same value may be applied to the case of ^{77}Br. This is justified since both were implanted

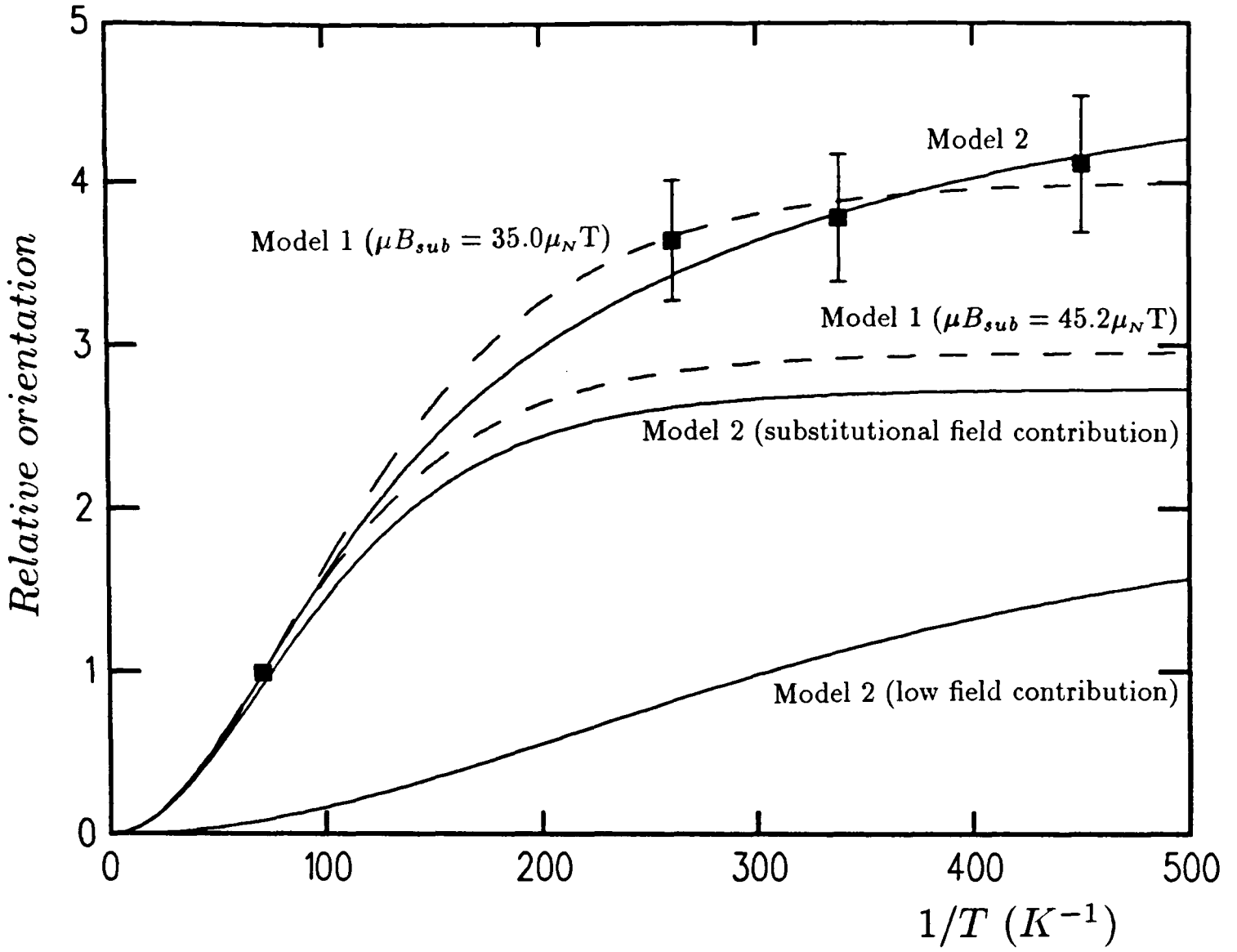

Figure 4.2. The contributions to the total orientation from the model lattice sites. The data is taken from transitions in the decay of ^{76}Br. The model 1 and model 2 fitted curves are distinguished by dashed and solid lines respectively.

under the same conditions and with similar dosage. Further, it is likely that the experimental error in f is sufficient large to take account of any minor variations between the samples.

In contrast the magnetic moment of ^{77}Br $3/2^-$ had not previously been measured. The experiment was therefore performed in two parts. The first took a full temperature dependence down to a temperature of 6 mK as deduced from the anisotropy of a ^{60}CoCo(hcp) thermometer. The second was conceptually identical to the previous ^{76}Br experiment, employing the $PrNi_5$ demagnetization stage to extend and saturate the temperature dependence data.

The decay scheme of ^{77}Br is given in figure 5.1 [12]. Again no U_2A_2 coefficients are calculable *a priori* even though most of the level spins are known. The variable model 1 parameters are therefore μ and fU_2A_2, while for model 2 there remains μ and U_2A_2, since f and B_{low} are considered as known. It should be noted that the site distribution parameter f is *not* the same in the two models. Figure 4.3 shows the temperature dependences of the 304, 439, 575 and 585 keV transitions obtained using the dilution refrigerator alone. The results of both model fits to

this data are shown in table 4.2 for a total of ten transitions. From these results an average model 1 moment of $\mu = 0.82(3)\mu_N$ is obtained. For model 2 a moment of $\mu = 0.92(5)\mu_N$ is extracted. Notice that as a result of the higher temperatures there is only an 11(7)% disagreement between the two models. Comparing the χ^2 values of the two sets of model fits, which are to all intents and purposes identical, it can be seen that even with data of such relatively good quality the integral LTNO method is unable to distinguish between the two models.

Table 4.2. The fitted moments of ^{77}Br.

E_γ (keV)	Model 1 fitted moment (μ_N)	χ^2	Model 2 fitted moment (μ_N)	χ^2
239	0.76(30)	5.4	0.90(71)	5.4
250	0.87(19)	1.7	0.99(37)	1.7
304	0.79(10)	0.8	0.90(11)	0.7
385	0.87(11)	1.1	1.00(23)	1.1
439	0.83(12)	0.8	0.95(16)	0.8
485	1.04(26)	0.5	1.22(60)	0.5
521	0.93(19)	3.3	1.14(41)	3.2
575	0.76(5)	0.5	0.85(9)	0.6
585	0.90(8)	0.4	1.04(14)	0.4
755	0.73(21)	1.0	0.81(30)	1.1

Finally, the data taken with the demagnetization stage will be considered. This is illustrated in figure 4.4 . Although both parts of the experiment used the same sample, at a given temperature the anisotropies of the demagnetization data are consistently greater than those obtained using the dilution refrigerator alone. This is due to the unsoldering and slight cleaning of the surface of the host iron foil prior to resoldering onto the demagnetization stage in preparation for the latter part of the experiment. This resulted in a small loss of surface activity. Model 1 fits to these anisotropies resulted in moment of $0.81(4)\mu_N$. The close agreement of the two model 1 values indicate that this model is equally valid both before and after the sample was cleaned. In turn this suggests that only surface activity, with no significant hyperfine interaction, was removed. Since the lattice site occupation has clearly changed it is no longer justifiable to take the model 2 site distribution parameter from ^{76}Br. Thus μ, U_2A_2 and now also f must be considered as variable parameters in model 2. However, just as in the case of ^{76}Br, the demagnetization temperature dependence is rather sparse and certainly insufficient for meaningful three parameter fits to be performed. Therefore the model 2 value of μ already derived is assumed and a two parameter fit is performed to obtain f and U_2A_2. In this way

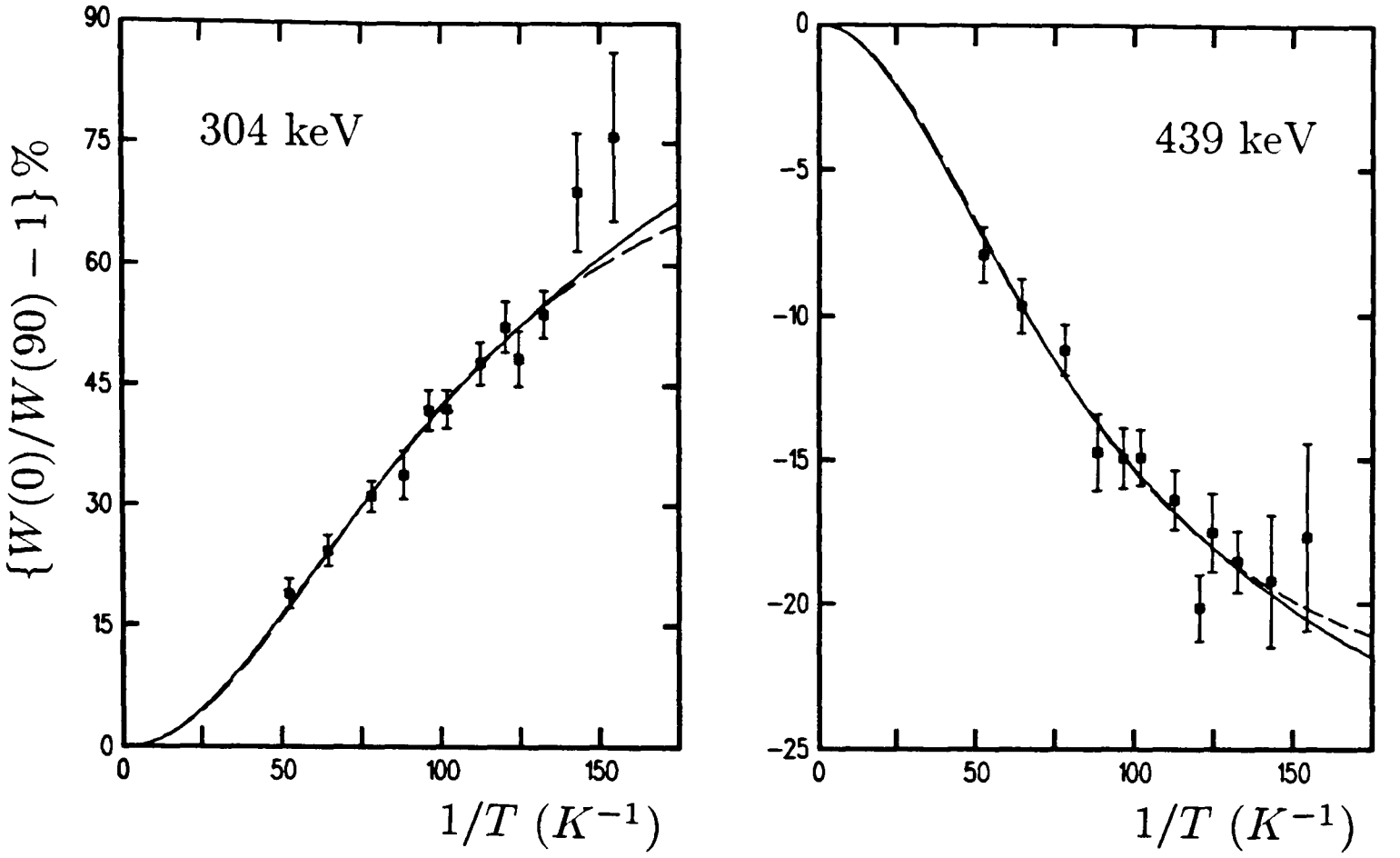

Figure 4.3. The temperature dependences down to 6 mK of the 304, 439, 575 and 585 keV transitions in the decay of ^{77}Br. Both the model 1 (dashed) and model 2 (solid) fitted curves are shown for comparison.

the new site distribution parameter $f = 78(9)\%$ is obtained. Again the χ^2 values of the two models are virtually identical. Since this data has no relevance to the magnetic moment, further discussion will be postponed until chapter 5.

4.4 The isotopes $^{72-75}$Br

These isotopes were on-line implanted into a cold iron foil at the DOLIS-COLD facility where temperatures as low as 8 mK were achieved, as deduced from the anisotropy of a ^{57}Co<u>Fe</u> thermometer. Unlike the previous case, there is no control isotope with a known moment with which to determine f. Therefore within the framework of model 2 there are at least four unknown parameters, μ, f, $U_\lambda A_\lambda$ and B_{low}. In order to be able to extract reliable values for the magnetic moment from the fitting procedure it is desirable to reduce this number to two. Since the $U_\lambda A_\lambda$ coefficients are not generally known *a priori* they must be considered as variable parameters. Therefore not only B_{low}, but also a range of values for the site distribution parameter f is assumed.

The variation in f as a function of implantation conditions of ^{82}Br<u>Fe</u> has also been studied by Herzog *et al.* [7]. It is apparent from this work that the value of f is considerably dependent upon implantation dose and also the method of production. However, the values for different on-line implantations were all found to lie within $75\% \geq f \geq 58\%$. Although some dependence upon the method of preparation of the iron foil might also be expected, this range will be considered to be valid for the present work. Since all iron foils used in the present experiments were prepared in an identical manner this will not lead to any problems with internal self consistency. Thus the likely variation in f will be spanned if a maximum value of 75%, model 2a, and a minimum value of 58%, model 2b, is taken. It should be noted that the choice of 58% as the minimum value for the site distribution parameter in on-line samples coincides the value deduced for the off-line prepared samples ^{76,77}Br. That the site distribution parameter is probably lower for off-line rather than for on-line prepared samples is apparent from the data of Herzog *et al.* The likely reason for this behaviour in such "insoluble" implants is discussed in subsection 1.3.3.

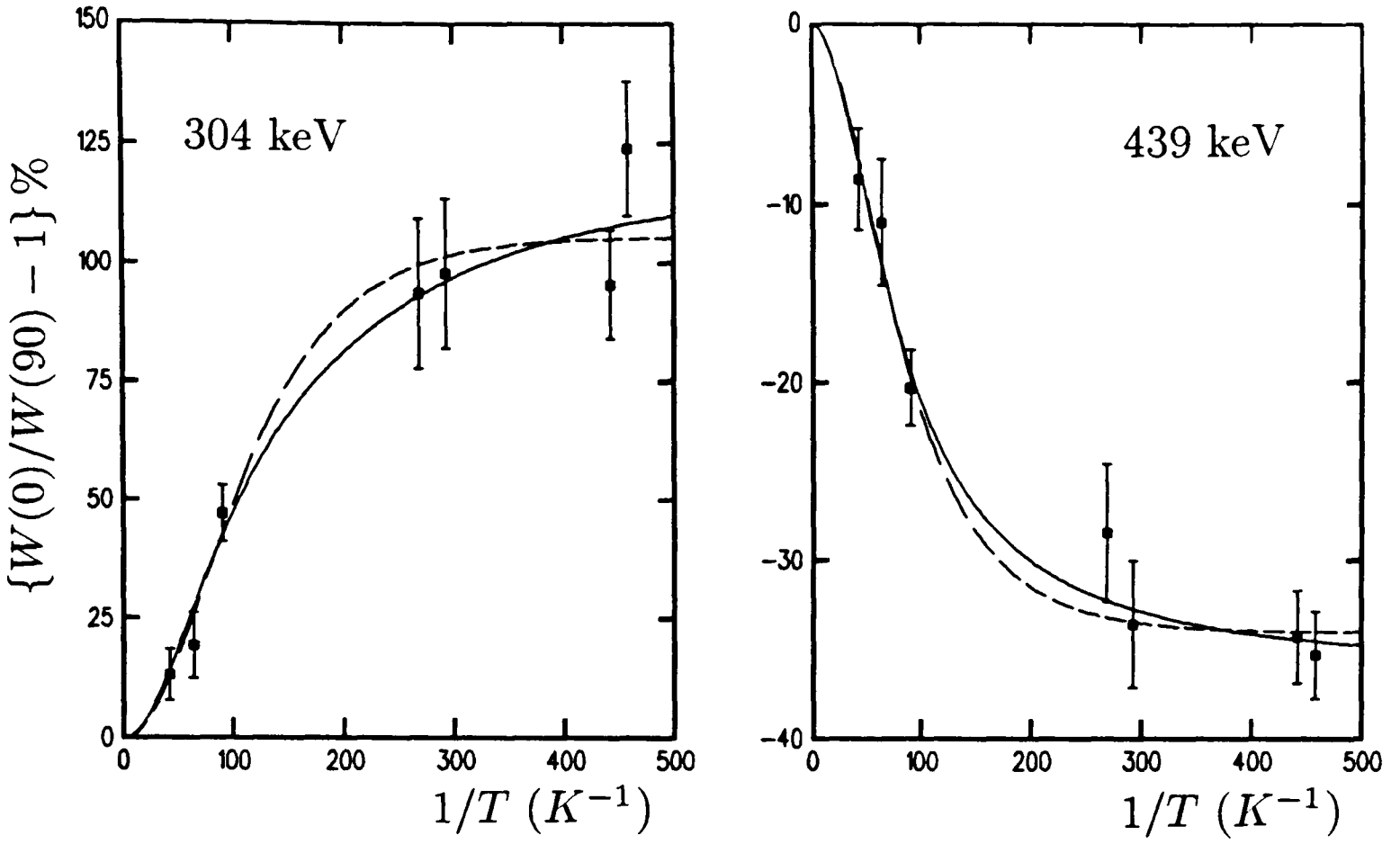

Figure 4.4. The temperature dependences down to 2 mK of the 304, 439, 575 and 585 keV transitions in the decay of ^{77}Br. Both the model 1 (dashed) and model 2 (solid) fitted curves are shown for comparison.

4.4.1 The isotope ^{75}Br

The presence in the DOLIS output of an inactive contaminant beam at this mass required that the ^{75}Br source was built up by implanting for 2.5 h at approximately 50 mK. This was then followed by a period of cooling down to temperatures of 9 mK with the isotope separator closed off. The cycle was repeated several times.

With the exception of the 377 keV transition, which gave data of good statistical accuracy, the resulting anisotropies were rather small. The temperature dependence of this peak is illustrated in figure 4.5 . In addition and uniquely among all the isotopes studied, the U_2A_2 coefficient can be calculated for this transition with sufficient accuracy to enable some constraint to be placed on the fitting procedure. The decay scheme is illustrated in figure 5.3 [13]. Using the 664 keV level de-orientation coefficient deduced in section 5.4, in conjunction with the previously known mixing ratio for the 377 keV transition ($\delta(377) = -0.73(45)$ [13]) leads to the inequality $+0.62 \leq U_2A_2 \leq +0.81$. The model 2 fitted U_2A_2 coefficient is compatible with this result to within one standard deviation for all site distribution parameters $f \geq 44\%$, which greatly exceeds the likely range of variation given above. Therefore the limiting values 75% (model 2a) and 58% (model 2b) are retained and with f thus fixed the inequality for U_2A_2 is used to limit the error on the fitted moment. The results of the fitting procedure are shown in table 4.3 for models 1, 2a and 2b, both with and without the constraint on U_2A_2. Of course in model 1 this constraint has no effect on the fitted moment and merely serves to provide the inequality $f \geq 53\%$.

Note that despite the large difference between the site distribution parameters of model 2a and 2b there is only a very slight difference in the fitted moments.

Table 4.3. The fitted moments of ^{75}Br. †The values tabulated in the second row are constrained by the known U_2A_2 coefficient of the 377 keV transition.

E_γ (keV)	Model 1 fitted moment (μ_N)	Model 2a ($f = 75\%$) fitted moment (μ_N)	Model 2b ($f = 58\%$) fitted moment (μ_N)
377	0.73(9)	0.75(19)	0.78(24)
377†	0.73(9)	0.75(15)	0.78(17)

4.4.2 The isomer $^{74}Br^{m}$

The heavy ion reaction of 150 MeV ^{28}Si on ^{54}Fe preferentially produced the high spin isomer. The proportion of the ground state present, as deduced from the intensity ratio of the 615 to 634 keV transitions, was less than 5% and therefore essentially negligible. Large anisotropies with small statistical errors were observed for the 634, 728 and 1250 keV transitions, shown in figure 4.5, and also for the 615, 839, 1201 and 1269 keV transitions.

The decay scheme of $^{74}Br^{m}$ is shown in figure 5.4 [14]. The isomeric spin has been deduced by atomic beam resonance methods to be $I = 4$ [15]. As will be discussed in sections 5.5 and 7.5.2, the tentative negative parity assignment to this state, made on the basis of proposed first unique forbidden β^{+}/EC decays to levels in ^{74}Se, appears to be wrong. Partly as a result of this, but mainly due to the complex decay scheme, no $U_\lambda A_\lambda$ coefficients are known or can be calculated *a priori*. Further, since the parent has spin $I > 3/2$, these coefficients involve two terms corresponding to $\lambda = 2$ and 4.

Table 4.4. The fitted moments of $^{74}Br^{m}$ excluding $\lambda = 4$ terms.

E_γ (keV)	Model 2a ($f = 75\%$) fitted U_2A_2	fitted moment (μ_N)
615	−0.31(3)	1.80(26)
634	−0.21(1)	1.50(8)
728	−0.34(1)	1.70(7)
839	−0.41(5)	1.35(18)
1201	−0.33(5)	1.88(29)
1250	−0.50(3)	1.95(14)
1269	−0.26(4)	1.61(27)

As a first step towards dealing with this extra parameter the data was fitted to model 2a ignoring fourth rank terms. The results are listed in table 4.4 for the seven transitions given above. The weighted mean of these moments is $1.64(5)\mu_N$ for which at 10 mK the ratio of the high field orientation parameters is $B_4(B_{sub})/B_2(B_{sub}) \sim 30\%$. Although this ratio is likely to become smaller when allowance is made for the relative effects of the two $U_\lambda A_\lambda$ terms, the fourth rank terms possibly constitute a sizeable effect. Generally the quality of the temperature dependences is not sufficient to allow the parameter U_4A_4 to be varied meaningfully. However, the temperature dependences of the strong 634 and 728 keV transitions might allow for this extra degree of freedom. Since statistically these contribute most to the final moment there is little to be lost in considering these exclusively. The three fitted parameters for the two transitions

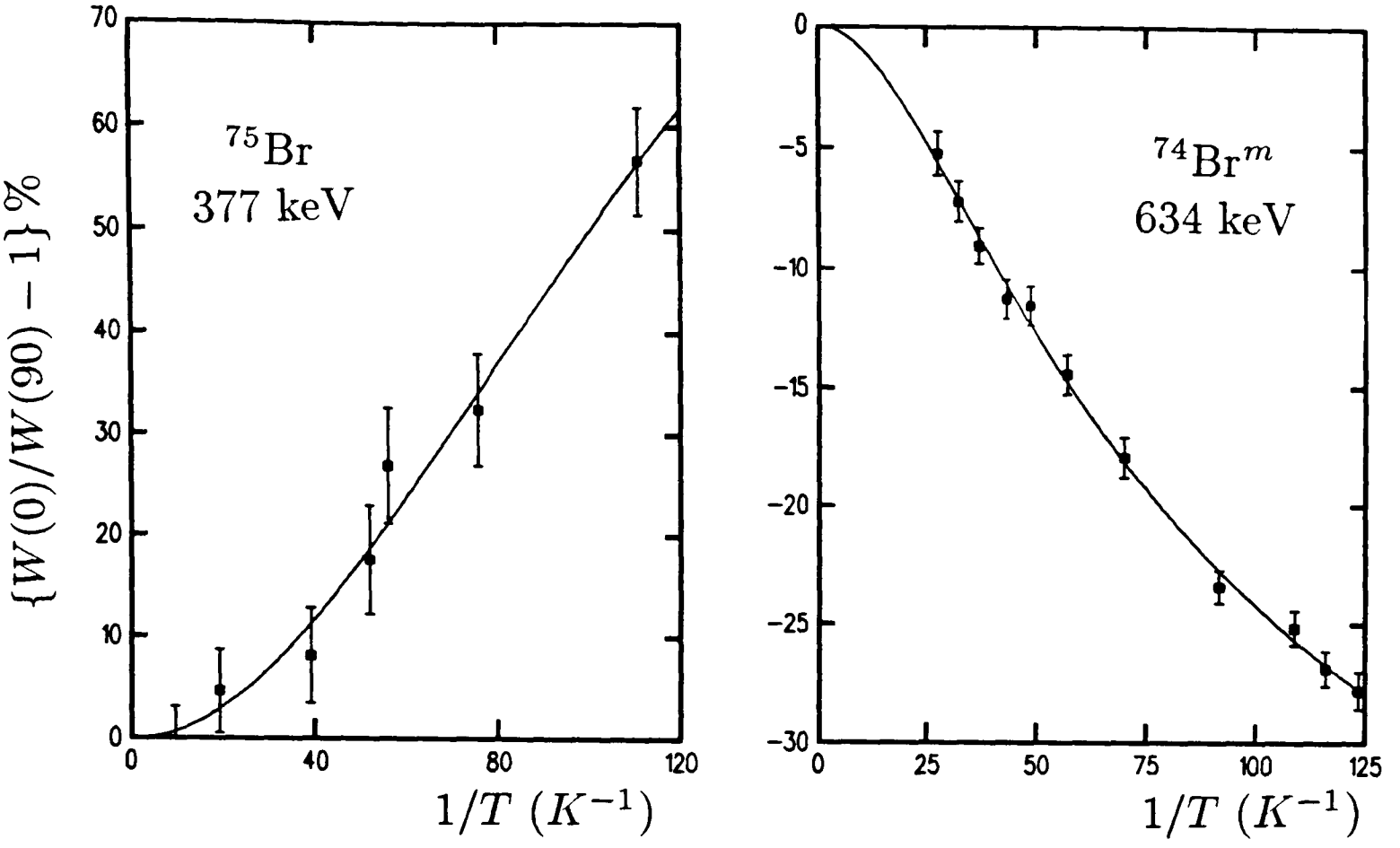

Figure 4.5. The temperature dependences of the 377 keV transition in the decay of ^{75}Br and the 634, 728 and 1250 keV transitions in the decay of ^{74}Br^m. The model 1 and model 2 fitted curves coincide.

are shown in table 4.5 from which the weighted averages of the fitted moments are found to be 1.63(6), 1.59(8) and 1.77(11) μ_N for models 1, 2a and 2b respectively. Once again the relatively small difference in the model 2a and 2b moments demonstrates their limited sensitivity to the assumed site distribution parameter.

Table 4.5. The fitted moments of $^{74}Br^m$ including $\lambda = 4$ terms.

E_γ	Model 1			Model 2a ($f = 75\%$)			Model 2b ($f = 58\%$)		
(keV)	U_2A_2	U_4A_4	μ	U_2A_2	U_4A_4	μ	U_2A_2	U_4A_4	μ
634	−0.10(1)	−0.25(6)	1.95(15)	−0.13(1)	−0.25(7)	1.96(22)	−0.18(1)	−0.18(6)	1.91(17)
728	−0.30(1)	+0.02(8)	1.56(7)	−0.39(1)	+0.21(9)	1.54(8)	−0.42(1)	+0.21(11)	1.68(14)

4.4.3 The isotope ^{73}Br

Anisotropies were observed for 16 of the strongest transitions in the decay of ^{73}Br. These are tabulated in section 5.6. The anisotropy of the ^{57}CoFe thermometer corresponds to an average temperature of 12 mK. All the ^{73}Br effects are consistent with zero orientation. Since the iron foil in which ^{73}Br was studied was the same as that used to successfully orient $^{72,74m}Br$ in the same on-line run, there can be no possibility of a non-nuclear origin for this lack of anisotropy.

The decay scheme of ^{73}Br is shown in figure 4.6 [14]. Experimentally the ground state spin of ^{73}Br had been assigned $(1/2, 3/2, 5/2)^-$ as a consequence of its allowed β^+/EC decay to the 26 keV $3/2^-$ level in ^{73}Se. On the basis of systematics in the neighbouring odd A isotopes this was assumed to be $3/2^-$. However, the lack of anisotropy is at variance with this hypothesis.

If the ground state were $3/2^-$ and had a moment similar to that of $^{75,77}Br$ then the relaxation time would be of the order of 5 s (see subsection 4.4.4). When compared to the 3.4 m half life it is clear that incomplete relaxation cannot be responsible for reducing the orientation to the virtually zero levels observed.

It must therefore be concluded that the lack of observed anisotropy is due to the presence of one or more un-oriented spin 1/2 levels. The transitions in ^{73}Se originate from many different levels which are independently fed in the decay. A recent spectroscopic study of the decay of ^{73}Br [16] has assigned spins to some of the levels assuming that the parent spin is $3/2^-$. While most of these are tentative it is clear that not all of the levels which give rise to the observed

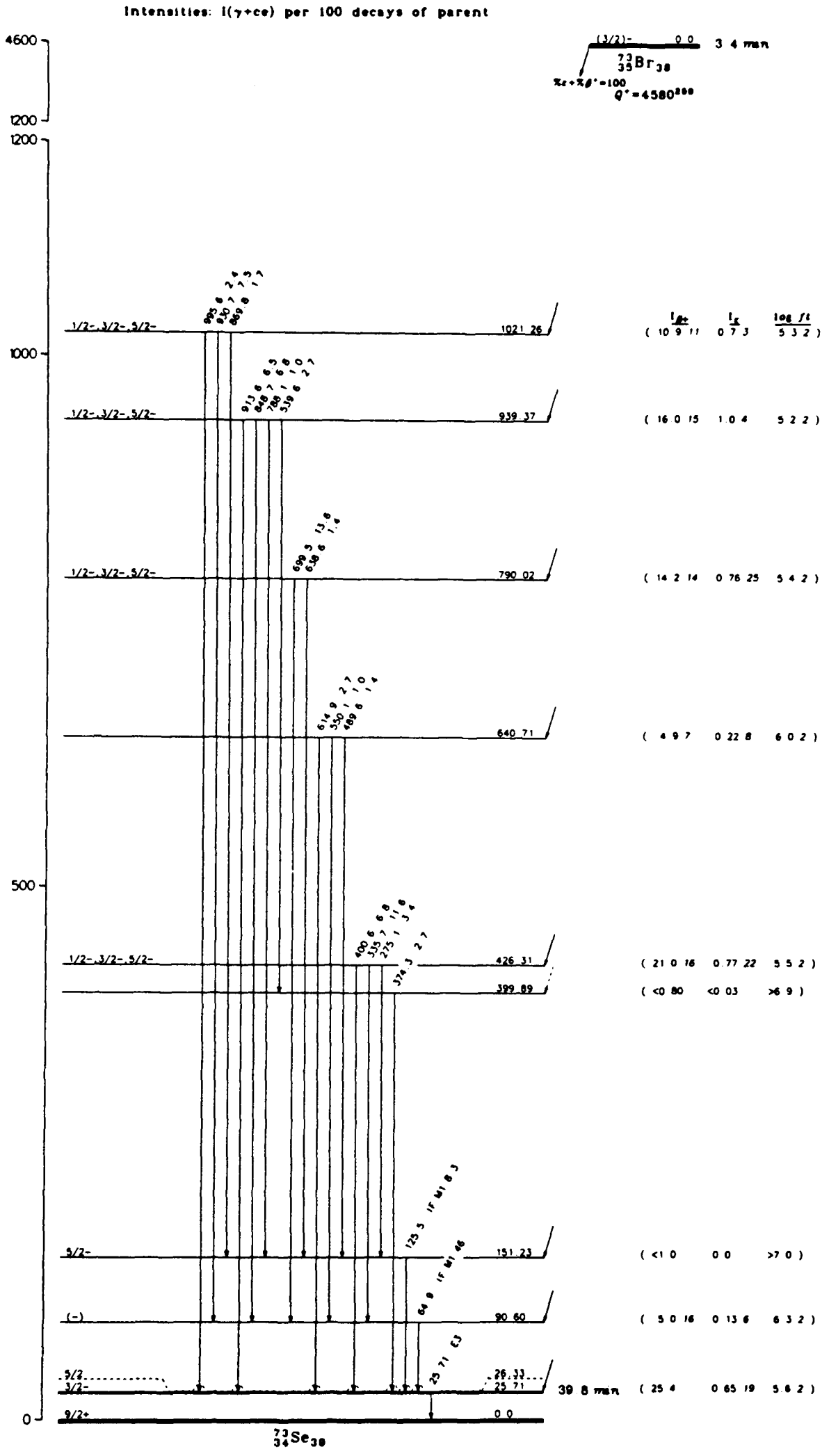

Figure 4.6. The decay scheme of ^{73}Br [14].

gamma transitions are likely to be of spin 1/2. It is therefore most probable that at least a few of the relevant levels in ^{73}Se should be capable of orientation. In principle the lack of orientation might also be due to unfortunate values of the gamma multipole mixing ratios which lead to near zero angular distribution coefficients. This possibility is also inherently unlikely to be simultaneously true for several transitions. Two levels in ^{73}Se (other than the ground state) are in fact known to have spins other than 1/2 [14]. Unfortunately neither figure prominently in this work. The 151 keV $5/2^-$ level gives rise only to the 126 keV transition which lies between the 122 and 136 keV peaks of the thermometer, ^{57}CoFe. Although the triplet is resolved, the background is discontinuous making its subtraction difficult and ambiguous. However, a crude manual background subtraction showed no significant anisotropy for this transition. The second level at 26 keV ($3/2^-$, 40 m) is isomeric and therefore orients in its own right.

One concludes therefore that it is in fact the parent nucleus, ^{73}Br, which has a ground state spin $1/2^-$. Although such an assignment differs from the spin $3/2^-$ ground states of all the heavier odd isotopes up to ^{87}Br, it is fully consistent with all known features of the decay.

4.4.4 The ground state and isomer ^{72}Br^{g,m}

Both the ground and isomeric states of ^{72}Br were produced, if rather weakly, in the heavy ion reaction and gave small, but nevertheless non-zero, anisotropies. Part of the reason for the modest anisotropies lies in the fact that the half-lives of the ground and isomeric states, 1.3 m and 10.1 s respectively, are not significantly larger than the spin-lattice relaxation times.

Herzog *et al.* [6], by assuming a single exponential recovery of the anisotropy after a period of resonance, obtained a spin-lattice relaxation time constant [17] of 19.2(14) s for ^{82}BrFe at a temperature of 7.3(1) mK. This enables the value $(\mu/I)^2 C_k = 0.032(2)$ to be determined from figure 1.5 (which is appropriate for the oriented spin of ^{82}Br). This is an isotope independent quantity which allows a self consistent calculation to be performed on the data of ^{72}Br taking into account the effects of imperfect relaxation on the observed anisotropies.

Firstly the β^+/EC decay of ^{72}Br^g, illustrated in figure 5.5 [18], will be considered. The spin parity of this state has been assigned $(3)^+$ [19]. A brief review of the underlying arguments leading to this assignment will be given in section 5.7. Unfortunately this could not be confirmed by the particle-rotor calculations of subsection 7.5.3.

As a result of the weak anisotropies only the strongest line in the decay, at 862 keV, yielded a resonable temperature dependence. This is illustrated in figure 4.7 . As in the case of ^{74}Br^m it is in principle necessary to consider terms of fourth rank. As a first approximation it is assumed

that only the second rank orientation parameters associated with the full substitutional hyperfine field need be considered. In this limit, where the low field orientation is ignored, model 2 becomes formally identical to model 1. Thus from a model 1 fit to the data a moment of $0.56(30)\mu_N$ is obtained.

Further, the U_2A_2 coefficient of the 775 keV $(3)^+ \rightarrow 4^+ \rightarrow 2^+$ transition is calculated to be -0.41. Therefore from the average anisotropy of this transition, $-6.9(45)\%$ at 15 mK (see table 5.6), one obtains $fB_2(B_{sub}) = 0.14(9)$. This is corrected for the $\sim$ 15% attenuation of orientation at this temperature due to relaxation effects. Had data of better statistical accuracy been available it would have been possible to extract the site distribution parameter from this result. As it is, a value $f = 67(9)\%$ is assumed (see section 4.5) which leads to a moment of $0.54(28)\mu_N$. This is in satisfactory agreement with the value obtained from the fit to the temperature dependence of the 862 keV transition. However, with due regard for the size of the errors, this gives no independent verification of the assumptions that $f = 67(9)\%$ nor that $I^\pi(^{72}\mathrm{Br}^g) = 3^+$. Averaging the two results leads to a moment of $0.55(21)\mu_N$.

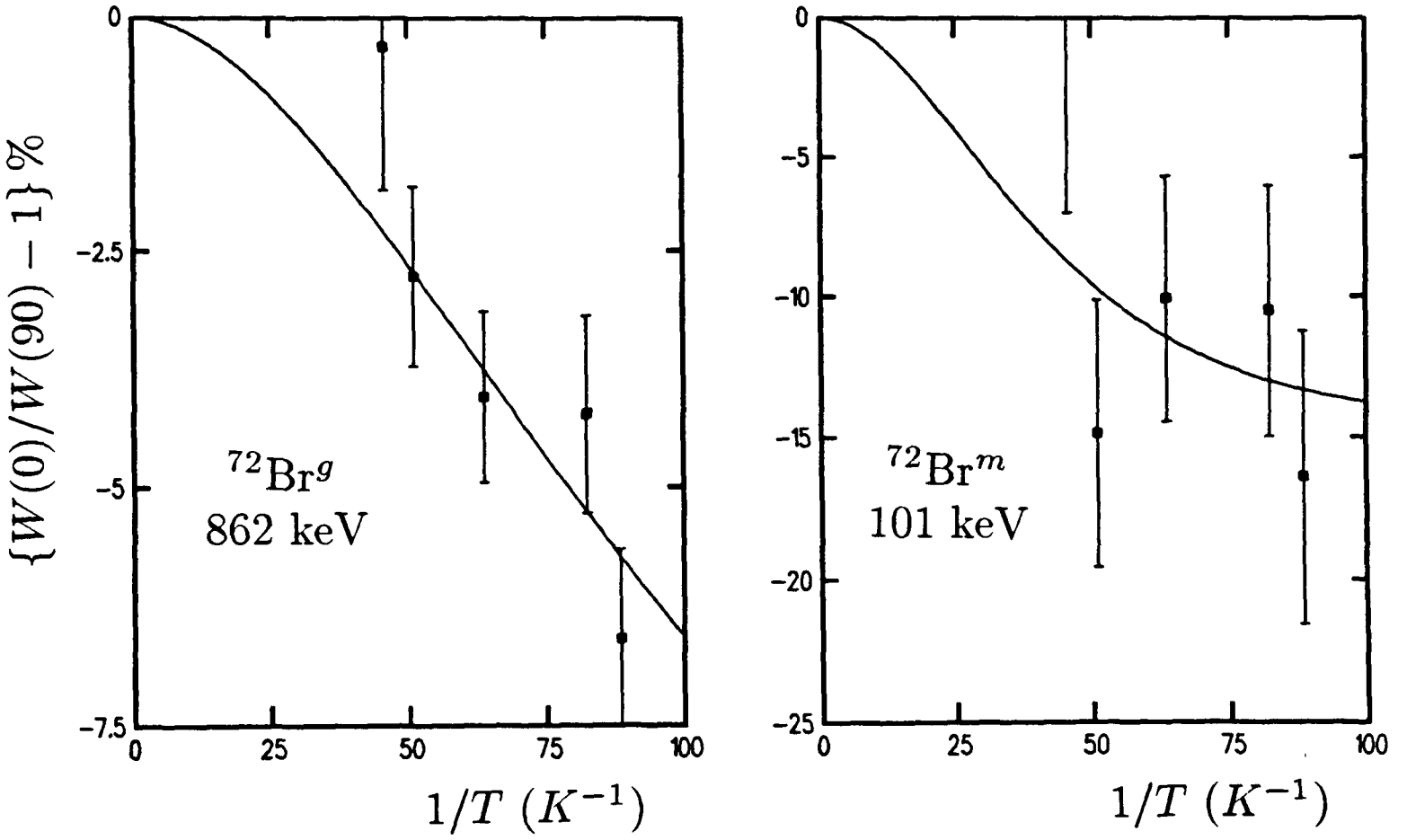

Figure 4.7. The temperature dependences of the 862 keV and 101 keV transitions in the decays of $^{72}\mathrm{Br}^g$ and $^{72}\mathrm{Br}^m$ respectively. The fitted model 1 curves are shown.

With this moment the ratio of the high field orientation parameters at the average temperature of 15 mK is calculated to be $B_4(B_{sub})/B_2(B_{sub}) \sim 2\%$. Thus the neglect of the fourth order orientation parameters is justified *a posterior*. The model dependence of this result is

determined by the ratio $B_2(B_{low})/B_2(B_{sub}) \sim 15\%$. Since this is well within the statistical error the final moment of $^{72}Br^g$ is taken to be $0.55(21)\mu_N$.

Consider now the 101 keV transition from the 10.1 s isomeric state to the ground state. The $(1)^-$ spin parity assignment [18,19] was made on the basis of an assumed M2 multipolarity for this transition. This has been confirmed in the present work by means of an electron conversion measurement (see section 5.8).

Returning to the LTNO data, due to difficulties in subtracting the photopeak from the large Compton background at 101 keV the form of the temperature dependence was relatively poor. A model 1 fit to this data, which is illustrated in figure 4.6, results in a fitted moment of $1.3(^{+10.0}_{-0.6})\mu_N$. As before the model dependence is well within the experimental error.

Finally, it should be pointed out that as a result of the partial orientation of the isomeric state the ground state is not produced with randomly populated sublevels, contrary to the assumptions of the relaxation model based on (1.99). From the intensity ratio of the 101 keV to 862 keV gamma rays it can be deduced that only 20(1)% of the total feed to the ground state comes from the isomer. (This has been corrected for detection efficiency by comparison with the ratio of the 65 to 849 keV gamma rays in the decay of ^{73}Br which were measured in the same experiment). Since at 15 mK the isomer only ever achieves $\sim 60\%$ of its equilibrium orientation before decay, it can be concluded that only a small fraction of the ensemble ground states are modestly pre-oriented in this way. In relation to the large experimental errors this constitutes a negligible effect.

4.5 Conclusion

LTNO measurements on the light bromine nuclei have yielded the nuclear magnetic dipole moments of ^{72g,72m,74m,75,76,77}Br. Apart from ^{76}Br none of these have been previously measured. In addition the ground state spin of ^{73}Br has been established as $1/2^-$.

The experimental data has been analysed within the framework of the two models described in sections 4.2 and 4.4. The results of this analysis are summarised in table 4.6 . It has been shown, both here for the case of ^{76}Br and by Herzog *et al.* for the case of ^{82}Br, that model 1 fails to predict the correct moment. Therefore it is necessary to adopt the more flexible model 2. This requires an extra parameter, B_{low}, which has been deduced by Herzog *et al.* and also causes f and $U_\lambda A_\lambda$ to become independent. Since the $U_\lambda A_\lambda$ coefficients are generally not known

Table 4.6. A summary of the fitted moments of $^{72-77}$Br.

Nuclide	Fitted Moment (μ_N) Model 1	Model 2a (f=75%)	Model 2b (f=58%)	Adopted Moment (μ_N)
^{77}Br	0.82(2)	—	0.92(5)	±0.92(5)
^{76}Br	0.43(3)	—	0.55	±0.55 [10]
^{75}Br	0.73(9)	0.75(15)	0.78(17)	±0.76(18)
^{74}Br^{m}	1.63(6)	1.59(8)	1.77(11)	±1.68(18)
^{72}Br^{g}	0.55(21)	0.55(21)	0.55(21)	±0.55(21)
^{72}Br^{m}	> 0.7	> 0.7	> 0.7	$\|\mu\| > 0.7$

a priori for the isotopes studied, a limited range of values for f has been assumed in order to reduce the number of free parameters to be extracted from the experimental data.

For ^{77}Br, f is taken to be the same as that deduced from the data on the control isotope ^{76}Br since the two were produced under similar conditions. For that part of the data on ^{77}Br collected using the demagnetization stage the iron foil was treated in a different manner leading to a somewhat different site distribution. The parameter f was therefore unknown *a priori* and so the data is unuseable in terms of extracting a magnetic moment, although it is still useful in the calculation of U_2A_2 coefficients (see subsection 5.2). For $^{72-75}$Br no such control exists and it is necessary to adopt a range of likely values for f, taken to be $75\% \geq f \geq 58\%$ (models 2a and 2b respectively). It has been shown that within this range the model 2 extracted moments have only a limited sensitivity to the value of f.

In addition to this it is in principle necessary to also consider the effects of a variable low field B_{low} since this need not correspond to a well defined field but, instead, to some average over many fields. However, the work of Herzog [7] has given some evidence that B_{low} varies by no more than 2 T between different warm or cold implantations. The value of f on the other hand varied by 20% between warm and cold implantations and so it is clear that this and not B_{low} should be treated as the variable parameter.

In view of the proven inability of model 1 to correctly describe the experimental data the adopted moments are taken to be those derived from model 2. In the case of ^{74m,75}Br, where both models 2a and 2b have been applied, the mean of the two results is taken with errors chosen so as to encompass the range of values emerging from the two models. Effectively this corresponds to the assumption that $f = 67(9)\%$. The resulting increase in the errors is relatively modest despite realistically reflecting the site distribution uncertainties. These adopted moments are also given in table 4.6. Clearly precise NMR/ON values would be of great value and this would be the natural direction for future work. Nonetheless these results allow clear nuclear structure deductions to be made in chapter 7.

References

[1] . R. Bengtsson *et al.*, Phys. Scripta **29** (1984) 402

[2] . W. Nazarewicz *et al.*, Nucl. Phys. **A435** (1985) 397

[3] . L. Luhmann *et al.*, Phys. Rev. **C31** (1985) 828

[4] . K.P. Lieb and J.J. Kolata, Phys. Rev. **C15** (1977) 939

[5] . R.B. Piercey *et al.*, Phys. Rev. **C19** (1979) 1344

[6] . P. Herzog *et al.*, Z. Phys. **B64** (1986) 353

[7] . P. Herzog *et al.*, Nucl. Instr. and Meth. **B26** (1987) 471

[8] . R.B. Alexander *et al.*, Phys. Rev. **B9** (1974) 3022

[9] . P.T. Callaghan *et al.*, Hyp. Int. **3** (1977) 267

[10] . C.M. Lederer and V.S. Shirley, Table Of Isotopes, (Wiley, 1978)

[11] . Nuclear Data Sheets **42** (1984)

[12] . Nuclear Data Sheets **29** (1980)

[13] . Nuclear Data Sheets **32** (1981)

[14] . Nuclear Data Sheets **51** (1987)

[15] . C. Ekstrom and L. Robertsson, Phys. Scripta **22** (1980) 344

[16] . K. Heiguchi *et al.*, Nucl. Phys. **A474** (1987) 484

[17] . P.K. James *et al.*, Phys. Rev. **B13** (1976) 59

[18] . Nuclear Data Sheets **56** (1989)

[19] . G. Garcia-Bermudez *et al.*, Phys. Rev. **C25** (1982) 1396

Chapter 5

The spectroscopy of the light selenium isotopes

5.1 Introduction

This chapter will deal with that spectroscopic information on the daughter selenium isotopes which can be deduced from the LTNO data on the decay of the light bromine parents.

Firstly those quantities will be defined which are relevant to this analysis. The $U_\lambda A_\lambda$ coefficients are related to the axial to equatorial anisotropy ratio, E, via the expression (3.9)

$$\begin{aligned} E = \frac{W(0)}{W(\frac{\pi}{2})} - 1 &= \frac{\sum_j \{N/p\}_j(0)}{\sum_k \{N/p\}_k(0)} \times \frac{\sum_k \{N/p\}_k(\frac{\pi}{2})}{\sum_j \{N/p\}_j(\frac{\pi}{2})} - 1 \\ &= \frac{\sum_{\lambda i} f_i B_\lambda(B^i_{hyp}) U_\lambda A_\lambda Q_\lambda P_\lambda(1)}{\sum_{\lambda i} f_i B_\lambda(B^i_{hyp}) U_\lambda A_\lambda Q_\lambda P_\lambda(0)} - 1. \end{aligned} \tag{5.1}$$

In order to improve statistics, those spectra corresponding to the lower temperatures attained for each isotope are included in the summation over the index j. The quoted anisotropies therefore correspond to some average of the low temperature data points presented in chapter 4. The factor $\sum_{\lambda i} f_i B_\lambda(B^i_{hyp})$ is calculated within the framework of model 2 using the adopted moments of table 4.6 in conjunction with the two hyperfine fields, B_{sub} and B_{low} and their associated populations f and $1-f$, as summarised in section 4.5. The solid angle correction factors Q_λ are calculated individually for each detector and gamma ray energy.

For those parent nuclei whose oriented spin is less than 2, the fourth and higher rank terms disappear so that (5.1) may be inverted to yield the U_2A_2 terms directly

$$U_2A_2 = \frac{1}{Q_2 \sum_i f_i B_2(B^i_{hyp})} \times \left\{ \frac{2E}{E+3} \right\}. \tag{5.2}$$

Further, where two or more gamma transitions arise from the same level, then by using (5.2) and the fact that the de-orientation coefficients are identical

$$\begin{aligned} A(\gamma_m : \gamma_n) &= \frac{A_2(\gamma_m)}{A_2(\gamma_n)} \\ &= \frac{E_m(E_n+3)}{E_n(E_m+3)}. \end{aligned} \tag{5.3}$$

This ratio is independent of any site distribution or hyperfine field assumptions and its error arises solely from uncertainties in the measured anisotropy.

In those cases where the oriented spin is greater than or equal to 2, namely $^{74}Br^{m}$ and $^{72}Br^{g}$, fourth rank terms must also be considered. In the former case the U_2A_2 and U_4A_4 coefficients are extracted separately from a least squares fit to the temperature dependent data. For the latter isotope it has been shown that at the temperatures achieved experimentally the fourth rank terms are negligible so that both (5.2) and (5.3) may be applied.

Finally, the errors on all quantities are obtained from the standard propagation expression

$$\Delta F^2 = \sum_p \left\{ \frac{\partial F}{\partial x_p} \Delta x_p \right\}^2 . \qquad (5.4)$$

5.2 The isotope ^{77}Se

As was noted in section 4.3, the decay of ^{77}Br was studied using both the dilution unit alone and latterly in conjunction with the $PrNi_5$ demagnetization stage. The averaged anisotropies, taken from those spectra corresponding to the lowest temperatures, for both parts of the experiment are listed in table 5.1 . For the former experiment these anisotropies correspond to a temperature of 9.8 mK and for the latter 2.5 mK. Taking the site distribution parameters to be $f = 58(9)\%$ and $78(9)\%$ for the two parts of the experiment results in the values $\sum fB_2 = 0.48(5)$ and $0.96(2)$ respectively. The U_2A_2 coefficients extracted from the two essentially independent sets of data are in extremely good agreement, giving a clear indication of the basic soundness of the assumed site distribution model and the reliability of the resulting $\sum fB_2$ values. These coefficients are also given, together with their mean values, in table 5.1.

The decay scheme of ^{77}Br, shown in figure 5.1 , is taken from Nuclear Data Sheets [1]. This includes a number of E2/M1 mixing ratios † which are mostly from the work of Braga *et al.* [2]. A few independent mixing ratios are also given by Mohsen *et al.* [3], Robinson *et al.* [4] and Zell *et al.* [5]. Mixing ratios derived from the present results which are not consistent with previous electron conversion measurements by Tokunaga *et al.* [6] are enclosed thus [ ].

1005 *keV level* : $3/2^-$

The mixing ratio of the 755 keV transition has been measured by both Braga *et al.* and more recently by Mohsen *et al.* to be $\delta(755) = +0.31^{+8}_{-9}$ and $+0.30(1)$ respectively. These

† Unless otherwise stated all electromagnetic mixing ratios δ refer to E2/M1 multipoles.

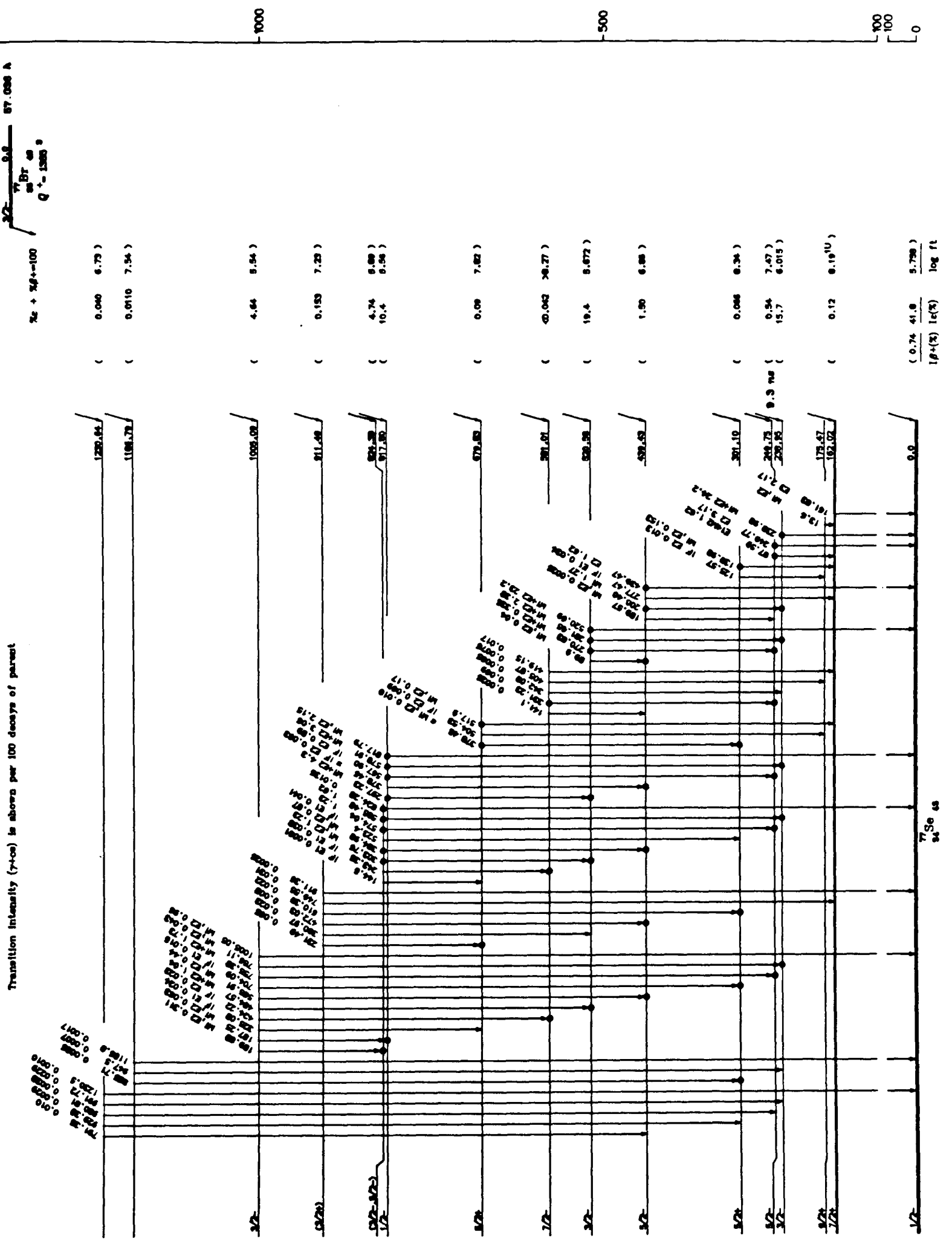

Figure 5.1. The decay scheme of ^{77}Br [1].

Table 5.1. The axial/equatorial anisotropies and U_2A_2 coefficients observed in the decay of ^{77}Br at 9.8 mK and 2.5 mK. * indicates that the error is multiplied by 10 and † indicates a doublet.

Energy(keV)	E (Unit) (%)	U_2A_2	E (Demag) (%)	U_2A_2	mean U_2A_2
88	− 1.2(1.5)	−0.02(2)	0.8(5.6)	0.01(4)	−0.01(2)
181	− 8.6(5.1)	−0.13(8)	− 40.8(16.7)	−0.34(16)	−0.17(7)
200	6.9(1.2)	0.10(2)	11.8(4.8)	0.08(3)	0.09(2)
239	1.7(0.2)	0.02(0)	4.5(0.5)	0.03(0)	0.03(*2)
250	− 5.4(0.5)	−0.08(1)	− 8.5(1.6)	−0.06(1)	−0.07(1)
282	− 1.5(0.6)	−0.02(1)	− 0.6(2.0)	−0.00(1)	−0.02(1)
297	0.3(0.4)	0.00(1)	1.9(1.3)	0.01(1)	0.01(*4)
304	42.9(1.4)	0.55(6)	106.7(8.5)	0.57(4)	0.57(3)
379†	−11.9(8.9)	−0.18(14)	− 22.9(35.7)	−0.18(31)	−0.18(13)
385	−21.3(1.0)	−0.34(4)	− 44.3(3.1)	−0.38(3)	−0.36(2)
439	−15.4(0.6)	−0.24(3)	− 33.7(1.8)	−0.28(2)	−0.27(1)
485	− 8.1(0.8)	−0.12(2)	− 15.7(3.0)	−0.12(2)	−0.12(1)
521	3.1(0.2)	0.05(1)	7.1(0.5)	0.05(0)	0.05(*3)
568†	0.4(0.6)	0.01(1)	− 2.5(2.6)	−0.02(2)	0.00(1)
575	−24.0(0.5)	−0.38(4)	− 46.5(1.5)	−0.40(2)	−0.40(2)
579	0.2(0.4)	0.00(1)	− 0.6(1.3)	−0.00(1)	0.00(*5)
585	19.0(0.7)	0.26(3)	36.4(2.9)	0.24(2)	0.24(2)
755	6.3(0.6)	0.09(1)	15.3(3.2)	0.11(2)	0.09(1)
766	−11.0(9.1)	−0.17(15)	25.4(56.0)	0.17(35)	−0.12(13)
818	− 0.4(0.5)	−0.01(1)	− 5.3(2.2)	−0.04(2)	−0.01(*6)
911	0.3(6.9)	0.00(10)	− 11.9(13.6)	−0.09(11)	−0.04(7)
1005	− 4.6(0.9)	−0.07(2)	− 15.2(4.6)	−0.12(4)	−0.08(1)

predict an angular distribution coefficient of $A_2(755) = +0.45(1)$ and thence from the measured U_2A_2 value one obtains $U_2(1005) = +0.20(2)$. This is exactly consistent with a pure G-T $(3/2^- \rightarrow 3/2^- : U_2 = +0.20)$ β^+/EC transition to this level. Assuming this to be the case, then

$$A_2(1005) = -0.40(5) \qquad 3/2^- \rightarrow 1/2^- \quad \delta(1005) = +0.50^{+4}_{-3} \text{ or } -18^{+6}_{-17}$$

$$A_2(766) = -0.60(65) \qquad 3/2^- \rightarrow 3/2^- \quad \delta(766) \geq -0.29$$

$$A_2(755) = +0.45(5) \qquad 3/2^- \rightarrow 5/2^- \quad \delta(755) = +0.30^{+5}_{-4}$$

$$A_2(485) = -0.60(5) \qquad 3/2^- \rightarrow 3/2^- \quad \delta(485) = +0.14^{+4}_{-4} \text{ or } \left[+2.4^{+3}_{-2}\right]$$

$$A_2(181) = -0.85(35) \text{ if } 3/2^- \rightarrow 3/2^- \quad \delta(181) = +0.07 \rightarrow +3.0$$

$$\text{if } 3/2^- \rightarrow 5/2^- \quad A_2 \geq -0.38$$

The results for the 181 keV transition will be discussed further under the 824 keV level heading.

911 *keV level* : $3/2^+$

The 911 keV pure E1 transition yields the result $U_2(911) = -0.08(14)$. This is to be compared with the theoretical de-orientation coefficients for pure $j_\beta = 0, 1, 2$ transitions of

$U_2 = +1.00$, $+0.20$ and -0.60 respectively. The experimental value clearly indicates that the lepton field is partly of quadrupole character. In the assumed absence of $j_\beta = 0$ the calculated lepton mixing ratio is $\Delta^2(j_\beta = 2/j_\beta = 1) = 0.54(41)$, while in the assumed absence of $j_\beta = 1$ a value of $\Delta^2(j_\beta = 2/j_\beta = 0) = 2.1(8)$ is obtained. Thus in the presence of all possible first forbidden components $0.13 \leq \Delta^2(j_\beta = 2/j_\beta = 0,1) \leq 2.9$.

824 *keV level* : $(3/2^-, 5/2^-)$

The spin and parity assignments of this level were established on the basis of angular correlation measurements [2] and transition strengths respectively [1].

The possibility of positive parity can be ruled out by the present measurements since this would imply that the 304 and 585 keV transitions are pure E1 $(3/2^+, 5/2^+ \rightarrow 3/2^-)$ and therefore must have identical U_2A_2 values. From the results of table 5.1 this is clearly not the case.

Turning now to the question of the level spin, both possibilities have been considered in the calculation of the mixing ratio of the 181 keV transition from the 1005 keV level. The large negative angular distribution coefficient of this transition, $A_2 = -0.85(35)$, is inconsistent with a $5/2^-$ spin assignment for the 824 keV level, since then the theoretical minimum would be $A_2 = -0.38$. On this basis the 824 keV level spin is temporarily taken to be $3/2^-$. With this assumption, from the U_2A_2 coefficient of the 304 keV transition $(3/2^- \rightarrow 3/2^- : A_2 \leq +0.60)$ the de-orientation parameter for this level is calculated to be $U_2(824) = +0.95(5)$. The level feeding is 94% direct β^+/EC and 6% via the 181 keV transition. From the above values of $U_2(1005)$ and $\delta(181)$ a partial de-orientation coefficient of $-0.08 \leq U_2 \leq +0.03$ can be calculated for the gamma feed. Since the F and G-T components of the allowed β^+/EC feed have $U_2 = +1.00$ and $+0.20$ respectively, a purely F lepton field results in a calculated total de-orientation parameter of $+0.93 \leq U_2(824) \leq +0.94$, in excellent agreement with the experimental data. Ignoring therefore any possible small G-T admixtures the following results are obtained

$$A_2(575) = -0.43(2) \quad \text{if} \quad 3/2^- \rightarrow 5/2^- \quad A_2 \geq -0.38$$

$$A_2(304) = +0.61(3) \quad \text{if} \quad 3/2^- \rightarrow 3/2^- \quad \delta(304) = \left[-1.6 \rightarrow -1.0\right]$$

These results present a number of inconsistencies. Firstly, since ^{77}Br is not a mirror nucleus the F matrix elements of the β^+/EC decay are likely to be hindered by the $\Delta T = 0$ isospin selection rule. Since a similar decay to the 1005 keV level has already been shown to be essentially pure G-T, a pure F decay to the present level is unlikely. Secondly, the present mixing ratio for the 304 keV transition is not predicted to be of mainly M1 character as required by the electron conversion measurements of Tokunaga *et al.* Finally, the theoretical angular distribution

coefficient for the 575 keV transition has as its lower limit the value $A_2 = -0.38$. However, the experimental value of $A_2 = -0.43(2)$ lies outside this range. In fact the discrepancy ($\sim 2.5\sigma$) is greater than that of the 181 keV transition ($\sim 1.3\sigma$) upon which the presently assumed level assignment is based.

For these reasons it would appear that a 824 keV level spin of $3/2^-$ is not compatible with the present data and that the measured anisotropy of the 181 keV transition is one of the 20% of observations which are expected exceed their true values by more than 1.3σ. The spin of the 824 keV level is therefore taken to be $5/2^-$. Such an assignment is supported by the fact that this level is only weakly populated in the (n,γ) reaction [7] and the tentatively placed transition [6] to the 162 keV $7/2^+$ level.

With this level assignment the β^+/EC feed is now pure G-T which, with the inclusion of 181 keV gamma feed, leads to a level de-orientation coefficient of $U_2(824) = +0.71$. The resulting mixing ratios are given below

$$A_2(585) = +0.34(3) \quad \text{if} \quad 5/2^- \rightarrow 3/2^- \quad \delta(585) = +0.03^{+1}_{-2} \quad \text{or} \quad -3.7^{+3}_{-3}$$
$$A_2(575) = -0.56(3) \quad \text{if} \quad 5/2^- \rightarrow 5/2^- \quad \delta(575) = +0.11^{+4}_{-4} \quad \text{or} \quad +1.3^{+1}_{-1}$$
$$A_2(385) = -0.51(3) \quad \text{if} \quad 5/2^- \rightarrow 5/2^- \quad \delta(385) = +0.05^{+3}_{-3} \quad \text{or} \quad +1.5^{+1}_{-1}$$
$$A_2(304) = +0.80(4) \quad \text{if} \quad 5/2^- \rightarrow 3/2^- \quad \delta(304) = -0.23^{+3}_{-3} \quad \text{or} \quad \left[-1.8^{+1}_{-1}\right]$$

All of the experimental angular distribution coefficients are now within their corresponding theoretical limits and the former of the two predicted mixing ratios for the 304 keV transition is consistent with the work of Tokunaga *et al.*

521 *keV level* : $3/2^-$

Using the known feeding intensities to this level it is possible to deduce that $+0.12 \leq U_2(521) \leq +0.77$. Thus

$$+0.06 \leq A_2(521) \leq +0.42 \qquad 3/2^- \rightarrow 1/2^- \quad \delta(521) = +0.05 \rightarrow +0.24 \quad \text{or} \quad \left[-3.4 \rightarrow -1.9\right]$$
$$-0.25 \leq A_2(282) \leq -0.01 \qquad 3/2^- \rightarrow 3/2^- \quad \delta(282) = -0.25 \rightarrow -0.10 \quad \text{or} \quad \geq \left[+6.3\right]$$

439 *keV level* : $5/2^-$

From the angular distribution coefficient of the 439 keV E2 transition a level de-orientation factor of $U_2(439) = +0.51(2)$ can be calculated. Thus from the ratio $A_2(200:439) = -0.39(6)$

$$A_2(200) = +0.21(3) \qquad 5/2^- \rightarrow 3/2^- \quad \delta(200) = +0.09^{+2}_{-2} \quad \text{or} \quad \left[-4.8^{+4}_{-4}\right]$$

239 keV level : $3/2^-$

Drawing on the present results for higher lying levels from which the feeding gamma rays originate enables a theoretical de-orientation coefficient in the range $+0.09 \leq U_2(239) \leq +0.72$ to be calculated. Thus

$$+0.04 \leq A_2(239) \leq +0.33 \qquad 3/2^- \rightarrow 1/2^- \quad \delta(239) = +0.09 \rightarrow +0.25 \quad \text{or} \quad \left[-3.5 \rightarrow -2.2\right]$$

Discussion

With the exception of the 755 keV transition the mixing ratios obtained in this work disagree entirely with those of Braga *et al.* which have been adopted by Nuclear Data Sheets. Independent mixing ratios are available only for the 200, 239 [4,5] and 755 [3] keV transitions. The various experimental values obtained for 200 and 239 keV mixing ratios are tabulated below. The experimental methods are indicated.

Energy (keV)	Present $\gamma(\theta, H, T)$	NDS [1]	Braga [2] $\gamma\gamma(\theta)$	Robinson [4] Coul. ex. $\gamma(\theta)$	Zell [5] ^{74}Ge$(\alpha, n\gamma)$ $\gamma(\theta)$
200	+0.09(2)	−0.094(3)	+0.00(9)	+0.05(3)	+0.094(3)
239	$+0.09 \rightarrow +0.25$	−0.184(30)	−0.13(4)	+0.18(3)	+0.188(30)

Braga *et al.* claims agreement with Robinson *et al.* on the value of $\delta(239)$. However the former work uses the convention of Rose and Brink [8] while the latter uses that of Biedenharn and Rose [9]. Since the 239 keV gamma ray is the *de-orienting* transition in the Coulomb excitation experiment of Robinson *et al.* and the mixing is such that $L' = L + 1$, these conventions differ in sign. Therefore the apparent agreement in the quoted values is in fact false. The present work uses the convention of Krane and Steffen [10] which in this case is identical to that of Biedenharn and Rose. Therefore the values of Braga *et al.* and Nuclear Data Sheets are in disagreement with both the present results and those of Robinson *et al.* and Zell *et al.* (The values tabulated above are all expressed in the convention of Krane and Steffen).

To illustrate these discrepancies further, the possibility that the present U_2A_2 coefficients are erroneous as a result of assuming incorrect values for $\sum fB_2$ will now be investigated. Thus, for example, the 239 keV mixing ratio of Braga *et al.* predicts an angular distribution coefficient of $A_2 = +0.70(5)$ as compared with the present value of $+0.04 \leq A_2 \leq +0.33$. In order to achieve agreement the effective orientation parameters $\sum fB_2$ would have to be *reduced* by a factor of at least 2. On the other hand, the 304 keV mixing ratio of Braga *et al.*, $\delta(304) = -0.09^{+4}_{-5}$, predicts

that $A_2 = +0.54(9)$. With the present experimental value of $A_2 = +0.80(4)$ consistency would require an *increase* of the effective orientation parameters by a factor of 1.5. Since the effective orientation parameter for the demagnetization part of the experiment is virtually at the limiting value of unity, no such increase is possible. By applying these arguments to other transitions it is found that no common value for the required correction factor exists. Thus the discrepancies in the mixing ratios are clearly *not* a result of the factors $\sum fB_2$ being incorrect.

Conversely, a comparison of the A_{22} angular correlation coefficients predicted by the present results and the experimental values of Braga *et al.* are given below. For the sake of argument both the $3/2^-$ and $5/2^-$ spin assignments for the 824 keV level are considered, even though the former has been excluded by the present results.

Energy	Spin Sequence	predicted A_{22}	observed A_{22} [2]
$755-250$	$3/2 \rightarrow 5/2 \rightarrow 1/2$	$-0.46 \rightarrow -0.45$	$-0.460(27)$
$575-250$	if $3/2 \rightarrow 5/2 \rightarrow 1/2$	$\sim +0.41$	$+0.038(27)$
	if $5/2 \rightarrow 5/2 \rightarrow 1/2$	$+0.14 \rightarrow +0.19$	
		or $-0.25 \rightarrow -0.23$	
$385-440$	if $3/2 \rightarrow 5/2 \rightarrow 1/2$	$+0.34 \rightarrow +0.46$	$+0.086(14)$
	if $5/2 \rightarrow 5/2 \rightarrow 1/2$	$+0.18 \rightarrow +0.22$	
		or $-0.25 \rightarrow -0.24$	
$385-200$	if $3/2 \rightarrow 5/2 \rightarrow 3/2$	$-0.21 \rightarrow -0.12$	$-0.100(26)$
	if $5/2 \rightarrow 5/2 \rightarrow 3/2$	$-0.10 \rightarrow -0.06$	
		or $+0.08 \rightarrow +0.11$	
$200-239$	$5/2 \rightarrow 3/2 \rightarrow 1/2$	$-0.01 \rightarrow +0.00$	$+0.033(13)$
$282-239$	$3/2 \rightarrow 3/2 \rightarrow 1/2$	$-0.24 \rightarrow -0.02$	$-0.153(\ 3)$
$304-521$	if $3/2 \rightarrow 3/2 \rightarrow 1/2$	$-0.41 \rightarrow -0.05$	$+0.162(19)$
	if $5/2 \rightarrow 3/2 \rightarrow 1/2$	$+0.02 \rightarrow +0.17$	
$485-521$	$3/2 \rightarrow 3/2 \rightarrow 1/2$	$-0.10 \rightarrow -0.01$	$+0.011(10)$

It is interesting to note that there is only disagreement between prediction and experiment where the experimental A_{22} value is small. It is possible therefore that there are small, undetected errors in the work of Braga *et al.* which by propagating through their analysis have lead to an incorrect interpretation of the angular correlation data. The universal agreement on the 755 keV mixing ratio can then be attributed to the fact that the experimental A_{22} value is both large ***and*** the 755 keV gamma ray is taken in coincidence with the 250 keV pure E2 transition. Therefore the only unknown to be extracted from the data is the 755 keV mixing ratio. This is in

contrast to the other cascades which exhibit large A_{22} coefficients. There both transitions in the cascade are mixed so that two unknown parameters are involved which requires the knowledge of a second experimental quantity, A_{44}. Since the experimental A_{44} coefficients are invariably small with large errors these two mixing ratios are not reliably extracted.

Finally, it should be noted that the predicted A_{22} coefficient for the 304 → 521 keV cascade, calculated using the present results, disagrees in sign with the experimental value of Braga *et al.* if the 824 keV level is taken to have spin $3/2^-$. Since the experimental A_{22} value is comparatively large it may be presumed that the fitting procedure employed by Braga *et al.* is relatively reliable. This may therefore be taken as further evidence for the present $5/2^-$ spin assignment of the 824 keV level.

To conclude this section on the spectroscopy of ^{77}Se, the mixing ratios derived from the present work are listed below. Only those values consistent with electron conversion measurements [1,6] are included. For comparison the values of Braga *et al.* are also tabulated.

Present	: Braga [2]
$\delta(1005) = +0.50^{+4}_{-3}$ or $-18^{+}_{-17}{}^{6}$	
$\delta(766) \geq -0.29$	
$\delta(755) = +0.30^{+5}_{-4}$	: $+0.31^{+8}_{-9}$
$\delta(585) = +0.03^{+1}_{-2}$ or -3.7^{+3}_{-3}	
$\delta(575) = +0.11^{+4}_{-4}$ or $+1.3^{+1}_{-1}$	: $+0.33^{+9}_{-8}$
$\delta(521) = +0.05 \rightarrow +0.24$	: -0.17^{+7}_{-6}
$\delta(485) = +0.14^{+4}_{-4}$	: $+0.27^{+3}_{-4}$
$\delta(385) = +0.05^{+3}_{-3}$ or $+1.5^{+1}_{-1}$	: $+0.23^{+5}_{-7}$
$\delta(304) = -0.23^{+3}_{-3}$	: -0.09^{+4}_{-5}
$\delta(282) = -0.25 \rightarrow -0.10$	: $+0.12^{+4}_{-3}$
$\delta(239) = +0.09 \rightarrow +0.25$	: -0.13^{+4}_{-4}
$\delta(200) = +0.09^{+2}_{-2}$	: $+0.00^{+9}_{-9}$

5.3 The isotope ^{76}Se

Anisotropies were measured for 42 gamma transitions in the decay of ^{76}Br at an average temperature of 2.9 mK. The site distribution parameter f was measured to be 58(9)% (see section 4.3) leading to the value $\sum fB_2 = 0.59(3)$. The anisotropies and U_2A_2 coefficients thus deduced are listed in table 5.2 . It is unfortunate that despite the full orientation achieved the anisotropies observed from this $I = 1$ nucleus were all rather small, limiting the precision of the extracted decay parameters. The decay scheme, illustrated in figure 5.2 , is taken from Nuclear Data Sheets [11].

3971 *keV level* : $(1^+, 2^+)$

The presence of a transition direct to the 0^+ ground state and the observation of orientation limits the spin of this level to $1^\pm$, 2^+. The 1301 keV transition between this level and the 2670 keV (2^-) level has an observed U_2A_2 coefficient of $-0.69(23)$. The theoretical coefficients for the possible spin sequences are listed below

$$1^- \rightarrow 1^+ \rightarrow 2^- \; : \; U_2A_2 = -0.04 \rightarrow +0.07$$

$$1^- \rightarrow 1^- \rightarrow 2^- \; : \; U_2A_2 = -0.35 \rightarrow +0.71$$

$$1^- \rightarrow 2^+ \rightarrow 2^- \; : \; U_2A_2 = -0.25 \rightarrow +0.25$$

None of these are consistent with the observed coefficient to within 1.5σ. This brings into doubt the (2^-) spin assignment of the 2670 keV level. As will be discussed later, there is reason to believe that the spin of the 2670 keV level can also be assigned to 1^+, 2^+ or 3^+. The theoretical coefficients for these spin sequences are

$$1^- \rightarrow 1^+ \rightarrow 1^+ \; : \; U_2A_2 = -1.41 \rightarrow +0.71$$

$$1^- \rightarrow 1^- \rightarrow 1^+ \; : \; U_2A_2 = -0.35 \rightarrow +0.18$$

$$1^- \rightarrow 2^+ \rightarrow 1^+ \; : \; U_2A_2 = -0.56 \rightarrow +0.63$$

$$1^- \rightarrow 1^+ \rightarrow 2^+ \; : \; U_2A_2 = -0.35 \rightarrow +0.71$$

$$1^- \rightarrow 1^- \rightarrow 2^+ \; : \; U_2A_2 = -0.04 \rightarrow +0.07$$

$$1^- \rightarrow 2^+ \rightarrow 2^+ \; : \; U_2A_2 = -0.48 \rightarrow +0.48$$

$$1^- \rightarrow 1^+ \rightarrow 3^+ \; : \; U_2A_2 = -0.10 \rightarrow +0.05$$

$$1^- \rightarrow 1^- \rightarrow 3^+ \; : \; U_2A_2 = -0.35 \rightarrow +0.70$$

$$1^- \rightarrow 2^+ \rightarrow 3^+ \; : \; U_2A_2 = -0.53 \rightarrow +0.53$$

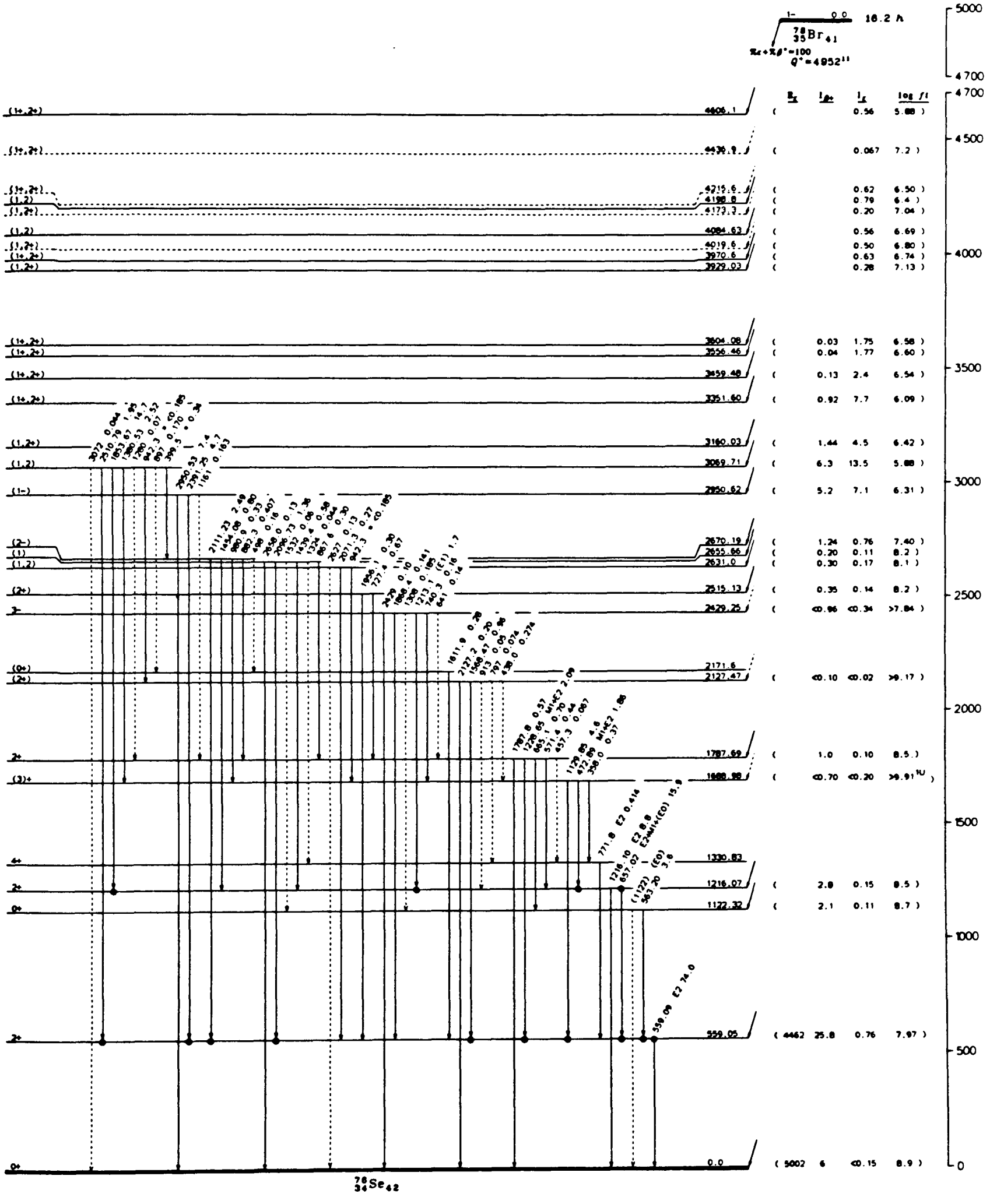

Figure 5.2. The decay scheme of ^{76}Br (Part 1 of 2) [11].

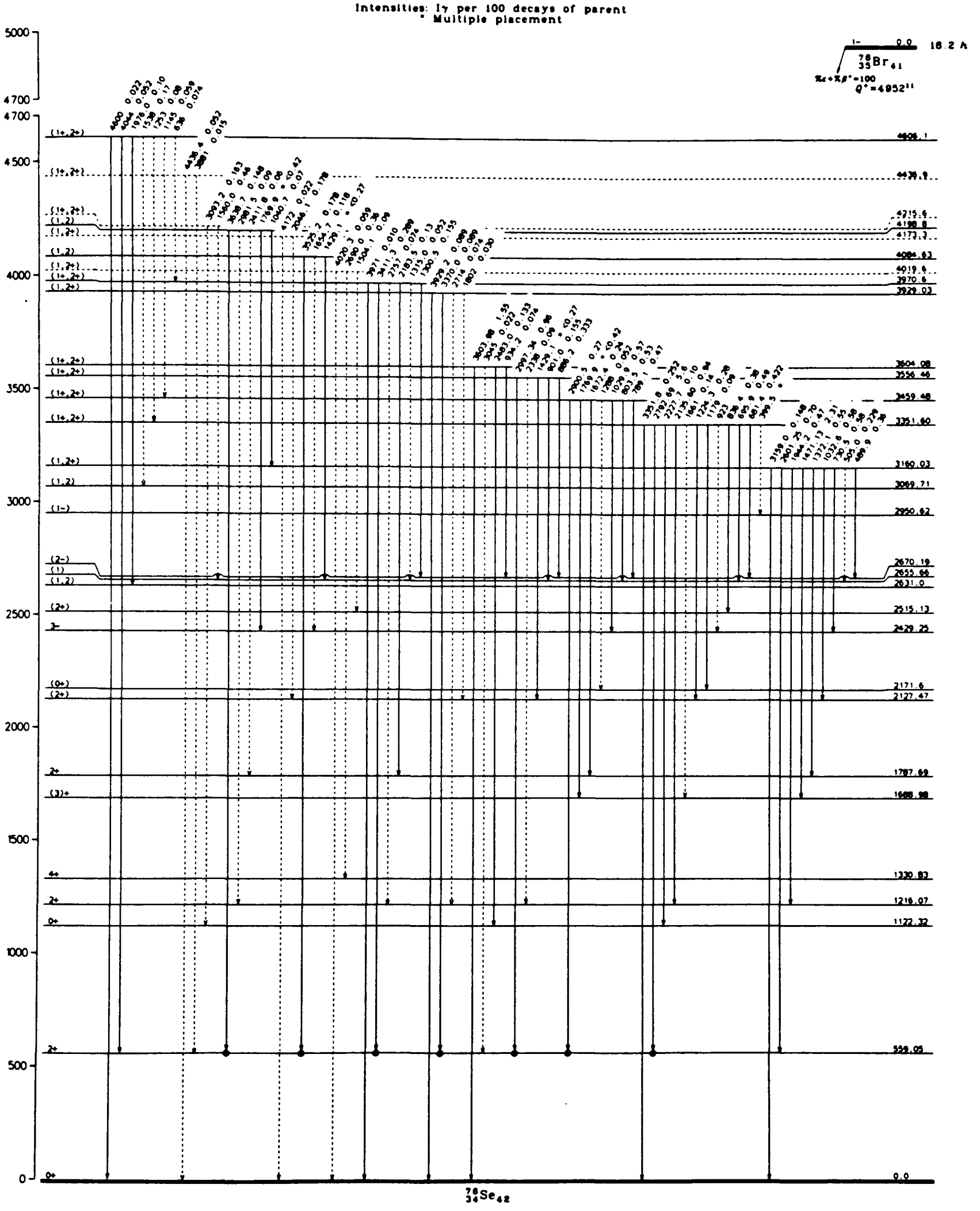

Figure 5.2. The decay scheme of ^{76}Br (Part 2 of 2) [11].

Table 5.2. The axial/equatorial anisotropies and U_2A_2 coefficients observed in the decay of ^{76}Br at 2.9 mK.

Energy (keV)	E (%)	U_2A_2
473	−9.2(1.8)	−0.11(2)
490	18.0(10.3)	0.20(10)
559	3.8(0.3)	0.04(1)
599	−1.5(4.6)	−0.01(5)
604	3.7(8.4)	0.04(9)
657	−0.6(0.4)	−0.01(5)
665	−0.8(3.7)	−0.01(4)
681	−8.8(4.8)	−0.10(6)
696	2.7(4.8)	0.03(5)
728	−1.1(4.7)	−0.01(5)
731	6.7(4.2)	0.07(4)
772	−1.0(6.1)	−0.01(7)
789	−6.2(5.6)	−0.07(6)
804	9.3(5.8)	0.10(6)
882	−5.1(5.8)	−0.06(7)
886	−17.5(7.7)	−0.22(10)
1030	1.6(6.7)	0.01(7)
1033	−13.4(6.1)	−0.16(8)
1130	−14.2(0.9)	−0.17(1)
1213	2.0(3.4)	0.02(3)
1216	−4.1(1.0)	−0.04(1)
1229	2.5(1.8)	0.02(2)
1301	−48.8(13.8)	−0.69(23)
1372	−13.7(6.4)	−0.17(8)
1381	4.8(1.3)	0.05(1)
1439	−5.7(4.2)	−0.06(5)
1454	−5.6(3.2)	−0.06(3)
1471	4.3(1.8)	0.05(2)
1560	−12.4(5.3)	−0.15(6)
1568	−4.2(4.2)	−0.05(5)
1672	−22.1(12.5)	−0.28(17)
1788	−0.9(5.6)	−0.01(6)
1854	−9.5(0.5)	−0.11(1)
1944	−12.1(6.9)	−0.15(8)
2097	2.1(2.8)	0.02(3)
2111	−3.1(1.6)	−0.03(1)
2136	−4.7(3.2)	−0.05(3)
2511	−10.6(1.8)	−0.13(2)
2601	−8.1(4.7)	−0.09(5)
2793	−2.0(0.9)	−0.02(1)
2901	−9.1(4.2)	−0.11(5)
2951	−12.9(0.7)	−0.16(1)

Thus the 1301 keV transition spin changes are limited to $1^+ \rightarrow 1^+$ and $2^+ \rightarrow 1^+, 2^+, 3^+$. The 3971 keV level spin is therefore 1^+ or 2^+. This confirms the previous assignment, based on the $\log ft$ value and angular momentum transfer in the (^{3}He, d) reaction [12].

Finally, a $2^+ \rightarrow 3^+$ spin assignment for the 1301 keV transition would imply a level deorientation coefficient of $U_2(3971) \leq -0.78(26)$. This corresponds to an almost pure $j_\beta = 2$ decay ($U_2 = -0.59$) to the 3971 keV level. However, the corrected beta transition probability [13] ($\log f^{1U}t = 7.31$) is far too small to correspond to a unique first forbidden decay and so this spin sequence must be discarded. The spin of the 2670 keV level is not therefore 3^+.

3459 *keV level* : $(1^+, 2^+)$

The β^+/EC transition to this level is too fast to be unique first forbidden and so, since anisotropies were also observed, the spin assignment is limited to $1^\pm$ and $2^\pm$. Taking these spins in turn the following results are obtained

			experiment	theory
if	1^+	$U_2A_2(\ 804,\ 1^- \rightarrow 1^+ \rightarrow 1^-) =$	$+0.10(\ 6)$	$-0.35 \rightarrow +0.18$
if	1^-	$U_2A_2(1672,\ 1^- \rightarrow 1^- \rightarrow 2^+) =$	$-0.28(17)$	$-0.04 \rightarrow +0.07$
if	1^-	$U_2A_2(2901,\ 1^- \rightarrow 1^- \rightarrow 2^+) =$	$-0.11(\ 5)$	$-0.04 \rightarrow +0.07$
if	2^+	$U_2A_2(\ 804,\ 1^- \rightarrow 2^+ \rightarrow 1^-) =$	$+0.10(\ 6)$	$-0.25 \rightarrow +0.25$
if	2^-	$U_2A_2(1672,\ 1^- \rightarrow 2^- \rightarrow 2^+) =$	$-0.28(17)$	-0.25
if	2^-	$U_2A_2(2901,\ 1^- \rightarrow 2^- \rightarrow 2^+) =$	$-0.11(\ 5)$	-0.25

Therefore the observed U_2A_2 coefficients rule out the possibility of spins 1^- and 2^-, confirming the previous (1^+, 2^+) assignment [11,12].

3160 *keV level* : $(1, 2^+)$

Using an identical argument to that presented for the 3459 keV level the spin assignment is limited to $1^\pm$ and $2^\pm$. Assuming these values in turn

			experiment	theory
if	1^+	$A(490,\ 1^+ \rightarrow (2^-):\ 1471,\ 1^+ \rightarrow 3^+) =$	$+4.0(2.7)$	-0.7
if	1^-	$A(731,\ 1^- \rightarrow\ 3^-\ :\ 1033,\ 1^- \rightarrow 2^+) =$	$-0.47(36)$	-1.4
		$A(731,\ 1^- \rightarrow\ 3^-\ :\ 1372,\ 1^- \rightarrow 2^+) =$	$-0.46(36)$	-1.4
		$A(731,\ 1^- \rightarrow\ 3^-\ :\ 1944,\ 1^- \rightarrow 2^+) =$	$-0.52(44)$	-1.4
		$A(731,\ 1^- \rightarrow\ 3^-\ :\ 2601,\ 1^- \rightarrow 2^+) =$	$-0.78(67)$	-1.4
if	2^+	$A(490,\ 2^+ \rightarrow (2^-):\ 731,\ 2^+ \rightarrow 3^-) =$	$+2.6(2.1)$	-3.5
if	2^-	$U_2A_2(1033,\ 1^- \rightarrow 2^- \rightarrow 2^+) =$	$-0.16(8)$	-0.25
		$U_2A_2(1372,\ 1^- \rightarrow 2^- \rightarrow 2^+) =$	$-0.17(8)$	-0.25
		$U_2A_2(1471,\ 1^- \rightarrow 2^- \rightarrow 3^+) =$	$+0.05(2)$	$+0.07$
		$U_2A_2(1944,\ 1^- \rightarrow 2^- \rightarrow 2^+) =$	$-0.15(8)$	-0.25
		$U_2A_2(2601,\ 1^- \rightarrow 2^- \rightarrow 2^+) =$	$-0.09(5)$	-0.25

Apparently none of these spin assignments are favoured by the data. However it has already been argued that the 2670 keV level, to which the 490 keV transition decays, is not (2^-). Therefore the above comparisons serve only to rule out the possibility of spins 1^- and 2^-. Taking the 2670 keV level to have spin 1^+ or 2^+ would allow both spin 1^+ and 2^+ for the present level. However, in view of the presence of gamma transitions to levels of spin 0^+, 2^+ and $3^\pm$, a spin 1^+ assignment is unlikely. Hence the spin of the 3160 keV level is taken to be 2^+.

With this assumption, the U_2A_2 coefficient of the 731 keV $2^+ \rightarrow 3^-$ transition yields $U_2(3160) = +0.59(33)$, whence a lepton field mixing ratio of $\Delta^2(j_\beta = 2/j_\beta = 1) \leq 0.38$ is derived. Further, from the experimental ratio $A(\gamma : 731)$ the following mixing ratios can be calculated

$A_2(2601) = -0.15(12)$	$2^+ \rightarrow 2^+$	$\delta(2601) = -0.21^{+10}_{-10}$	or	$+4.6^{+3.5}_{-1.4}$
$A_2(1944) = -0.23(20)$	$2^+ \rightarrow 2^+$	$\delta(1944) = -0.12^{+10}_{-16}$	or	$+3.3^{+3.2}_{-1.3}$
$A_2(1471) = +0.08(\ 6)$	$2^+ \rightarrow 3^+$	$\delta(1471) = -0.02^{+\ 4}_{-\ 5}$	or	$-5.2^{+1.1}_{-1.7}$
$A_2(1372) = -0.26(21)$	$2^+ \rightarrow 2^+$	$\delta(1372) = -0.10^{+18}_{-17}$	or	$+3.0^{+3.5}_{-1.2}$

3070 *keV level* : (1,2)

Again the spin assignment can be limited to $1^{\pm}$, $2^{\pm}$. Hence

			experiment	theory
if	1^+	$U_2A_2(1381,\ 1^- \rightarrow 1^+ \rightarrow 3^+) =$	$+0.05(1)$	$-0.10 \rightarrow +0.05$
if	1^-	$U_2A_2(1854,\ 1^- \rightarrow 1^- \rightarrow 2^+) =$	$-0.11(1)$	$-0.04 \rightarrow +0.07$
if	1^-	$U_2A_2(2511,\ 1^- \rightarrow 1^- \rightarrow 2^+) =$	$-0.13(2)$	$-0.04 \rightarrow +0.07$
if	2^-	$U_2A_2(1854,\ 1^- \rightarrow 2^- \rightarrow 2^+) =$	$-0.11(1)$	-0.25
if	2^-	$U_2A_2(2511,\ 1^- \rightarrow 2^- \rightarrow 2^+) =$	$-0.13(2)$	-0.25

Consistency for a 2^+ assignment may be also by achieved by a suitable choice of mixing ratio. Thus the experimental anisotropies indicate that the 3070 keV level is of positive parity with possible spins 1^+ or 2^+.

2951 *keV level* : (1^-)

From the U_2A_2 coefficient of the 2951 keV $(1^-) \rightarrow 0^+$ transition it is possible to calculate a de-orientation parameter $U_2(2951) = -0.23(1)$. The G-T to F mixing in the allowed β^+/EC decay is therefore $\Delta^2(j_\beta = 1/j_\beta = 0) = 4.6(2)$.

2670 *keV level* : (2^-)

The observed beta reduced transition probability to this level is $\log ft = 7.40$. Assuming a unique first forbidden decay then this can be corrected to $\log f^{1U}t = 8.38$, which is just slow enough to be plausible. Therefore the β^+/EC feed to this level limits the possible spins to $0^{\pm}, 1^{\pm}$, $2^{\pm}$ or 3^+. The presence of gamma transitions to levels of spin 2^+ and 3^+ and the observation of non-zero anisotropies further limit the assignments to 1^+, $2^{\pm}$ or 3^+. From previous arguments relating to the 3971 and 3160 keV levels the spins 2^- and 3^+ can also be excluded. In fact the possibility of spin 2^- can be also be ruled out directly from the anisotropies of the 2111, 1454 and 882 keV transitions from this level. All the feeding gamma transitions arise from levels assigned $(1^+, 2^+)$, some of which are verified in the present work. Therefore it is possible to calculate their contribution to the total de-orientation coefficient of the 2670 keV level. Thus for transitions $1^- \rightarrow 1^+ \rightarrow 2^-$; $-0.3 \leq U_2 \leq +0.60$, while for transitions $1^- \rightarrow 2^+ \rightarrow 2^-$; $-0.30 \leq U_2 \leq +0.30$. Since the beta feed would be pure G-T and using the measure de-orientation coefficient for the 3160 keV level, then the total level de-orientation coefficient is calculated to lie in the range $+0.18 \leq U_2(2670) \leq +0.58$. The expected

U_2A_2 coefficient for the 2111, 1454 and 882 keV E1 transitions to levels of spin 2^+ is then predicted to be $-0.24 \leq U_2A_2 \leq -0.08$. When compared to the respective experimental values of $-0.03(1)$, $-0.06(3)$ and $-0.06(7)$ it is clear that the former value at least is inconsistent with the assumption of spin 2^-. Therefore the spin of this level must be either 1^+ or 2^+. Such an assignment disagrees with the conclusions of Kaur *et al.* [14] who proposed spin 2^- on the basis of $\gamma\gamma(\theta)$ measurements in the decay of ^{76}As. However the possibility of positive parity was not considered since the beta decay to this level was assumed to be allowed.

2656 *keV level* : 1^-

From the U_2A_2 coefficients of the 1439 and 2097 keV E1 transitions the level de-orientation coefficient is calculated to be $U_2(2656) = -0.01(36)$.

2429 *keV level* : 3^-

From the anisotropy of the 1213 keV E1 transition the coefficient $U_2(2429) = +0.58(87)$ is obtained.

1788 *keV level* : 2^+

The de-orientation coefficient for this level is $U_2(1788) = +0.02(6)$, as calculated from the 665 and 1788 keV $2^+ \rightarrow 0^+$ transitions.

1689 *keV level* : 3^+

The angular distribution coefficient for the 1130 keV transition has been measured by Subber *et al.* in the β^- decay of ^{76}As [15] to be $A_2 = -0.73(15)$. From this it can be deduced that $U_2(1689) = 0.23(5)$. Further, from the ratio $A(473 : 1130) = +0.64(14)$

$$A_2(473) = -0.47(14) \qquad 3^+ \rightarrow 2^+ \quad \delta(473) = +0.47^{+12}_{-10} \quad \text{or} \quad +5.0^{+38}_{-17}$$

This mixing ratio agrees with, but is more accurate than, the corresponding result of Subber *et al.* [15] and is consistent with the earlier work of Matsuzaki *et al.* [16].

1331 *keV level* : 4^+

The de-orientation coefficient is calculated to be $U_2(1330) = +0.02(16)$ from the 772 keV E2 transition.

1216 *keV level* : 2^+

From the known angular distribution coefficient of the 1216 keV E2 transition the level de-orientation parameter $U_2(1216) = +0.07(2)$ is obtained. Also $A(657 : 1216) = +0.14(10)$, thus

$$A_2(657) = -0.09(6) \qquad 2^+ \rightarrow 2^+ \quad \delta(657) = -0.26^{+5}_{-5} \quad \text{or} \quad +5.8^{+23}_{-15}$$

The latter of the two mixing ratios is consistent with the previously known values of +4.2(2) [15] and +5.2(2) [17].

559 *keV level* : 2^+

The total feeding to this level is 36% by direct β^+/EC and 64% by preceeding gamma transitions. The contribution of the gamma feeding to the total level de-orientation coefficient may be estimated from the the present results. Taking the above de-orientation coefficients and mixing ratios as appropriate (and also $\delta(1229)$ [14,15], $\delta(1130)$ [11] and $\delta(657)$ [15,17] from other works) allows a partial intensity weighted de-orientation coefficient of $-0.05 \leq \sum_\gamma I_\gamma U_2(\gamma) \leq +0.07$ to be calculated. This corresponds to 43% of the total feeding. The contribution of the remaining 21% of the gamma feed, for which no experimental values exist, may be estimated by taking the maximum and minimum theoretical values for the spin sequence $1^- \rightarrow 1,2 \rightarrow 2^+$, which are +0.12 and −0.12 respectively. Again these values are intensity weighted. In this way the total intensity weighted gamma de-orientation coefficient is estimated to be $-0.17 \leq \sum_\gamma I_\gamma U_2(\gamma) \leq +0.19$.

Together with the de-orientation coefficient corresponding to the lepton decay this may be related to the total measured coefficient thus

$$U_2(559) = I_\beta U_2(\beta) + \sum_\gamma I_\gamma U_2(\gamma). \tag{5.5}$$

The observed level de-orientation coefficient, as deduced from the 559 keV E2 transition, is $U_2(559) = -0.075(7)$. Thus $-0.76 \leq U_2(\beta) \leq +0.28$. With limiting theoretical values of +0.59 and −0.59 for $j_\beta = 1,2$ respectively this result leads to a lepton mixing ratio of $\Delta^2(j_\beta = 2/j_\beta = 1) \geq 0.36$.

In practice the limits assumed for the gamma de-orientation coefficients will be rather too generous. The mid-point value of the partial intensity weighted de-orientation coefficient for the gamma feeds with known parameters is +0.01 and there is little reason to expect much difference for the remaining unknown feeds. Thus the actual total gamma de-orientation coefficient is likely to be fairly close to zero. In this more realistic approximation the lepton mixing ratio is calculated to be $\Delta^2 \sim 1.3$ implying a very significant, but not necessarily pre-eminent, contribution from the quadrupole field.

The corrected first unique forbidden transition probability [13] is calculated to be $\log f^{1U}t = 9.5$. This is entirely in order with the values of other such transitions in this region which are

typically ~ 10 and so the present result is certainly not without foundation. On the other hand, the present lepton mixing ratio of the first forbidden decay to the higher lying 3160 keV level suggests little, if any, contribution from the quadrupole field. An increasing presence of $j_\beta = 2$ components as the decay energy becomes greater might in fact explain the gradual increase in the observed $\log ft$ values towards the lower part of the level scheme.

5.4 The isotope ^{75}Se

The anisotropies of gamma transitions in the decay of ^{75}Br were observed at an average temperature of 12.7 mK. Using the measured moment of $0.76(18)\mu_N$ and the site distribution parameter $f = 67(9)\%$, an effective orientation parameter $\sum fB_2 = 0.32(9)$ is obtained. The experimental anisotropies and U_2A_2 coefficients are listed in table 5.3 .

The decay scheme, shown in figure 5.3 , is taken from Nuclear Data Sheets [18]. In addition, several spin and parity assignments have been given more recently by Tokunaga *et al.* [19].

Table 5.3. The axial/equatorial anisotropies and U_2A_2 coefficients observed in the decay of ^{75}Br at 12.7 mK.

Energy (keV)	E (%)	U_2A_2
141	−0.5(8.7)	−0.01(19)
236	−5.7(9.8)	−0.12(22)
287	0.9(0.4)	0.02(1)
377	41.1(4.3)	0.79(23)
428	−12.1(2.2)	−0.27(9)
432	7.1(3.0)	0.15(7)
573	−5.5(4.8)	−0.12(11)
609	−8.4(3.7)	−0.18(10)
702	−29.6(15.0)	−0.71(45)
952	14.5(6.4)	0.30(15)

1561 *keV level* : (5/2)

The $\log ft$ value for the β^+/EC decay to this level indicates an allowed or non-unique first forbidden transition from the $3/2^-$ ground state of ^{75}Br. The observation of orientation in the 702 keV transition rules out spins $1/2^\pm$ absolutely and the presence of gamma transitions to levels of spin $3/2^-$, $5/2^+$ and $7/2^+$ further limit the possible spins to $3/2^+$ or $5/2^\pm$. Further,

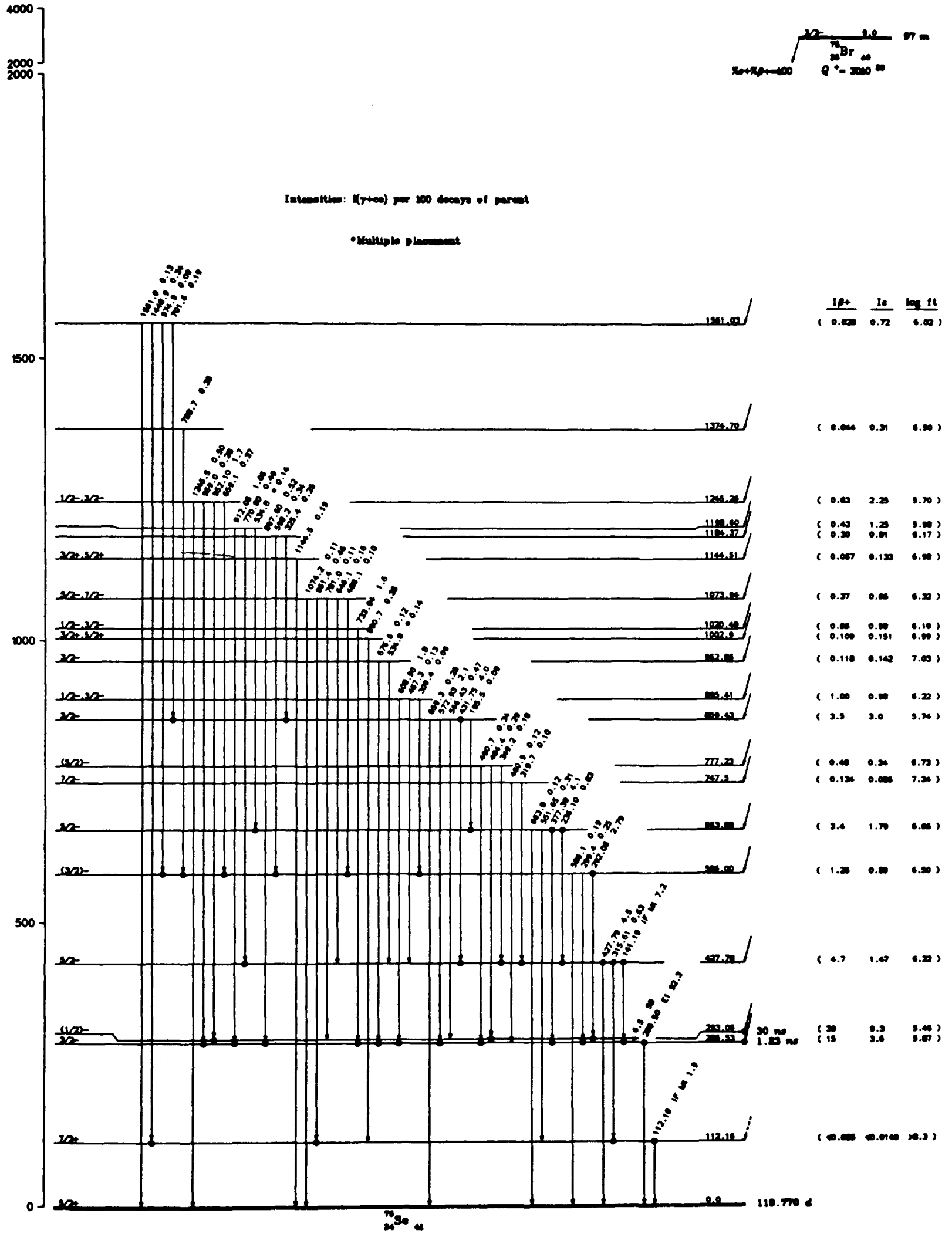

Figure 5.3. The decay scheme of ^{75}Br [18].

an assignment of $5/2^+$ can be excluded as this would imply that the U_2A_2 coefficient of the 702 keV transition is in the range $-0.04 \rightarrow +0.28$, contrary to the observed value of $-0.71(45)$. Since Tokunaga *et al.* have tentatively proposed a spin assignment of (5/2), the 1561 keV level spin is taken to be $5/2^-$.

With this assignment the β^+/EC decay is pure G-T, so that

$$A_2(702) = -0.95(60) \qquad 5/2^- \rightarrow 3/2^- \quad \delta(702) \geq +0.40$$

1245 *keV level* : $1/2^-$, $3/2^-$

The fact that anisotropies were observed for the 952 keV transition, which decays to the 293 keV $1/2^-$ level, can be used to limit the spin assignment for this level to $3/2^{\pm}$ or $5/2^-$. The latter possibility can be excluded since it would predict that $U_2A_2 = -0.40$, in contrast to the observed positive value. The present data is consistent with both $3/2^-$ and $3/2^+$ spin assignments. Previous reaction transfer data [18,20] have suggested a spin of either $1/2^-$ or $3/2^-$. Therefore the spin of this level is taken to be $3/2^-$.

The level de-orientation coefficient then lies in the range $+0.2 \leq U_2(1245) \leq +1.0$ and hence

$$A_2(952) \geq +0.15 \qquad 3/2^- \rightarrow 1/2^- \quad -2.9 \leq \delta(952) \leq +0.18$$

895 *keV level* : $1/2^-$, $3/2^-$

Again previous transfer data [18,20] have suggested level spin assignments of $1/2^-$ or $3/2^-$. Since the 609 keV transition exhibits anisotropy the former possibility may be excluded. The 895 keV level spin is therefore $3/2^-$.

The level de-orientation coefficient thus lies in the same range as for the 1245 keV level, whence

$$A_2(609) \leq -0.08 \qquad 3/2^- \rightarrow 3/2^- \quad \delta(609) \geq -0.20$$

859 *keV level* : $3/2^-$

Taking the previously known mixing ratio for the 432 keV transition of $\delta(432) = +0.34(24)$ [18,20,21] yields the theoretical angular distribution coefficient $A_2 = +0.49(23)$. Thus the level de-orientation coefficient is calculated to be $U_2(859) = +0.31(20)$. Only 6% of the total feeding to this level is by preceeding gamma transitions which can therefore be neglected. Thus the lepton mixing ratio $\Delta^2(j_\beta = 1/j_\beta = 0) \geq 1.6$ is deduced.

Further, from the experimental ratio $A(573:432) = -0.81(79)$

$$A_2(573) = -0.40(43) \qquad 3/2^- \rightarrow 3/2^- \quad \delta(573) \geq -0.24$$

664 *keV level* : $5/2^-$

This level is fed almost entirely (97%) by pure G-T beta decay with a theoretical de-orientation parameter $U_2 = +0.75$. The known mixing ratio of the 377 keV transition [20] has already been used to limit the error on the fitted moment of ^{75}Br (see subsection 4.4.1). In addition

$$A_2(236) = -0.16(29) \qquad 5/2^- \rightarrow 5/2^- \quad \delta(236) = -0.24^{+26}_{-26} \quad \text{or} \quad \left[1.6 \rightarrow 17\right]$$

Electron conversion measurements by Tokunaga *et al.* [19] give $|\delta(236)| = 0.31^{+15}_{-31}$, in agreement with the former of the present values.

5.5 The isotope ^{74}Se

The averaged anisotropies of gamma rays resulting from the β^+/EC decay of ^{74}Br^m are listed in table 5.4 . Since the oriented spin is $I = 4$ [22] the directional distribution of these gamma rays in general contain terms of both second and fourth rank. Taking the fitted moment of $1.68(18)\mu_N$ and site distribution parameter $f = 67(9)\%$ leads to effective orientation parameters $\sum fB_2 = 0.92(9)$ and $\sum fB_4 = 0.26(5)$ at the average experimental temperature of 9.8 mK.

From the relative magnitudes of the two effective orientation parameters it is clear that fourth rank terms may contribute significantly to the anisotropies appearing in table 5.4. The two $U_\lambda A_\lambda$ coefficients must therefore be determined from the temperature dependence of the anisotropies. With the moment and site distribution parameter fixed to the above values, U_2A_2 and U_4A_4 are thus extracted separately as the only variable parameters. (It has been stated in subsection 4.4.2 that such a fitting procedure, including U_2A_2 and U_4A_4 as variable parameters, is only reliable for the 634 and 728 keV transitions. There, however, the moment was also a variable parameter). The resulting fourth rank terms, generally having the smaller contribution to the anisotropy, are of rather poor precision and necessarily the error in the corresponding second rank terms is increased. In this respect, where it can be shown theoretically that the

U_4A_4 coefficient of a given gamma transition either vanishes or is comparatively small, then it is better to consider the second rank terms exclusively by applying (5.2) to the averaged anisotropy point. There is then no additional error in U_2A_2 introduced by the uncertainty in the fitted value of U_4A_4. Values thus derived are denoted $\overline{U_2A_2}$ in order to highlight the fact that in the general case they represent some mean value of the U_2A_2 and U_4A_4 coefficients. The $\overline{U_2A_2}$ coefficients together with the fitted values U_2A_2 and U_4A_4 are also given in table 5.4. Only the former quantities are tabulated for the statistically weaker transitions.

Table 5.4. The axial/equatorial anisotropies and U_2A_2 coefficients observed in the decay of $^{74}Br^m$ at 9.8 mK. † indicates a doublet.

Energy (keV)	E (%)	$\overline{U_2A_2}$	U_2A_2	U_4A_4
615	−38.7(1.8)	−0.33(3)	−0.39(6)	0.27(38)
634†	−23.5(0.4)	−0.19(2)	−0.19(4)	−0.10(14)
679	−26.5(12.3)	−0.22(11)	—	—
728	−39.4(0.6)	−0.34(3)	−0.38(5)	0.11(25)
745	13.8(7.9)	0.10(5)	—	—
839	−41.8(2.0)	−0.36(4)	−0.33(7)	−0.25(32)
868	−41.1(10.7)	−0.36(11)	—	—
980	−45.6(16.5)	−0.40(17)	—	—
985†	−33.1(3.3)	−0.28(4)	−0.22(6)	−0.53(31)
1201†	−41.3(2.4)	−0.36(4)	−0.42(9)	0.45(53)
1204	−33.4(8.4)	−0.28(8)	−0.30(17)	−0.28(99)
1250	−58.8(1.3)	−0.55(5)	−0.68(10)	0.55(46)
1269	−30.3(1.8)	−0.25(2)	−0.26(6)	−0.08(33)
1367	−35.6(5.2)	−0.30(5)	−0.29(11)	−0.38(83)

Although the isomeric spin has been firmly assigned, the parity has not. Negative parity was tentatively assigned on the basis of $\log f^{1U}t$ values to the 2231 keV 6^+ level and to several (2^+) states in ^{74}Se [23]. However by their very nature such first unique forbidden beta transitions have very low intensities. In view of the highly complex decay scheme, illustrated in figure 5.4 [24], the small gamma intensity imbalances from which they are deduced could well be accounted for by weak unobserved gamma transitions. As a result the negative parity assignment is by no means definite.

In fact a comparison of the band structures in $^{74,76}Br$ [25] has lead to the proposal of positive parity. Strong corroborative evidence for this assignment is provided by the present magnetic moment of $^{74}Br^m$ which only finds an explanation in the particle-rotor model for a positive parity configuration (see subsection 7.5.2).

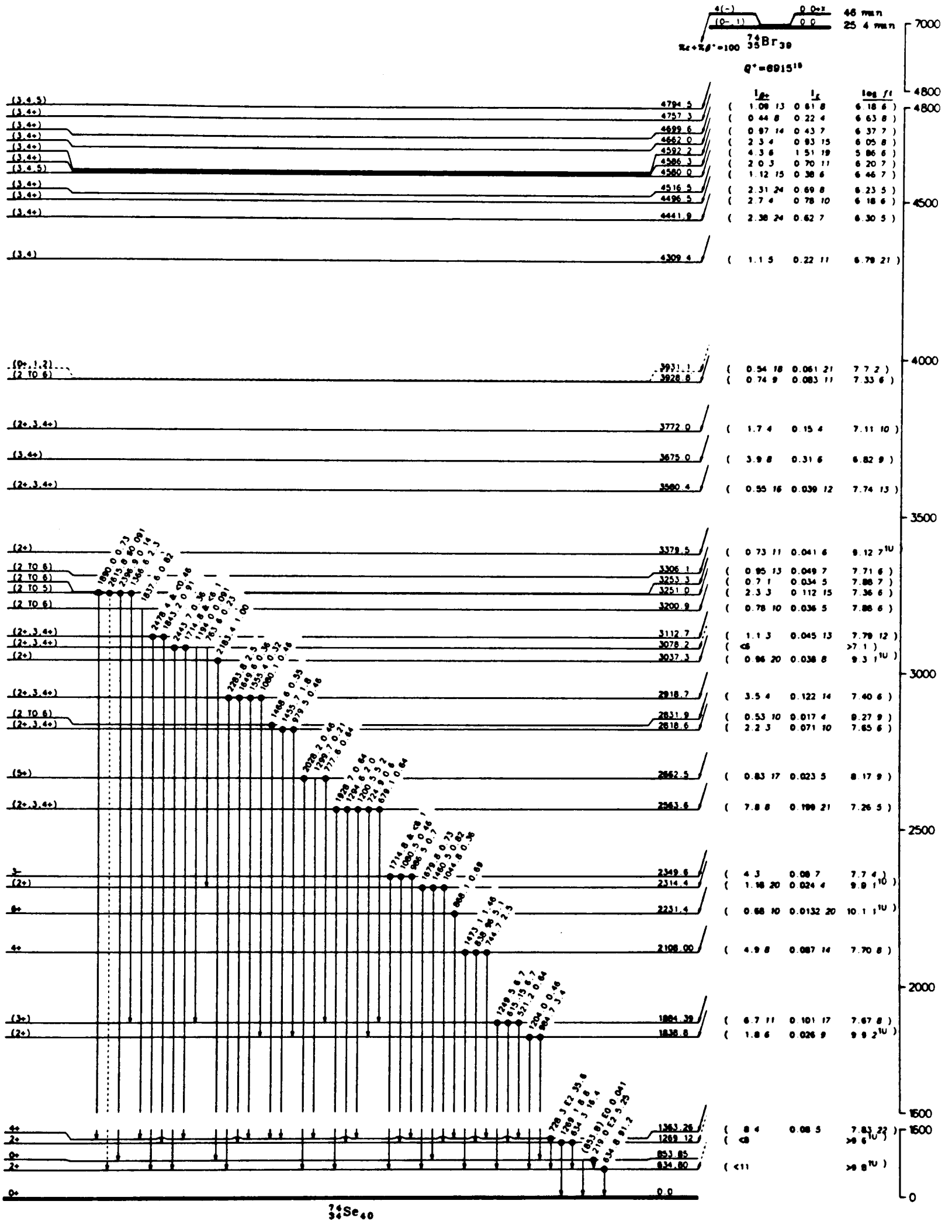

Figure 5.4. The decay scheme of $^{74}Br^{m}$ (Part 1 of 2) [24].

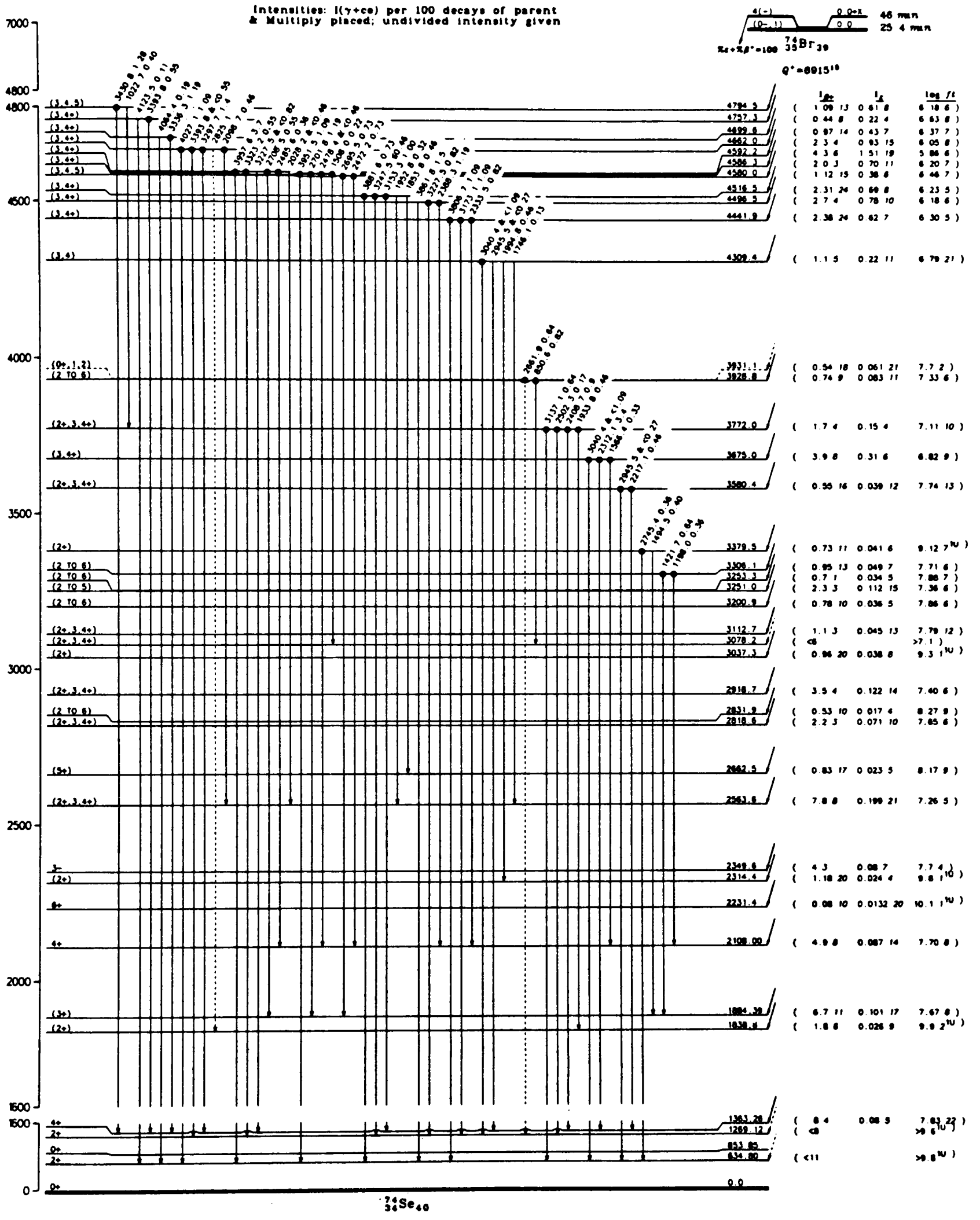

Figure 5.4. The decay scheme of $^{74}Br^{m}$ (Part 2 of 2) [24].

Unfortunately, the present spectroscopic data is not able to confirm the parity assignment either way. Consider, for example, the 868 keV E2 transition arising from the 2231 keV 6^+ level. For a negative parity oriented state this must involve a first unique forbidden β^+/EC decay with de-orientation coefficients $U_2 = +0.90$ and $U_4 = +0.69$. With the above effective site distribution parameters this leads to a predicted anisotropy of $-43(3)\%$ at 9.8 mK, fully consistent with the experimental value of $-41(11)\%$. If the parity of the oriented state was positive then the β^+/EC feeding intensity to this level would be negligible and all the feeding must arise from (hitherto unobserved) gamma transitions. In order to be consistent with the observed anisotropy to the one standard deviation limit this gamma feeding must have approximately $U_2 > +0.60$. The theoretical de-orientation coefficients for transitions in the spin range $I = 4 \rightarrow 6$ could well be expected to satisfy this inequality. Indeed, such high values are exhibited by many of the experimental de-orientation coefficients given below, in spite of the complex feedings which many of these levels possess. Thus both parity assignments are consistent with the present spectroscopic data.

Therefore in the light of the magnetic moment evidence and without any firm evidence to the contrary, the assignment $I^\pi(^{74}\mathrm{Br}^m) = 4^+$ will be assumed in this analysis.

As it turns out, none of the mixing ratios derived below are affected by the parity of the isomeric parent. Only the mixing ratios of the 615 and 634 keV transitions were known previously [24].

2108 keV level : 4^+

The experimental $U_\lambda A_\lambda$ coefficients for the 839 keV E2 transition lead to the level de-orientation parameters $U_2(2108) = +0.74(16)$ and $U_4(2108) = +0.82(105)$. From the former value, in conjunction with $\overline{U_2 A_2}(745) = +0.10(5)$, one obtains

$$\overline{A_2}(745) = +0.14(7) \qquad 4^+ \rightarrow 4^+ \quad \overline{\delta}(745) = -0.76^{+12}_{-14} \quad \text{or} \quad +6.1^{+6.1}_{-2.0}$$

It is now necessary to investigate the effects of the neglected fourth rank terms in the 745 keV analysis. The fourth rank angular distribution coefficients corresponding to the two mixing ratios given above are $A_4 = -0.18(4)$ and $-0.49(1)$ respectively. In the absence of a sufficiently accurate experimental value for U_4 it will be assumed that $U_4/U_2 \sim +1$. In this rather pessimistic approximation the respective ratios $\sum f B_4 U_4 A_4 / \sum f B_2 U_2 A_2 \sim -0.3$ and -1.0 are obtained, the negative signs implying that $A_2 > \overline{A_2}$. Since the proportional error on $\overline{A_2}$ is 0.5, one would expect that in the former case the effect of the fourth rank term is already contained within the experimental error. In the latter case, the fourth order orientation may be as large as that

of the second. Thus, naively, $A_2 = 2\overline{A_2} = +0.28$. Despite this large increase in the angular distribution coefficient, the corresponding mixing ratio simply increases towards infinity.

Therefore, after correcting for the effects of fourth rank terms, the mixing ratio of the 745 keV transition is predicted either to lie in the range $-0.90 \rightarrow -0.64$, or > 4.1 corresponding to an essentially pure E2 multipolarity.

1884 *keV level* : (3^+)

The feeding to this level is 48% by direct lepton decay for which $U_2 = +0.90$ and the remaining 52% by preceeding gamma transitions. The spins of the levels from which these gamma transitions arise are not certain, a number of possibilities being given (see figure 5.4). Taking the maximum and minimum possible de-orientation coefficients for the spin sequences allowed by the suggested level spins leads to $+0.20 \leq U_2 \leq +0.88$. Thus, by taking the intensity weighted sum of these two contributions, the second rank level de-orientation coefficient is predicted to lie in the range $+0.54 \leq U_2(1884) \leq +0.89$. Hence using the experimental $U_2 A_2$ values

$$A_2(1250) \leq -0.65 \quad \text{if} \quad 3^+ \rightarrow 2^+ \quad \delta(1250) = +0.65 \rightarrow +3.0$$

$$A_2(\ 615) \leq -0.37 \quad \text{if} \quad 3^+ \rightarrow 2^+ \quad \delta(\ 615) = +0.40 \rightarrow +7.3$$

The mixing ratio of the 615 keV transition has been measured previously by Piercey *et al.* [26] to be $\delta(615) = +0.3(1)$, which agrees with the present result at the one standard deviation limit. Such an agreement implies that the 1884 keV level de-orientation coefficient lies in the region of $U_2 \sim +0.89$. This is the theoretical maximum value and corresponds to a favourable combination of a number of assumed spin sequences and mixing ratios, none of which have been verified experimentally. Therefore such a value must be viewed with caution. On the other hand, agreement to within two standard deviations requires only that $U_2 \geq +0.51$. This is a much more likely result both theoretically and experimentally, as can be seen from the experimental values for other levels in the decay. For example, the de-orientation coefficient of the 2108 keV level is $U_2 = +0.74(16)$, while those for the 1363 and 1269 keV levels are $U_2 = +0.85(11)$ and $U_2 = +0.44(10)$, as calculated from the 728 and 1269 keV E2 transitions respectively.

Thus the mixing ratio of Piercey *et al.* and the present result together favour value in the range of $\delta(615) = +0.4 \rightarrow +0.5$.

5.6 The decay of ^{73}Br

Table 5.5 lists the anisotropies observed for 16 of the strongest transitions which occur in the decay of ^{73}Br [24] at a temperature of 12.2 mK. None of these showed any significant degree of orientation. Also tabulated are the anisotropy to error ratios. The number of transitions whose anisotropy to error ratio lies within 0.25, 0.50, 0.75, 1.00, 1.25 and 1.50 are 2, 6, 8, 11, 13 and 16 respectively. These compare favourably with the numbers expected for a normal distribution with a mean of zero, namely 3, 6, 9, 11, 13 and 14. Therefore the measured anisotropies are all consistent with the statistical fluctuations expected in the observation of zero orientation.

The probable cause of this has already been discussed in subsection 4.4.3 and is not considered to have any bearing on the spectroscopy of ^{73}Se.

Table 5.5. The axial/equatorial anisotropies observed in the decay of ^{73}Br at 12.2 mK.

Energy (keV)	E (%)	anisotropy/σ
65	0.6(0.6)	1.0
275	0.8(4.9)	0.2
336	0.8(1.6)	0.5
374	−1.6(5.2)	−0.3
401	−0.8(2.0)	−0.4
490	7.0(8.4)	0.8
540	−0.3(3.7)	−0.1
550	4.1(7.3)	0.6
615	−6.5(4.4)	−1.5
639	−6.5(10.3)	−0.6
700	1.9(1.4)	1.4
788	−10.0(11.0)	−0.9
849	−0.3(1.1)	−0.3
870	6.6(4.8)	1.4
914	3.1(2.9)	1.1
931	1.5(1.5)	0.9

5.7 The isotope ^{72}Se

On the basis of observed β^+/EC decays to several levels of spin 2^+ and 4^+ in ^{72}Se and also a gamma transition from the 162 keV 1^+ level in ^{72}Br, the ground state spin-parity has been assigned $I^\pi(^{72}\mathrm{Br}^g) = (3)^+$ [27]. The decay scheme of $^{72}\mathrm{Br}^g$ is illustrated in figure 5.5 [27]

As a consequence of this spin value, the directional distribution of subsequent gamma radiation will contain both second and fourth rank terms. However, as noted in subsection 4.4.4, the ratio of these terms is only of order $\sim 2\%$ and hence the latter terms may be neglected. The extraction of the U_2A_2 coefficients can therefore be carried out using (5.2) without recourse to the fitting procedure which was necessary in the case of $^{74}\mathrm{Br}^m$.

The observed anisotropies are listed in table 5.6 . These correspond to an average temperature of 15.1 mK for which an effective orientation parameter of $\sum fB_2 = 0.11(8)$ can be calculated for the $^{72}\mathrm{Br}^g$ nuclei, using the results of subsection 4.4.4. This includes the $\sim 15\%$ attenuation introduced by the effects of incomplete relaxation. The calculated U_2A_2 coefficients are also included in table 5.6. The errors on these coefficients suffer rather badly from the non-linearity introduced by the fact that the proportional errors in both the anisotropy *and* the effective orientation parameter are not small, let alone infinitesimal as assumed in (5.4). Thus although the anisotropy of the 1317 keV transition is negative, the corresponding U_2A_2 coefficient is calculated to be of either sign within the one standard deviation limits. In order to avoid such anomalies table 5.6 also includes a second set of errors, enclosed in braces, which represent the limits of the variation in U_2A_2 as E and $\sum fB_2$ are varied within their respective one standard deviation limits.

Table 5.6. The axial/equatorial anisotropies and U_2A_2 coefficients observed in the decay of ^{72}Br at 15.1 mK.

Energy (keV)	E (%)	U_2A_2
101	−10.9(3.1)	see text
455	−1.6(2.1)	$-0.10(0.15)\{^{+\ 12}_{-\ 78}\}$
753	11.3(7.9)	$0.69(0.68)\{^{+353}_{-\ 57}\}$
775	−6.9(4.5)	$-0.45(0.44)\{^{+\ 36}_{-217}\}$
862	−4.1(0.6)	$-0.26(0.19)\{^{+\ 13}_{-\ 86}\}$
1055	−5.9(5.2)	$-0.38(0.44)\{^{+\ 35}_{-232}\}$
1062	−14.3(3.6)	$-0.95(0.74)\{^{+\ 54}_{-355}\}$
1136	1.1(5.8)	$0.06(0.37)\{^{+154}_{-\ 24}\}$
1317	−3.2(2.4)	$-0.20(0.21)\{^{+\ 17}_{-110}\}$

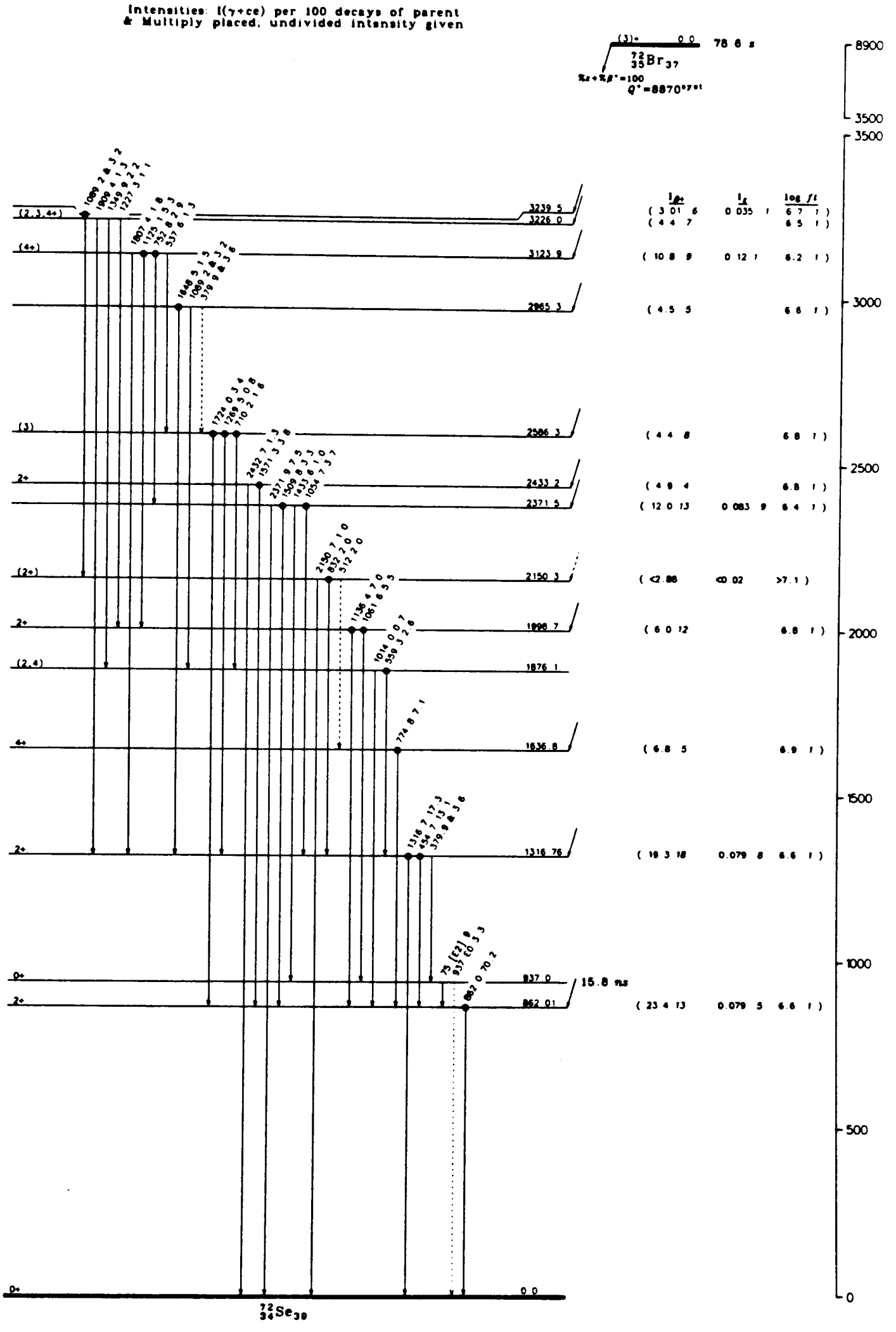

Figure 5.5. The decay scheme of $^{72}Br^{g}$ [27].

No mixing ratios in ^{72}Se have been previously measured.

1999 *keV level* : 2^+

Using the theoretical angular distribution coefficient of the 1062 keV E2 transition and the experimental ratio $A(1136:1062) = -0.07(38)$

$$A_2(1136) = +0.04(23) \qquad 2^+ \rightarrow 2^+ \quad \delta(1136) = -0.36^{+18}_{-24} \quad \text{or} \quad \geq +4.0$$

1317 *keV level* : 2^+

The ratio $A(455:1317) = +0.50(76)$ and the fact that the 1317 keV ground state transition is pure E2 gives

$$A_2(455) = -0.30(45) \qquad 2^+ \rightarrow 2^+ \quad \delta(455) = -0.09^{+46}_{-38} \quad \text{or} \quad \geq +1.0$$

5.8 The isomer ^{72}Br^m

In the present work the isomeric 101 keV ground state transition has been studied both by LTNO and electron conversion measurements. The latter were performed by collecting the ^{72}Br activity on the motorized tape of the DOLIS mini-beam line. Every few seconds this was transported to a position where simultaneous electron and gamma ray measurements were made, using a cooled Si(Li) and a Ge detector respectively. The relative electron to gamma intensities were normalized by the 75 keV ($0^+ \rightarrow 2^+$) E2 transition in ^{72}Se using the theoretical E2 conversion coefficient.

The resulting conversion coefficient for the 101 keV transition is $\alpha_K = 1.4(3)$ [28], corresponding to a predominantly M2 transition with an E3 octupole admixture of 7(6)% ($|\delta(\text{M2/E3})| = 0.27^{+12}_{-17}$). (The possibility of an E2/M3 character cannot be completely ruled out, but the significant M3 content argues strongly against such an assignment). This confirms the previous value of $0.9 \leq \alpha_K \leq 2.5$ obtained indirectly [29] from gamma intensity imbalances and which lead to the assignment $I^\pi(^{72}\text{Br}^m) = (1)^-$ on the basis that $I^\pi(^{72}\text{Br}^g) = (3)^+$. The suggestion of an M2 character for this transition implies a hindrance factor of 10^5 compared to the Weißkopf single particle estimate. Such a highly retarded M2 transition (57 keV, 1.3 s) has also been found in the neighbouring nucleus ^{76}Br [30].

The observed anisotropy of the isomeric transition is given in table 5.6. Taking the maximum values of f and B_2 (100% and full saturation respectively) enables one to set a lower limit on the magnitude of A_2, whence $A_2 \leq -0.08$. This inequality leads to a M2/E3 mixing ratio of $-1.3 \leq \delta \leq +0.03$. When combined with the more precise electron conversion value this result implies that the negative sign should be taken, hence $\delta(101\ \mathrm{M2/E3}) = -0.27^{+17}_{-12}$.

5.9 Conclusion

The present data has lead to much new spectroscopic information on the light selenium isotopes $^{72-77}$Se. A number of electromagnetic and leptonic multipole mixing ratios have been determined, many for the first time.

In ^{77}Se, 12 mixing ratios have been deduced. It has been argued that the results of an earlier $\gamma\gamma(\theta)$ study by Braga *et al.* [2] are erroneous. Two independent studies [4,5] fully support the present values. In addition to the mixing ratios, the spin of the 824 keV level has been assigned $5/2^-$.

A significant proportion of $j_\beta = 2$ mixing has been established in the first forbidden decay of ^{76}Br to the 559 keV level in ^{76}Se. Also a number of spin assignments have been suggested and mixing ratios deduced.

Mixing ratios have also been derived for several gamma transitions in ^{72,74,75}Se. The M2 nature of the 101 keV isomeric transition in ^{72}Br has been confirmed by an electron conversion measurement.

Unfortunately an important potential result of this analysis, namely a precise value for the site distribution parameter in $^{72-75}$Br, was not forthcoming. With this objective in mind further LTNO experiments on these isotopes, using greater source strengths, might prove to be very fruitful. Certainly data on the weaker transitions would enable many new spin assignments and hence mixing ratios to be obtained, particularly so for the plethora of higher lying levels in ^{74,76}Se.

References

[1] . Nuclear Data Sheets **29** (1980)

[2] . R.A. Braga and D.G. Sarantites, Phys. Rev. **C9** (1974) 1493

[3] . M. Mohsen and F. Pleiter, Hyp. Int. **39** (1988) 123

[4] . R.L. Robinson *et al.*, Phys. Rev. **C125** (1962) 1373

[5] . K.O. Zell *et al.*, Z. Phys. **A276** (1976) 371

[6] . Y. Tokunaga *et al.*, Nucl. Phys. **A439** (1985) 427

[7] . D. Rabenstein and H. Vonach, Z. Naturforsch **26a** (1971) 458

[8] . H.J. Rose and D.M. Brink, Rev. Mod. Phys. **39** (1967) 306

[9] . L.C. Biedenharn and M.E. Rose, Rev. Mod. Phys. **25** (1953) 729

[10] . K.S. Krane and R.M. Steffen, Phys. Rev. **C2** (1970) 724

[11] . Nuclear Data Sheets **42** (1984)

[12] . D. Ardouin *et al.*, Phys. Rev. **C12** (1975) 1745

[13] . A.H. Wapstra *et al.*, Nuclear Spectroscopy Tables, (North Holland, 1959)

[14] . R. Kaur *et al.*, J. Phys. Soc. Japan **49** (1980) 1214

[15] . A.R.H. Subber *et al.*, J. Phys. **G13** (1987) 807

[16] . T. Matsuzaki and H. Taketani, Nucl. Phys. **A390** (1982) 413

[17] . J.A. Barclay *et al.*, Phys. Rev. **C13** (1976) 1991

[18] . Nuclear Data Sheets **32** (1981)

[19] . Y. Tokunaga *et al.*, Nucl. Phys. **A430** (1984) 269

[20] . N.E. Sanderson and R.G. Summers-Gill, Nucl. Phys. **A261** (1976) 93

[21] . Y.K. Argawal *et al.*, Pramana **3** (1974) 243

[22] . C. Ekstrom and L. Robertsson, Phys. Scripta **22** (1980) 344

[23] . A. Coban *et al.*, Part. Nucl. **4** (1972) 108

[24] . Nuclear Data Sheets **51** (1987)

[25] . G. Winter *et al.*, Z. Phys. **A309** (1983) 243

[26] . R.B. Piercey *et al.*, Phys. Rev. **C19** (1974) 1344

[27] . Nuclear Data Sheets **56** (1989)

[28] . B.D.D. Singleton, private communication (1988)

[29] . G. Garcia Bermudez *et al.*, Phys. Rev. **C25** (1982) 1396

[30] . M. Behar *et al.*, Nucl. Phys. **A282** (1977) 331

Chapter 6

Collective models of the nucleus

6.1 Introduction

This chapter will briefly review the collective models of low energy nuclear excitations, concentrating in particular on the particle-rotor models. It is intended both as an introduction to the calculations presented in the next chapter and to develop the formalism by which the particle-rotor models have been extended to include soft cores in this work.

6.2 The collective quadrupole motion of even-even nuclei

6.2.1 The surface variables and the collective Hamiltonian

In the laboratory frame, nuclear deformations, as evidenced by non-zero quadrupole moments and B(E2) values, can be conveniently expressed by the relation

$$R(\vartheta,\varphi,t) = R_0 \left\{ 1 + \sum_{\lambda\mu} \alpha_{\lambda\mu}(t) Y^*_{\lambda\mu}(\vartheta,\varphi) \right\} \tag{6.1}$$

where R defines the location of a point on the surface and R_0 is the average nuclear radius. The $\alpha_{\lambda\mu}$ are the components of the surface collective tensor $\alpha^{\{\lambda\}}$, where λ determines the multipolarity of the nuclear motion. The $\lambda = 0$ mode merely scales the nuclear volume, while the $\lambda = 1$ mode corresponds (for small deformations at least) to a trivial translation of the center of mass. Therefore the $\lambda = 2$ quadrupole mode is the lowest order mode of interest. The $\lambda = 3$ octupole modes correspond, in general, to higher lying excitations. Hence only quadrupole terms will be considered and the index λ will be dropped.

In this approximation the Hamiltonian may be separated into a kinetic energy $T\left(\pi^{\{2\}}, \alpha^{\{2\}}\right)$ and a potential energy $V\left(\alpha^{\{2\}}\right)$. Assuming a series expansion in terms of the small quantities $\alpha^{\{2\}}$ and their canonically conjugate momenta $\pi^{\{2\}}$ leads to

$$T\left(\pi^{\{2\}}, \alpha^{\{2\}}\right) = \frac{\sqrt{5}}{2B_2}[\pi^{\{2\}} \times \pi^{\{2\}}]^{\{0\}} + B_3\left[[\pi^{\{2\}} \times \alpha^{\{2\}}] \times \pi^{\{2\}}\right]^{\{0\}} + \cdots \tag{6.2}$$

and

$$V\left(\alpha^{\{2\}}\right) = \frac{\sqrt{5}}{2}C_2[\alpha^{\{2\}} \times \alpha^{\{2\}}]^{\{0\}} + C_3\left[[\alpha^{\{2\}} \times \alpha^{\{2\}}] \times \alpha^{\{2\}}\right]^{\{0\}} + \cdots \tag{6.3}$$

The coupling of the various tensor products to degree zero ensures that the Hamiltonian is scalar and therefore rotationally invariant. Further, the condition of invariance under time reversal requires that the kinetic energy only contains products of even numbers of conjugate momenta. The parameters B and C characterize the inertia of the collective motion and the stiffness of the collective potential energy respectively. To third order the kinetic energy (6.2) may be written

$$T = \frac{1}{2}B_2 \sum_{\mu} \dot{\alpha}^*_{\mu}\dot{\alpha}_{\mu} + B_3 \sum_{\mu\nu\upsilon} \begin{pmatrix} 2 & 2 & 2 \\ \mu & \nu & \upsilon \end{pmatrix} \dot{\alpha}_{\mu}\alpha_{\nu}\dot{\alpha}_{\upsilon}. \tag{6.4}$$

For spherical nuclei the potential of deformation may be expanded about $\alpha^{\{2\}} = 0$ as was assumed in (6.3) and so to second order the Hamiltonian becomes

$$H_{vib} = \frac{1}{2}B_2 \sum_{\mu} \dot{\alpha}^*_{\mu}\dot{\alpha}_{\mu} + \frac{1}{2}C_2 \sum_{\mu} \alpha^*_{\mu}\alpha_{\mu}. \tag{6.5}$$

This is the *vibrational* Hamiltonian [1] in which the nucleus is considered to perform harmonic vibrations about spherical shape.

When static nuclear deformation is introduced, it is more convenient to work in the intrinsic (body fixed) frame in which the five quadrupole surface collective variables are denoted a_{ν}. From the invariance of (6.1) under rotations it follows that the surface variables must transform according to

$$\alpha_{\mu} = \sum_{\nu} D^2_{\mu\nu}(\phi, \theta, \psi)a_{\nu} \tag{6.6}$$

where ϕ, θ and ψ are the Euler angles of the rotation. Without any loss of generality this transformation may be chosen such that

$$a_0 = \beta\cos\gamma, \quad a_{\pm 1} = 0 \quad \text{and} \quad a_{\pm 2} = \frac{1}{\sqrt{2}}\beta\sin\gamma. \tag{6.7}$$

In terms of the five intrinsic variables $(a_0, a_2, \phi, \theta, \psi)$ the collective kinetic energy to third order (6.4) is therefore

$$T = \frac{1}{2}\sum_k \Im_k(a_0, a_2)\omega_k^2(\dot{\phi}, \dot{\theta}, \dot{\psi}) + \frac{1}{2}B_2\dot{a}_0^2(1 - 2B'a_0) + B_2\dot{a}_2^2(1 + 2B'a_0) + 4B_2B'a_2\dot{a}_0\dot{a}_2 \quad (6.8)$$

where ω_k is the angular velocity about the intrinsic axes labelled by k and

$$B' = \sqrt{\frac{2}{35}}\frac{B_3}{B_2}. \quad (6.9)$$

In this approximation the moment of inertia is given by

$$\Im_k(a_0, a_2) = 4B_2\beta^2\left\{1 + 2B'\beta\cos\left(\gamma - \frac{2\pi}{3}k\right)\right\}\sin^2\left(\gamma - \frac{2\pi}{3}k\right). \quad (6.10)$$

Together with the potential energy, expanded quadratically around the deformed equilibrium position, (6.8) forms the basis of the *rotation-vibration* Hamiltonian [2].

If this potential is infinitely stiff around the deformed minimum then the intrinsic surface variables become constant. As a result only the D-matrices of (6.6) contribute to the time dependence of the laboratory surface variables appearing in (6.4). The collective Hamiltonian then reduces to its purely *rotational* limit [3]

$$H_{rot} = \frac{1}{2}\sum_k \Im_k(a_0, a_2)\omega_k^2 \quad (6.11)$$

with moments of inertia, to lowest order,

$$\Im_k(a_0, a_2) = 4B_2\beta^2\sin^2\left(\gamma - \frac{2\pi}{3}k\right). \quad (6.12)$$

6.2.2 The generalized rotational basis

Let the collective nuclear wavefunction be denoted by $|IM\varrho\rangle$, where I is the total angular momentum, M its component on the laboratory 3-axis and ϱ any other quantum numbers required to specify the state. As a solution of the collective Hamiltonian, $|IM\varrho\rangle$ depends on the five quadrupole coordinates $\beta, \gamma, \phi, \theta$ and ψ. Thus the transformation from the laboratory frame to the intrinsic frame gives

$$|IM\varrho\rangle = \sqrt{\frac{2I+1}{8\pi^2}} \sum_K A_K^{I\varrho}(\beta,\gamma) D_{MK}^I(\phi,\theta,\psi) \tag{6.13}$$

where K is the projection of the total angular momentum on the intrinsic 3-axis and $A_K^{I\varrho}$ is the wavefunction in the intrinsic system. This collective wavefunction must be a single valued function of the laboratory surface variables α_μ. There are 24 different sets of right handed intrinsic axes which alter the intrinsic quadrupole coordinates in such a way as to leave the α_μ invariant. These possibilities are all obtainable through various combinations of the transformation operators $\hat{R}_1$, $\hat{R}_2$ and $\hat{R}_3$, where

$$\begin{aligned} \hat{R}_1(1,2,3) &= (1,-2,-3) \\ \hat{R}_2(1,2,3) &= (2,-1,\ \ 3) \\ \hat{R}_3(1,2,3) &= (3,\ \ 1,\ \ 2). \end{aligned} \tag{6.14}$$

The action on these operators on the rotation matrices are

$$\begin{aligned} \hat{R}_1 D_{MK}^I &= \exp^{i\pi(I-K)} D_{M-K}^I \\ \hat{R}_2 D_{MK}^I &= \exp^{i\pi K/2} D_{MK}^I \\ \hat{R}_3 D_{MK}^I &= \sum_{K'} D_{KK'}^{I*}\left(\frac{\pi}{2},0,\frac{\pi}{2}\right) D_{MK'}^I \end{aligned} \tag{6.15}$$

so that $|IM\varrho\rangle$ is invariant under these transformations provided that the intrinsic system wavefunction satisfies

$$\begin{aligned} A_{-K}^{I\varrho}(\beta,\gamma) &= (-1)^{I+K} A_K^{I\varrho}(\beta,\gamma) \\ A_K^{I\varrho}(\beta,\gamma) &= (-1)^{K/2} A_K^{I\varrho}(\beta,-\gamma) \\ A_K^{I\varrho}(\beta,\gamma) &= \sum_{K'} D_{KK'}^I\left(\frac{\pi}{2},0,\frac{\pi}{2}\right) A_{K'}^{I\varrho}\left(\beta,\gamma-\frac{2\pi}{3}\right). \end{aligned} \tag{6.16}$$

It follows that if $A_K^{I\varrho}(\beta,\gamma)$ is known in any $\pi/3$ sector of γ then its value is determined for all other principle values. Further, by applying the second equation of (6.16) twice, it is clear that K is restricted to even values. Thus the symmetrized collective wavefunction (6.13) becomes

$$|IM\varrho\rangle = \sum_{K=0,2,\cdots} A_K^{I\varrho}(\beta,\gamma)|IMK\rangle \tag{6.17}$$

where

$$|IMK\rangle = \sqrt{\frac{2I+1}{16\pi^2(1+\delta_{K,0})}}\left\{D^I_{MK} + (-1)^I D^I_{M-K}\right\}. \tag{6.18}$$

This symmetrization forbids $K = 0$ components when I is odd and therefore no states of $I = 1$ are allowed in this representation.

6.2.3 The rotational states of even-even nuclei

When expressed in terms of the intrinsic frame components I_k of the total angular momentum operator, the rotational limit (6.11) of the collective Hamiltonian becomes, after some rearrangement,

$$H_{rot} = \frac{1}{4}\left\{\frac{1}{\Im_1}+\frac{1}{\Im_2}\right\}\{I^2 - I_3^2\} + \frac{1}{4}\left\{\frac{1}{\Im_1}-\frac{1}{\Im_2}\right\}\{I_1^2 - I_2^2\} + \frac{1}{2\Im_3}I_3^2 \tag{6.19}$$

where the elements of irrotational moment of inertia (6.12) are written

$$\Im_k = \frac{4}{3}\Im_0 \sin^2\left(\gamma - \frac{2\pi}{3}k\right). \tag{6.20}$$

The β dependence of the moment of inertia parameter $\Im_0$ is often approximated by the empirical relation of Grodzins [4].

The diagonalization of the Hamiltonian matrix in the basis (6.17) is relatively straight forward. The matrix elements are given in appendix A.1 together with a computer code which has been written to initiate the matrix.

The states near to the yrast line constitute two separate band structures, the ground state band ($0_1^+, 2_1^+, 4_1^+ \cdots$) and the higher lying gamma band ($2_2^+, 3_1^+, 4_2^+ \cdots$). The energy eigenvalues of the ground state and gamma bands are illustrated in figure 6.1 . Since the intrinsic coordinate β merely scales the Hamiltonian via the moment of inertia, the relative energies are governed entirely by the asymmetry parameter γ. It can be seen that while the energies of the ground state band remain relatively unchanged, the energies of the gamma band decrease rapidly as γ increases. The position of the rotational gamma band relative to the ground state band therefore gives a clear indication of the degree of static nuclear triaxiality.

At large triaxial deformations the sequence of even-odd spins above $I = 5$ in the gamma band is predicted to reverse. In this feature the asymmetric rotor model [3] is distinct from the rotation-vibration [5] and IBA [6] models. While the stretched E2 transition strengths within the gamma band always remain quite large, the transitions from even I to odd I states decrease to zero as full triaxiality is approached [7]. Thus it is more appropriate to consider the 2_2^+, 4_2^+, $\cdots$ and 3_1^+, 5_1^+, $\cdots$ states as separate band structures for large γ deformations.

Analytic expressions for the energies of the low spin states may be easily derived. Those which will be employed are, in units of $3\hbar^2/4\Im_0$,

$$E_{2_{1,2}^+} = \frac{9}{\sin^2(3\gamma)} \left\{ 1 \pm \sqrt{1 - \frac{8}{9}\sin^2(3\gamma)} \right\} \tag{6.21}$$

$$E_{3_1^+} = \frac{18}{\sin^2(3\gamma)} \tag{6.22}$$

while the three spin 4 energy levels are the roots of

$$E^3 - \frac{90}{\sin^2(3\gamma)}E^2 + \frac{48}{\sin^4(3\gamma)}\left\{27 + 26\sin^2(3\gamma)\right\}E - \frac{640}{\sin^4(3\gamma)}\left\{27 + 7\sin^2(3\gamma)\right\} = 0. \tag{6.23}$$

The relationship between static and dynamic electric quadrupole moments and the deformation coordinates β, γ are also of interest. Thus, using the collective elements of the operators defined in subsection 6.3.5, one obtains for the first excited member of the ground state band [3]

$$Q_{2_1^+} = -Q_0 \frac{6\cos(3\gamma)}{7\sqrt{9 - 8\sin^2(3\gamma)}} \tag{6.24}$$

and

$$B(\mathrm{E2}; 2_1^+ \rightarrow 0^+) = \frac{e^2 Q_0^2}{32\pi} \left\{ 1 + \frac{3 - 2\sin^2(3\gamma)}{\sqrt{9 - 8\sin^2(3\gamma)}} \right\} \tag{6.25}$$

where the intrinsic macroscopic electric quadrupole moment Q_0 is given by

$$Q_0 = \frac{3}{\sqrt{5}} Z R_0^2 \beta. \tag{6.26}$$

Within the framework of this model the asymmetry parameter γ may thus be derived from the ratio $E_{2_2^+}/E_{2_1^+}$ and subsequently β from either (6.24) or (6.25).

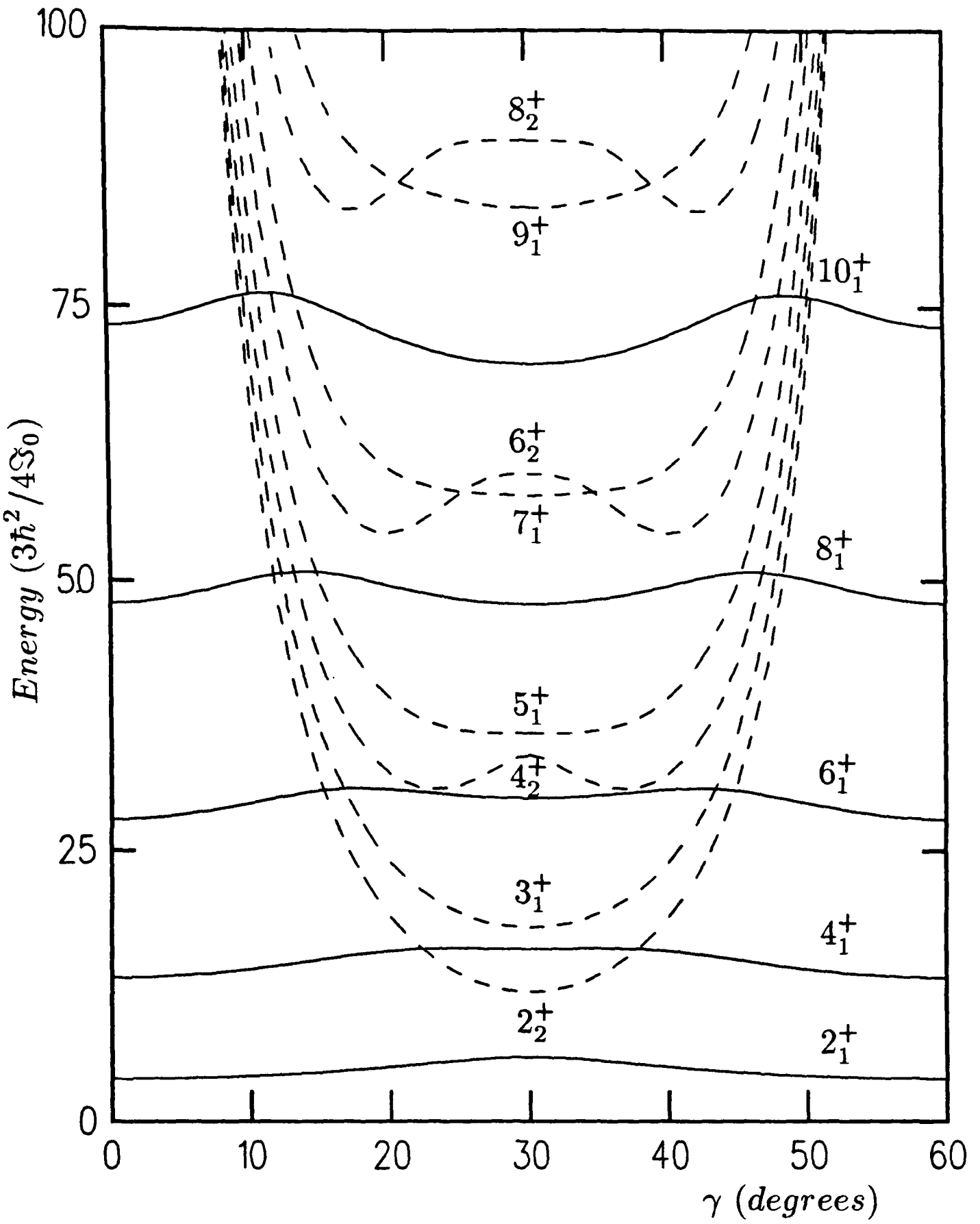

Figure 6.1. The excitation energies of the ground state (solid) and gamma (dashed) bands of the asymmetric rigid rotor as a function of the asymmetry parameter γ.

6.3 The unified model of odd nuclei

The many body Hamiltonian of an odd mass nuclear system can be approximated by

$$H = H_{core}(\alpha) + H_{part}(\overline{\alpha}) + H_{int}(\alpha) \tag{6.27}$$

where H_{core} is the collective Hamiltonian for the even-even core, H_{part} is the single particle Hamiltonian in an adiabatic field corresponding to some fixed set $\overline{\alpha}$ of the surface collective variables and H_{int} takes into account the effect of the odd particle on that part of the core field not already included in H_{part}.

If a spherical shell model potential $V_0(r, \mathbf{l}, \mathbf{s})$ is assumed, then the potential

$$V(\alpha, r, \mathbf{l}, \mathbf{s}) = V\left(\frac{r}{1 + \sum_{\lambda\mu} \alpha_{\lambda\mu} Y^*_{\lambda\mu}}, \mathbf{l}, \mathbf{s}\right) \tag{6.28}$$

has an equipotential on the nuclear surface $r = R_0 \left\{1 + \sum_{\lambda\mu} \alpha_{\lambda\mu} Y^*_{\lambda\mu}\right\}$. Expanding (6.28) about $\overline{\alpha} = 0$ gives to first order

$$\begin{aligned} V(\alpha, r, \mathbf{l}, \mathbf{s}) &= V(0, r, \mathbf{l}, \mathbf{s}) + \sum_{\mu} \left.\frac{\partial V}{\partial \alpha_{\lambda,\mu}}\right|_0 \alpha_{\lambda\mu} + \cdots \\ &= V_0\,(r, \mathbf{l}, \mathbf{s}) - r\frac{dV_0}{dr} \sum_{\lambda\mu} \alpha_{\lambda\mu} Y^*_{\lambda\mu} + \cdots \end{aligned} \tag{6.29}$$

where by definition $V_0(r, \mathbf{l}, \mathbf{s}) = V(0, r, \mathbf{l}, \mathbf{s})$. The Hamiltonian (6.27) may therefore be written

$$H = H_{core}(\alpha) + H_{part}(\overline{\alpha} = 0) - r\frac{dV_0}{dr} \sum_{\lambda} \left[\alpha^{\{\lambda\}} \times Y^{\{\lambda\}}\right]^{\{0\}} + \cdots \tag{6.30}$$

where the the zeroth order potential $V_0(r, \mathbf{l}, \mathbf{s})$ is absorbed into H_{part}. The remaining potential energy terms constitute H_{int} which, since the gradient of a typical Woods Saxon potential is only different from zero near the nuclear surface, represents a surface coupling.

This expansion is employed in the *weak coupling* model [8] which considers the interaction between the single particle and the collective motion of a spherical vibrational core (6.5). In principle the only limitation to the Hamiltonian of (6.30) lies in the neglect of higher order terms in α. In practice a further difficulty arises when the first order terms are more than a small perturbation, since then the size of the single particle basis required for convergence becomes unmanageably large. In such cases it is appropriate to expand the shell model potential around a fixed set of intrinsic surface variables $\overline{a}$ which correspond to the static average of the core field and minimize H_{int}. Thus

$$V(a, r, \mathbf{l}, \mathbf{s}) = V(\overline{a}, r, \mathbf{l}, \mathbf{s}) + \sum_{\lambda\mu} \left.\frac{\partial V}{\partial a_{\lambda\mu}}\right|_{\overline{a}_{\lambda\mu}} \{a_{\lambda\mu} - \overline{a}_{\lambda\mu}\} + \cdots \tag{6.31}$$

If all but the zeroth order term of this deformed shell model potential is neglected then vibrational contributions to H_{int} disappear and only the orientation coordinates of the intrinsic frame

(ϕ, θ, ψ) remain as dynamic variables. The collective motion is then restricted to the rotational form of (6.11) leading to the *particle-rotor* Hamiltonian

$$H = \sum_k \frac{1}{2\Im_k} R_k^2(\phi, \theta, \psi) + H_{part+int}(\overline{a}, \phi, \theta, \psi) \tag{6.32}$$

where **R** is the angular momentum of the core taken with respect to the intrinsic axes k. By diagonalizing (6.32) in the *strong coupling* basis states (subsection 6.3.3), which are not themselves eigenstates of the core, the contributions from the particle-rotation interaction are transformed from H_{part} and into H_{core}. Thus, expressing **R** as the vector difference between the total angular momentum **I** and the single particle contribution **j**, (6.32) becomes

$$H = \sum_k \frac{1}{2\Im_k} \left\{ I_k^2(\phi, \theta, \psi) - 2I_k(\phi, \theta, \psi) j_k + j_k^2 \right\} + H_{part}(\overline{a}). \tag{6.33}$$

In this representation the particle-rotation coupling emerges in the form of a Coriolis term $\sum Ij/\Im$ and a recoil term $\sum j^2/2\Im$.

The nature of this Hamiltonian will be discussed in more detail after the deformed single particle solutions have been derived.

6.3.1 The Nilsson modified harmonic oscillator potential

The basis for most discussions of the nuclear shell model lies in the self-consistent Hartree-Fock one-body potential calculated from the nuclear two-body interactions. Perhaps the most realistic of these, together with the spin-orbit term, is the Wood-Saxon potential with constant surface diffuseness [9]

$$V_{WS} = V(r) + V_{LS} + V_{coul} \tag{6.34}$$

with

$$V(r) = -V_0 \Big/ \{1 + \exp[dist(\mathbf{r}, \alpha)/a]\} \tag{6.35}$$

where a is the surface diffuseness and $dist(\mathbf{r}, \alpha)$ denotes the distance (taken to be negative within the surface) between the radius vector **r** and the nuclear surface defined by (6.1). The spin-orbit potential V_{LS} takes the form

$$V_{\mathrm{LS}} = \mathbf{s} \cdot \nabla V_{so}(r) \times \mathbf{p} \tag{6.36}$$

where **s** and **p** denote the nucleon spin and linear momentum operators and V_{so} is an appropriate radial function which need not necessarily be identical to the potential $V(r)$. The coulomb potential V_{coul} enters only for protons and is generated by a charge $(Z-1)e$ uniformly distributed within the nuclear volume.

However, the Woods-Saxon potential suffers from the disadvantage that its matrix elements cannot be solved analytically. In this respect a far better choice is the Nilsson modified harmonic oscillator potential [10]

$$V_{mho} = V_{osc} + V_{corr} + V_{\mathrm{LS}}. \tag{6.37}$$

The shape of the harmonic oscillator term

$$V_{osc} = \frac{1}{2} m \sum_{k} \varpi_k^2 x_k'^2 \tag{6.38}$$

is defined by the quadrupole deformation parameters δ and γ_δ, which are related to the oscillator frequencies ϖ_k through the equations

$$\varpi_k^2 = \varpi_0^2(\delta, \gamma_\delta)\left\{1 - \frac{4}{3}\delta\cos\left(\gamma_\delta - \frac{2\pi}{3}k\right)\right\}. \tag{6.39}$$

V_{corr} is a corrective term which to some degree bridges the differences between V_{osc} and (6.35). Since the Woods-Saxon potential has greater depth than V_{osc} close to the nuclear surface, high orbital angular momentum states, which have correspondingly large rms radii, are depressed relative to those in an oscillator potential. Empirically therefore, the high l oscillator states may be adjusted by the addition of a term

$$V_{corr} = -\kappa\mu\hbar\varpi_0 l^2 \tag{6.40}$$

where κ and μ are constant parameters. In fact, since the matrix elements of $-l^2$ within an oscillator shell are the same as those of $2r^4$ apart from additive constants, V_{corr} can also be viewed as the next term in a radial expansion of (6.38).

The spin-orbit term may be calculated from (6.36) on the assumption that the functional form of V_{so} is identical to that of the oscillator potential V_{osc}. Thus in the limit of spherical symmetry

$$V_{\mathrm{LS}} = -2\kappa\hbar\varpi_0 \mathbf{l}\cdot\mathbf{s}. \tag{6.41}$$

Table 6.1. Typical $\mathbf{l} \cdot \mathbf{s}$ and l^2 strength parameters, κ and μ, of the modified oscillator potential. Values are given for both protons and neutrons in the various oscillator shells.

N	κ_p	μ_p	κ_n	μ_n
0	0.120	0.00	0.120	0.00
1	0.120	0.00	0.120	0.00
2	0.105	0.00	0.105	0.00
3	0.090	0.30	0.095	0.18
4	0.065	0.57	0.080	0.22
5	0.060	0.65	0.062	0.43
6	0.054	0.69	0.062	0.34

This form is generally retained even when spherical symmetry is violated. Values for the parameters κ and μ are frequently quoted in the literature. A typical example, illustrating the oscillator shell number dependence, is given in table 6.1 [11].

It is well known that the nuclear density and therefore the nuclear volume is approximately constant for any deformation. Due to the short range of the nuclear two-body interactions a given nuclear equipotential surface should also be required to enclose a fixed volume independent of deformation. For V_{corr} and V_{LS} this condition is rather hard to apply rigorously. Instead, volume conservation is achieved in an approximate manner by subtracting the average of these terms, $\langle l^2 \rangle_N$ and $\langle \mathbf{l} \cdot \mathbf{s} \rangle_N$ respectively, taken over an oscillator shell. With the addition of these two corrections to the total potential V_{mho}, the volume conservation condition may then be applied to V_{osc} in isolation. For ellipsoidal deformations this requires that

$$\prod_k \varpi_k = \mathring{\varpi}^3. \tag{6.42}$$

Together with (6.39) this equation determines the deformation dependence of $\varpi_0(\delta, \gamma_\delta)$. The deformation independent constant $\mathring{\varpi}$ is chosen such that the rms radius of the nucleus reproduces the empirical value $R_0 A^{\frac{1}{3}}$. Taking $R_0 = 1.2$ fm leads to the approximate formula

$$\begin{Bmatrix} \mathring{\varpi}^N \\ \mathring{\varpi}^Z \end{Bmatrix} = 41 A^{-\frac{1}{3}} \left\{ 1 \pm \frac{1}{3} \frac{N-Z}{A} \right\}. \tag{6.43}$$

The difference in the proton and neutron oscillator frequencies reflects the effect of the hitherto neglected Coulomb force.

With the introduction of the "unstretched" coordinates defined by $x_k = x'_k \sqrt{m\varpi_0/\hbar}$, the modified harmonic oscillator Hamiltonian may be written

$$H_{mho} = \frac{1}{2}\hbar\varpi_0(\delta,\gamma_\delta)\left\{-\nabla^2+r^2\right\} - \kappa\hbar\mathring{\omega}_0\left\{2\mathbf{l}\cdot\mathbf{s}+\mu\left(l^2-\langle l^2\rangle_N\right)\right\} - \frac{1}{2}\hbar\varpi_0(\delta,\gamma_\delta)r^2\frac{4}{3}\sqrt{\frac{4\pi}{5}}\delta\left\{\cos\gamma_\delta Y_{20}+\frac{1}{\sqrt{2}}\sin\gamma_\delta\left(Y_{22}+Y_{2-2}\right)\right\}. \tag{6.44}$$

The diagonalization of the Hamiltonian matrix is performed in one of the harmonic oscillator basis sets: $|Njl\Omega\rangle$ (coupled), $|Nj\Lambda\Sigma\rangle$ (decoupled) or $|Nn_3\Lambda\Sigma\rangle$ (cylindrical), where N is the principal oscillator quantum number, n_3 the number of quanta along the 3-axis and Λ,Σ,Ω are the quantum numbers of l_3, s_3 and j_3 respectively. The quadrupole terms of (6.44) have non-zero matrix elements between basis states whose principal quantum numbers differ by zero or two units. The resultant mixing of the oscillator shells requires that the basis must span at least three shells of a given parity to achieve convergence. This inconvenience may be avoided by a introducing the "stretched" representation $\xi_k = x'_k\sqrt{m\varpi_k/\hbar}$, with the quadrupole deformation parametrized by

$$\varpi_k = \varpi_0(\epsilon,\gamma_\epsilon)\left\{1-\frac{2}{3}\epsilon\cos\left(\gamma_\epsilon-\frac{2\pi}{3}k\right)\right\}. \tag{6.45}$$

The frequency parameter $\varpi_0(\epsilon,\gamma_\epsilon)$ is scaled to conserve the nuclear volume in an identical fashion to before. The stretched Hamiltonian H^t_{mho} may then be expressed as the sum of a spherically symmetric term, H_0 and two quadrupole coupling terms, H_1 and H_2, which arise from the potential and kinetic energy terms respectively. These may be written

$$H_0 = \frac{1}{2}\hbar\varpi_0(\epsilon,\gamma_\epsilon)\left\{-\nabla^2_\rho+\rho^2\right\} - \kappa\hbar\mathring{\omega}_0\left\{2\mathbf{l_t}\cdot\mathbf{s}+\mu\left(l^2_t-\langle l^2_t\rangle_{N_t}\right)\right\}$$

$$H_1 = -\frac{1}{2}\hbar\varpi_0(\epsilon,\gamma_\epsilon)\rho^2\frac{2}{3}\sqrt{\frac{4\pi}{5}}\epsilon\left\{\cos\gamma_\epsilon Y^t_{20}+\frac{1}{\sqrt{2}}\sin\gamma_\epsilon\left(Y^t_{22}+Y^t_{2-2}\right)\right\}$$

and

$$H_2 = -\frac{1}{2}\hbar\varpi_0(\epsilon,\gamma_\epsilon)\epsilon\left\{\frac{1}{3}\cos\gamma_\epsilon\left(\frac{\partial^2}{\partial\xi_1^2}+\frac{\partial^2}{\partial\xi_2^2}-2\frac{\partial^2}{\partial\xi_3^2}\right)+\frac{1}{\sqrt{3}}\sin\gamma_\epsilon\left(-\frac{\partial^2}{\partial\xi_1^2}+\frac{\partial^2}{\partial\xi_2^2}\right)\right\} \tag{6.46}$$

where ρ is the stretched radius vector. The index t denotes those quantities which are defined with respect to the stretched coordinate system in an exactly analogous manner to the similar quantities appearing in (6.44) which are defined in the unstretched coordinates. An exact mapping between the two coordinate systems would require that $\mathbf{l}$ transforms into $\mathbf{l_t}$ together with some deformation dependant residual terms. To first order in ϵ the magnitude of these residual corrections constitute only $\sim$ 10% of the strength of the quadrupole coupling terms

$H_1 + H_2$ and can therefore be neglected [10]. Further, in the presence of nuclear deformation the spin-orbit potential (6.36) no longer reduces to $\mathbf{l} \cdot \mathbf{s}$. The difference between the true spin-orbit coupling and the assumed $\mathbf{l} \cdot \mathbf{s}$ form is of the same order of magnitude as the difference between $\mathbf{l} \cdot \mathbf{s}$ and $\mathbf{l_t} \cdot \mathbf{s}$. Similarly it is questionable as to whether a spherically symmetric l^2 correction to the potential shape is still appropriate when the oscillator shape is itself deformed. Thus it appears that the effect of the residual correction terms is entirely within the range of ambiguity in the definition of the $\mathbf{l} \cdot \mathbf{s}$ and l^2 terms for the deformed nucleus.

The matrix elements of H_1 and H_2 in the stretched basis are such that [10]

$$\langle N_t|H_1 + H_2|N_t'\rangle = 2\langle N_t|H_1|N_t'\rangle\delta_{N_t,N_t'}. \tag{6.47}$$

Therefore within a given shell, H^t_{mho} has the same matrix elements in the stretched representation as H_{mho} (6.44) has in the unstretched representation apart from the change of deformation parameters. However, contrary to the unstretched case, the matrix elements of H^t_{mho} vanish identically between states belonging to different oscillator shells (provided only quadrupole deformations are considered), so that the basis for diagonalization is greatly reduced. There are however some disadvantages in the use of this representation.

The first of these has already been mentioned, namely that the spherical (i.e. unstretched) orbital angular momentum operators do not map exactly into the corresponding operators defined in the stretched space. As has been remarked this is not of great importance with regard to the largely empirical terms appearing in the modified oscillator potential. However when single particle angular momentum matrix elements are required, as for example in the case of the particle rotor Hamiltonian (6.82), appropriate corrections may be necessary. For small nuclear deformations these corrections are small and are usually neglected. Secondly, the stretched coordinates change with deformation. Thus wavefunctions at different deformations must be transformed into the unstretched basis if detailed comparisons are to be made.

Generally the Hamiltonians (6.44) or (6.46) must be diagonalized numerically. Here the basis chosen for this purpose are the coupled wavefunctions $|Njl\Omega\rangle$. The single particle wavefunctions χ_i are thus obtained as

$$\chi_i = \sum_{Njl\Omega} B^i_{Njl\Omega}|Njl\Omega\rangle. \tag{6.48}$$

However perturbative solutions are possible where the nuclear potential is close to either spherical or cylindrical symmetry. These will be enumerated for H^t_{mho}. Only the case of axial symmetry will be discussed so that j_3 commutes with the total Hamiltonian and consequently $\Omega = \Lambda + \Sigma$ is a good quantum number.

Consider first the case of small deformations using the coupled basis, $|Njl\Omega\rangle$. The index t will be dropped since the choice of coordinate system is obvious from the deformation parameter. The spherically symmetric sub-Hamiltonian H_0 (6.46) is diagonal in this representation with energy eigenvalues

$$E_0(N,j,l,\Omega) = \hbar\mathring{\varpi}\left\{N + \frac{3}{2} - \kappa\left[\Gamma + \mu\left(l(l+1) - \frac{1}{2}N(N+3)\right)\right]\right\} \tag{6.49}$$

where $\Gamma = l$ or $-(l+1)$ if $j = l + 1/2$ or $l - 1/2$ respectively. The $(2j+1)$-fold degeneracy in the j subshells is lifted by the quadrupole coupling terms, $H_1 + H_2 = 2H_1$, which gives a first order contribution

$$E_{1+2}(N,j,\Omega) = \frac{1}{6}\hbar\varpi_0\left\{N + \frac{3}{2}\right\}\epsilon\frac{3\Omega^2 - j(j+1)}{j(j+1)}. \tag{6.50}$$

These splittings are clearly seen in figure 7.1.

For increasing deformations the above method soon becomes inapplicable. At large deformations it is more appropriate to introduce a representation that exactly diagonalizes the harmonic oscillator field (6.38) and to treat the $\mathbf{l}\cdot\mathbf{s}$ and l^2 terms as perturbations. The representation in question is the cylindrical (asymptotic) basis, $|Nn_3\Lambda\Sigma\rangle$, in which (6.38) has the energy eigenvalues

$$E(N,n_3) = \hbar\varpi_0\left\{N + \frac{3}{2}\right\} + \frac{1}{3}\epsilon\hbar\varpi_0\left\{N - 3n_3\right\}. \tag{6.51}$$

The additional first order perturbative energies of the $\mathbf{l}\cdot\mathbf{s}$ and l^2 terms are

$$E_{\mathbf{l}\cdot\mathbf{s}+l^2}(N,n_3,\Lambda,\Sigma) = -\kappa\hbar\varpi_0\left\{2\Lambda\Sigma + \mu\left[\Lambda^2 + 2n_\perp n_3 + 2n_3 + n_\perp - \frac{1}{2}N(N+3)\right]\right\} \tag{6.52}$$

where $n_\perp = N - n_3$ is the number of oscillator quanta along the 1- and 2-axes. The effect of this perturbation is to lift the $2(n_\perp+1)$-fold degeneracy in Λ and Σ of the $n_\perp$ sublevels, leaving only the two-fold time reversal degeneracy.

At intermediate deformations the off-diagonal matrix elements are still sufficiently small that the asymptotic quantum numbers $[Nn_3\Lambda]\,\Omega$ remain essentially preserved and are generally used to label orbitals in nuclear spectroscopy, as in figures 7.1 and 7.3.

The approach to the asymptotic limit can be observed in figure 7.1 with a general trend towards the n_3 energy splittings of (6.50). At the intermediate deformations illustrated the perturbative effects (6.51) are best seen in the four $N = 3, n_3 = 0$ orbitals. These favour states of large Λ^2 with Λ and Σ parallel leading to the observed ordering.

In a γ deformed potential only the time reversal symmetry is generally preserved. Parity only remains as a good quantum number provided that no odd multipole deformations are introduced so that the even and odd oscillator shells remain uncoupled. (In the case of the modified harmonic oscillator potential N_t also remains good provided that quadrupole deformations are considered exclusively and even then only on the condition that the orbital angular momentum residual correction terms are neglected). There are no other exact or even approximately good quantum numbers to replace the asymptotic labels which are used in the axial limit. The single particle energies along a closed path in the (ϵ, γ) plane are illustrated in figure 7.3 in the vicinity of the third oscillator shell. The orbitals are labelled in the asymptotic notation $[Nn_3\Lambda]\,\Omega$ for prolate ($\gamma = 0$) and oblate ($\gamma = \pi/3$) shapes.

Finally, the relationship between the Bohr shape parametrization β, γ_β and the Nilsson parametrizations δ, γ_δ and $\epsilon, \gamma_\epsilon$ will be discussed. Qualitatively all three pairs are similar and lead to the same physical effects. The correspondence between the two sets of Nilsson parameters can be obtained from a comparison of (6.39) and (6.45) [12]. As can be seen from (6.44) and (6.46) the oscillator equipotentials in these parametrizations are

$$r^2 \propto \left\{1 - \frac{4}{3}\sqrt{\frac{4\pi}{5}}\delta\left(\cos\gamma_\delta Y_{20} + \frac{1}{\sqrt{2}}\sin\gamma_\delta\,[Y_{22} + Y_{2-2}]\right)\right\}^{-1} \tag{6.53}$$

with a similar form for the stretched system. This is contrary to the formalism of the previous sections where the radius vectors of the nuclear equipotentials are given by (6.1)

$$r \propto \left\{1 + \beta\left(\cos\beta_\delta Y_{20} + \frac{1}{\sqrt{2}}\sin\gamma_\beta\,[Y_{22} + Y_{2-2}]\right)\right\}. \tag{6.54}$$

The relationship between the Bohr and Nilsson parametrizations follows by equating (6.53) and (6.54). An exact mapping requires the admixture of higher multipole deformations [13]. These have been neglected thus far, although the generalization of the single particle Hamiltonian to include higher orders of deformation is straight forward [14]. In practice an empirical correspondence between the quadrupole Bohr and Nilsson parametrizations is achieved by requiring that both correspond to the same macroscopic electric quadrupole moment [15].

6.3.2 The pairing interaction

In addition to the average one-body shell model potential there acts a relatively short range residual force between the nucleons which energetically favours states in which the nucleons are pairwise coupled to states of zero total angular momentum. This residual two-body force is simulated by the pairing interaction H^G which is characterized by having non-vanishing matrix elements of constant magnitude, $-G$, for time conjugate pairs of states $(i, \bar{i})$ and $(i', \bar{i}')$.

If a_i^+ is the creation operator of single particle state $|i\rangle$, then

$$H^G = -GF^+F \tag{6.55}$$

where $F^+ = \sum_i a_i^+ a_{\bar{i}}^+$ and the summation does not extend to the time reversed states $|\bar{i}\rangle$. The single particle creation operators are related to the creation operators $b_{Nj\Omega}^+$ of the coupled basis states by the second quantized analogue of (6.48)

$$a_i^+ = \sum_{Nj\Omega} B_{Nj\Omega}^i b_{Nj\Omega}^+ \tag{6.56}$$

while the creation operator of the corresponding time reversed state is (6.78)

$$a_{\bar{i}}^+ = \sum_{Nj\Omega} (-1)^{j-\Omega} B_{Nj\Omega}^i b_{Nj-\Omega}^+. \tag{6.57}$$

The pairing Hamiltonian may be rewritten as

$$\begin{aligned} H^G &= -G(F^+ - \langle F^+\rangle + \langle F^+\rangle)(F - \langle F\rangle + \langle F\rangle) \\ &= -G\langle F^+\rangle(F^+ + F) - G(F^+ - \langle F^+\rangle)(F - \langle F^+\rangle) + G\langle F^+\rangle^2 \end{aligned} \tag{6.58}$$

using the fact that $\langle F^+\rangle = \langle F\rangle$ for a BCS wavefunction. Assuming that the second term is small and can be neglected leads to the linearized Hamiltonian

$$H^\Delta = -\Delta(F^+ + F) + \frac{\Delta^2}{G} \tag{6.59}$$

where

$$\Delta = G\langle F^+\rangle. \tag{6.60}$$

The pair field Hamiltonian H^Δ is an approximation of the full pairing Hamiltonian H^G and describes the emission or absorption of a pair of particles. Although much simplified H^Δ fails to commute with the particle number operator $\hat{N} = \sum_i (a_i^+ a_i + a_{\bar{i}}^+ a_{\bar{i}})$. As a result the associated

wavefunction contains components with different numbers of particles. It is therefore necessary to diagonalize the combined single particle one-body and pair field Hamiltonian

$$H(\Delta) = \sum_i e_i(a_i^+ a_i + a_{\bar{i}}^+ a_{\bar{i}}) - \Delta \sum_i (a_i^+ a_{\bar{i}}^+ + a_{\bar{i}} a_i) - \lambda \hat{N} \tag{6.61}$$

where e_i represents the energy eigenvalues of the one-body Hamiltonian. The Lagrange multiplier λ ensures that the average particle number is correct. If the resulting eigenvector with lowest energy is $|\Upsilon_\Delta\rangle$ then it must be required to satisfy the subsidiary conditions

$$G\langle\Upsilon_\Delta|F^+|\Upsilon_\Delta\rangle = \Delta \tag{6.62}$$

and

$$\langle\Upsilon_\Delta|\hat{N}|\Upsilon_\Delta\rangle = n \tag{6.63}$$

where n is the number of particles. Performing the unitary transformation to the quasiparticle operators α^+ and α [16]

$$\begin{aligned} a_i^+ &= U_i\alpha_i^+ + V_i\alpha_{\bar{i}} \qquad & a_{\bar{i}}^+ &= U_i\alpha_{\bar{i}}^+ - V_i\alpha_i \\ a_i &= U_i\alpha_i + V_i\alpha_{\bar{i}}^+ \qquad & a_{\bar{i}} &= U_i\alpha_{\bar{i}} - V_i\alpha_i^+ \end{aligned} \tag{6.64}$$

(where the canonical nature of the transform requires that $U_i^2 + V_i^2 = 1$) leads to the Hamiltonian

$$\begin{aligned} H(\Delta) = \quad & \sum_i \left\{2V_i^2(e_i - \lambda) - 2\Delta U_i V_i\right\} + \frac{\Delta^2}{G} \\ & + \sum_i \left\{(U_i^2 - V_i^2)(e_i - \lambda) + 2\Delta U_i V_i\right\} \left\{\alpha_i^+\alpha_i + \alpha_{\bar{i}}^+\alpha_{\bar{i}}\right\} \\ & + \sum_i \left\{2U_i V_i(e_i - \lambda) - \Delta(U_i^2 - V_i^2\right\} \left\{\alpha_i^+\alpha_{\bar{i}}^+ + \alpha_i\alpha_{\bar{i}}\right\}. \end{aligned} \tag{6.65}$$

With a suitable choice of U_i and V_i, namely

$$\left\{\begin{matrix} U_i \\ V_i \end{matrix}\right\} = \sqrt{\frac{1}{2}\left\{1 \pm \frac{e_i - \lambda}{\sqrt{(e_i - \lambda)^2 + \Delta^2}}\right\}} \tag{6.66}$$

the last term in (6.65) can be made to disappear so that the Hamiltonian becomes diagonal in the quasiparticle representation. Thus, using (6.66)

$$\begin{aligned} H(\Delta) = \quad & \sum_i \left\{2V_i^2(e_i - \lambda) - 2\Delta U_i V_i\right\} + \frac{\Delta^2}{G} \\ & + \sum_i E_i \left\{\alpha_i^+\alpha_i + \alpha_{\bar{i}}^+\alpha_{\bar{i}}\right\} \end{aligned} \tag{6.67}$$

where the quasiparticle energy $E_i = \sqrt{(e_i - \lambda)^2 + \Delta^2}$ has been introduced. Since $E_i > 0$, it is clear that the lowest energy state of this Hamiltonian, $|\Upsilon_\Delta\rangle$, must be the quasiparticle vacuum defined by $\alpha_i|\Upsilon_\Delta\rangle = \alpha_{\bar{i}}|\Upsilon_\Delta\rangle = 0$. Such a state may be constructed as

$$|\Upsilon_\Delta\rangle \propto \prod_i \alpha_i \alpha_{\bar{i}}|0\rangle \tag{6.68}$$

where $|0\rangle$ is the particle vacuum state, $a_i|0\rangle = 0$. When expressed in terms of ordinary particle operators, $|\Upsilon_\Delta\rangle$ reduces to the BCS wavefunction

$$|\Upsilon_\Delta\rangle \propto \prod_i (U_i + V_i a_i^+ a_{\bar{i}}^+|0\rangle. \tag{6.69}$$

The constraints (6.62) and (6.63) can now be solved to give

$$\Delta = G\sum_i U_i V_i \qquad n = 2\sum_i V_i^2 \tag{6.70}$$

from which the Fermi level λ and the pairing gap Δ can be obtained. With the introduction of (6.70) the total single particle Hamiltonian is given as

$$H(\Delta) = 2\sum_i V_i^2(e_i - \lambda) - \frac{\Delta^2}{G} + \sum_i E_i \left\{\alpha_i^+\alpha_i + \alpha_{\bar{i}}^+\alpha_{\bar{i}}\right\}. \tag{6.71}$$

The first two terms of this expression represent the constant energy of the quasiparticle vacuum, the former part denoting the single-particle energy while the latter gives the correlation due to the pairing interaction. The third term is the multi-quasiparticle excitation energy. In particular the energy of a 1-qp excitation $|i\rangle$ measured relative to the quasiparticle vacuum is just E_i, so that Δ is seen to represent odd-even mass difference.

Finally, quasiparticle matrix elements can be obtained by a transformation of the operators from the particle variables a^+, a to the quasiparticle variables α^+, α. Thus the one particle operator F may be expressed as

$$\begin{aligned} F = & \sum_{i_1 i_2}\langle i_2|F|i_1\rangle a^+(i_2)a(i_1) \\ = & \sum_{i>0}(1-c)V_i^2\langle i|F|i\rangle \\ & + \sum_{i_1 i_2}(U_1U_2 + cV_1V_2)\langle i_2|F|i_1\rangle\alpha^+(i_2)\alpha(i_1) \\ & + \sum_{i_1<i_2}(V_1U_2 - cU_1V_2)\left\{\langle i_2|F|\bar{i_1}\rangle\alpha^+(i_2)\alpha^+(i_1) + \langle\bar{i_1}|F|i_2\rangle\alpha(i_1)\alpha(i_2)\right\}. \end{aligned} \tag{6.72}$$

The factor c is the dichotomous quantum number of the particle-hole conjugation operator acting on F

$$\langle \overline{i_1}|F|\overline{i_2}\rangle = -c\langle i_2|F|i_1\rangle \tag{6.73}$$

which has the value $c = 1$ for magnetic operators and $c = -1$ for electric operators. In particular the matrix elements of the magnetic operators j_k between single ($v = 1$) quasiparticle states are

$$\langle v = 1; i_2|j_k|v = 1; i_1\rangle = (U_1U_2 + V_1V_2)\langle i_2|j_k|i_1\rangle. \tag{6.74}$$

The matrix elements of j_k^2 can be calculated by inserting a complete set of v-qp intermediate states $|v;\varsigma\rangle$, thus

$$\langle v = 1; i_2|j_k^2|v = 1; i_1\rangle = \sum_{v\varsigma}\langle v = 1; i_2|j_k|v;\varsigma\rangle\langle v;\varsigma|j_k|v = 1; i_1\rangle. \tag{6.75}$$

From (6.72) it can be seen that the matrix elements of j_k^2 are linked by both 1- and 3-qp intermediate states. The resulting expression is rather complicated [17] and in the following sections it will be assumed that the matrix elements can be approximated by an expression of a similar form to (6.74).

To conclude, the effects of the pairing interaction can be incorporated into the one-body Hamiltonian by replacing the single particle energies e_i by the corresponding single quasiparticle energies E_i and by introducing the appropriately transformed single particle operators into the subsequent calculations.

6.3.3 The strong coupling basis

Having derived the deformed single particle solutions it is now possible to diagonalize the total Hamiltonian (6.27) of the odd mass system. This may be performed in either the *weak* or *strong* coupling bases. The former are discussed in section 6.7. However, as has been pointed out in section (6.3), when dealing with particle-(rigid) rotor Hamiltonian it is convenient to use the strong coupling basis so that the matrix calculation may be performed entirely in the intrinsic frame. Neglecting for the moment pairing, the unsymmetrized strong coupling basis states may be written

$$|IMKi\rangle = \sqrt{\frac{2I+1}{8\pi^2}}D^I_{MK}\chi_i \tag{6.76}$$

where M and K are the projections of the total angular momentum (both core and single particle) onto the laboratory and intrinsic axes respectively and χ_i is the single particle wavefunction (6.48). Being expressed in the intrinsic frame this wavefunction is subject to the symmetry requirements (6.14). The action of the $\hat{R}_k$ operators on the rotation matrices has already been given in (6.15), while the behavior of the χ_i may be deduced by converting from the intrinsic to laboratory axes. Thus

$$\begin{aligned}\hat{R}_1|Njl\Omega\rangle &= \hat{R}_1 \sum_{\mu} D^{j*}_{\mu\Omega}|Njl\mu\rangle' \\ &= \sum_{\mu} \exp^{-i\pi(j-\Omega)} D^{j*}_{\mu-\Omega}|Njl\mu\rangle' \\ &= (-1)^{-(j-\Omega)}|Njl-\Omega\rangle\end{aligned} \tag{6.77}$$

where the prime denotes the wavefunction referred to the laboratory axes which are invariant under the $\hat{R}$ operations. Hence

$$\hat{R}_1\chi_i = \chi_{\bar{i}} = \sum_{Njl\Omega} (-)^{j-\Omega} B^i_{Njl\Omega}|Njl-\Omega\rangle. \tag{6.78}$$

Similarly

$$\hat{R}_2|Njl\Omega\rangle = \exp^{-i\pi\Omega/2}|Njl\Omega\rangle. \tag{6.79}$$

Therefore the symmetrized strong coupling basis wavefunction may be written

$$|IMKi\rangle = \sqrt{\frac{2I+1}{16\pi^2}} \sum_{Njl\Omega} B^i_{Njl\Omega} \left\{D^I_{MK}|Njl\Omega\rangle + (-1)^{I-j} D^I_{M-K}|Njl-\Omega\rangle\right\} \tag{6.80}$$

with $K-\Omega$ restricted to even values. These can be chosen such that both K and Ω take only the values $\cdots -3/2, 1/2, 5/2 \cdots$

In a paired system the corresponding strong coupling basis states are

$$|IMKi\rangle = \sqrt{\frac{2I+1}{16\pi^2}} \left\{D^I_{MK}\alpha^+_i + (-1)^{I-K} D^I_{M-K}\alpha^+_{\bar{i}}\right\}|BCS\rangle \tag{6.81}$$

where $|BCS\rangle$ denotes the quasiparticle vacuum state (6.68).

6.3.4 The particle rotor model

The particle-rotor Hamiltonian, written in a suitable form for the strong coupling basis, has already been introduced in section 6.3. With the inclusion of pairing and after some rearrangement the Hamiltonian (6.33) becomes

$$\begin{aligned} H = \; & \frac{1}{4}\left\{\frac{1}{\Im_1}+\frac{1}{\Im_2}\right\}\left\{I^2 - I_3^2 + j^2 - j_3^2 - (I_+ j_- + I_- j_+)\right\} \\ & + \frac{1}{8}\left\{\frac{1}{\Im_1}-\frac{1}{\Im_2}\right\}\left\{I_+^2 + I_-^2 + j_+^2 + j_-^2 - 2(I_+ j_+ + I_- j_-)\right\} \\ & + \frac{1}{2\Im_3}\left\{I_3 - j_3\right\}^2 + \sum_i E_i \alpha_i^+ \alpha_i \end{aligned} \tag{6.82}$$

where in the last term the constant energy of the quasiparticle vacuum has been neglected. Onto all single quasiparticle angular momentum operators must be attached the pairing factor $U_i U_{i'} + V_i V_{i'}$ of (6.74). The special nature of the recoil terms j_k^2 is therefore ignored. Since all other operators are diagonal in the single particle space and $U_i^2 + V_i^2 = 1$, this can be achieved by multiplying the entire Hamiltonian matrix element by the appropriate pairing factor. The moments of inertia $\Im_k$ are taken to be of the form (6.20). The total angular momentum operators I_k being defined with respect to the intrinsic axes upon which they themselves operate do not follow the usual angular momentum commutation rules but instead, as is also the case in the even-even rotor, follow those of (A.2). The required matrix elements for this Hamiltonian are given explicitly by Larsson *et al.* [18].

In order to clarify some of the properties of the particle-rotor Hamiltonian it will be assumed that axial symmetry is preserved so that Ω is a good quantum number. Further, in the necessary absence of any collective motion along this axis, $K = \Omega$. The Hamiltonian therefore reduces to

$$\begin{aligned} H &= \frac{1}{2\Im}\left\{I^2 - 2\mathbf{I}\cdot\mathbf{j} + j^2\right\} + \sum_i E_i \alpha_i^+ \alpha_i \\ &= \frac{1}{2\Im}\left\{I^2 - I_3^2 + j^2 - j_3^2 - (I_+ j_- + I_- j_+)\right\} + \sum_i E_i \alpha_i^+ \alpha_i . \end{aligned} \tag{6.83}$$

The nature of the resulting band structure depends on the relative influences of the particle-core coupling and the Coriolis force, $\mathbf{I}\cdot\mathbf{j}$.

Consider first the *decoupling* limit in which the coupling of the odd particle to the quadrupole deformation of the core is broken by the Coriolis force which acts to align the intrinsic and core spins along a common axis. To illustrate this it will be assumed that the single particle occupies a pure subshell of angular momentum j whose component ζ on the collective rotation axis is approximately a good quantum number. The single particle wavefunction (6.48) can then be projected onto the nuclear symmetry axis, thus

$$\chi_i = |j\zeta\rangle = \sum_{\Omega} d^j_{\zeta\Omega}(\pi/2)|j\Omega\rangle. \tag{6.84}$$

Naturally this expansion is such that most of amplitude resides in the lowest Ω orbitals, decreasing monotonically as Ω increases. With these assumptions the strong coupled basis (6.80) becomes

$$\begin{aligned} |IMj\zeta\rangle &= \sqrt{\frac{2I+1}{16\pi^2}} \sum_{\Omega} d^j_{\zeta\Omega}(\pi/2) \left\{ D^I_{M\Omega}|j\Omega\rangle + (-1)^{I-j} D^I_{M-\Omega}|j-\Omega\rangle \right\} \\ &= \sqrt{\frac{2I+1}{16\pi^2}} \sum_{\Omega} d^j_{\zeta\Omega}(\pi/2) D^I_{M\Omega}|j\Omega\rangle \left\{ 1 + (-1)^{I-\zeta} \right\} \end{aligned} \tag{6.85}$$

where the phase $d^j_{\zeta\Omega}(\pi/2) = (-1)^{j-\zeta} d^j_{\zeta-\Omega}(\pi/2)$ has been used. Provided that $I \gg \Omega$ this state behaves as an approximate eigenfunction of (6.83) with the corresponding eigenvalue [19]

$$E(I,j,\zeta) = \sum_{\Omega} d^j_{\zeta\Omega}(\pi/2) e_{\Omega} + \frac{\hbar^2}{2\Im} \{ I(I+1) - 2I\zeta + j(j+1) \} \tag{6.86}$$

where the single particle energies e_{Ω} are given to first order by (6.50). Clearly the rotational energy is minimized when $\zeta = j$, since then full alignment of the intrinsic and collective spins is achieved and hence the Coriolis force is maximal. The symmetrization of the wavefunction (6.85) implies that the resulting *decoupled* band structure contains only the spins $I = j, j \pm 2, j \pm 4, \cdots$ with relative energies

$$\begin{aligned} E &= \frac{\hbar^2}{2\Im} \{ I(I+1) - 2Ij + j(j+1) \} \\ &= \frac{\hbar^2}{2\Im} R(R+1) \end{aligned} \tag{6.87}$$

where $R = I - j$. Thus the rotational spectrum of this *favoured* band follows that of the even-even core. For a lesser degree of alignment, $\zeta = j - 1$, the strength of the Coriolis force is reduced and so one obtains a higher lying *unfavoured* band with spins $I = j \pm 1, j \pm 3, \cdots$

For this coupling scheme to be fully realized the Coriolis force must dominate the particle-core quadrupole coupling. The former term depends on both the magnitude and direction of j. For the required alignment of j it is necessary to be able to spread the single particle amplitude over the entire subshell, with the low spin $\Omega = 1/2$ states dominating. The energy required to affect this distribution is represented by the first term in (6.86) and is intimately connected with the quadrupole coupling strength which to first order increases linearly with deformation. Therefore the decoupling scheme is only favourable for a single odd particle lying in a low-Ω orbital of a high-j shell interacting with a weakly deformed core.

As the core deformation increases and hence also the energy splittings of the Ω substates, the Coriolis force becomes gradually less significant and reduces to the status of a small perturbation. The matrix elements $I_+j_- + I_-j_+$ representing the Coriolis force in (6.83) link only states differing by one unit in K and Ω, so that to first order these are only none zero between states of $\Omega = 1/2$. Thus in this adiabatic approximation the intrinsic orbitals remain unmixed and the single particle becomes *strongly* coupled to the deformation of the core, its angular momentum precessing about the symmetry axis with constant projection. The excitation energy eigenvalues of the rotational band are then given as

$$E(I,K) = e + \frac{\hbar^2}{2\Im}\left\{I(I+1) - K^2 + \delta_{K,\frac{1}{2}}a(-1)^{I+\frac{1}{2}}\left(I+\frac{1}{2}\right)\right\} \tag{6.88}$$

where the purely intrinsic recoil terms j^2 and j_3^2 have been included into the single particle energy e since they are constant for a given band.

Unlike the decoupled case there are no symmetry selection rules on the total spin so that each rotational band exhibits the spins $I = K, K+1\cdots$ For $\Omega \neq 1/2$ the rotational levels follow the $I(I+1)$ energy dependence characteristic of a *strongly* coupled band.

Orbitals with spin projections $\Omega = 1/2$ are also subject to the Coriolis force since there is necessarily some spin alignment along the axis of core rotation. This additional interaction is represented by the last term in (6.88). Its strength is determined by the decoupling parameter a, given by

$$a = \langle\chi_i|j_+|\chi_{\bar{i}}\rangle = \langle\chi_{\bar{i}}|j_-|\chi_i\rangle. \tag{6.89}$$

The spin dependent phase factor in this term leads to a signature splitting between the $I = K, K+2, \cdots$ and $I = K+1, K+3, \cdots$ band members, reminiscent of the decoupled limit.

The exact nature of the particle-rotor band structure is illustrated in figure 6.2 for the case an odd $g_{9/2}$ nucleon with the Fermi level placed on the lowest Nilsson level.

Close to sphericity and centered on the core energies, the nearly degenerate multiplets of the weak coupling scheme are apparent. However as a result of the deformation dependence of the moment of inertia (6.12), at such deformations these energies are sufficiently large that it is doubtful that any collective model should apply. Thus in the present context it is not clear that the weak coupling of the odd particle to collective rotational states will be valid anywhere. As the nuclear deformation and hence the moment of inertia increases, the rotational energy decreases below the quasiparticle excitation energies and so the collective rotational model becomes applicable.

For deformed prolate shapes ($\gamma = 0$) the Fermi level lies on the $\Omega = 1/2$ orbital giving rise to a decoupled band structure. The unfavoured decoupled band $I = 11/2, 15/2, \cdots$ (parallel alignment) and $I = 7/2, 3/2$ (antiparallel alignment) lies high above the favoured $I = 9/2, 13/2, \cdots$ (parallel) and $I = 9/2, 5/2, 1/2$ (antiparallel) band. As the deformation increases the Nilsson levels diverge. Correspondingly the energy of unfavoured band, which due to its lesser alignment with the core rotation is built upon higher lying orbitals, shifts upwards. Also the alignment of the odd particle in the favoured band shifts towards the nuclear symmetry axis. With this tendency towards strong coupling there is a reduction in the staggering of the band causing the 5/2 level to become the band head. The extent to which this staggering can be removed at large deformations is determined by the decoupling parameter a.

On the oblate side ($\gamma = \pi/3$) the single particle angular momentum is fully aligned along the axis of nuclear symmetry. This gives rise to a strongly coupled $I = 9/2, 11/2, 13/2 \cdots$ band structure. Here the decoupled limit is never realized, even at small deformations, since the ζ population is always inverted relative to the required $d^j_{\Omega\zeta}(\pi/2)$ distribution. (Notice that the roles of ζ and Ω have been reversed with respect to previous discussions. This is as a result of the shape parametrization, which for $\gamma = \pi/3$ leads to the reversal of the axes of nuclear symmetry and collective rotation compared to the case $\gamma = 0$).

The two types of alignment are connected via the γ degree of freedom which gradually transforms the alignment of the single particle spin from the axis of collective rotation ($\gamma = 0$) to the axis of nuclear symmetry ($\gamma = \pi/3$). As a result the favoured-unfavoured signature splitting is seen to reduce to zero.

6.3.5 Electromagnetic moments and transition probabilities

The electromagnetic M1 and E2 multipole operators are given in the laboratory frame by the expressions

$$\begin{aligned} M(\mathrm{M1};\mu) &= \mu_N \sqrt{\frac{3}{4\pi}} \{g_R I_\mu + (g_l - g_R) j_\mu + (g_s - g_l) s_\mu\} \\ M(\mathrm{E2};\mu) &= \sum_i \delta_p e r_i^2 Y_{2\mu}(\vartheta_i, \varphi_i) \end{aligned} \tag{6.90}$$

where $\delta_p = 1$ for protons and 0 for neutrons. Here the total contribution to the electric quadrupole operator is calculated microscopically by summing contributions from the individual proton orbitals i up to the Fermi level. In practice this is often separated into a contribution

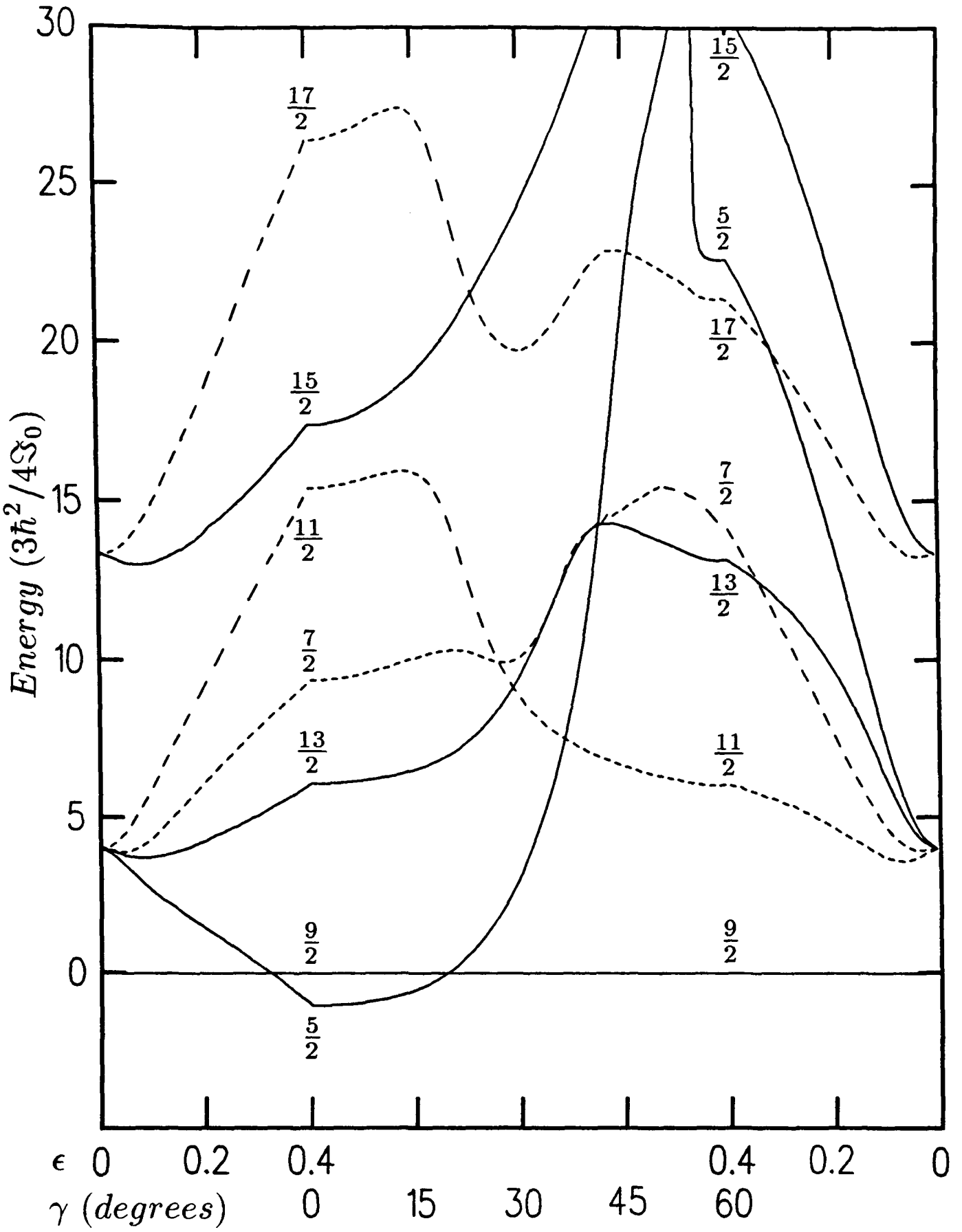

Figure 6.2. The deformation dependence of the particle-rotor band structure in the (ϵ, γ) plane for an odd $g_{9/2}$ nucleon. The solid and dashed lines distinguish the two signatures.

arising from the single odd nucleon, together with a term corresponding to the macroscopic quadrupole moment of the core expressed in terms of the surface variables α

For the present Hamiltonian these operators must be expressed in the intrinsic frame of reference using the transformation

$$M(\lambda\mu) = \sum_{\nu} D^{\lambda}_{\mu\nu} M(\lambda\nu) \tag{6.91}$$

which leads to the operators

$$\begin{aligned} M(\mathrm{M1};\mu) &= \mu_N \sqrt{\frac{3}{4\pi}} \sum_{\nu} D^{1}_{\mu\nu} \left\{ g_R I_\nu + (g_l - g_R) j_\nu + (g_s - g_l) s_\nu \right\} \\ M(\mathrm{E2};\mu) &= \sum_{\nu} \delta_p e D^{2}_{\mu\nu} r^2 Y_{2\nu} + \frac{3}{4\pi} Z R_0^2 e\beta \left\{ D^{2}_{\mu 0} \cos\gamma + \frac{1}{\sqrt{2}} \left(D^{2}_{\mu 2} + D^{2}_{\mu -2} \sin\gamma \right) \right\}. \end{aligned} \tag{6.92}$$

In this case $M(\mathrm{E2})$ is expressed in terms of the macroscopic quadrupole moment of the core, written here to first oder in the β, γ coordinates. A similar expression holds for the two Nilsson parametrizations with, again to first order, β replaced by $\frac{2}{3}\sqrt{\frac{4\pi}{5}}\left\{\begin{smallmatrix}\epsilon\\ \delta\end{smallmatrix}\right\}$[15].

The effects of pairing are included by attaching onto each term arising from to the single odd particle the factors $U_i U_{i'} + V_i V_{i'}$ or $U_i U_{i'} - V_i V_{i'}$ for magnetic and electric terms respectively.

From these operators can be calculated the reduced electromagnetic transition probabilities $B(\pi\lambda, I_i \rightarrow I_f)$, defined by

$$B(\pi\lambda, I_i \rightarrow I_f) = \frac{1}{2I_i + 1} |\langle I_f || M(\pi\lambda) || I_i \rangle|^2$$

and also the static moments defined by

$$\begin{aligned} \mu_I &= (II10|II)\sqrt{\frac{4\pi}{3}} \langle I || M(M1) || I \rangle \\ eQ_I &= (II20|II)\sqrt{\frac{16\pi}{5}} \langle I || M(E2) || I \rangle. \end{aligned} \tag{6.93}$$

Finally, with the magnetic and electric reduced matrix elements expressed in units of μ_N and eb respectively, the E2/M1 mixing ratio is given by

$$\delta = \sqrt{0.7} E_{if} \frac{\langle I || M(E2) || I \rangle}{\langle I || M(M1) || I \rangle} \tag{6.94}$$

where E_{if} is the energy of the transition in MeV.

6.4 The unified model of odd-odd nuclei

Following on from the Hamiltonian (6.27) of the odd mass system, that of an odd-odd nucleus must treat explicitly the coupling of (at least) two quasiparticles to the collective core. Hence

$$H = H_{core}(\alpha) + \{H_{part}(\overline{\alpha}) + H_{int}(\alpha)\}^{p,n} + V_{pn} \tag{6.95}$$

where the terms in braces are taken twice, once for the odd proton and once for the odd neutron. The residual proton-neutron interaction is represented by the term V_{pn}. Only the particle-rotor limit of this Hamiltonian will be considered.

As before the unsymmetrized strong coupled basis states may be written

$$|IMKpn\rangle = \sqrt{\frac{2I+1}{8\pi^2}} D^I_{MK} \chi_{pn}. \tag{6.96}$$

The intrinsic wavefunction χ_{pn} comprises two distinct product states, $\chi_{pn} = |p\rangle|n\rangle$ and $|p\rangle|\overline{n}\rangle$. In the case of axial symmetry these two products correspond to $K = \Omega_p + \Omega_n$ and $K = \Omega_p - \Omega_n$ respectively. With the same restrictions on Ω as in the odd mass case it is clear that K is even (odd) if the intrinsic product state does (does not) contain the conjugate neutron orbital. This is true even when axial symmetry is violated. The two fully symmetrized strong coupled wavefunctions in the quasiparticle representation are therefore

$$|IMKpn\rangle = \sqrt{\frac{2I+1}{16\pi^2}} \left\{ D^I_{MK} \alpha^+_p \alpha^+_n + (-1)^{I+1} D^I_{M-K} \alpha^+_{\overline{p}} \alpha^+_{\overline{n}} \right\} |BCS\rangle \tag{6.97}$$

for $K = \pm 1, \pm 3, \ldots, \pm(I-1)$ or $\pm I$ and

$$|IMKp\overline{n}\rangle = \sqrt{\frac{2I+1}{16\pi^2}} \left\{ D^I_{MK} \alpha^+_p \alpha^+_{\overline{n}} + (-1)^{I+1} D^I_{M-K} \alpha^+_{\overline{p}} \alpha^+_n \right\} |BCS\rangle \tag{6.98}$$

for $K = \pm 0, \pm 2, \ldots, \pm(I-1)$ or $\pm I$. The phase factor of (6.98) incorporates the fact that for Fermions $\alpha^+_{\overline{n}} = -\alpha^+_n$ (6.57). With the core spin written as $\mathbf{R} = \mathbf{I} - \mathbf{j_p} - \mathbf{j_n}$, the particle-rotor Hamiltonian becomes [20]

$$\begin{aligned} H = \; & \frac{1}{4}\left\{\frac{1}{\Im_1} + \frac{1}{\Im_2}\right\}\{I^2 - I_3^2 + j_p^2 - j_{3p}^2 + j_n^2 - j_{3n}^2 + j_{+p}j_{-n} + j_{-p}j_{+n} \\ & \qquad - I_+(j_{-p} + j_{-n}) + I_-(j_{+p} + j_{+n})\} \\ & + \frac{1}{8}\left\{\frac{1}{\Im_1} - \frac{1}{\Im_2}\right\}\{I_+^2 + I_-^2 + j_{+p}^2 + j_{-p}^2 + j_{+n}^2 + j_{-n}^2 + 2(j_{+p}j_{+n} + j_{-p}j_{-n}) \\ & \qquad - 2I_+(j_{+p} + j_{+n}) - 2I_-(j_{-p} + j_{-n})\} \\ & + \frac{1}{2\Im_3}\{I_3 - j_{3p} - j_{3n}\}^2 + \sum_p E_p \alpha^+_p \alpha_p + \sum_n E_n \alpha^+_n \alpha_n + V_{pn}. \end{aligned} \tag{6.99}$$

It then remains to multiply onto both the proton and neutron single particle angular momentum operators the appropriate pairing factor, $U_iU_{i'} + V_iV_{i'}$.

As with the odd A case, the resulting band structure depends on the orientation of the two single particle spins relative to the collective rotation. Where the position of the proton and neutron Fermi levels favours the alignment of both odd particles along either the nuclear symmetry or the collective rotation axes, then the respective strongly coupled and decoupled bands occur of a nature directly analogous to the odd A spectra discussed previously. In addition there is now the possibility that the two particles exhibit conflicting alignments leading to a rather more complex band structure. The nature of these extreme strongly coupled, decoupled and conflicting cases have been expounded by Kreiner [21] and Toki *et al.* [22].

For the residual proton-neutron interaction V_{pn} a phenomenological force of the type considered by Boisson *et al.* [23] is assumed. This can be written

$$V_{pn} = V(r)\{u_o + u_1\sigma_{\mathbf{p}}\cdot\sigma_{\mathbf{n}} + u_2P_m + u_3\sigma_{\mathbf{p}}\cdot\sigma_{\mathbf{n}}P_m + V_TS_{12} + V_{TM}S_{12}P_m\} \tag{6.100}$$

where P_m is the space exchange operator, σ is a Pauli spin matrix and S_{12} is the tensor force

$$S_{12} = \frac{(\sigma_{\mathbf{p}}\cdot\mathbf{r})(\sigma_{\mathbf{n}}\cdot\mathbf{r})}{r^2} - \frac{1}{3}(\sigma_{\mathbf{p}}\cdot\sigma_{\mathbf{n}}). \tag{6.101}$$

The strengths of these various terms are characterized by the parameters u_o, u_1, u_2, u_3, V_T and V_{TM} and have been determined in the rare earth region by Boisson *et al.* The radial dependence $V(r)$ is taken to be of the dual range Gaussian form

$$V(r) = \exp^{-r^2/r_S^2} + \alpha_L \exp^{-r^2/r_L^2} \tag{6.102}$$

where r_S and r_L denote the short and long ranges and α_L expresses the proportion of the long range component present. In the special case of a zero range force (6.100) reduces to

$$V_{pn} = -4\pi W_1\left[\frac{\pi}{\sqrt{2}}\left(\frac{\hbar}{m\varpi_0}\right)^3\right]^{\frac{1}{2}}\{(1-W_0) + W_0\sigma_{\mathbf{p}}\cdot\sigma_{\mathbf{n}}\} \tag{6.103}$$

with just two parameters W_0 and W_1.

The transformation of the residual proton-neutron interaction to the quasiparticle representation is achieved by the methods of (6.72). The required matrix elements of V_{pn} in the strong coupling basis are then

$$\begin{aligned}\langle IMK'p'n'|V_{pn}|IMKpn\rangle = \delta_{K',K}\,\{A\langle p'n'|V_{pn}|pn\rangle - B\langle p'\overline{n}|V_{pn}|p\overline{n}'\rangle\}\\ + (-1)^{I+1}\delta_{K',-K}\,\{A\langle\overline{p}'\,\overline{n}'|V_{pn}|pn\rangle + B\langle\overline{pn}'|V_{pn}|p'n\rangle\}\end{aligned} \tag{6.104}$$

for K odd and

$$\begin{aligned}\langle IMK'p'\overline{n}'|V_{pn}|IMKp\overline{n}\rangle = \delta_{K',K}\,\{A\langle p'\overline{n}'|V_{pn}|p\overline{n}\rangle - B\langle p'n|V_{pn}|pn'\rangle\}\\ + (-1)^{I+1}\delta_{K',-K}\,\{A\langle\overline{p}'n'|V_{pn}|p\overline{n}\rangle + B\langle\overline{p}n'|V_{pn}|p'\overline{n}\rangle\}\end{aligned} \tag{6.105}$$

for K even, where A and B are the pairing factors

$$\begin{aligned}A &= U_{p'}U_pU_{n'}U_n + V_{p'}V_pV_{n'}V_n\\ B &= U_{p'}U_pV_{n'}V_n + V_{p'}V_pU_{n'}U_n.\end{aligned} \tag{6.106}$$

From those terms in V_{pn} which have negative parity under particle hole conjugation ($c = -1$) contributions from (6.72) involving sums over all occupied proton and neutron orbital are also obtained. They represent the quasiparticle *condensate* expectation value of the operator and are therefore discarded.

The main features of the residual proton-neutron interaction can be illustrated by considering only the diagonal matrix elements of V_{pn}. Thus for odd K

$$\langle IMKpn|V_{pn}|IMKpn\rangle = \{A\langle pn|V_{pn}|pn\rangle - B\langle p\overline{n}|V_{pn}|p\overline{n}\rangle\} \tag{6.107}$$

and for even K

$$\begin{aligned}\langle IMKp\overline{n}|V_{pn}|IMKp\overline{n}\rangle = \{A\langle p\overline{n}|V_{pn}|p\overline{n}\rangle - B\langle pn|V_{pn}|pn\rangle\}\\ + (-1)^{I+1}\delta_{K,0}(A+B)\langle\overline{p}n|V_{pn}|p\overline{n}\rangle.\end{aligned} \tag{6.108}$$

The numerical difference between these two matrix elements leads to the Gallagher-Moszkowski splitting. The nature of this splitting is expressed by the empirical Gallagher-Moszkowski rule [24] which states that the lowest lying of the two partner states $\Omega_p \pm \Omega_n$ is that for which the projections of the intrinsic spins Σ_p and Σ_n are parallel. This is the generalization to the asymptotic region of the Nordheim rules [25] for spherical nuclei. Ultimately it must fail in the region of small deformations as a result of the increasing dominance of the spin-orbit term in the Nilsson potential which has off diagonal matrix elements in Σ space.

In the special case of $K = 0$ the latter term in (6.108) leads to the staggering of the resultant odd and even band members by virtue of its spin dependant phase factor. This signature splitting is the so called Newby shift [26].

Finally, the electromagnetic moments and transition probabilities are calculated from the suitably generalized operators of subsection 6.3.5.

6.5 The Variable Moment of Inertia model

The existence of many even-even spectra in the well deformed region which follow the $I(I+1)$ rotational rule is well established. Those nuclei for which the law fails exhibit consistently smaller band spacings than would be expected from this law. These deviations can be incorporated into the axially symmetric collective rotational model, for which

$$E_I = \frac{\hbar^2}{2\Im} I(I+1), \quad I = 0, 2, 4, \cdots \tag{6.109}$$

by allowing the moment of inertia $\Im$ to vary with spin. To account for the observed band structures within this framework the moment of inertia is required to increase monotonically with spin, ultimately tending towards some limit which corresponds to the value expected for a rigid body of the given nuclear geometry.

Nielsen's analysis [27] has shown that these deviations are essentially independent of the properties of the second 2^+ state, at least for highly deformed nuclei. The existence of such a state is of course the most characteristic consequence of the non-axial degree of freedom γ. Thus although non-axial deformations result in a departure from the $I(I+1)$ law, they are not the principal cause of the observed deviations.

Phenomenologically these deviations are accurately reproduced by certain two parameter fits. For instance Harris [28], by expanding the nuclear energy in terms of the angular velocity ω, showed that the following relations are generally valid

$$\begin{aligned} E_I &= \frac{1}{2}\omega^2(\Im_0 + 3B\omega^2 + \cdots) \\ \{I(I+1)\}^{\frac{1}{2}} &= \omega(\Im_0 + 2B\omega^2 + \cdots) \end{aligned} \tag{6.110}$$

where $\Im_0$ and B are variable parameters. Even retaining just the two lowest order terms the agreement with the experimental rotational bands is remarkable.

An alternative approach was considered by Diamond *et al.* [29] who assumed that the centrifugal stretching of the nucleus was chiefly responsible for the changing moment of inertia via the hydrodynamical relationship $\Im = 3B\beta^2$ (6.12). Thus, with a the addition of a harmonic restoring force, the semi-classical energy may be written

$$E(\beta_I) = \frac{\hbar^2}{6B\beta_I^2} I(I+1) + \frac{1}{2}C(\beta_I - \beta_0)^2. \tag{6.111}$$

This is subject to the minimization condition $\partial E(\beta_I)/\partial\beta_I = 0$, from which β_0 is seen to represent the ground state static deformation. By treating B and C as variable parameters good fits can be obtained to the bands of strongly deformed nuclei. However, bands outside the deformed region cannot be satisfactorily reproduced with any reasonable degree of accuracy. Another difficulty arose when studies of isomer shifts using both the Mössbauer effect [30] and muonic atoms [31] indicated that the true increase in deformation is much smaller than is required by such a centrifugal stretching model.

These results obtained support from theoretical considerations [32] which showed that the decrease in the effective pairing force has a even greater influence on the moment of inertia with increasing I than does the centrifugal stretching. Both of these effects are incorporated in the form of the moment of inertia obtained from a fourth order perturbation treatment of the cranking model [28]. In this way the moment of inertia becomes

$$\Im(\omega) = \Im_0 + 3B\omega^2. \tag{6.112}$$

The form of this expression is the same as that appearing in brackets in the first of the Harris two parameter model equations (6.110) although now $\Im_0$ and B are explicitly related to the nuclear matrix elements. In particular and in the absence of pairing

$$\Im_0 = 2\hbar^2 \sum_{i\neq 0} \frac{|\langle i|j_1|0\rangle|^2}{e_i - e_0}. \tag{6.113}$$

In fact it can be shown [33] for an equilibrated independent particle system in some static potential that the moment of inertia resulting from (6.113) is approximately equal to $\Im_{rigid}$, where

$$\Im_{rigid} = \left\langle \sum_{i=1}^{A} m(x_2^2 + x_3^2)_i \right\rangle \tag{6.114}$$

denotes the rigid moment of inertia corresponding to system of A particles of mass m rotating about the 1-axis.

The pairing field is introduced by replacing the energy denominator with the sum of the corresponding quasiparticle energies and attaching the appropriate pairing factor to the operator j_1. Since this operator links the BCS ground state with the 2-qp states it is seen from (6.72) that this is just $U_iV_{i'} - V_iU_{i'}$. Thus

$$\Im_0(\Delta) = 2\hbar^2 \sum_{i>i'} \frac{|\langle i|j_1|i'\rangle|^2}{E_i + E_{i'}} (U_i V_{i'} - V_i U_{i'})^2. \tag{6.115}$$

Both the pairing factor and the quasiparticle denominator lead to a reduction in the moment of inertia.

These pairing correlations are opposed by interactions induced by the nuclear rotation. The coriolis force, which is manifest in the j_1 operator, acts so as to align all single particle angular momenta along the axis of rotation. Thus with increasing nuclear rotation the pairing correlations, which tend to pair particles with vanishing (anti-parallel) total angular momentum, will be gradually destroyed. This has the effect of increasing the moment of inertia and ultimately for some critical value of the angular momentum, the nucleus undergoes a transition from the superconducting to the normal phase. Simultaneously the nuclear moment of inertia increases up to the rigid limit provided by (6.113).

In addition to this Coriolis Anti-Pairing effect the moment of inertia also increases with spin as a result of the angular velocity dependent term in (6.112). This latter dependence approximates the centrifugal stretching effect.

Clearly then a combination of CAP and centrifugal stretching embodies the main features of the spin dependence of the moment of inertia. Such a formulation though, based as it is upon microscopic features, is not readily applicable to the macroscopic Bohr Hamiltonian of section 6.2 where the intrinsic structure is not considered. However, the sweeping regularities exhibited by the ground state rotational bands suggest that a description of the spin dependence of the moment of inertia in terms of macroscopic variables is possible. Mariscotti *et al.* [34] suggested a Variable Moment of Inertia approach based on an expression similar to (6.111) but with the deformation being replaced by the moment of inertia itself

$$E_I = \frac{\hbar^2}{2\Im_I} I(I+1) + \frac{1}{2} C \left(\frac{\Im_I}{\hbar^2} - \frac{\Im_0}{\hbar^2} \right)^2 \tag{6.116}$$

subject to the equilibrium condition $\partial E_I(\Im)/\partial \Im_I = 0$. It was shown that this formalism was capable of reproducing not only the ground state but also the γ band to a very satisfactory degree of accuracy, using only the two parameters C and $\Im_0$. In fact, although it is not obvious *a priori*, this VMI procedure is mathematically equivalent to the two parameter model of Harris.

The extent to which this variable moment of inertia deviates from the ground state value $\Im_0$ for a given spin is expressed by the quantity $d\Im/\Im dI$. In particular for $I = 0$

$$S = \frac{1}{\Im} \frac{d\Im}{dI}\bigg|_{I=0} = \frac{\hbar^6}{2C\Im_0^3}. \tag{6.117}$$

Thus defined, the nuclear softness S provides a useful two parameter identification of each nucleus. For a perfectly rigid core $S = 0$ and the VMI equations yield the usual $I(I+1)$ law.

6.6 The generalization of the VMI procedure to triaxial rotors

The natural extension of the VMI model to asymmetrically deformed nuclei leads to the Hamiltonian [35]

$$\begin{aligned} H = &\sum_k \frac{1}{2\Im_{kI\varrho}} I_k^2 + \frac{1}{2} C \left(\frac{\Im_{I\varrho}}{\hbar^2} - \frac{\Im_0}{\hbar^2} \right)^2 \\ &+ C_{\Im\gamma} \left(\frac{\Im_{I\varrho}}{\hbar^2} - \frac{\Im_0}{\hbar^2} \right) (\gamma_{I\varrho} - \gamma_0) + \frac{1}{2} C_\gamma (\gamma_{I\varrho} - \gamma_0)^2 . \end{aligned} \tag{6.118}$$

The three components of the moment of inertia tensor are related via the usual expression

$$\Im_{kI\varrho} = \frac{4}{3} \Im_{I\varrho} \sin^2 \left(\gamma - \frac{2\pi}{3} k \right) \tag{6.119}$$

where the spin dependent parameters $\Im_{I\varrho}$ and indeed the asymmetric deformation $\gamma_{I\varrho}$ are chosen to minimize the resulting energy eigenvalues.

It will be assumed here that the gamma band is due to a static gamma asymmetry of the nucleus and that the gamma vibrational states lie high enough to be disregarded ($C_\gamma = C_{\Im\gamma} = \infty$). In practice this assumption restricts γ to the same value for each core state. Further it will be assumed that the moment of inertia parameter $\Im_{I\varrho}$ depends only upon the magnitude of the spin and not upon its various orientations labelled ϱ. Thus the triaxial VMI Hamiltonian reduces to the form

$$H = \sum_k \frac{1}{2\Im_{kI}} I_k^2 + \frac{1}{2} C \left(\frac{\Im_I}{\hbar^2} - \frac{\Im_0}{\hbar^2} \right)^2 \tag{6.120}$$

Since the ratios $\Im_{1I} : \Im_{2I} : \Im_{3I}$ remain unchanged with respect to a rigid core and the potential energy term is a constant, this VMI Hamiltonian has the same eigenvectors as in the rigid case with energy eigenvalues

$$E_{I\varrho}(\Im_I, \gamma) = \frac{\hbar^2}{2\Im_I} \eta_{I\varrho}(\gamma) I(I+1) + \frac{1}{2} C \left(\frac{\Im_I}{\hbar^2} - \frac{\Im_0}{\hbar^2} \right)^2 . \tag{6.121}$$

The dimensionless quantity $\eta_{I\varrho}(\gamma)$ represents the deviation the triaxial rigid rotor energy eigenvalues from those of the corresponding axial rotor.

From this equation the moment of inertia parameter $\Im_I$ is determined by the equilibrium condition $\partial E_{I\varrho}/\partial \Im_I = 0$, which in a ϱ independent form becomes

$$\frac{\Im_I^2}{\hbar^4}\left\{\frac{\Im_I}{\hbar^2} - \frac{\Im_0}{\hbar^2}\right\} = \frac{1}{2C} I(I+1). \tag{6.122}$$

The VMI parameters $C, \Im_0$ and the non-axial deformation γ are determined by fitting the energy eigenvalues to the experimental $2_1^+, 2_2^+$ and 4_1^+ level energies. A solution to this problem is given in appendix A.2.

6.6.1 The range of validity of the asymmetric VMI model

By combining (6.121) and (6.122) the energy ratio $\Re_I = E_{I1}/E_{21}$ is given as

$$\Re_I = \frac{I(I+1)}{6}\frac{\Im_2}{\Im_I}\left[\frac{\eta_{I1} + \hbar^6 I(I+1)/4C\Im_I^3}{\eta_{21} + \hbar^6 6/4C\Im_2^3}\right]. \tag{6.123}$$

In particular in the limit of small nuclear softness $S = 0$

$$\Re_I = \frac{I(I+1)}{6}\frac{\eta_{I1}}{\eta_{21}} \tag{6.124}$$

while for large softness $S \to \infty$

$$\Re_I = \left\{\frac{I(I+1)}{6}\right\}^{\frac{2}{3}}\left[\frac{2\eta_{I1}+1}{2\eta_{21}+1}\right]. \tag{6.125}$$

These limiting values are given below for the case of $\Re_2$ and $\Re_4$ and also for the ratio $\Re_3' = E_3/(E_{21}+E_{22})$

	rigid rotor $S=0$		$S \to \infty$	
	$\gamma = 0$	$\frac{\pi}{6}$	$\gamma = 0$	$\frac{\pi}{6}$
$\Re_2$	∞	2.00	∞	1.75
$\Re_4$	3.33	2.67	2.23	1.90
$\Re_3'$	1.00	1.00	0.79	0.79

Thus the present VMI prescription extends the range of nuclei which may be described by the rotational model well into the harmonic region $\Re_4 \sim \Re_2 \sim 2$. It is also to possible to describe nuclei for which the ratio $\Re_2$ is less than 2.

An illustration of the agreement with the experimental band structures than can be achieved with the VMI model is shown in figure 6.3 for the nucleus ^{76}Se. With the ratios $\Re_2 = 2.18$, $\Re_4 = 2.38$ and $\Re'_3 = 0.95$ this nucleus lies outside the region which may be described by the rigid rotor ($S = 0$) model. In contrast the VMI model gives an excellent reproduction of the experimental data.

6.7 The VMI in the particle-rotor models

The inclusion of the VMI core Hamiltonian (6.120) into the particle-rotor Hamiltonians (6.82) and (6.99) allows a correspondingly precise description of the rotational band structures of both odd and odd-odd nuclei.

However the VMI Hamiltonian together with the equilibrium equation (6.122) is written in terms of the core spin R as opposed to the total spin, I. Therefore the assignment of a suitable moment of inertia parameter $\Im_R$ for a given core spin R can only be made in a basis in which the core spin is a good quantum number. In particular this is not true of the strong coupling wavefunctions. Thus the diagonalization of the core Hamiltonian is performed in a basis which couples the *laboratory* quasiparticle states to the core eigenfunctions. This will be referred to as the weak coupling basis although the name is more generally associated with a vibrational Hamiltonian of the type (6.30) referred to the laboratory system, neither of with are the case here.

The formalism for these calculations will be presented below.

6.7.1 1-qp excitations: odd A nuclei

The weak coupling basis for 1-qp excitations may be written

$$|IMR\varrho j\rangle = \sum_{M_R m} (RM_R jm|IM)|RM_R\varrho\rangle\beta^+_{Njlm}|BCS\rangle \tag{6.126}$$

where the β^+_{Njlm} are the creation operators of spherical quasiparticles in the laboratory system and the $|RM_R\varrho\rangle$ are the eigenfunctions of the VMI core Hamiltonian. These are expressed in the generalized rotational basis of subsection 6.2.2

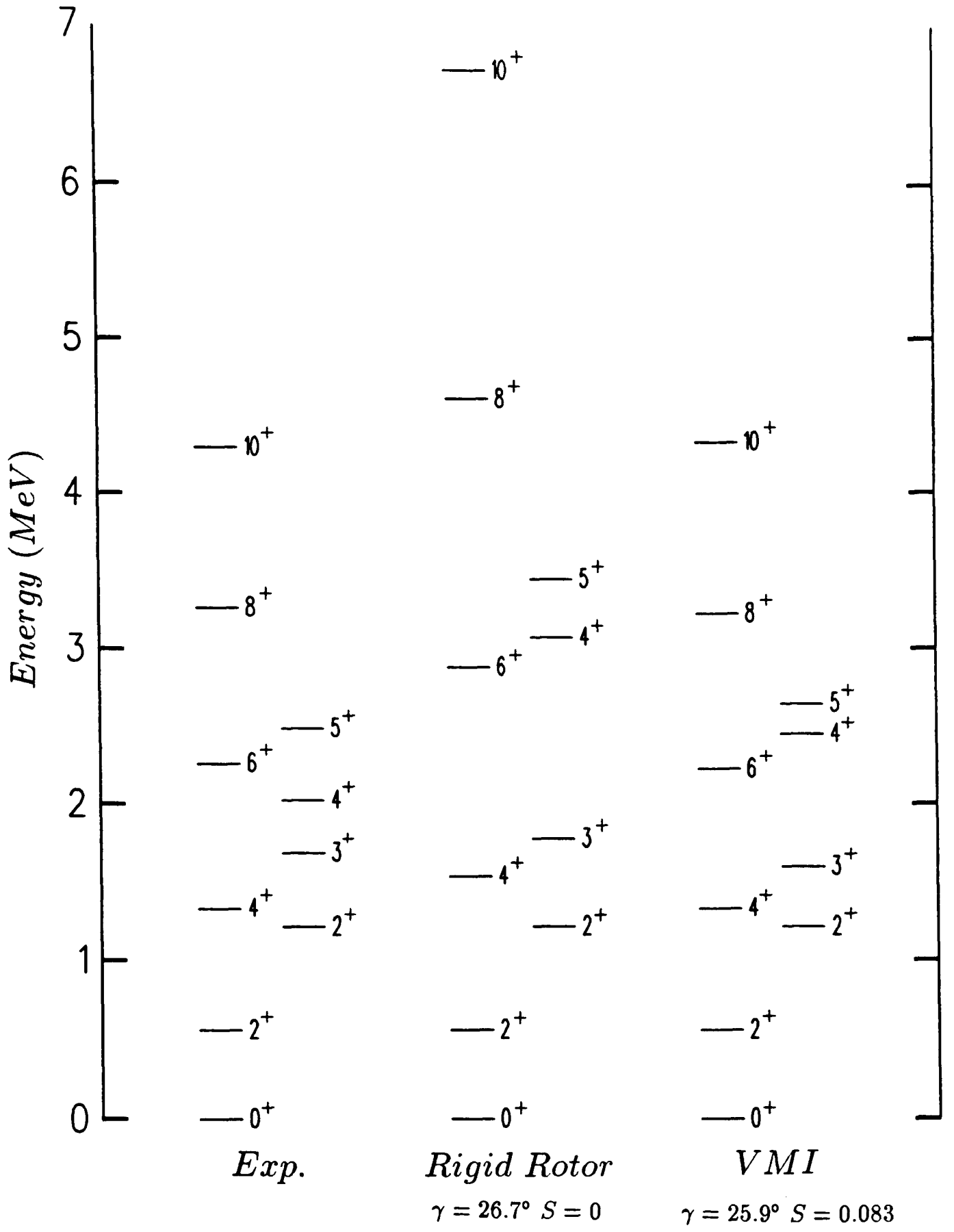

Figure 6.3. A comparison of the VMI and rigid rotor models with the experimental band structure of ^{76}Se. The parameters are chosen to reproduce the experimental energies of the 2_1^+ and 2_2^+ levels for the rigid rotor and also that of the 4_1^+ level for the VMI model.

$$|RM_{R\varrho}\rangle = \sum_{R_3} A_{R_3}^{R\varrho} \sqrt{\frac{2R+1}{16\pi^2(1+\delta_{R_z,0})}} \{D^R_{M_R R_3} + (-1)^R D^R_{M_R -R_3}\} \tag{6.127}$$

With the core states written in this form the symmetrization of the weak coupling basis states

with respect to the intrinsic axis permutation operators $\hat{R}_k$ is guaranteed.

While the core Hamiltonian is diagonal in the weak coupling basis the single particle Hamiltonian, being referred to the intrinsic frame, is not. Rather, the single particle Hamiltonian is diagonal in the strong coupling basis $|IMKi\rangle$. To exploit these features the particle-rotor Hamiltonian is written in the form

$$H = \sum_{IMKi} |IMKi\rangle E_i \langle IMKi| + \sum_{IMR\varrho j} |IMR\varrho j\rangle E_{R\varrho} \langle IMR\varrho j| \tag{6.128}$$

where $E_{R\varrho}$ denotes the VMI rotational energy (6.121) of the core and E_i represents the single quasiparticle energies.

Either the strong or weak coupling bases may be chosen to perform the final diagonalization of the this Hamiltonian. Here the strong coupling basis will be employed in order to comply with the pre-existing particle-rigid rotor computer codes [18,20]. Thus the required matrix elements are

$$\langle IMKi|H|IMK'i'\rangle = E_i \delta_{K,K'} \delta_{i,i'} + \sum_{NjlR\varrho} \langle IMKi|IMR\varrho j\rangle E_{R\varrho} \langle IMR\varrho j|IMK'i'\rangle. \tag{6.129}$$

In order to be able to calculate the unitary transformation brackets $\langle IMKi|IMR\varrho j\rangle$ it is necessary to express the weak coupling basis entirely in the intrinsic frame. The laboratory frame quasiparticle operators may be related to the corresponding operators in the intrinsic system by the expression

$$\beta^+_{Njlm} = \sum_{\Omega} D^j_{m\Omega} \beta^+_{Njl\Omega}. \tag{6.130}$$

Thus, using the Clebsh-Gordon series for the D-matrices [36]

$$\sum_{ab} (AaBb|Cc) D^A_{a\alpha} D^B_{b\beta} = (A\alpha B\beta|C\gamma) D^C_{c\gamma} \tag{6.131}$$

and (6.127), the weak coupling basis functions become

$$\begin{aligned} |IMR\varrho j\rangle = \sum_{\substack{R_3=0,2,\cdots \\ \Omega\overline{\Omega}}} \sqrt{\frac{2R+1}{16\pi^2(1+\delta_{R_3,0})}} A^{R\varrho}_{R_3} \Big\{ & (RR_3 j\Omega|IR_3+\Omega) D^I_{MR_3+\Omega} \\ & + (-1)^R (R-R_3 j\Omega|I-R_3-\Omega) D^I_{M-R_3+\Omega} \Big\} \beta^+_{Njl\Omega}|BCS\rangle. \end{aligned} \tag{6.132}$$

The summation is taken over both normal Ω and time conjugate states $\overline{\Omega} = -\Omega$. Finally, using the relations

$$\beta^{+}_{Nj|\Omega} = \sum_{i} B_{Nj|\Omega}\alpha^{+}_{i} \tag{6.133}$$

$$\beta^{+}_{Nj|\overline{\Omega}} = \sum_{i} (-1)^{j+\overline{\Omega}} B_{Nj|\Omega}\alpha^{+}_{\overline{i}} \tag{6.134}$$

which are the quasiparticle inverses of expressions (6.56) and (6.57) and the orthogonality of the D-matrices, the overlaps between the weak coupling basis (6.132) and the strong coupling basis

$$|IMKi\rangle = \sqrt{\frac{2I+1}{16\pi^2}} \left\{ D^{I}_{MK}\alpha^{+}_{i} + (-1)^{I-j} D^{I}_{M-K}\alpha^{+}_{\overline{i}} \right\} |BCS\rangle \tag{6.135}$$

are obtained as

$$\begin{aligned}
\langle IMKi|IMR\varrho j\rangle = \frac{1}{2}\sqrt{\frac{2R+1}{2I+1}} \Bigg\{ & \sum_{\Omega} \frac{A^{\varrho}_{K-\Omega}}{\sqrt{1+\delta_{K-\Omega,0}}} (RK-\Omega j\Omega|IK) B^{i}_{Nj|\Omega} \\
& + (-1)^{R} \sum_{\Omega} \frac{A^{\varrho}_{\Omega-K}}{\sqrt{1+\delta_{\Omega-K,0}}} (R\Omega-Kj\Omega|IK) B^{i}_{Nj|\Omega} \\
& + (-1)^{I-j} \sum_{\overline{\Omega}} \frac{A^{\varrho}_{-K-\Omega}}{\sqrt{1+\delta_{-K-\Omega,0}}} (R-K-\Omega j\Omega|I-K) B^{i}_{Nj|-\Omega} \\
& + (-1)^{R+I-j} \sum_{\overline{\Omega}} \frac{A^{\varrho}_{K+\Omega}}{\sqrt{1+\delta_{-K-\Omega,0}}} (R-K-\Omega j\Omega|I-K) B^{i}_{Nj|-\Omega} \Bigg\}
\end{aligned} \tag{6.136}$$

A computer program which has been written to calculate these overlaps and to construct the strong coupling particle-rotor Hamiltonian is given in appendix A.3.

6.7.2 2-qp excitations: odd-odd A nuclei

The formalism for the inclusion of a VMI core into the odd-odd Hamiltonian proceeds in an identical manner to the previous case. The 2-qp weak coupling basis is

$$|IMR\varrho Jj_p j_n\rangle = \sum_{M_R M_J m_p m_n} (j_p m_p j_n m_n|JM_J)(JM_J RM_R|IM)|R\varrho M_R\rangle \beta^{+}_{p}\beta^{+}_{n}|BCS\rangle \tag{6.137}$$

where J is the quantum number of the the total quasiparticle angular momentum operator $\mathbf{J} = \mathbf{j_p} + \mathbf{j_p}$ whose projection onto the laboratory 3-axis is $M_J = m_p + m_n$.

Again the choice of the strong coupling basis in which to perform the diagonalization of the full particle-rotor Hamiltonian matrix has been guided by the previous rigid core computer code [20]. In this basis this Hamiltonian may be written

$$\langle IMKpn|H|IMK'p'n'\rangle = (E_p + E_n)\delta_{K,K'}\delta_{p,p'}\delta_{n,n'} + \sum_{j_pj_nJR_\varrho} \langle IMKpn|IMR_\varrho Jj_pj_n\rangle E_{R_\varrho} \langle IMR_\varrho Jj_pj_n|IMK'p'n'\rangle + \langle IMKpn|V_{pn}|IMK'p'n'\rangle. \tag{6.138}$$

Again, in order to calculate the transformation brackets the weak coupling wave function must be expressed entirely in the intrinsic frame. Thus

$$|IMR_\varrho Jj_pj_n\rangle = \sum_{\substack{R_3=0,2,\cdots \\ (\Omega\overline{\Omega})_{p,n}}} \sqrt{\frac{2R+1}{16\pi^2(1+\delta_{R_3,0})}} A^{R_\varrho}_{R_3}\Big\{(Jk_JRR_3|IR_3+k_J)D^I_{MR_3+k_J} + (-1)^R(Jk_JR-R_3|Ik_J-R_3)D^I_{MK_J-R_3}\Big\}(j_p\Omega_pj_n\Omega_n|Jk_J)\beta^+_p\beta^+_n|BCS\rangle. \tag{6.139}$$

The overlaps with the two strong coupling basis functions (6.97) and (6.98) are therefore

$$\begin{aligned}\langle IMKpn|IMR_\varrho Jj_pj_n\rangle = \frac{1}{2}\sqrt{\frac{2R+1}{2I+1}}\Bigg\{ & \sum_{\Omega_p\Omega_n} \frac{A^\varrho_{K-\Omega_p-\Omega_n}}{\sqrt{1+\delta_{K-\Omega_p-\Omega_n,0}}}(j_p\Omega_pj_n\Omega_n|J\Omega_p+\Omega_n) \\ & \times (J\Omega_p+\Omega_nRK-\Omega_p-\Omega_n|IK)B^p_{(Njl\Omega)_p}B^n_{(Njl\Omega)_n} \\ +(-1)^R & \sum_{\Omega_p\Omega_n} \frac{A^\varrho_{\Omega_p+\Omega_n-K}}{\sqrt{1+\delta_{\Omega_p+\Omega_n-K,0}}}(j_p\Omega_pj_n\Omega_n|J\Omega_p+\Omega_n) \\ & \times (J\Omega_p+\Omega_nRK-\Omega_p-\Omega_n|IK)B^p_{(Njl\Omega)_p}B^n_{(Njl\Omega)_n} \\ +(-1)^{I+j_p+j_n} & \sum_{\overline{\Omega}_p\overline{\Omega}_n} \frac{A^\varrho_{-K-\Omega_p-\Omega_n}}{\sqrt{1+\delta_{-K-\Omega_p-\Omega_n,0}}}(j_p\Omega_pj_n\Omega_n|J\Omega_p+\Omega_n) \\ & \times (J\Omega_p+\Omega_nR-K-\Omega_p-\Omega_n|IK)B^p_{(Njl-\Omega)_p}B^n_{(Njl-\Omega)_n} \\ +(-1)^{I+R+j_p+j_n} & \sum_{\overline{\Omega}_p\overline{\Omega}_n} \frac{A^\varrho_{\Omega_p+\Omega_n+K}}{\sqrt{1+\delta_{\Omega_p+\Omega_n+K,0}}}(j_p\Omega_pj_n\Omega_n|J\Omega_p+\Omega_n) \\ & \times (J\Omega_p+\Omega_nR-K-\Omega_p-\Omega_n|IK)B^p_{(Njl-\Omega)_p}B^n_{(Njl-\Omega)_n}\Bigg\}\end{aligned} \tag{6.140}$$

for K odd and

$$\langle IMKp\overline{n}|IMR\varrho Jj_pj_n\rangle = \frac{1}{2}\sqrt{\frac{2R+1}{2I+1}}\Bigg\{$$

$$(-1)^{j_n+\Omega_n}\sum_{\Omega_p\overline{\Omega}_n}\frac{A^{\varrho}_{K-\Omega_p-\Omega_n}}{\sqrt{1+\delta_{K-\Omega_p-\Omega_n,0}}}(j_p\Omega_p j_n\Omega_n|J\Omega_p+\Omega_n)$$

$$\times(J\Omega_p+\Omega_nRK-\Omega_p-\Omega_n|IK)B^p_{(Njl\Omega)_p}B^n_{(Njl-\Omega)_n}$$

$$+(-1)^{R+j_n+\Omega_n}\sum_{\Omega_p\overline{\Omega}_n}\frac{A^{\varrho}_{\Omega_p+\Omega_n-K}}{\sqrt{1+\delta_{\Omega_p+\Omega_n-K,0}}}(j_p\Omega_p j_n\Omega_n|J\Omega_p+\Omega_n)$$

$$\times(J\Omega_p+\Omega_nRK-\Omega_p-\Omega_n|IK)B^p_{(Njl\Omega)_p}B^n_{(Njl-\Omega)_n}$$

$$+(-1)^{I+1+j_p+\Omega_p}\sum_{\overline{\Omega}_p\Omega_n}\frac{A^{\varrho}_{-K-\Omega_p-\Omega_n}}{\sqrt{1+\delta_{-K-\Omega_p-\Omega_n,0}}}(j_p\Omega_p j_n\Omega_n|J\Omega_p+\Omega_n)$$

$$\times(J\Omega_p+\Omega_nR-K-\Omega_p-\Omega_n|IK)B^p_{(Njl-\Omega)_p}B^n_{(Njl\Omega)_n}$$

$$+(-1)^{I+R+1+j_p+\Omega_n}\sum_{\overline{\Omega}_p\Omega_n}\frac{A^{\varrho}_{\Omega_p+\Omega_n+K}}{\sqrt{1+\delta_{\Omega_p+\Omega_n+K,0}}}(j_p\Omega_p j_n\Omega_n|J\Omega_p+\Omega_n)$$

$$\times(J\Omega_p+\Omega_nR-K-\Omega_p-\Omega_n|IK)B^p_{(Njl-\Omega)_p}B^n_{(Njl\Omega)_n}\Bigg\} \tag{6.141}$$

for K even.

A listing of the computer program which performs these calculations is given in appendix A.4.

6.8 Core truncation and the choice of basis states

In this work the choice of basis in which to perform the final diagonalization of the Hamiltonian matrix has been guided by the pre-existing computer codes. However both the strong and weak coupling bases have definite advantages and disadvantages.

Using (6.72) it can be shown that the particle and quasiparticle angular momentum commutators are identical only in the case where the pairing factors $U_iU_{i'}+V_iV_{i'}$ are unity and the basis does not contain states differing by two quasiparticles. With these constraints the angular momentum algebra may be used to transform the quasiparticle operators from the laboratory to the intrinsic frames (6.130).

It has already been pointed out that when expressed in the strong coupling basis the pairing factors $U_iU_{i'}+V_iV_{i'}$ may be multiplied onto the matrix elements as a whole, rather than attaching

them to the single particle angular momentum operators separately. As a result the strong coupling matrix elements of the Hamiltonian can be calculated using an exact transformation between reference frames under the condition $U_iU_{i'} + V_iV_{i'} = 1$. Once derived this condition may be relaxed and the matrix elements multiplied by the pairing factor $U_iU_{i'} + V_iV_{i'}$. Thus both the reference frame transformation and the pairing are handled exactly, although only in the case where the special nature of the recoil terms is ignored.

Had the weak coupling basis been employed for the final diagonalization this method could not have been employed since the Hamiltonian matrix is no longer diagonal in the single particle space. It is therefore necessary either to treat the frame transformation exactly using the new quasiparticle angular momentum algebra which includes the pairing factors implicitly or to maintain the constraint $U_iU_{i'} + V_iV_{i'} \equiv 1$. For large deformations ($\beta > 0.3$) it is not clear that such a constraint is valid [22,37].

On the other hand, it is clear that high lying core states of high spin and/or ϱ will not contribute to the low lying eigenfunctions. In view of the large number of summations associated with the transformation bracket between the strong and weak coupling bases it is advantageous computationally to be able to truncate the core basis as appropriate. While this is trivial in the weak coupling representation the strong coupling basis is particularly inappropriate for this purpose.

Here the content of the various core states in the strong coupling basis functions as expressed by the overlap integrals (6.136), (6.140) and (6.141) is governed by vector coupling rather than energy considerations. As a result both high and low lying core states generally occur with similar amplitudes in the same strong coupling basis vectors. The *ab initio* removal of high lying core states from the strong coupling basis is therefore impossible and is only achieved in the linear combinations of basis states which result from the final diagonalization.

However a certain degree of simplification occurs in the case of axial symmetry. There the core becomes diagonal in the basis $|RM_RR_3\rangle$. In particular the ground state band members $|RM_R1\rangle$ map only into the strong coupling states $|IMK = \Omega\rangle$, while the remaining core states which lie arbitrarily high in energy map only into the strong coupling states $|IMK \neq \Omega\rangle$. Thus by confining the strong coupling basis to states of $|IMK = \Omega\rangle$ it is possible to restrict the core summations of (6.129) and (6.138) to the ground state band ($\varrho = 1$), although even in this case truncation with respect to R is still not possible. This truncation has been employed in the calculation of the matrix elements given in appendices A.3 and A.4.

Thus although the diagonalization of the VMI Hamiltonian in the strong coupling basis allows the inclusion of pairing, it is at a distinct disadvantage compared to the weak coupling

basis with respect to the number of calculations required for a given degree of convergence. In the case of odd A the increase in CPU time incurred by a VMI calculation in the full strong coupling basis space compared with the same rigid rotor calculation is modest, typically 4 s compared with 1 s. For odd-odd calculations the vastly increased basis space leads to rather large CPU times. For extensive calculations therefore a truncated weak coupling basis is at a definite advantage. Set against this is the failure of the pairing assumption $U_i U_{i'} + V_i V_{i'} \equiv 1$ for the larger deformations, which thus limits the generality of the model. For this reason it is not used in the present computer code.

6.9 Conclusion

The present work has increased the flexibility of pre-existing particle-rotor computer codes by allowing the calculations to be performed in a space in which the core Hamiltonian is diagonal. Thus the rigid rotor assumption may be relaxed and a more complete description of the rotational band structure in odd and odd-odd nuclei may be achieved by considering a VMI rotor instead.

With the core rotational energies thus calculated it is possible to test more directly the assumptions made in coupling the single particles to the core, without the restrictions imposed by an inadequate treatment of the core rotational energies.

A non-empirical approach to the changing moment of inertia requires a microscopic description of the core. Indeed it has been shown for a few particular cases in even-even nuclei [38] that the VMI effect is well reproduced by the coupling of 0-qp rigid rotor states to yrare 2-qp states, via the number non-conserving terms in the quasiparticle operators (6.72). Although such calculations provide a more profound understanding of the true nuclear mechanisms, in the general case, particularly when extended to odd (1-qp and 3-qp excitations) and odd-odd (2-qp and 4-qp excitations), the required calculations are prohibitive.

In this respect the more empirical VMI calculations presented here provide the only method to achieve fully quantitative reproductions of the observed nuclear rotational band structures.

References

[1] . A. Bohr, Mat. Fys. Medd. Dan. Vid. Selsk. **26** (1952) No. 14

[2] . A. Faessler and W. Greiner, Z. Phys. 168 (1962) 425

[3] . A.S. Davydov and G.F. Filippov, Nucl. Phys. **8** (1958) 237

[4] . L. Grodzins, Phys. Lett. **2** (1962) 88

[5] . A. Faessler *et al.*, Nucl. Phys. **70** (1965) 33

[6] . F. Iachello and A. Arima, Phys. Lett. **53B** (1974) 309

[7] . H. Toki and A. Faessler, Z. Phys. **A276** (1976) 35

[8] . A. de Shalit, Phys. Rev. **122** (1961) 1530

[9] . J. Dudek *et al.*, J. Phys. **G5** (1979) 1359

[10] . S.G. Nilsson, Dan. Mat. Fys. Medd. **29** (1955) No. 16

[11] . I. Ragnarsson and R.K. Sheline, Phys. Scripta **29** (1984) 385

[12] . R.K. Sheline *et al.*, J. Phys. **G14** (1988) 1201

[13] . S.G. Nilsson *et al.*, Nucl. Phys. **A131** (1969) 1

[14] . S.E. Larsson *et al.*, Nucl. Phys **A261** (1976) 77

[15] . K.E.G. Löbner *et al.*, Atomic and Nuclear Data Sheets **A7** (1970) 495

[16] . N.N. Bogoliubov, Soviet Phys. JETP **7** (1958) 41
J.G. Valatin, Nuovo Cimento **7** (1958) 843

[17] . E.Osnes *et al.*, Nucl. Phys. **A253** (1975) 45

[18] . S.E. Larsson *et al.*, Nucl. Phys. **A307** (1978) 189

[19] . F.S. Stephans *et al.*, Phys. Lett. **44b** (1973) 429

[20] . I. Ragnarsson and P.B. Semmes, Hyp. Int. **43** (1988) 425

[21] . A.J. Kreiner, Z. Phys. **A288** (1978) 373

[22] . H.Toki *et al.*, Z. Phys. **A292** (1979) 79

[23] . J.P. Boisson *et al.*, Physics Reports **26** (1976) 99

[24] . C.J. Gallagher and S.A. Moszkowski, Phys. Rev. **111** (1958) 1282

[25] . L.W. Nordheim, Phys. Rev. **78** (1950) 294

[26] . N.D. Newby, Phys. Rev. **125** (1962) 2063

[27] . O.B. Nielsen, in Proceedings of the Rutherford Jubilee International Conference, Manchester, ed. J.B. Birks (Heywood and Co., 1961)

[28] . S.M. Harris, Phys. Rev. **138** (1965) B509

[29] . R.M. Diamond *et al.*, Phys. Lett. **11** (1964) 315

[30] . D. Yeboah-Amankwah *et al.*, Phys. Rev. Lett. **18** (1967) 791

[31] . S. Bernow *et al.*, Phys. Rev. Lett. **18** (1967) 787

[32] . D.R. Bes *et al.*, Phys. Rev. **166** (1968) 1045

[33] . A. Bohr and B.R. Mottelson, Mat. Fys. Medd. Dan. Vid Selsk. 30, no 1, (1955)

[34] . M.A.J. Mariscotti *et al.*, Phys. Rev. **178** (1968) 178

[35] . H. Toki and A. Faessler, Z. Phys. **A276** (1976) 35

[36] . D.M. Brink and G.R. Satchler, Angular Momentum (Oxford, 1968)

[37] . H. Toki *et al.*, Nucl. Phys. **A279** (1977) 1

[38] . H.L. Yadav *et al.*, Phys. Rev. Lett. **39** (1977) 1128

Chapter 7

The single particle configurations of the light bromine isotopes

7.1 Introduction

The single particle level density in the A $\sim$ 75 region of nuclei is noticeably lower than in, for example, the rare earth region. Indeed, with the number of single particle states per unit energy smaller by a factor of two, the single particle energy gaps and more generally the shell structure effects manifest themselves in a comparatively dramatic way in these nuclei. In particular they give rise to a strong shape variation as a function of both particle number and spin and lead to pronounced shape coexistent effects.

This chapter will attempt to interpret the low lying nuclear structure of the isotopes $^{72-77}$Br in terms of the particle -VMI rotor model, with particular reference to the present magnetic moment measurements described in chapter 4. As an introduction to the single particle level scheme, a general discussion of the ground state configurations expected to occur in the odd A bromines will now be given.

7.2 The single particle level scheme

The microscopic structure of nuclei in the A $\sim$ 75 region is dominated by the $4g_{9/2}$, $3p_{1/2}$, $3f_{5/2}$, $3p_{3/2}$ and $3f_{7/2}$ orbitals. These are illustrated in figure 7.1 for protons in an axially symmetric prolate deformed Nilsson potential. Although in many cases the wavefunctions are strongly mixed, the asymptotic quantum numbers $[Nn_z\Lambda]\Omega$ are used to label individual levels. For small deformations the spherical quantum numbers $(N)l_j$ are also given.

The odd A bromine nuclei $^{75-87}$Br, with atomic number 35, are all known or thought to have ground state spins of $3/2^-$. From figure 7.1 it can be seen that for prolate nuclei the last odd proton is indeed expected to occupy the [301]3/2 orbital for quadrupole deformations up

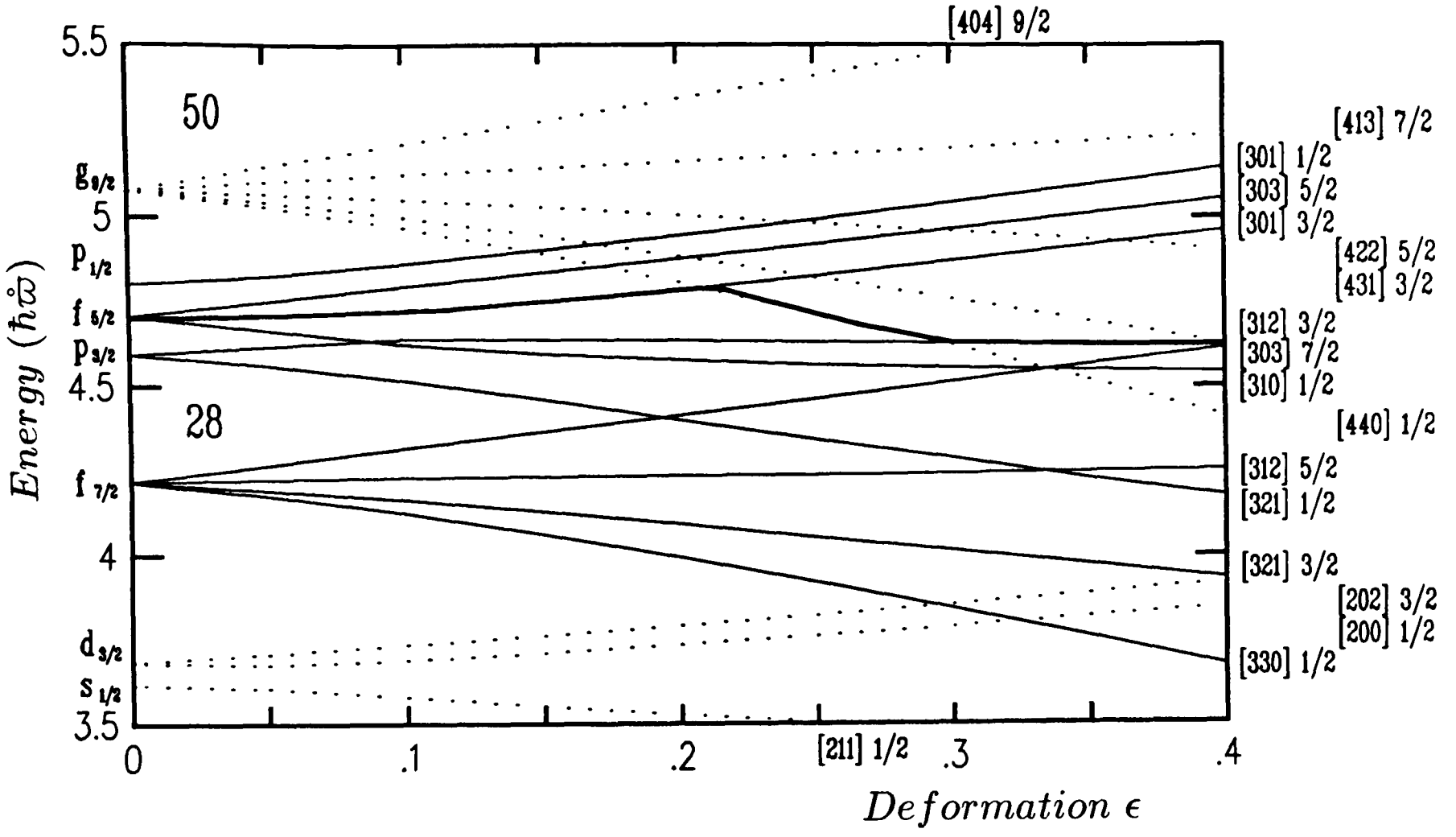

Figure 7.1. Proton single particle levels in the A $\sim$ 75 mass region as a function of the quadrupole deformation ϵ. The approximate position of the bromine Fermi level is indicated by the heavy line. The potential strength parameters $\kappa_p = +0.068$, $\mu_p = +0.38$ are used.

to $\epsilon \sim 0.22$ and the [312]3/2 orbital at larger deformations in the range $0.30 < \epsilon < 0.40$. As these levels are associated with magnetic dipole moments of approximately +2.3 and $+0.75\mu_N$ respectively, the experimental magnetic moments of the $3/2^-$ ground states give a clear signature of the orbitals involved and hence the magnitude of the nuclear deformation.

Since the orbitals of interest to the odd A bromine ground states have the same component of angular momentum and can therefore intermix, the transition between high and low moment is not sharp, but instead has a definite deformation dependence. This is most sensitive in the region $0.22 < \epsilon < 0.30$ where, with increasing deformation, the Fermi level shifts from the [301]3/2 to the [312]3/2 orbital via the [440]1/2 state. As a consequence, the dominant single particle contribution to the total wavefunction changes between the two configurations and is accompanied by a smooth and rather rapid drop in the magnetic moment from +2.3 to $+0.75\mu_N$. The variation of the ground state moment with deformation is illustrated in figure 7.2. Only the positions of the negative parity [301]3/2, [312]3/2 and [303]7/2 bandheads, together with the $1/2^-$ and $3/2^-$ members of the [310]1/2 band are shown.

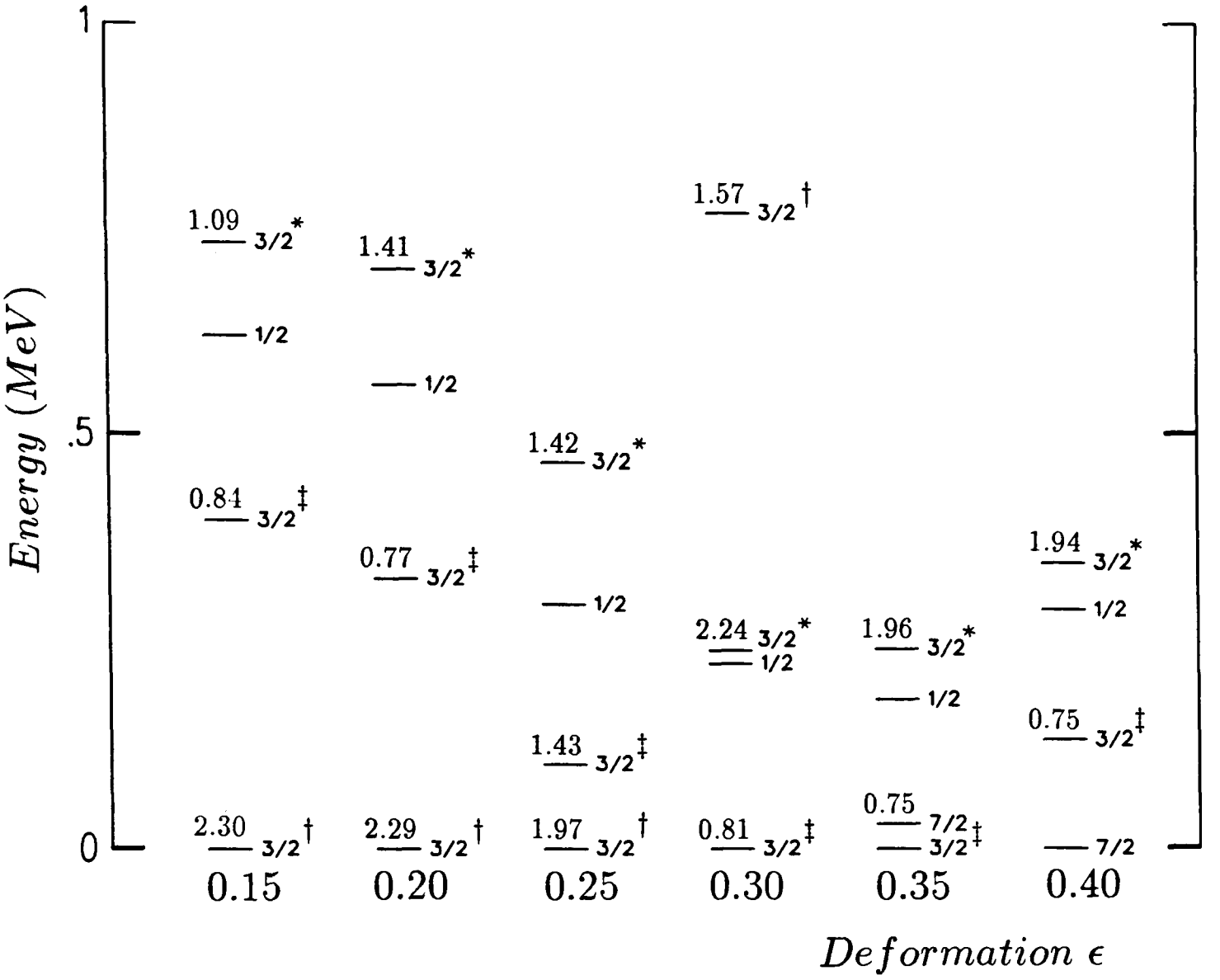

Figure 7.2. A typical deformation dependence of the ground state magnetic dipole moment in the odd A bromine isotopes. The positions of the [301]3/2 (†), [312]3/2 (‡) and [303]7/2 bandheads, together with the 1/2 and 3/2 (*) members of the [310]1/2 band are indicated. The magnetic moments of these three lowest lying $3/2^-$ states are given in μ_N.

The details of this transition and in particular the region of deformation in which it occurs are determined by the the relative splittings of the $4g_{9/2}$, $3f_{5/2}$ and $3p_{3/2}$ subshells. In turn these depend upon the parameters, κ and μ, of the Nilsson potential (see subsection 6.3.1). From the experimental relationship between the magnetic moments and deformations, as deduced from the electric quadrupole moments, it is therefore possible to evaluate the proton potential strength parameters in this mass region to be $\kappa_p = +0.068$ and $\mu_p = +0.38$. The details will be discussed fully in subsection 7.4.1.

Previously, these strength parameters have been evaluated by minimizing the deviation between theoretical and experimental single particle levels in the spherical nuclei ^{16}O, ^{40}Ca, ^{48}Ca, ^{56}Ni and ^{208}Pb and in the deformed A $\sim$ 25, A $\sim$ 165 (rare earth) and A $\sim$ 242 (actinide) regions. While the mass dependence of κ can be approximated by a linear function, it is clear that μ cannot. There is therefore some ambiguity in interpolating μ to the present mass region.

Within these limitations the values $\kappa_p = +0.069$, $\mu_p = +0.42$ and $\kappa_n = +0.072$, $\mu_n = +0.31$ for protons and neutrons respectively can be expected in the region A $\sim$ 75 [1]. These interpolated proton parameters agree fairly well with the values derived from the bromine electromagnetic data which will be used here. Since the only information on the neutron potential strength parameters available from the bromine nuclei derives from the highly complicated odd-odd systems, the interpolated neutron values will be assumed in the subsequent analysis.

Although the description of the $3/2^-$ ground states of the higher mass odd A bromine nuclides in terms of prolate single particle configurations is fairly clear, the $1/2^-$ ground state observed in ^{73}Br presents something of a problem.

As can be seen from figure 7.1, which uses the proton potential strength parameters $\kappa_p = +0.068$, $\mu_p = +0.38$, the bromine Fermi level does not appear include an appropriate prolate Nilsson orbital. The [440]1/2 state can be excluded immediately since it has both the wrong parity and, as a result of the strong Coriolis interaction, leads to a $5/2^+$ bandhead which has been identified experimentally [2]. On the other hand, with the present potential strength parameters the [310]1/2 orbital is expected to lie reasonably close to the Fermi level, particularly for higher deformations as can be seen from figure 7.2. Therefore the potential parameters were varied slightly in order to rearrange the Nilsson diagram in an attempt to accommodate the ^{73}Br ground state. To this end μ was varied in the range $+0.30 \leq \mu \leq +0.55$, corresponding to a splitting of the spherical $3f_{5/2}$ and $3p_{3/2}$ subshells of between +0.14 and -0.04 $\hbar\mathring{\omega}$ respectively, where $\hbar\mathring{\omega} \sim 9.5$ MeV. The deformation was varied up to $\epsilon = 0.40$, by which time the [303]7/2 orbital invariably becomes the ground state.

For $\mu \sim +0.30$ the Nilsson diagram is little changed with respect to figure 7.1 and so the [310]1/2 orbital is still predicted to be no more than a low lying nuclear excitation. In contrast, with $\mu \sim +0.55$ the $3p_{3/2}$ subshell lies above the $f_{5/2}$ subshell. Then, for deformations in the range $0.20 < \epsilon < 0.37$, the Fermi level lies on the [310]1/2 orbital. However, due to the strong Coriolis interaction with nearby [312]3/2 level, the particle-rotor model predicts a $3/2^-$ rather than a $1/2^-$ bandhead. (Note that with a significantly rearranged Nilsson level scheme certain first order band crossings no longer occur. As a result the labelling is slightly different from that given in figure 7.1. Thus the [310]1/2 and [312]3/2 orbitals now originate in the spherical $3p_{3/2}$ and $3f_{5/2}$ subshells respectively). Further, the shift of the Fermi level between the [301]3/2 and [312]3/2 orbitals which is so crucial to the interpretation of the magnetic properties exhibited by the higher mass odd A nuclides no longer occurs. Therefore such a large value of μ should not be considered.

Thus, one concludes that there is *no* orbital which can give rise to a $1/2^-$ bandhead for axially symmetric prolate nuclear deformations in the particle-rotor model.

A more general Nilsson diagram, which illustrates the deformation dependence of the single particle orbitals along closed paths in the (ϵ, γ) plane, is shown in figure 7.3. The states are labelled by the asymptotic quantum numbers for axially symmetric deformations only. It can be seen from this figure that the axially symmetric prolate level ordering is not considerably altered when the nuclear asymmetry is increased towards $\gamma = \pi/6$. As a result, the conclusions drawn above for axial shapes also apply, at least qualitatively, in the entire region $0 \leq \gamma < \pi/6$. Therefore the possibility of a prolate-triaxial ground state for ^{73}Br may be excluded. Again this has been verified explicitly for various parametrizations of the single particle potential.

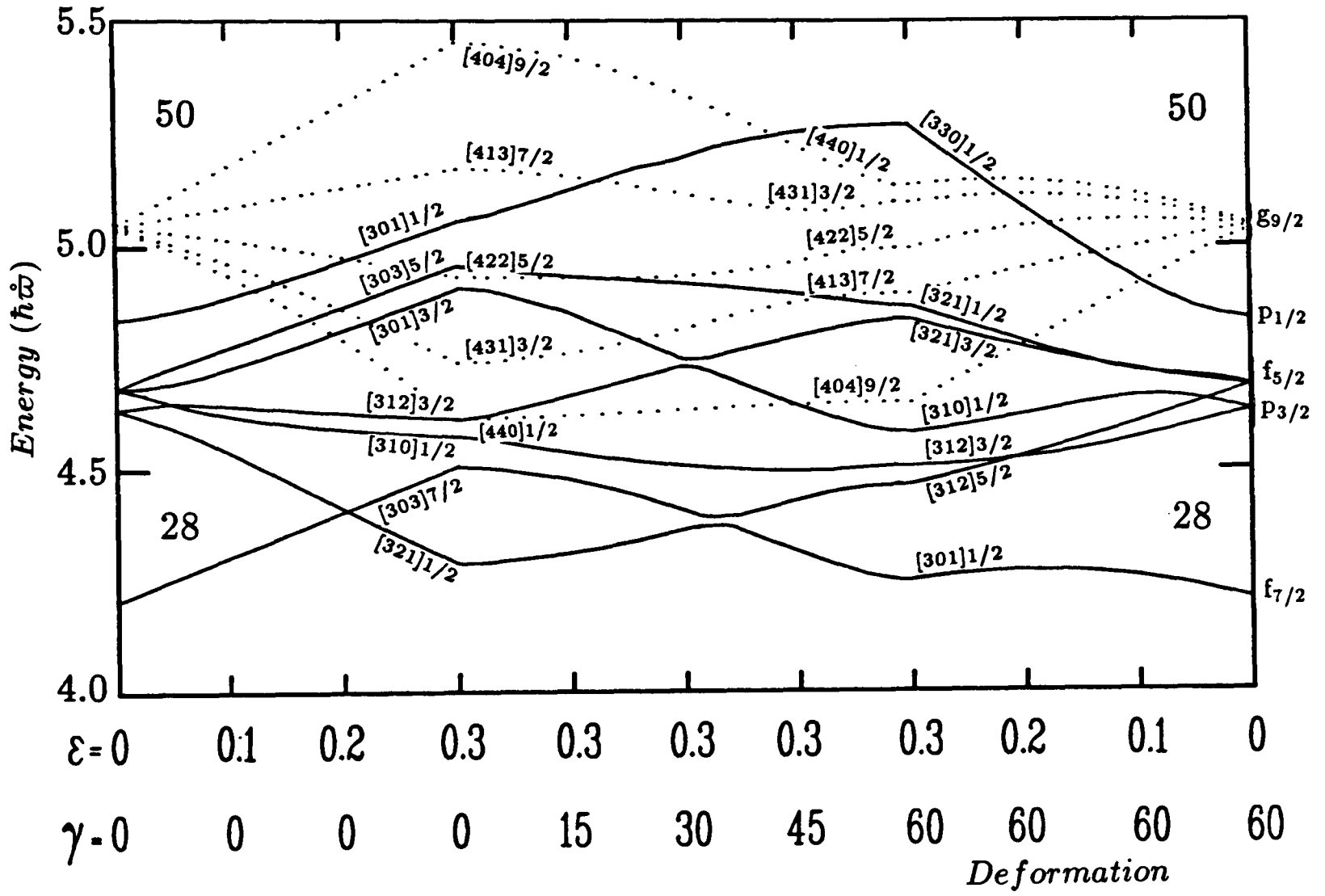

Figure 7.3. Proton single particle levels in the A $\sim$ 75 mass region in the (ϵ, γ) plane. The potential strength parameters $\kappa_p = +0.068$, $\mu_p = +0.38$ are used.

However for oblate-triaxial nuclear deformations, which appear on the right half of figure 7.3, there exist two possibilities for the ^{73}Br ground state; the [321]1/2 and [310]1/2 orbitals. The former lies on the Fermi level for oblate or oblate-triaxial deformations in the approximate

range $\epsilon < 0.25$, $\pi/6 < \gamma \leq \pi/3$. In fact it turns out that the large Coriolis interaction arising from the close proximity of the [321]1/2 and [321]3/2 orbitals, which persists from the spherical to the asymptotic limit, leads to a $5/2^-$ bandhead. (The same argument applied to the [321]3/2 orbital thus precludes the possibility of oblate-triaxial deformed ground states in the heavier isotopes). Therefore the latter [310]1/2 Nilsson orbital remains as the only candidate which is expected to result in a $1/2^-$ bandhead, thus confining the deformation of the ^{73}Br ground state to the region $\epsilon > 0.25$, $\pi/6 < \gamma \leq \pi/3$.

Finally, to reiterate the basic conclusion of this preliminary discussion, it is clear that the ground state nuclear deformation must undergo some form of transition between prolate-triaxial ($\gamma < \pi/6$) and oblate-triaxial ($\gamma > \pi/6$) shapes in passing from the heavier odd mass bromine nuclei to ^{73}Br.

7.3 The particle-rotor parameters

The analysis presented in this chapter utilizes the particle -VMI rotor model as described in the previous chapter. Before embarking on a detailed description of the nuclear structure of each isotope, some general points about the model parameters need to be made.

Firstly with regard to the shape parametrization, only quadrupole deformations in the stretched coordinate system (ϵ, γ) will be considered. These deformations will be confined to the region $\epsilon \geq 0$, $0 \leq \gamma \leq \pi/3$. Although this is a convenient parametrization it suffers from the disadvantage that the ellipsoidal symmetry axis coincides with the intrinsic 2-axis, rather than the 3-axis, for oblate shapes ($\gamma = \pi/3$). While this is of no consequence physically, it tends to confuse the interpretation of the wavefunctions since the basis states, as defined in chapter 6, are always referred to the 3-axis. In order to avoid this complication, the wavefunctions of oblate-triaxial nuclear shapes are quoted in the coordinate system $(-\epsilon, \pi/3-\gamma)$ which maintains the equivalence of the symmetry and intrinsic 3-axes.

The pairing parameters are taken to be $g_0 = +22.0$ and $g_1 = +8.0$ with $\sqrt{5Z}$ or $\sqrt{5N}$ single particle orbitals included above and below the Fermi surface [3]. With the pairing constant $-G$ thus defined, the Fermi level and BCS gap parameter are derived quantities rather than input parameters.

The g-factor of the intrinsic nucleon spin is taken to be 65% of the free value for both protons and neutrons. This is found to reproduce the limiting values $+2.3$ and $+0.75\mu_N$ of the

odd A bromine ground state moments which are observed experimentally. The core g-factor is assumed to be Z/A, while the core quadrupole moment is calculated macroscopically.

For odd A nuclei, 8 deformed single particle orbitals $|i\rangle$ of a given parity were included into the particle-rotor basis while for odd-odd nuclei, 5 proton and neutron states, $|p\rangle$ and $|n\rangle$, of each parity were considered. The errors introduced by this truncation should be negligible.

The parameters of the residual proton-neutron interaction (6.100) are assumed to be identical to those of the rare earth region, as determined by Boisson *et al.* [4]. The tensor force was not included, thus $u_0 = -50.0$ MeV, $u_1 = -9.22$ MeV, $u_2 = +0.52$ MeV, $u_3 = -6.20$ MeV and $V_T = V_{TM} = 0$.

7.3.1 The VMI core parameters

In the particle -VMI rotor model, a natural choice for the VMI parameters are those of the even-even core nuclei themselves. However, the structures of the even-even cores ^{70,72,74,76}Se are by no means trivial. In all these nuclei a low lying 0_2^+ level is observed which cannot be accommodated within the framework of the asymmetric rotor model.

In ^{76}Se there exists a low lying 2_2^+ state associated with a $\Delta I = 1$ gamma band [5]. A description of this nucleus in terms of an asymmetric rotator therefore seems possible and in fact a good agreement between the experimental and theoretical ground and gamma bands may be obtained, as illustrated in figure 6.3.

In contrast, the yrast bands of ^{72,74}Se are not purely rotational but instead are found to exhibit both vibrational and rotational structures, a phenomenon which has been ascribed to shape isomerism. The low spin members of the band are assigned to a vibrational spectrum built upon a near spherical ground state which is crossed at around spin 4 by a $K = 0$ rotational band built upon a well deformed prolate shape lying at an excitation energy of about 900 keV. Thus ^{72}Se develops from a shape coexistent ground state with a rms deformation $\langle\epsilon\rangle \sim 0.20$ into a prolate rotor with $\epsilon \sim 0.31$ [6]. Similar properties are observed in ^{74}Se although the deformation, both static and dynamic, is rather more constant at $\epsilon \sim 0.30$ [7]. In the light of these observations it has been suggested that the 2_2^+ level is associated with a $\Delta I = 2$ beta band built upon the 0_2^+ state. This is not however a unique assignment and the 2_2^+ level in ^{74}Se has also been proposed as the gamma bandhead [8].

Despite the possible shortcomings of an asymmetric rotational description of these nuclei, by identifying the 2_2^+ level (rightly or wrongly!) as the gamma bandhead leads to the VMI parameters listed in table 7.1 . These have been calculated using the program VMIPAR (see

appendix A.2). The cores ^{70,72}Se, with ratios $\Re_2 = 1.69$ and 1.52 respectively, lie outside the region which can be described by the VMI model (see subsection 6.6.1). This could either be a result of perturbative interactions between the 2_2^+ state and levels of the same spin in the vibrational and beta bands, or simply that the level is not gamma but rather beta rotational. (Presumably similar possibilities exist for ^{74}Se, although $\Re_2$ lies within the model limits). Therefore in the case of ^{70,72}Se the maximum gamma asymmetry is assumed and the VMI parameters are deduced by fitting to the 2_1^+ and 4_1^+ levels. This approximation results in an adequate, though not perfect, reproduction of the ground state bands.

Table 7.1. The VMI core parameters of ^{70,72,74,76}Se.

Core	$E_{2_1^+}$ $E_{2_2^+}$ $E_{4_1^+}$ (MeV)	γ (deg)	$\Im_0$ ($\hbar^2$ MeV^{-1})	C (MeV^3)	S
^{76}Se	0.56 1.22 1.33	25.9°	6.44	0.023	0.083
^{74}Se	0.64 1.27 1.36	26.8°	4.05	0.011	0.684
^{72}Se	0.86 1.32 1.64	30.0°	1.52	0.014	10.16
^{70}Se	0.95 1.60 2.04	30.0°	3.26	0.049	0.297

As will be shown in the following section, the presence of additional odd nucleons induces a substantial increase in the core deformations. With this polarization the deformed core may be stabilized into one particular shape, so that the interference between vibrational and rotational structures present in the isolated core need not be reflected in the corresponding odd A or odd-odd nucleus. In view of these facts it is not clear that VMI parameters, as deduced from an asymmetric rotational description of the even-even cores, may be applied to the odd A and odd-odd nuclei. Therefore in the following sections an independent choice of the VMI parameters will be made where the "true" core parameters seem less appropriate.

7.4 The odd A nuclei ^{73,75,77}Br

7.4.1 The negative parity states

The high spin negative parity spectra of ^{73,75,77}Br appear as a regular sequence of two stretched E2 bands. Connecting dipole transitions have also been observed up to spin $11/2^-$ in ^{75}Br [9] and up to $21/2^-$ in ^{77}Br [10]. In both cases the bands terminate at the $3/2^-$ ground state. In-beam spectroscopic studies of ^{73}Br [2] have identified a band sequence which bears a remarkable resemblance to that of ^{75}Br. However, the last stretched E2 transition terminates not on the ground state but instead on an excited level at 178 keV which has therefore been assigned as $3/2^-$.

The results of a particle-rotor analysis of these $3/2^-$ yrast bandheads and also those of ^{79,81}Br are shown in table 7.2 . By requiring that the calculations reproduce the previously known magnetic moments of ^{79,81}Br [11] at the nuclear deformations implied by the ground state static electric quadrupole moments [11], it is possible to extract the Nilsson proton potential parameters $\kappa_p = +0.068$ and $\mu_p = +0.38$ quoted previously. For the remaining isotopes, ^{73,75,77}Br, the deformations are calculated from the electric quadrupole transition strengths [2,9,10] with particular emphasis on the stretched E2 transitions to the bandheads. For reasons which will be discussed later, the negative parity states are considered to be axially symmetric.

These quadrupole moments point to a gradual increase in nuclear deformation from $\epsilon = 0.22, \gamma = 0$ in ^{81}Br to $\epsilon = 0.32, \gamma = 0$ in ^{73}Br. This is accompanied by a drop in the experimental magnetic dipole moments from $+2.3$ to $\pm 0.76 \mu_N$. As can be seen from table 7.2, this trend in the magnetic moments is well reproduced by the theory and indicates a transition of the single particle Fermi level from the [301]3/2 to the [312]3/2 orbital. The calculations show that the ground state composition of ^{81}Br is dominated by the [301]3/2 orbital, ^{79}Br is transitional, while the yrast bandheads in ^{73,75,77}Br are almost entirely of [312]3/2 character. (At this juncture it should be restated that the asymptotic quantum numbers serve only to *label* the Nilsson orbitals. Therefore the results presented in the last column of table 7.2 represent the relative contributions from two the Nilsson levels and do not necessarily reflect the exact single particle configurations).

The particle-rotor fits to the band structures in ^{73,75,77}Br are shown in figure 7.4. The VMI parameters of ^{75,77}Br were taken from the corresponding even-even cores while the parameters of ^{73}Br were chosen to be identical to those of ^{75}Br in view of the marked similarities between

Table 7.2. The negative parity yrast bandhead properties of the odd A nuclei $^{73-81}$Br. The electric moment data includes both static quadrupole moments Q (b) and quadrupole transition strengths B(E2; 7/2 → 3/2) (W.u.), denoted † and ‡ respectively. The magnetic dipole moments are quoted in units of μ_N. The final column gives the composition of the bandhead.

Nucleus	Deformation (ϵ, γ)	Electric Moment exp.	theory	Magnetic Moment exp.	theory	Configuration [312]3/2	[301]3/2
^{81}Br	0.22, 0.0°	+0.276(4)†	+0.28	+2.27	+2.28	8%	84%
^{79}Br	0.24, 0.0°	+0.331(4)†	+0.33	+2.11	+2.11	33%	58%
^{77}Br	0.27, 0.0°	35(9)‡	33	±0.92(5)	+0.93	95%	4%
^{75}Br	0.32, 0.0°	61(5)‡	60	±0.76(18)	+0.75	98%	1%
^{73}Br	0.32, 0.0°	45(7)‡	59		+0.75	98%	1%

the band structures. Although the overall energy scaling in the $\alpha = +1/2$ band is relatively well reproduced the positions of the $\alpha = -1/2$ band members become considerably depressed relative to the theory, especially at high spins. The experimental and theoretical electric quadrupole transition strengths are compared in figure 7.5 . The experimental B(E2) values show interesting deviations from the particle-rotor predictions at both high and low spins. A cranked shell model analysis of the negative parity band in ^{75}Br [9] indicates that the aligned spin, although very small at low rotational frequencies, increases to $i \sim 4$ in the frequency range 0.3 MeV $\leq \hbar\omega \leq$ 0.4 MeV. This is attributed to a gradual $\pi^2(4g_{9/2})$ alignment leading to a band crossing around spins $17/2^- \rightarrow 21/2^-$. As a result the experimental B(E2) values begin to fall below the particle-rotor predictions in this spin region as seen in ^{73,75}Br.

At low spins the measured B(E2) values of ^{73}Br lie well above the values expected on the basis of the bandhead $7/2^- \rightarrow 3/2^-$ transition strength. Some low spin irregularities are also observed in ^{75}Br. These effects are possibly due to prolate-oblate shape coexistence in the even-even cores, ^{72,74}Se. Total energy surface calculations in ^{75}Br [9] indicate that an energy minimized prolate ($\epsilon = 0.33, \gamma = 0$) [312]3/2 ground state is expected to coexist with an oblate ($\epsilon = 0.19, \gamma = \pi/3$) [321]3/2 state lying at an excitation energy of only 560 keV. The interaction between such prolate and oblate states may be approximated by

$$\langle i_{pro}|V|i_{obl}\rangle = \langle \mathrm{core}_{pro}|V|\mathrm{core}_{obl}\rangle\langle i_{pro}|i_{obl}\rangle$$

where $\langle \mathrm{core}_{pro}|V|\mathrm{core}_{obl}\rangle$ is the effective interaction between the 0_1^+ ground state and 0_2^+ shape isomeric state of the even-even core. Since the structures of these prolate and oblate states are

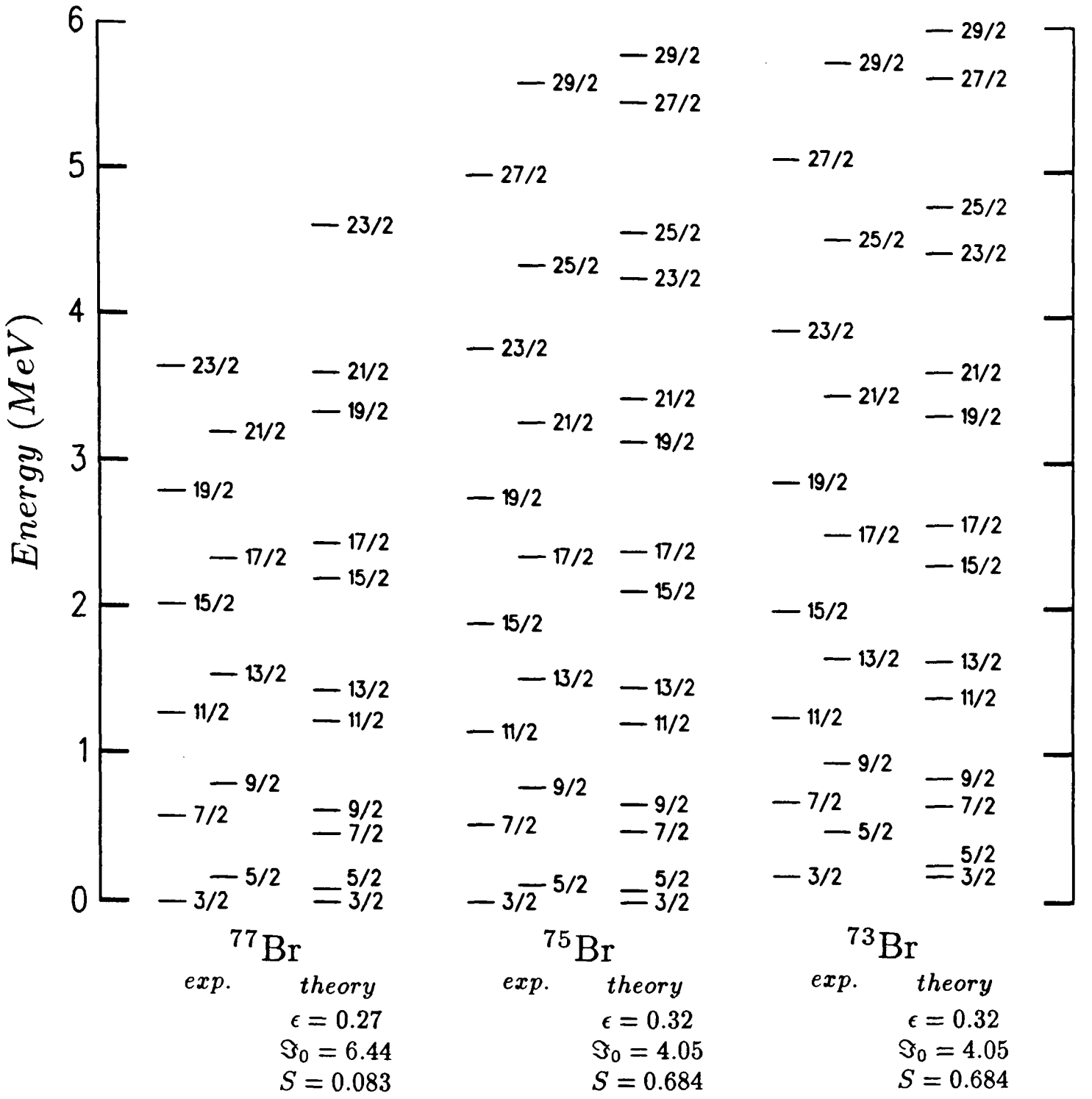

Figure 7.4. The negative parity band structures of the odd A nuclei ^{73,75,77}Br. The model parameters are indicated.

very similar with an 80% overlap of the single particle wavefunctions, a considerable amount of prolate-oblate interference may exist. Not only does this disturb the low spin band structure but it also reduces the transitional quadrupole moments and hence B(E2) values. Therefore fitting to the bandhead quadrupole transition strength might well lead to an underestimation of the nuclear deformation and B(E2) values at higher spins.

On the other hand, the even-even core ^{76}Se does not show shape coexistent effects and so one would not expect such considerations to influence the low spin structure of ^{77}Br. As can be seen from figure 7.5, the B(E2) values of ^{77}Br are indeed reproduced more closely.

The low lying energy levels of ^{73,75,77}Br [2,12,10] are shown in figure 7.6 . Notice that experimentally, besides the first two members of the ground state band, no states are observed

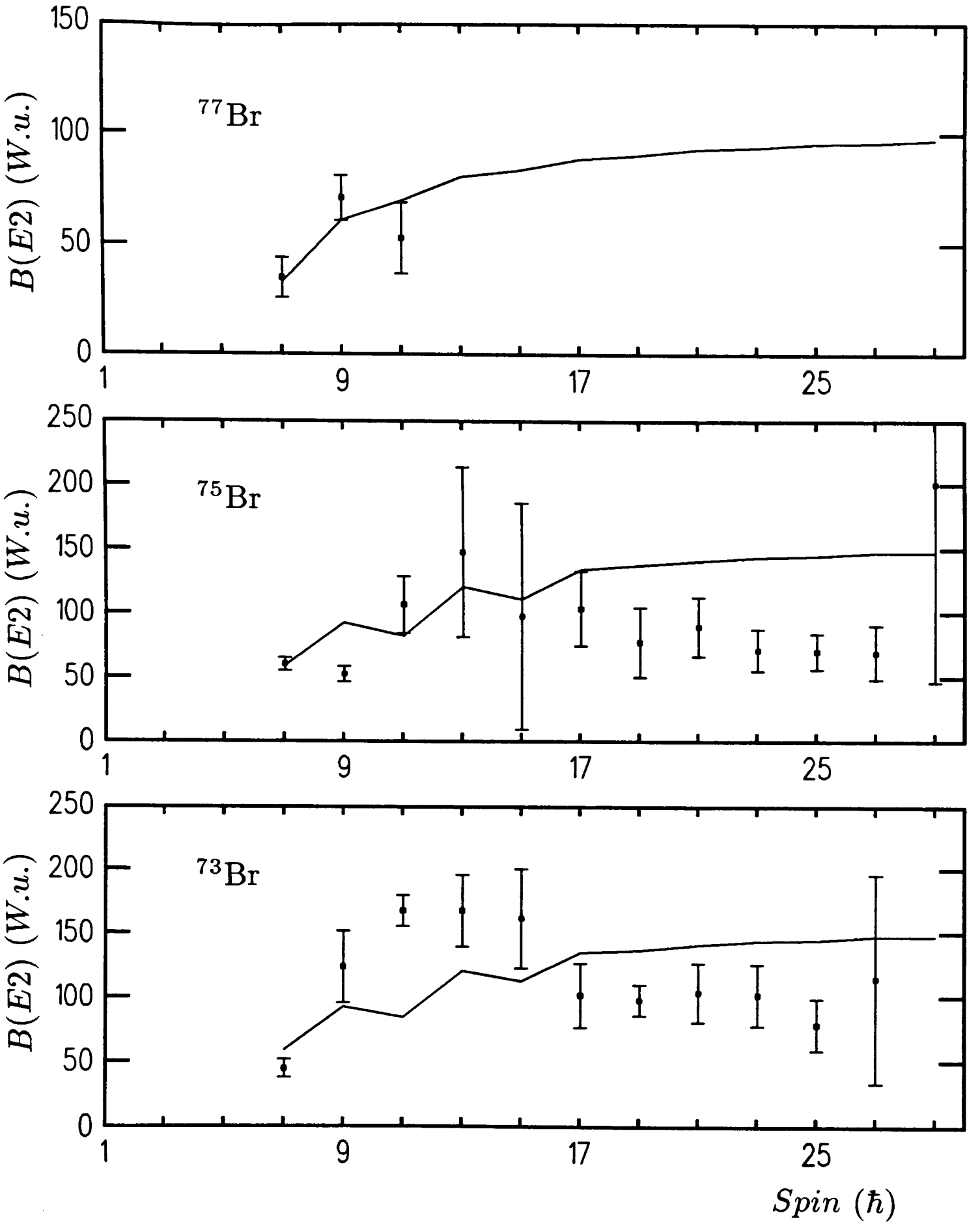

Figure 7.5. The experimental and theoretical B(E2) values in the negative parity bands of ^{73,75,77}Br. The quadrupole deformation is chosen so as to reproduce as far as possible the $7/2^- \rightarrow 3/2^-$ transition strength.

below 150 keV in ^{75,77}Br. Theoretically, this is also true in the case of axial symmetry. However for an axially asymmetric nucleus, using for instance the value $\gamma \sim 26°$ suggested by the even-even cores, several very low lying states (< 100 keV) are predicted. Also the enhanced

rotational alignment, resulting from the admixture of $\Omega = 1/2$ components into the single particle wavefunction when triaxiality is introduced, causes the $5/2^-$ member of the yrast band to become the ground state. Since this is expected to remain the case up to quite high deformations ($\epsilon < 0.30, \gamma = 26°$) the observed ground states of the lesser deformed isotopes ^{79,81}Br could not be reproduced. Further there are now two $3/2^-$ states built from the [312]3/2 orbital which correspond to orthogonal combinations of roughly equal amounts of the two angular momentum projections, $K = 1/2, 3/2$. The magnetic moments of both these states remain above $+1.1\mu_N$, in contrast to the much smaller experimental moments of ^{75,77}Br. For these reasons the negative parity states of ^{75,77}Br and the yrast band of ^{73}Br are considered to be axially symmetric.

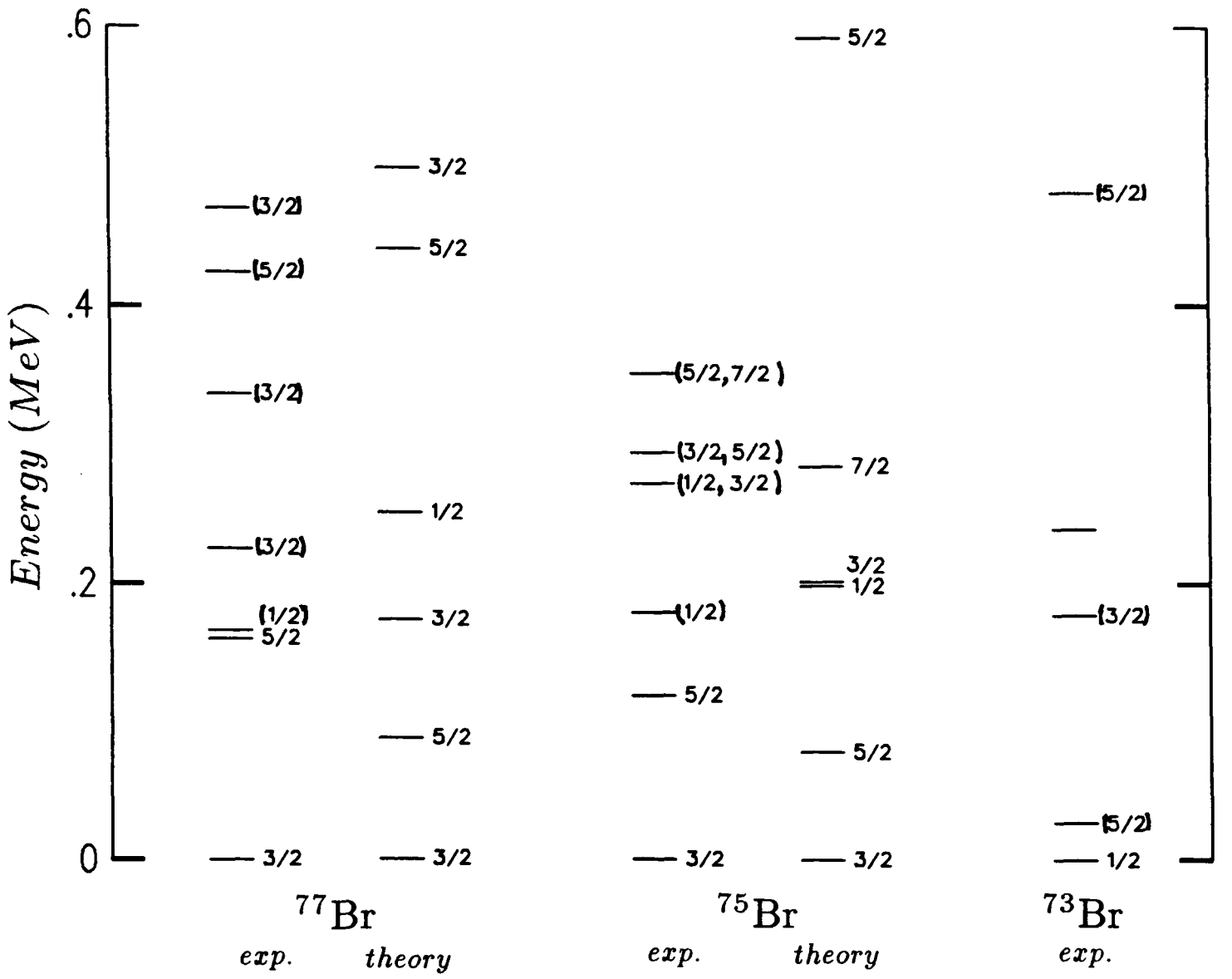

Figure 7.6. The low lying negative parity states of the odd A nuclei ^{73,75,77}Br. The theoretical levels are also given for comparison in the cases of ^{75,77}Br.

With axial symmetry, the $(1/2_1^+)$ and $(3/2_2^+)$ states in ^{75,77}Br may be associated with the [310]1/2 band. The reverse ordering of these levels predicted for ^{77}Br is peculiar to the deformation $\epsilon \sim 0.27, \gamma = 0$. Generally the normal ordering is reproduced by the theory, as can be seen from figure 7.2.

The low lying levels of ^{73}Br are somewhat different. The $(3/2^-)$ yrast bandhead and first excited state occur at 178 and 482 keV respectively. By analogy with the heavier bromine nuclides these have been interpreted in terms of a prolate nuclear shape. Below these lie the $1/2^-$ ground state and a presumed $(5/2^-)$ level at only 27 keV.

It has already been concluded that a $1/2^-$ ground state can only result from the [310]1/2 orbital for oblate or oblate-triaxial nuclear shapes. Both of these possibilities have been considered in the calculations. Oblate-triaxial ($\gamma \sim 26°$) nuclear deformations result in a normal $1/2^-$, $3/2^-$, $5/2^-$ ordering of the [310]1/2 band members, as do pure oblate deformations $\epsilon > 0.30$, $\gamma = \pi/3$. However for smaller oblate deformations $0.25 < \epsilon < 0.30$, $\gamma = \pi/3$ the required $1/2^-$, $5/2^-$ ordering is obtained. Since the $5/2^-$ level is expected to become the ground state for smaller deformations, the close proximity of the $1/2^-$ and $5/2^-$ band members suggests that the nuclear deformation lies at the lower end of this range.

Unfortunately, more quantitative calculations are not possible without a knowledge of the moment of inertia. With such a drastic change in both the magnitude and shape of the nuclear deformation it is unlikely that the VMI parameters assumed for the prolate [312]3/2 band will still apply. In fact with these parameters the $1/2^-$ ground state band is predicted to be yrast. The fact that this is not the case experimentally must imply that the oblate shape has a smaller moment of inertia than the prolate shape. Using Grodzins relation (6.12) this suggests that the magnitude of the oblate deformation is somewhat smaller than the prolate deformation ($\epsilon \sim 0.32, \gamma = 0$). Again this points to a value of the nuclear ground state deformation of ^{73}Br towards the lower end of the range $0.25 < \epsilon < 0.30$, $\gamma = \pi/3$.

The existence of such an oblate ground state in ^{73}Br is the first experimental evidence for the prolate-oblate shape transition in the bromine nuclides. This transition has been predicted by several total energy surface calculations [13,14,15], although it was expected to occur at higher masses between ^{78}Br and ^{79}Br [13]. However the ground state configurations deduced from the present magnetic moments prove that both ^{75}Br and ^{77}Br are still prolate. It is also interesting to note that shape coexistence calculations on the neighbouring krypton nuclei [15] indicate that the magnitude of the oblate deformation is smaller than that of the prolate deformation, as is possibly the case in ^{73}Br.

7.4.2 The positive parity states

A dominant and widespread feature of odd A nuclei in this mass region is the presence of positive parity band structures arising from the unique parity $4g_{9/2}$ subshell. In the lighter bromine nuclides these occur as low energy excitations [2,9,10], as shown in figure 7.7 . The large signature splitting indicates immediately their decoupled nature and hence an origin in the low-Ω members of the $4g_{9/2}$ subshell. Characteristically, the energy spacings within the favoured bands resemble those in the ground state rotational bands of the corresponding even-even cores.

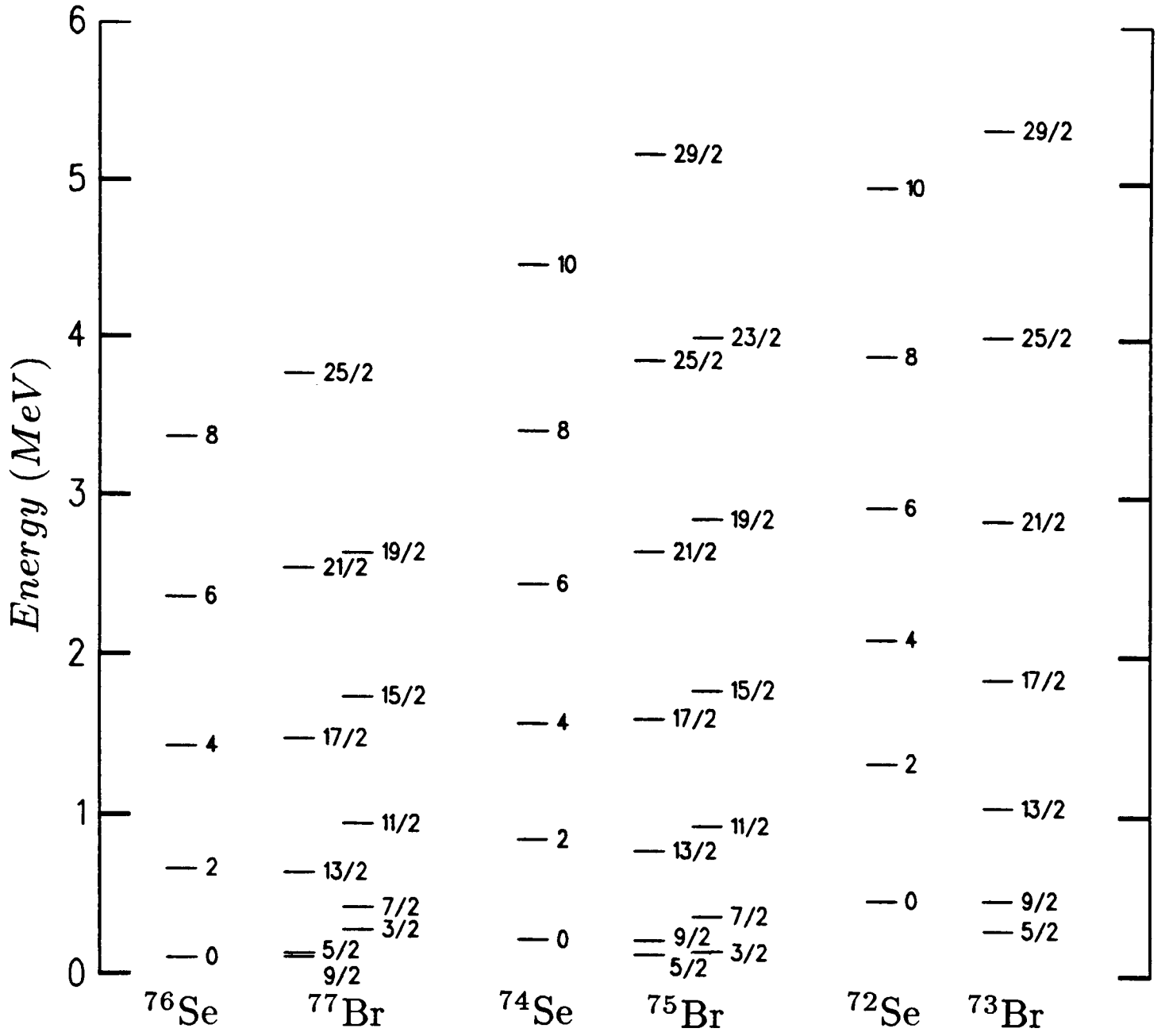

Figure 7.7. The positive parity band structures of the odd A nuclei ^{73,75,77}Br. The energy levels of the ground state rotational bands in the adjacent even-even cores are indicated for comparison.

In passing down the isotopic chain, the $5/2^+$ favoured band member is seen to systematically drop in energy, ultimately becoming the bandhead in ^{75}Br. Accompanying this is a fall in the excitation energies of the low spin $3/2^+$ and $7/2^+$ unfavoured band members. Quantitatively, these phenomena can be readily explained by an increase in the nuclear deformation with

reducing neutron number. This rise in deformation causes both the proton Fermi level to move towards the higher-Ω states in mid subshell and also the overall quadrupole substate splitting to increase. As a result, the Coriolis interaction weakens and there is an increasing tendency towards strong coupling characteristics.

Despite this simple interpretation, the particle-rotor model has some difficulty in reproducing these trends in a more quantitative manner. Figure 7.8 compares the experimental data on ^{75}Br with the theoretical levels for various parameter sets. The 8 single particle levels considered in the model space include the entire $4g_{9/2}$ subshell and several low lying members of the $4g_{7/2}$ and $4d_{5/2}$ subshells. In all cases the ϵ deformation is chosen so as to reproduce the experimental B(E2; $13/2 \rightarrow 9/2$) values [2,9,10].

It is clear from figure 7.8b that an axially symmetric ($\gamma = 0$) nuclear deformation places the unfavoured band too high in energy in comparison with the experimental data. As has been pointed out by Toki and Faessler [16], the signature splitting can be reduced by the introduction of axial asymmetry. An increase of γ deformation from 0 to $\pi/3$ transforms the region of the $4g_{9/2}$ subshell around the Fermi level from low to high-Ω states, as shown in figure 7.3. Consequently there is a gradual transition from the decoupling limit to the strong coupling limit where there is no distinction between favoured and unfavoured states. By taking the asymmetric deformation $\gamma = 26.8°$ and VMI parameters suggested by the even-even core, the position of the unfavoured band moves towards its experimental position (figure 7.8c). However, despite this improved agreement, the predicted positions of the $3/2^+$, $5/2^+$ and $7/2^+$ levels are still too high, suggesting that the calculations overestimate the strength of the Coriolis force and hence the degree of rotational alignment.

There are three ways by which the level of decoupling may be reduced. Firstly, the nuclear asymmetry may be increased further. This takes the nucleus into the oblate-triaxial region where the low lying nuclear structure is dominated by the strongly coupled bands characteristic of high-Ω orbitals. States with $I < K(\Omega)$ have no place in such a regime and so the $3/2^+$ and $5/2^+$ states shift upwards, rather than downwards, in energy.

Alternatively, the Coriolis force may be reduced directly by attenuating the (off-diagonal) matrix elements of the appropriate single particle operators by some constant factor, $\xi \leq 1.0$. Although there is a slight tendency towards the correct positioning of the low spin levels, even with a value as low as $\xi = 0.60$ the $5/2^+$ level is still far from becoming the favoured bandhead (figure 7.8d). Further, above spin $13/2^+$ the positions of the favoured-unfavoured band members are reversed compared to the observed level ordering.

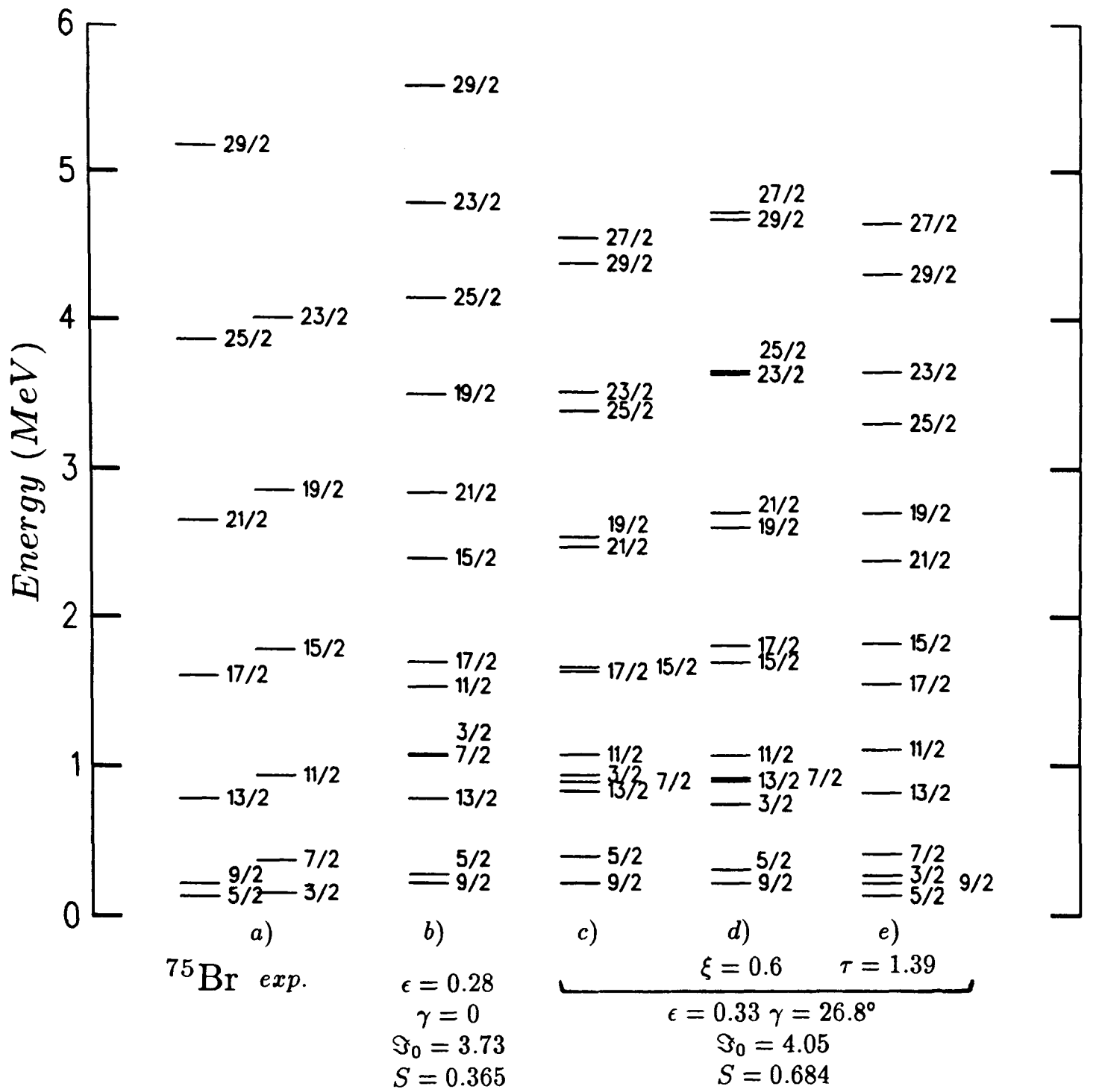

Figure 7.8. The experimental and theoretical positive parity excitation energies of ^{75}Br. The model parameters are indicated. The experimental energies are shown in a). The axial and triaxial theoretical levels are shown in b) and c) respectively. The effects of the parameters ξ and τ are demonstrated in d) and e).

Finally, the relative effectiveness of the Coriolis interaction may be reduced by increasing the quadrupole coupling strength of the nuclear potential by a factor, τ. In the present model there is an intimate connection between the quadrupole interaction strength and the electric quadrupole operator. By discarding this relationship, the quadrupole level splittings may be chosen without the constraints imposed by the electric multipole moments. With this extra degree of freedom a much improved reproduction of the experimental excitation energies becomes possible, as illustrated in figure 7.8e. Not only is the correct ordering of the favoured and unfavoured band members reproduced but the $3/2^+$, $5/2^+$ and $7/2^+$ states are placed close to their experimental energies. Therefore this, rather than a direct attenuation, seems to be the most satisfactory

resolution of the problem with the Coriolis interaction.

Similar conclusions may be drawn about the positive parity levels in ^{73,77}Br. The theoretical fits to these spectra are shown in figure 7.9 for the cases were the quadrupole interaction strength is constrained by the electric multipole moments (figures 7.8b and e) and allowed to vary freely (figures 7.8c and f). No Coriolis attenuation was introduced. As before, the best fit to the experimental energies is obtained when the quadrupole strength is allowed to vary freely. Again, the nuclear asymmetries and VMI parameters are taken from the even-even cores.

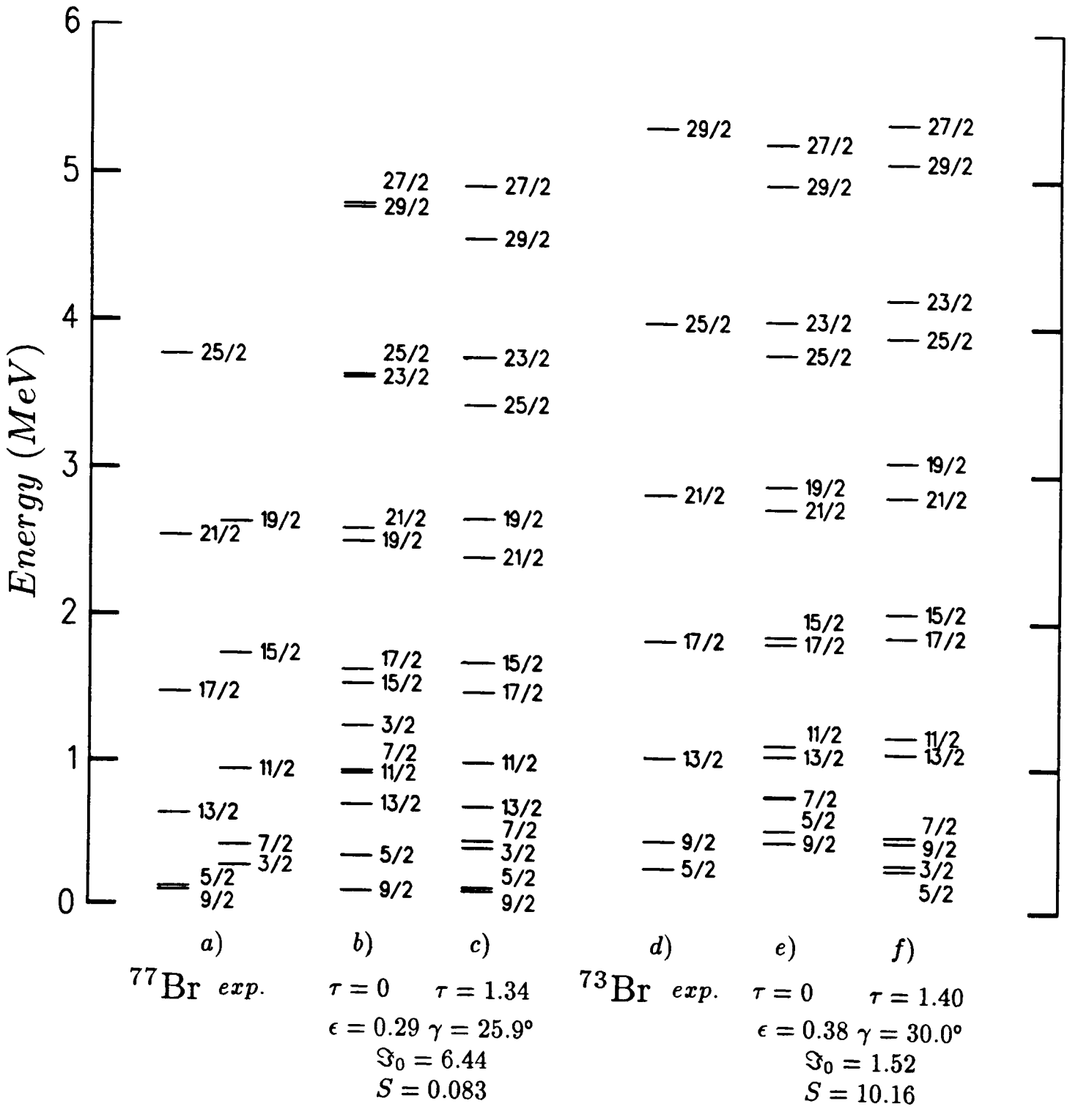

Figure 7.9. The theoretical and experimental positive parity excitation energies of ^{73,77}Br. The model parameters are indicated. The experimental energies are shown in a) and d). The theoretical levels corresponding to the standard and enhanced quadrupole strengths are shown in b), e) and c), f) respectively.

The experimental and theoretical B(E2) values are compared in figure 7.10 for the case where the quadrupole coupling strength is varied freely. As was the case in the negative parity bands, the experimental B(E2) values drop below the theoretical expectations around spin $17/2^+$. Again this may be attributed to a $\pi^2(4g_{9/2})$ alignment, although this can only be partial since full alignment is now blocked. However, in contrast to the negative parity case, the low spin B(E2) values seem to adequately accounted for in all three isotopes, indicating that the effects of prolate-oblate mixing at low spin are no longer present. Indeed, shape coexistence effects are expected to be weak for positive parity states since the prolate low-K $4g_{9/2}$ states have no structural analogues at oblate deformations where the high-K orbitals are present [9].

Table 7.3 lists both the deformation parameters of the positive parity states of ^{73,75,77}Br and the quadrupole strength factors τ derived from this analysis. From these results it would appear that in this particular case the Nilsson potential underestimates the quadrupole coupling strength by a factor of $\tau \sim 1.4$. This may be attributed to a failure of the Nilsson potential to describe the true radial form of the quadrupole potential term [17]. Since the positive parity band structures in the isotopes considered here are dominated by the $4g_{9/2}$ configurations then one may consider the present results to imply that the matrix elements of the true quadrupole radial potential, $\langle Nl|V_2(r)|Nl\rangle$, are numerically given by

$$\langle 44|V_2(r)|44\rangle \sim 1.4 \times \hbar\varpi_0 \frac{2}{3}\sqrt{\frac{4\pi}{5}}\langle 44|r^2|44\rangle.$$

The root of such a discrepancy in the Nilsson potential probably lies in the application of the correction potential V_{corr} (see subsection 6.3.1). The purpose of this term is to flatten the base of the pure spherical harmonic potential in a manner approximating the true nuclear one-body potential. However, V_{corr} is considered to retain its spherical form even when the potential is deformed. The quadrupole part of the deformed potential therefore remains that of a pure harmonic oscillator. Since V_{corr} is most important for the high orbital angular momentum orbitals it is not surprising that out of all the orbitals studied thus far such discrepancies only come to light for the $4g_{9/2}$ subshell.

It is worth noting that the basis for the apparent success of the simplified particle-rotor model of Toki and Faessler [18] in describing other positive parity $4g_{9/2}$ structures in this region [16,19,20] also lies in such an increase of the quadrupole strength. The model potential employs the Nilsson quadrupole coupling strength characteristic of the $N = 6$ shell [21]. The application of this same "rare earth" potential to the present mass region therefore strictly lies outside the formalism of the Nilsson model. In fact such an assumption overestimates the Nilsson quadrupole strength by a factor $\langle r^2\rangle_{N=6}/\langle r^2\rangle_{N=4} = 1.36$, almost identical to the present value.

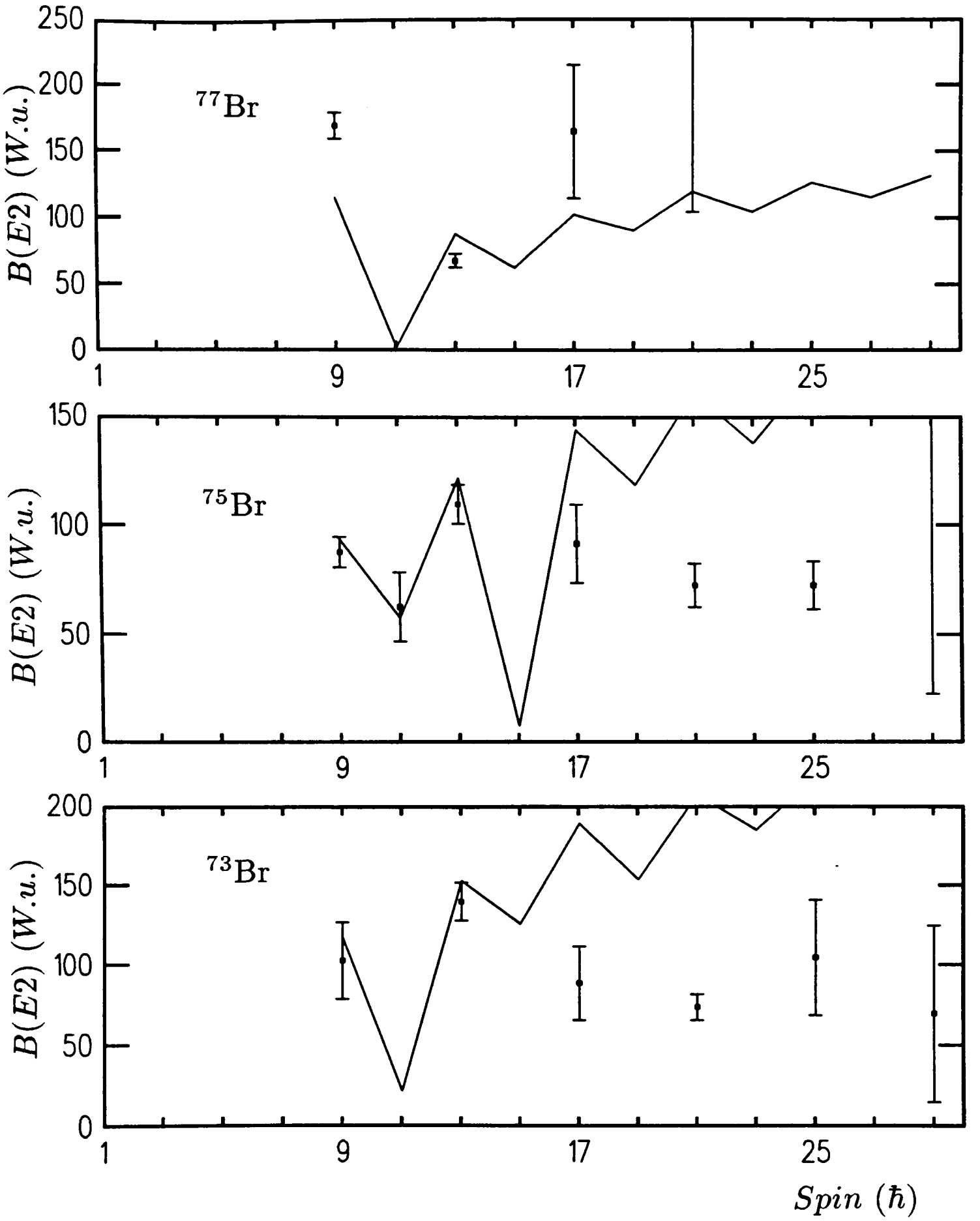

Figure 7.10. The experimental and theoretical B(E2) values in the positive parity bands of ^{73,75,77}Br.

It would be interesting to study decoupled (since strongly coupled bands are adiabatic and therefore insensitive to the quadrupole splitting) unique parity band structures in other mass regions in order to investigate this problem further.

Table 7.3. The positive parity nuclear deformations of ^{73,75,77}Br.

Nucleus	Quadrupole Deformation (ϵ, γ)	Quadrupole Strength Factor τ
^{77}Br	0.29, 25.9°	1.34
^{75}Br	0.33, 26.8°	1.39
^{73}Br	0.38, 30.0°	1.40

7.5 The odd-odd nuclei ^{72,74,76}Br

The conclusions drawn in the previous section relating to the Nilsson quadrupole coupling strength apply only to $\pi 4g_{9/2}$ orbitals. There is little reason to apply the same quadrupole strength factor to $\nu 4g_{9/2}$ orbitals, let alone the negative parity configurations. In general one might expect each proton and neutron subshell to be associated with a distinct quadrupole strength factor. As a result, there is no single value of τ which may be applied to the mixed proton and neutron configurations occurring in odd-odd nuclei. Therefore the more empirical Coriolis attenuation factor ξ will be applied where required.

As mentioned before, the interpolated parameters $\kappa_n = +0.072$, $\mu_n = +0.31$ [1] are assumed for the neutron potential. Since these are not greatly different from the corresponding proton parameters, figures 7.1 and 7.3 may be referred to for the neutron single particle level scheme.

7.5.1 ^{76}Br

Three $\Delta I = 1$ band structures are known in ^{76}Se, the ground state 1^- band and bands built upon an excited $(4)^-$ level at 302 keV and the isomeric $(4)^+$ state at 103 keV [22]. These are illustrated in figure 7.11 .

The static electromagnetic moments of the 1^- ground state have been measured previously to be $\mu = \pm 0.55 \mu_N$ and $Q = \pm 0.27(1)$ b [11]. This quadrupole moment implies a deformation of $\epsilon = 0.31, \gamma = 0$ which fits in well with the systematics of the odd A nuclear deformations (tables 7.2 and 7.3). Using the VMI core parameters of ^{74}Se the experimental band structure (figure 7.11a) is well reproduced by the particle-rotor calculations (figure 7.11c), although the 1^- bandhead is only placed below the 2^- level with a Coriolis attenuation of $\xi = 0.70$. The band head configuration is $\pi[312]3/2\nu[422]5/2$ K= 1 (96%) with predicted moments of $-0.77\mu_N$ and $Q = +0.27$ b. This confirms the previous configuration assignment [23]. In addition, the

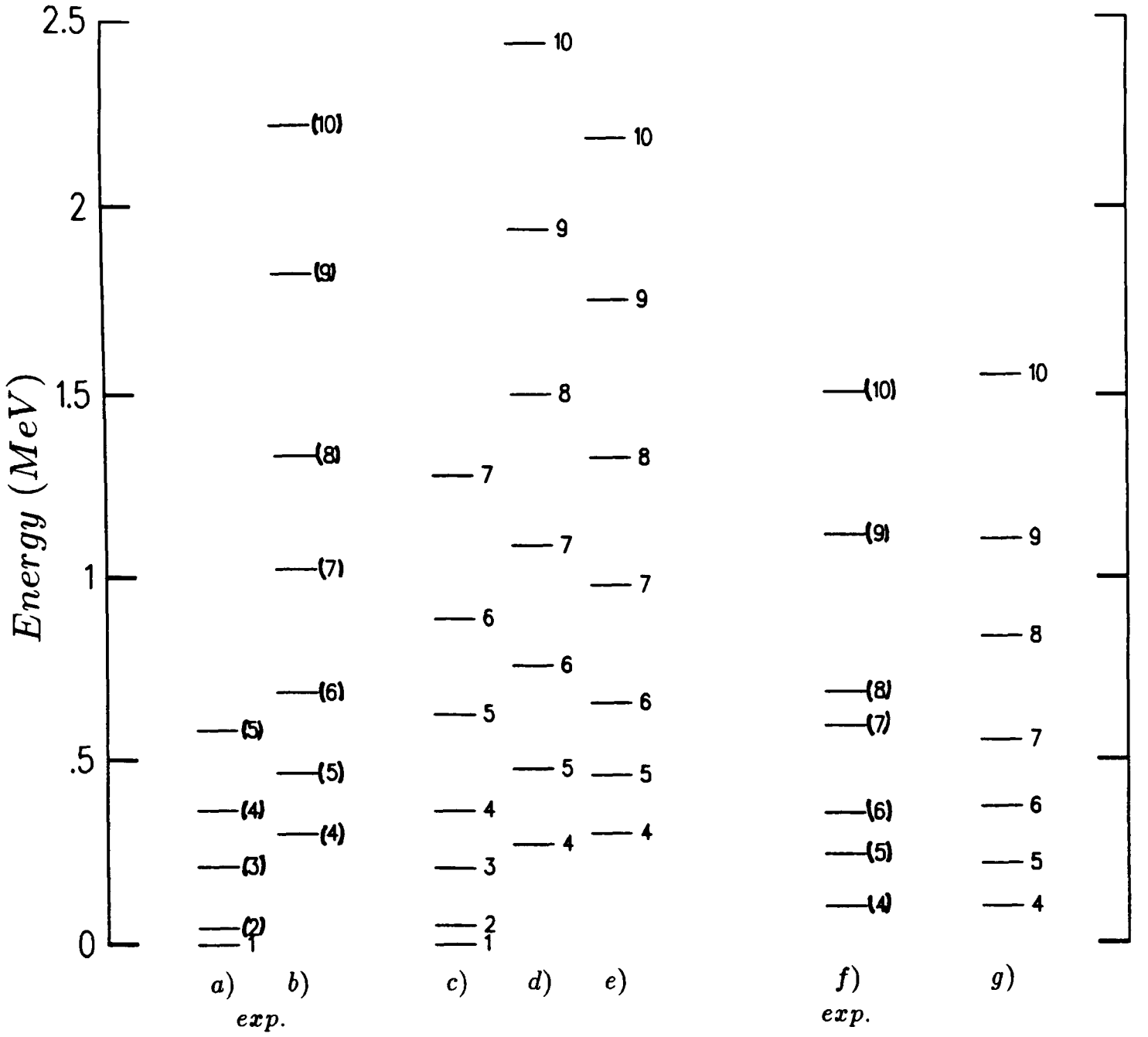

Figure 7.11. The experimental and theoretical band structures of ^{76}Br. The model parameters are indicated. The experimental energies are illustrated in a), b) $(-\pi)$ and f) $(+\pi)$. The corresponding theoretical levels are shown in c), d), e) $(-\pi)$ and g) $(+\pi)$.

theoretical electromagnetic strengths (in W.u.) of the $(2)^- \rightarrow 1^-$ transition, B(M1)= 0.132 and B(E2)= 111, are in good agreement with the corresponding experimental values, B(M1)= 0.100(5) and B(E2)< 160 respectively [24].

With this same deformation, a 4^- bandhead is predicted at an excitation energy of 271 keV corresponding to the $\pi[312]3/2\nu[422]5/2$ K= -4 (91%) configuration, the Gallagher-Moszkowski split conjugate of the ground state. This coincides reasonably well with the 302 keV experimental excitation energy of the $(4)^-$ bandhead. However, the $(7)^-$ and $(8)^-$ members of the experimental band (figure 7.11b) show a bunching which is not reproduced by the theory (figure 7.11d). Further, the large aligned angular momentum of this band ($i \sim 3$) indicates the participation of a $4g_{9/2}$ proton [22]. The possibility of such configurations has also been investigated.

Particle-rotor calculations show that there are two possible candidates. At the deformation $\epsilon = 0.31, \gamma = 0$ there exists the $\pi[440]1/2\nu[301]3/2$ K= 2 (39%), K= -1 (33%) configuration, while at slightly smaller deformations ($\epsilon \sim 0.28, \gamma = 0$) there is also the $\pi[440]1/2\nu[303]5/2$ K= 3 (41%), K= -2 (38%) configuration. The band structures are extremely similar and both give an excellent reproduction of the experimental levels and in particular the $(7)^-, (8)^-$ grouping. The former configuration is illustrated in figure 7.11e (the bandhead is placed at the experimental excitation energy). Again the Coriolis force was attenuated by $\xi = 0.70$ which leads to an expansion of the band to the degree observed experimentally. However, neither configuration corresponds to K= -4 and so a 4^- bandhead should not necessarily be expected. In fact the $\pi[440]1/2\nu[301]3/2$ band is predicted to have a low lying 2^- level which drops just below (25 keV) the 4^- level when the Coriolis attenuation is reduced to $\xi = 0.70$. No such level ordering has been observed as yet. In contrast, the 4^- level remains as the $\pi[440]1/2\nu[303]5/2$ bandhead in spite of the Coriolis attenuation so that this configuration might be preferred.

Like the $(4)^-$ band, the large aligned angular momentum ($i \sim 4$) of the isomeric $(4)^+$ band (figure 7.11f) and the $(7)^+, (8)^+$ grouping indicates the presence of a $4g_{9/2}$ proton [22]. The theoretical interpretation of this band structure in terms of a $\pi[431]3/2\nu[422]5/2$ configuration has already been given [25]. The present calculations give similar results although the $(7)^+, (8)^+$ grouping is not particularly well reproduced. At $\epsilon = 0.31, \gamma = 0$ the three lowest band members are predicted to be almost degenerate and ordered 5^+, 6^+, 4^+. Reducing the Coriolis coupling to $\xi = 0.70$ lifts this near degeneracy and restores the normal level ordering although overall the band is too compressed. Increasing the deformation to $\epsilon = 0.36, \gamma = 0$ expands the band to the approximate experimental spacings as shown in figure 7.11g. With these parameters the bandhead configuration is $\pi[431]3/2\nu[422]5/2$ K= -4 (83%).

This increase in deformation may well be a real phenomena since it is known from the odd A case that the $4g_{9/2}$ proton polarizes the core to higher deformations. On the other hand, an increase in the nuclear deformation is tantamount to increasing the quadrupole interaction strength, thus indicating an inadequacy in the Coriolis attenuation method which has already been noted in subsection 7.4.2. In fact an increase in the proton quadrupole strength by a factor of 1.5 was used in the previous analysis [25]. Clearly a measurement of the electric transition probabilities would be useful in distinguishing the two possibilities.

Finally, it is known from the positive parity band structures in the odd A nuclides that the $4g_{9/2}$ proton leads to triaxial nuclear shapes. For completeness the possibility of such shapes has also been considered. However, with $\gamma \sim 26°$ the $(4)^+$ bandhead is no longer the lowest

positive parity state, lying instead above many closely spaced levels. Since experimentally no positive parity levels are observed below the isomeric state this possibility may be ruled out.

7.5.2 ^{74}Br

In ^{74}Br two separate level schemes on top of the (0^-) ground and spin 4 isomeric state have been ascertained [26]. As has already been discussed in section 5.5, while the isomeric spin is well established [23] the parity is uncertain. Negative parity has been proposed on the basis of supposed first unique forbidden β/EC transitions to ^{74}Se [27], while positive parity has been suggested from a comparison with the $(4)^+$ and $(4)^-$ band structures in ^{76}Br [26]. In view of the fact that the corresponding neutron Fermi levels are virtually coincident in the region $0.3 < \epsilon < 0.4$, as can be seen from figure 7.1, such similarities between the states of ^{74,76}Br might well be expected.

Drawing on these similarities therefore, likely candidates for a 4^- isomeric state include the $\pi[312]3/2\nu[422]5/2$, $\pi[440]1/2\nu[301]3/2$ and $\pi[440]1/2\nu[303]5/2$ orbitals. However, the calculated moments of these configurations, -0.16, $+3.93$ and $+4.20\mu_N$ respectively, are all incompatible with the present experimental moment of $\pm 1.68(18)\mu_N$. The tentatively proposed $\pi[301]3/2\nu[422]5/2$ orbital [23], with a theoretical moment of $+1.71\mu_N$, never comes close enough to the Fermi level to be viable possibility. A search for other candidates over a wider region of deformation, both prolate and oblate, failed to find further configurations with suitable moments.

By contrast, the moment of the positive parity $\pi[431]3/2\nu[422]5/2$ configuration is calculated to be $+1.77\mu_N$, in excellent agreement with the experimental value. Therefore the present magnetic moment strongly favours a 4^+ assignment for the isomeric state.

A comparison between the theoretical and experimental isomeric band structures is given in figures 7.12a and b respectively. The VMI parameters were taken from the even-even core. As was the case with the corresponding $(4)^+$ band of ^{76}Br, the Coriolis force was attenuated by $\xi = 0.70$. In order to reproduce the approximate energy scaling of the band the deformation $\epsilon = 0.37, \gamma = 0$ was assumed, for which the isomeric state configuration is $\pi[431]3/2\nu[422]5/2$ K$= -4$ (89%).

Of the negative parity states, the (1^-) band lying 9.8 keV above the (0^-) ground state closely resembles that of the 1^- ground state band in ^{76}Br. This bandhead may therefore be identified with the $\pi[312]3/2\nu[422]5/2$ K$= 1$ configuration. The experimental and theoretical band structures are shown in figure 7.12d and f. The deformation was taken to be $\epsilon = 0.37, \gamma = 0$.

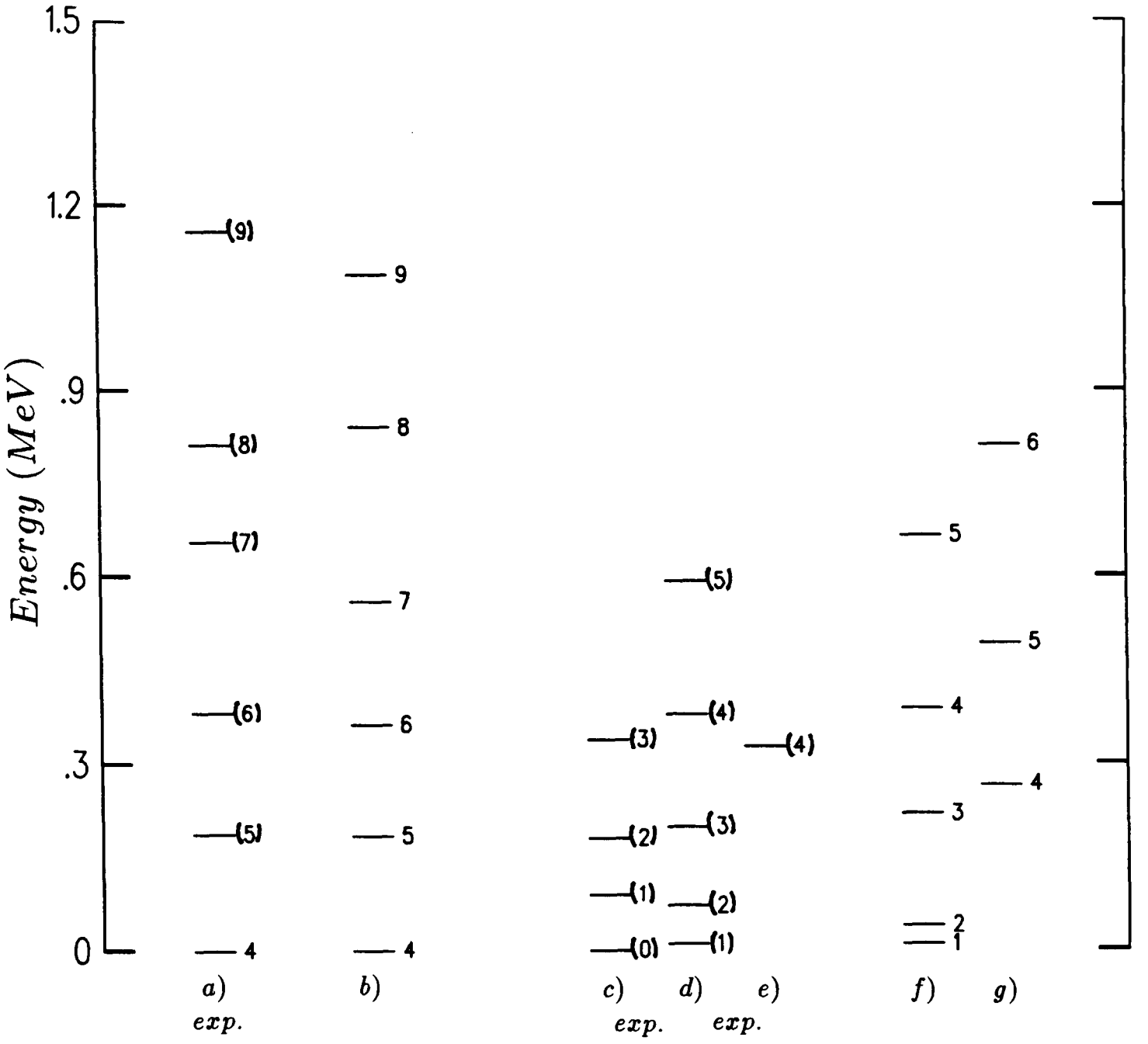

Figure 7.12. The experimental and theoretical band structures of ^{74}Br. The model parameters are indicated. The experimental energies are illustrated in a) $(+\pi)$ and c), d), e) $(-\pi)$. The corresponding theoretical levels are shown in b) $(+\pi)$ and f), g) $(-\pi)$.

Feeding into this band is a (4^-) state at 330 keV (figure 7.12e), close to the 275 keV excitation energy at which the K= -4 conjugate state is expected (figure 7.12g). However, as with ^{76}Br, this level is probably associated with a proton $4g_{9/2}$ configuration.

As this deformation there is no obvious candidate for the tentatively assigned (0^-) ground state (figure 7.12c). One possibility is the $\pi[312]3/2\nu[431]3/2$ configuration. However, as this only occurs for lower deformations in the region $\epsilon = 0.28, \gamma = 0$, this would not be expected to be associated with an extremely low lying (1^-) band as occurs in practice.

7.5.3 ^{72}Br

Recent in-beam gamma spectroscopy studies on ^{72}Br [28] have revealed three rotational bands. Electric transition strengths within the band terminating on the $(1)^-$ isomeric state indicate a nuclear deformation in the region $\epsilon \sim 0.30$. Shape coexistence at low spin is a real possibility and interestingly no band structure clearly associated with the $(3)^+$ ground state has been observed, reminiscent of the neighbouring nucleus ^{73}Br.

With this in mind, a search for a possible 3^+ ground state was carried out for a mesh of prolate, oblate and triaxial deformation points in the range $0.05 \leq \epsilon \leq 0.40, \gamma = 0, 15, 25, 35, 45, 60°$. Despite this extensive search no such ground state was found, nor did any low lying 3^+ states have moments consistent with the experimental value of $\pm 0.55(21)\mu_N$. A similar search for a isomeric 1^- state also failed to produce an obvious candidate.

In the light of these failures it seem reasonable to question the $(3)^+$ and $(1)^-$ spin-parity assignments of the ground and isomeric states [29], although, as outlined in sections 5.7 and 5.8, their justifications appear to well founded. Unfortunately predictive calculations are difficult, given the multiplicity of single particle product states in the vicinity of the Fermi level which can be formed. However it is probably worth pointing out that a 3^- $\pi[312]3/2\nu[440]1/2$ ground state with a moment of $-0.70\mu_N$ is expected at a deformation of $\epsilon \sim 0.28, \gamma = 0$. Several candidates for a low lying 1^+ state also exist.

7.6 Conclusion

The interpretation of the magnetic moment data on the nuclei $^{72-77}$Br within the framework of the particle-rotor model has lead to several positive configuration assignments for the long lived levels.

In the odd A nuclei it has been shown that there is a transformation in the character of the ground state configuration from the [301]3/2 orbital in ^{79,81}Br to the [312]3/2 orbital in ^{75,77}Br. The measured magnetic dipole moments are well reproduced by the theory and are fully consistent with the deformations suggested by the electric quadrupole data. While these magnetic moments are only compatible with prolate deformations, the ground state spin of ^{73}Br can only be interpreted in terms of an oblate nuclear shape. This is the first evidence in the bromine nuclei for the conjectured prolate-oblate shape transition. The presence in ^{73}Br of a low lying $(3/2^-)$ rotational band, whose nature is closely similar to the ground state band in ^{75}Br,

indicates the occurrence of coexisting oblate and prolate shapes. Clearly more spectroscopic work needs to be done on this nucleus in order to probe the effects of shape isomerism further.

In the odd-odd nuclei, the moment of the ^{76}Br ground state demonstrates the involvement of a $\pi[312]3/2$ orbital as observed in the neighbouring odd A nuclei, ^{75,77}Br. The magnetic moment of ^{74}Br^{m} has also been instrumental in assigning positive parity to the isomeric state. Unfortunately, it proved impossible to find candidates for the assumed $(3)^{+}$ ground state and $(1)^{-}$ isomeric state of ^{72}Br.

With regard to the particle-rotor model it has been shown that the Coriolis interaction is not satisfactorily treated, particularly so in the case of the high angular momentum $4g_{9/2}$ configurations. This appears to be the result of an underestimation of the quadrupole interaction strength in the Nilsson potential, rather than an overestimation of the Coriolis force itself. It would be interesting to determine whether a more realistic nuclear one-body potential could resolve this problem.

For the most part the VMI parameters have been taken from the even-even cores. In this region the cores exhibit shape coexistence and are readily polarized by addition unpaired nucleons. Thus, while this is a natural starting point, it is not clear that the core parameters will be completely applicable to the description of their odd A and odd-odd neighbours. The calculation of the VMI parameters by a Simplex minimization of the difference between the experimental and theoretical odd A and odd-odd band structures might therefore be more appropriate. However, such improved VMI parameters would only provide cosmetic changes to the calculations and make little or no additional contribution to the interpretation of the low lying nuclear structure presented here.

With no alternative guidance, the parameters of the proton-neutron interaction have been taken over from the rare earth region. Since no Gallagher-Moszkowski split conjugate pairs have been positively identified in this work, it is not possible to ascertain the validity of this assumption. It would therefore be useful to perform a study of the odd-odd nuclei in the region as a whole in order to test the parametrization of the residual interaction.

References

[1] . S.E. Larsson *et al.*, Nucl. Phys. **A261**(1976) 77

[2] . J. Heese *et al.*, Phys. Rev. **C36** (1987) 2409

[3] . S.G. Nilsson *et al.*, Nucl. Phys. **A131** (1969) 1

[4] . J.P. Boisson *et al.*, Physics Reports **26** (1976) 99

[5] . T. Matsuzaki and H. Taketani, Nucl. Phys. **A390** (1982) 413

[6] . K.P. Lieb and J.J. Kolata, Phys. Rev. **C15** (1977) 939

[7] . R.B. Piercey *et al.*, Phys. Rev. **C19** (1979) 1344

[8] . N. Yoshikawa *et al.*, Proc. Int. Conf. on Selected Topics in Nuclear Structure, Dubna, (Unpublished, 1976)

[9] . L. Lühmann *et al.*, Phys. Rev. **C31** (1985) 828

[10] . N. Nadon *et al.*, private communication to **NDS** (1989)

[11] . Table of Isotopes, eds. C.M. Lederer and V.S. Shirley, (Wiley, 1978)

[12] . G. Winter *et al.*, Nucl. Phys. **A367** (1981) 95

[13] . P. Moller and J.R. Nix, Atomic and Nuclear Data Tables **26** (1981) 165

[14] . R. Bengtsson *et al.*, Phys. Scripta **29** (1984) 402

[15] . W. Nazarewicz *et al.*, Nucl. Phys. **A435** (1985) 397

[16] . H. Toki and A. Faessler, Phys. Lett. **63B** (1976) 121

[17] . A. Faessler, private communication (1989)

[18] . A. Faessler, Rep. Prog. Phys. **45** (1982) 653

[19] . J. Panqueva *et al.*, Nucl. Phys. **A376** (1982) 367

[20] . J. Panqueva *et al.*, Nucl. Phys. **A389** (1982) 424

[21] . J. Meyer-ter-Vehn, Nucl. Phys. **A249** (1975) 111,141

[22] . J. Döring *et al.*, Z. Phys. **305** (1982) 365

[23] . C. Ekström and L. Robertsson, Phys. Scripta **22** (1980) 344

[24] . D. Lode *et al.*, Z. Phys. **260** (1973) 253

[25] . A.J. Kriener and M.A.J. Mariscotti, Phys. Rev. Lett. **43** (1979) 1150

[26] . G. Winter *et al.*, Z. Phys. **A309** (1983) 243

[27] . A. Coban *et al.*, Part. Nucl. **4** (1972) 108

[28] . S. Ulbig *et al.*, Z. Phys. **A329** (1988) 51

[29] . G. Garcia Bermudez *et al.*, Phys. Rev. **C** (1982) 1396

Chapter 8

Time reversal invariance in nuclear gamma decay

8.1 Introduction

With the discovery of CP-violation in the decay of the neutral kaon [1] there came the first and only evidence for the breakdown of T-reversal symmetry. This was implied by both the CPT theorem and also by an analysis of the kaon decay parameters [2]. Theories of such CP- and T-nonconservation may be divided in four general categories [3]

1. C- and T-violating electromagnetic interactions (with an expected coupling strength of $g_T \sim 10^{-4} \rightarrow 10^{-3}$ and a predicted neutron electric dipole moment $d_n \sim 10^{-23} \rightarrow 10^{-21}$ e cm).
2. C- and T-violating millistrong interactions ($g_T \sim 10^{-4} \rightarrow 10^{-3}$, $d_n \sim 10^{-23}$ e cm).
3. P- and T-violating milliweak interactions ($g_T \sim 10^{-9}$, $d_n \sim 10^{-24}$ e cm).
4. CP- and T-violating superweak interactions ($g_T \sim 10^{-15}$, $d_n \sim 10^{-29}$ e cm).

The T-violating coupling strengths predicted by these theories span some 12 orders of magnitude. In order to resolve this rather unsatisfactory situation a number of experimental tests of time reversal invariance have been performed. These tests concern the searches for atomic and nuclear electric dipole moments, the studies of the relative intensities of polarized hyperfine transitions using the Mössbauer effect, the investigations of the symmetry of reaction yields by detailed balance and various correlation experiments on nuclear radiation. To date no such T-violations have ever been observed in an atomic or nuclear system.

Perhaps the most accurate and easily interpretable experimental constraint on T-invariance arising from these experiments is provided by the current limit for the neutron electric dipole moment, $d_n < 2.6 \times 10^{-25}$ e cm [4]. By dimensional arguments this may be interpreted as an upper limit on the amplitude of a T-odd (P-odd) interaction of $10^{-5} \rightarrow 10^{-4}$.

In comparison, the detailed balance and gamma correlation class of experiments are consistent with time reversal invariance to at least the 10^{-3} level. The interpretation of such results is uncertain as they are connected to the fundamental force via complicated nuclear structure

considerations which may result in enhancements or cancelations of the T-odd (P-even) manifestation [5]. However, in general, dimensional arguments lead to coupling strengths of the same order as the measured T-odd variables themselves.

The present experimental limits on the T-violating coupling strength are therefore close to those predicted by the electromagnetic and millistrong theories. Further investigations of time reversal invariance can therefore provide important indicators as to the true nature of the effect.

8.2 Time reversal invariance in gamma transitions

Time reversal non-invariant effects manifest themselves in the reduced matrix elements of the electromagnetic transition operators. The ratio of the corresponding absolute transition amplitudes $\gamma(\pi L)$ [6] defines the mixing ratio

$$\delta = \gamma(\pi' L')/\gamma(\pi L) = |\delta| \exp^{i(\eta+\xi)} . \tag{8.1}$$

The time reversal phase angle η differs from 0 or π only in the presence of a T-violating interaction. The angle ξ, which will be discussed further in subsection 8.7.5, results from the atomic final state electromagnetic interaction and the Faraday effect. In general $\sin(\eta + \xi)$, if non-zero, appears in a T-odd observable which changes sign under time reversal.

Experimentally the quantities that can be measured are the nuclear spin $\mathbf{I}$, photon spin $\mathbf{S}$, wavevector $\mathbf{k}$ and linear polarization $\mathbf{e}$ whose signatures under time reversal are $-, -, -, +$ respectively. Any T-odd observable must involve at least three of these variables. Appropriate combinations have been tabulated by Boehm [7]. In general these involve the preparation of an polarized initial state from which $\mathbf{I}$ is determined and a measurement of two other quantities. A review of the various types of experiment which have been performed to date has recently been given [8].

In particular, T-odd P-even terms of the form $(\mathbf{I} \cdot \mathbf{k} \times \mathbf{e})(\mathbf{I} \cdot \mathbf{k})(\mathbf{I} \cdot \mathbf{e})$ may be constructed, requiring measurements of the wavevectors and linear polarization of gamma radiation emitted from an oriented source. Such an experiment, using a single counting method, has set the present lowest limit on the time reversal phase in the nuclear system of $\sin\eta = +2.9(6.6) \times 10^{-4}$ [9].

The present experiment follows the same principle. However, unlike the previous work the gamma ray linear polarization is detected by coincidence techniques with good energy resolution. The gamma rays of interest are therefore *clearly* separable from unwanted background events.

This is in stark contrast to the single counting method where energy separation relies on the Compton scattering process alone. The resulting resolution is therefore extremely poor, thereby limiting the nuclei which can be studied to cases where the gamma ray spectrum is sufficiently simple.

Thus although the present coincidence method suffers from a loss of statistical accuracy, its far superior energy resolution makes it applicable to a far wider range of nuclei.

8.3 The gamma ray linear polarization distribution of oriented nuclei

The general expression for the linear polarization distribution of gamma rays emitted from an axially symmetric polarized state can be derived from (1.57) using the appropriate efficiency matrix. In this way it can be shown that

$$W(\theta,\phi) = W_1(\theta) + W_2(\theta,\phi) + W_3(\theta,\phi) \tag{8.2}$$

where

$$W_1(\theta) = \sum_{\lambda=even} B_\lambda U_\lambda A_\lambda P_\lambda(\cos\theta) \tag{8.3}$$

$$W_2(\theta,\phi) = \sum_{\lambda=even} B_\lambda U_\lambda A_{\lambda 2} \left[\frac{(\lambda-2)!}{(\lambda+2)!}\right]^{\frac{1}{2}} (2) P_\lambda^2(\cos\theta)\cos(2\phi) \tag{8.4}$$

and

$$W_3(\theta,\phi) = \sum_{\lambda=odd} B_\lambda U_\lambda A_{\lambda 2} \left[\frac{(\lambda-2)!}{(\lambda+2)!}\right]^{\frac{1}{2}} (-2i) P_\lambda^2(\cos\theta)\sin(2\phi). \tag{8.5}$$

The first two terms of this angular distribution, W_1 and W_2, represent the ordinary directional distribution (1.70) and the ordinary linear polarization distribution of the gamma radiation respectively. Both of these remain invariant under the time reversal operation ($\theta \rightarrow \pi - \theta, \phi \rightarrow \pi + \phi$), while the linear polarization distribution W_3 reverses sign. This, therefore, is the T-violating term of interest.

As the lowest non-zero linear polarization angular distribution coefficients $A_{\lambda 2}$ [10] are of the second order, the leading term of this T-violating distribution is of the third rank. The angular dependence of this component, which is directly related to the quantity $(\mathbf{I}\cdot\mathbf{k}\times\mathbf{e})(\mathbf{I}\cdot\mathbf{k})(\mathbf{I}\cdot\mathbf{e})$, is $\sin^2\theta\cos\theta\sin(2\phi)$. Since this function reverses sign under both the transformations $(\theta,\phi) \rightarrow$

$(\theta, -\phi)$ and $(\theta, \phi) \rightarrow (\pi - \theta, \phi)$ there are two separate experimental asymmetries which are sensitive to time reversal effect

$$A_\phi = \frac{W(\theta,\phi) - W(\theta,-\phi)}{W(\theta,\phi) + W(\theta,-\phi)} = \frac{W_3}{W_1 + W_2} \tag{8.6}$$

and

$$A_\theta = \frac{W(\theta,\phi) - W(\pi-\theta,\phi)}{W(\theta,\phi) + W(\pi-\theta,\phi)} = \frac{W_3}{W_1 + W_2}. \tag{8.7}$$

These experimental time reversal asymmetries are maximized at the angles $(\theta' = 0.96, \phi'_n = n\pi/2 + \pi/4)$. Not only is W_3 greatest at these angles, but also the leading order directional distribution term and the entire ordinary linear polarization term W_2 vanish. The major contributors to the experimental asymmetries are therefore the $\lambda = 3$ term of the T-violating distribution W_3 in the numerator and the $\lambda = 4$ term of the ordinary directional distribution W_1 (higher order terms of which will vanish for dipole or quadrupole transitions) in the denominator.

Thus in the optimized time reversal geometry (θ', ϕ'_n) the experimental asymmetries may be written explicitly as

$$A_\theta = A_\phi = K \sin(\eta + \xi) \tag{8.8}$$

where the sensitivity function K is given by

$$K = \frac{1}{\sqrt{30}} \frac{Q B_3 U_3 F_3(LL' I_f I_i) |\delta| P_3^2(\cos\theta') \sin(2\phi'_n)}{1 + |\delta|^2 \{1 + B_4 U_4 F_4(LL' I_f I_i) P_4(\cos\theta')\}} \frac{\begin{pmatrix} L & L' & 3 \\ -1 & -1 & 2 \end{pmatrix}}{\begin{pmatrix} L & L' & 3 \\ 1 & -1 & 0 \end{pmatrix}} \tag{8.9}$$

and Q is the linear polarization detection efficiency defined in the following section.

8.4 The Compton polarimeter

The gamma ray linear polarization is detected using a standard Compton polarimeter. This consists of a central Ge(Li) detector which scatters incident radiation through an angle $\theta_c = \pi/2$ to be subsequently analyzed in one of four onlooking Ge(Li) detectors. Coincident events in the scatterer and analyzer are summed by the methods described in section 2.6, thus reconstructing the energy of the original gamma ray. A schematic diagram of such a Compton polarimeter is shown in figure 8.1 .

The four analyzers are mounted in mutually perpendicular directions upon a specially designed turnable which can be continuously rotated about the central axis of the scattering detector. The orientation of this central axis can be varied, so that all necessary values of θ and ϕ may be selected for experimentation.

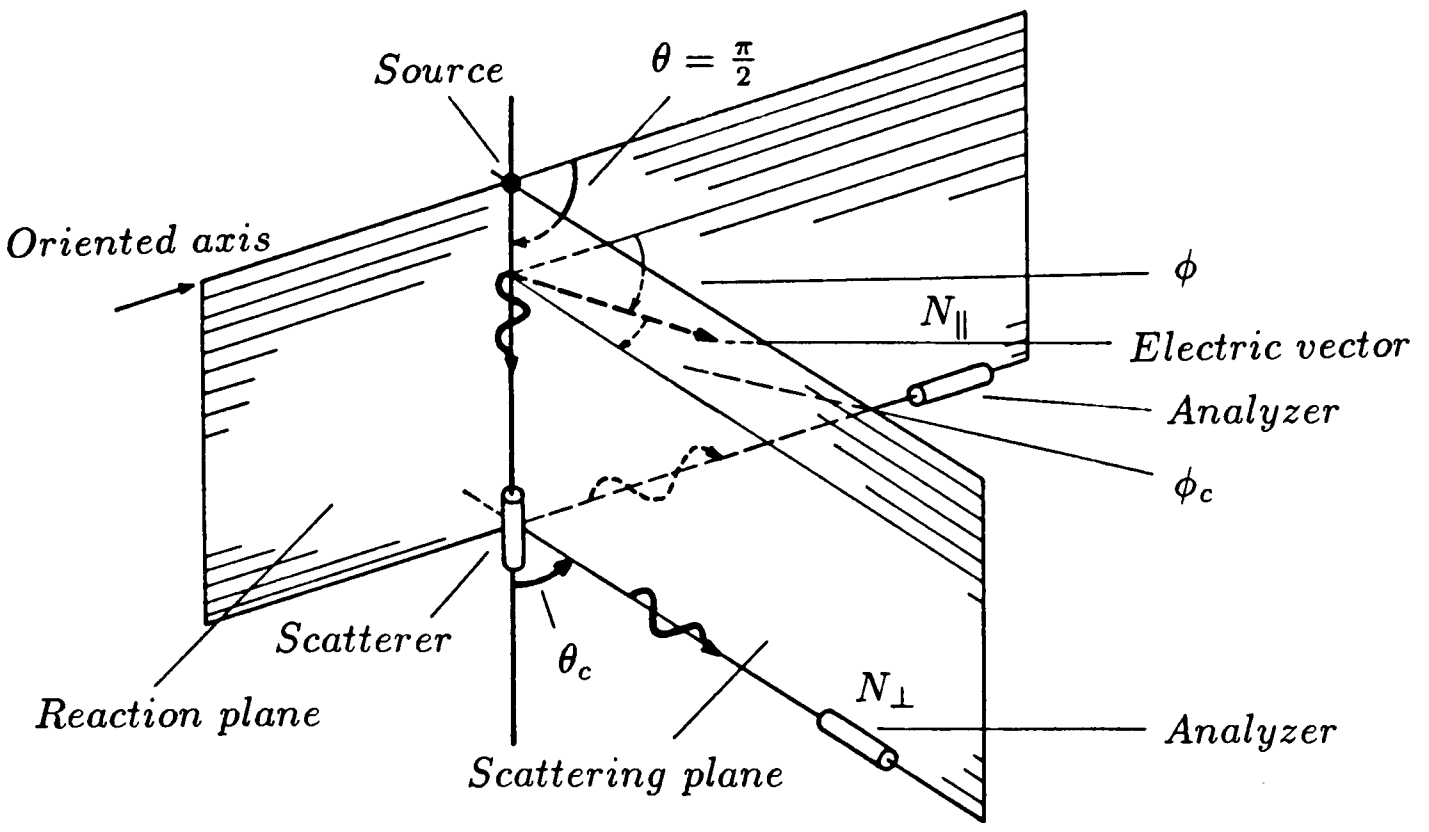

Figure 8.1. The geometry of a Compton polarimeter. Two of the four analyzers are shown.

The principle of the polarimeter relies upon the asymmetry with which photons are Compton scattered. This is governed by the cross section $d\sigma/d\Omega(\theta_c = \pi/2, \phi_c)$, where θ_c is the scattering angle and ϕ_c is the angle between the electric vector of the primary radiation and the scattering plane of the incident and scattered photons, as shown in figure 8.1. Since the scattered radiation is distributed over an extended range of angles the polarimeter is generally not fully efficient.

In order to illustrate the nature of this efficiency factor further, consider a measurement of ordinary linear polarization distribution, W_2. It is clear from (8.4) that the maximum difference

in this distribution occurs for the angles $(\theta = \pi/2, \phi = 0)$ and $(\theta = \pi/2, \phi = \pi/2)$. Therefore it is convenient to define the degree of linear polarization to be

$$P(\theta) = \frac{W(\theta, \phi = 0) - W(\theta, \phi = \frac{\pi}{2})}{W(\theta, \phi = 0) + W(\theta, \phi = \frac{\pi}{2})}. \tag{8.10}$$

Experimentally one measures the quantity

$$\Delta(\theta) = \frac{N_\perp(\theta_c = \frac{\pi}{2}) - N_\parallel(\theta_c = \frac{\pi}{2})}{N_\perp(\theta_c = \frac{\pi}{2}) + N_\parallel(\theta_c = \frac{\pi}{2})} \tag{8.11}$$

where $N_\parallel$ and $N_\perp$ are the intensities of the full energy peaks of the summed coincidence spectra in the analyzers parallel and perpendicular to the reaction plane respectively. Since $N_\parallel$ and $N_\perp$ are measured by separate detectors and therefore not directly comparable, they must first be normalized to the corresponding "warm" isotropic linear polarization distribution.

The measured full energy count rates can be expressed in terms of the theoretical polarization distributions by means of the expressions

$$\begin{aligned} N_\parallel(\theta_c = \frac{\pi}{2}, \phi_c = 0) = \; & \frac{d\sigma}{d\Omega}\left(\theta_c = \frac{\pi}{2}, \phi_c = 0\right) W(\theta, \phi = 0) \\ & + \frac{d\sigma}{d\Omega}\left(\theta_c = \frac{\pi}{2}, \phi_c = \frac{\pi}{2}\right) W\left(\theta, \phi = \frac{\pi}{2}\right) \end{aligned} \tag{8.12}$$

and

$$\begin{aligned} N_\perp\left(\theta_c = \frac{\pi}{2}, \phi_c = \frac{\pi}{2}\right) = \; & \frac{d\sigma}{d\Omega}\left(\theta_c = \frac{\pi}{2}, \phi_c = \frac{\pi}{2}\right) W(\theta, \phi = 0) \\ & + \frac{d\sigma}{d\Omega}\left(\theta_c = \frac{\pi}{2}, \phi_c = 0\right) W\left(\theta, \phi = \frac{\pi}{2}\right). \end{aligned} \tag{8.13}$$

Therefore the theoretical and experimental linear polarization asymmetries are related by the equation

$$P(\theta) = \frac{1}{Q}\Delta(\theta) \tag{8.14}$$

where the linear polarization detection efficiency Q is defined by

$$Q = \frac{\frac{d\sigma}{d\Omega}(\theta_c = \frac{\pi}{2}, \phi_c = \frac{\pi}{2}) - \frac{d\sigma}{d\Omega}(\theta_c = \frac{\pi}{2}, \phi_c = 0)}{\frac{d\sigma}{d\Omega}(\theta_c = \frac{\pi}{2}, \phi_c = \frac{\pi}{2}) + \frac{d\sigma}{d\Omega}(\theta_c = \frac{\pi}{2}, \phi_c = 0)}. \tag{8.15}$$

As can be seen from (8.15) the efficiency Q is independent of the angles θ and ϕ. Since it is only required that the radiation scattered through $\pi/2$ is detected in two mutually perpendicular directions, this ordinary linear polarization detection efficiency factor also applies to measurements in the time reversal geometry $(\theta' = 0.96, \phi'_n = n\pi/2 + \pi/4)$.

The efficiency Q appearing in (8.9) may therefore be evaluated from (8.14) by comparing the experimental and theoretical ordinary linear polarizations in the geometry ($\theta = \pi/2, \phi = 0, \pi/2$).

The theoretical energy dependence of this efficiency factor may be determined using the Klein-Nishina formula for the Compton scattering cross section. Thus from (8.15) one obtains

$$Q = \Gamma \frac{\alpha + 1}{\alpha^2 + \alpha + 1} \tag{8.16}$$

where α is the ratio of incident photon energy to the electron rest mass energy and for point detectors $\Gamma = 1$. In practice this limit is never realized as a result of photon absorption in the polarimeter detectors and the finite solid angle which they subtend. However, the experimental efficiencies may still be related to this expression by considering the coefficient Γ to have some functional energy dependence. Often a constant form is quite sufficient [11].

8.5 The choice of nucleus

In order to achieve the maximum response of the experimental time reversal asymmetry to the phase angles $\eta + \xi$, the sensitivity function K (8.9) must be maximized. In addition to the geometrical factors which have already been discussed, the choice of the experimental nucleus must also be guided by this criterion.

The parent nucleus must therefore be required to orient as completely as possible in order to maximize B_3. This requires a large nuclear hyperfine interaction $\mu B_{sub}/I$. Simultaneously the temperature must be kept as low as possible, despite the large source strengths required for good statistical accuracy. Thus nuclei which decay by β^- or EC are preferred to those which decay by β^+ emission. The daughter nucleus must then have a mixed ($\delta \sim 1$) transition with a suitably large U_3F_3 coefficient. Low (< 1 MeV) energy gamma transitions are preferred since these are associated with the largest polarimeter efficiencies (8.16).

A review of such nuclei [12] indicates that the parent nucleus ^{192}Ir, which decays by β^- emission to ^{192}Pt, has the most favourable sensitivity function at 10 mK. In addition, the half life (73.8 d) is sufficiently great to accommodate a long term experiment and the energy of the 604 keV mixed transition of interest falls in the region where it is estimated that the combination of polarimeter efficiency and (unwanted) gamma ray absorption is at its most favourable for the present experimental configuration [13]. This nucleus was therefore chosen as the best candidate for the present experiment.

The hyperfine interaction of the ^{192}IrFe system has been previously measured by NMR/ON techniques to be [14]

$$\mu = \pm 1.924(10)\mu_N \quad B_{sub} = -137.3(7) \text{ T}.$$

The decay scheme of ^{192}Ir is shown in figure 8.2 [15]. The seven dominant transitions which arise are listed below

Energy (keV)	E2/M1 mixing ratio [16]
296	+1 5(4)
308	+7.6(1)
316	E2
468	E2
589	E2
604	−1.4(1)
612	E2

8.6 Experimental details

The ^{192}Ir source of total activity $\sim 350\mu$Ci was prepared by the neutron irradiation of natural iridium at the Risley Research Reactor. This was then melted under vacuum with iron ($> 99.998\%$ purity) at $\sim$ 1500 °C. The sample was then soldered onto the tip of a specially constructed high purity copper cold finger. The design was such that the ratio of cross sectional area to length in the narrower tip was equal to that of the more substantial body. As a result the thermal transmission was maximized, reducing as far as possible the temperature gradient between the mixing chamber and source created by the large radioactive heating.

As has been pointed out in section 8.3, there are two distinct methods by which the time reversal asymmetry can be measured. The first of these (8.6) requires a comparison of count rates taken at two separate angles using separate detectors, in a similar fashion to the measurement of ordinary linear polarization. Experimentally there are a number of difficulties involved with this method. Firstly, the count rates in the two detectors are not directly comparable and so require normalization, inevitably reducing the experimental precision. Secondly, the ambiguity in the subtraction of background from photopeak can lead to difficulties when the different spectral shapes of the detectors are compared. Thirdly, the solid angles subtended at the source by the

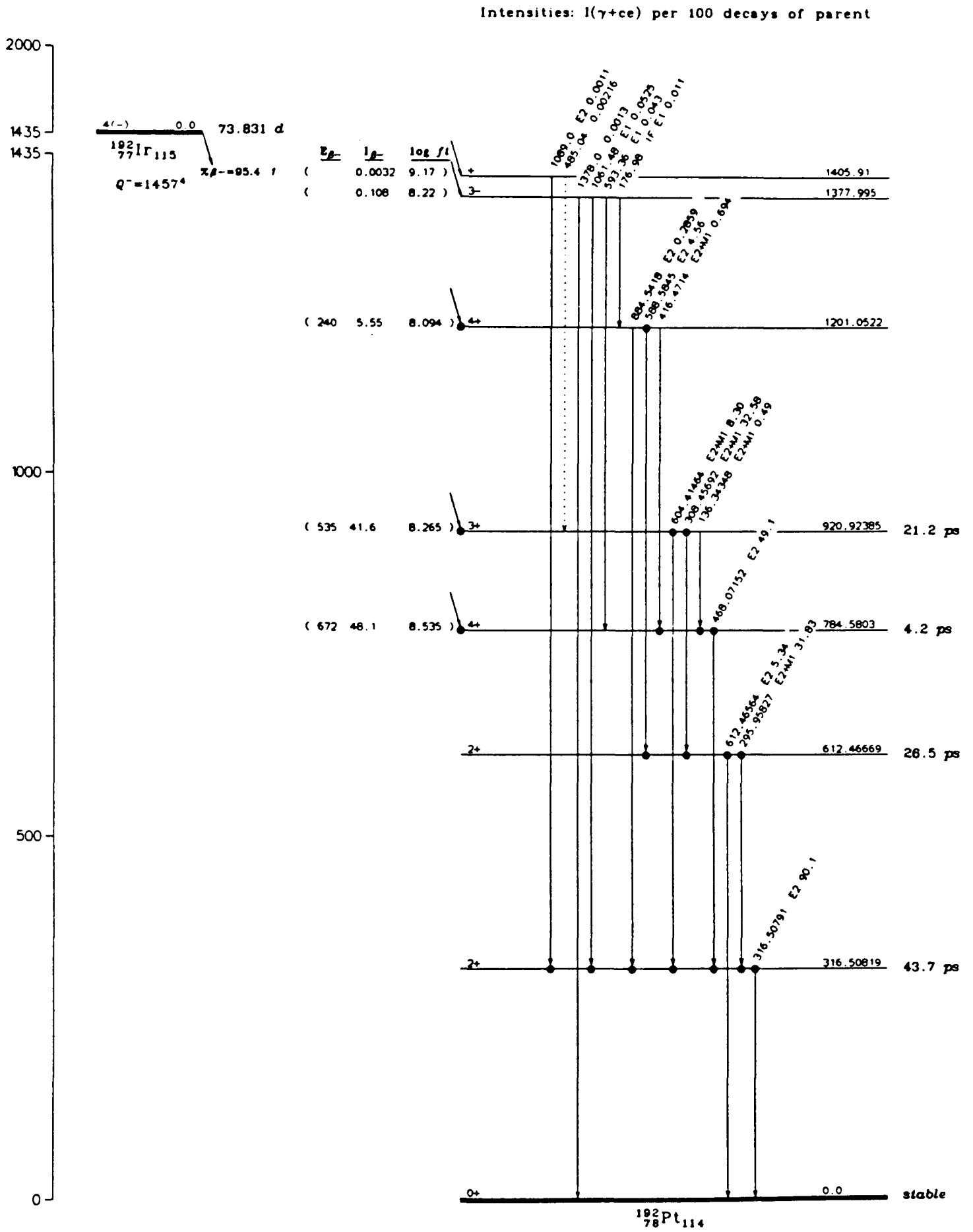

Figure 8.2. The decay scheme of ^{192}Ir [15].

two detectors will differ. While these considerations are unimportant in the measurement of the relatively large ordinary linear polarization effect, they can produce discernable systematic errors in the measurement of a "null" time reversal asymmetry.

However, the second type of time reversal asymmetry measurement (8.7) eliminates these drawbacks. The angle θ is measured from the quantization axis, which will be defined here

by the direction of the *applied* magnetic field. As a result the orientation of the Compton polarimeter can be fixed, the transformation $\theta \rightarrow \pi - \theta$ being performed by a reversal of the applied magnetic field. One then compares the count rates within a given analyzer as a function of magnetic field. There is thus no problem with differing solid angles and with no physical movement of the analyzer the two count rates are, in the absence of time reversal effects, identical thus avoiding the need for normalization. Also ambiguities in the background subtraction are rendered unimportant since the spectral shape remains unchanged. Having the smaller number of potential sources of systematic error, this latter method was chosen in favour of the former.

If $+B$ is the field direction for which $\theta = 0.96$ and $-B$ the reverse field for which $\theta = \pi - 0.96$, then the experimental time reversal asymmetry (8.7) becomes

$$A_B = \frac{W(+B,\phi) - W(-B,\phi)}{W(+B,\phi) + W(-B,\phi)}. \tag{8.17}$$

Despite the notation it should be noted that although in relative terms the two fields are of opposite sign, both are positive in their respective (θ, ϕ) coordinate systems.

The experimental procedure is outlined in figure 8.3 which illustrates an aquisition period of 25 spectra. The variation of the magnetic field is shown schematically at the top of the diagram. Spectra $1 \rightarrow 4$ accumulate the angular distribution data $W(+B)$. The field is reversed during spectrum 5 which is thus rendered void. Spectra $6 \rightarrow 9$ then record $W(-B)$. The field is then swept up once more during spectrum 10 and the cycle is repeated.

Spectra were acquired every 40 minutes (30 minutes live time). The field reversal was achieved by means of two current sources, one fixed the other variable, connected in parallel to the superconducting magnet coils. With the fixed current I opposed by the variable current $0 \rightarrow 2I$, a net current in the range $-I \rightarrow +I$ is transmitted to the magnet resulting the fields $-B \rightarrow +B$. The variable current source was electronically controlled by the data aquisition system. The applied field was set to 0.7 T. The duration of the sweep was set to 5 minutes, a compromise to avoid the worst effects of eddy current heating while giving the temperature ample time to recover before the start of the next data set. The corresponding temperatures, as monitored by an axial Ge(Li) detector recording the directional distribution $W_1(\theta = 0)$ in singles mode, are shown in the lower half of the diagram. The dramatic increase in temperature coinciding with the changing magnetic field is evident. However this is somewhat misleading since much of this increase can be attributed to the loss of polarization in the iron host as the field reverses through zero. In any event the temperature fully recovers in time for the start of the following four spectrum data set. The base temperature is seen to be absolutely constant within statistics, indicating that the degree to which the domains within the iron foil

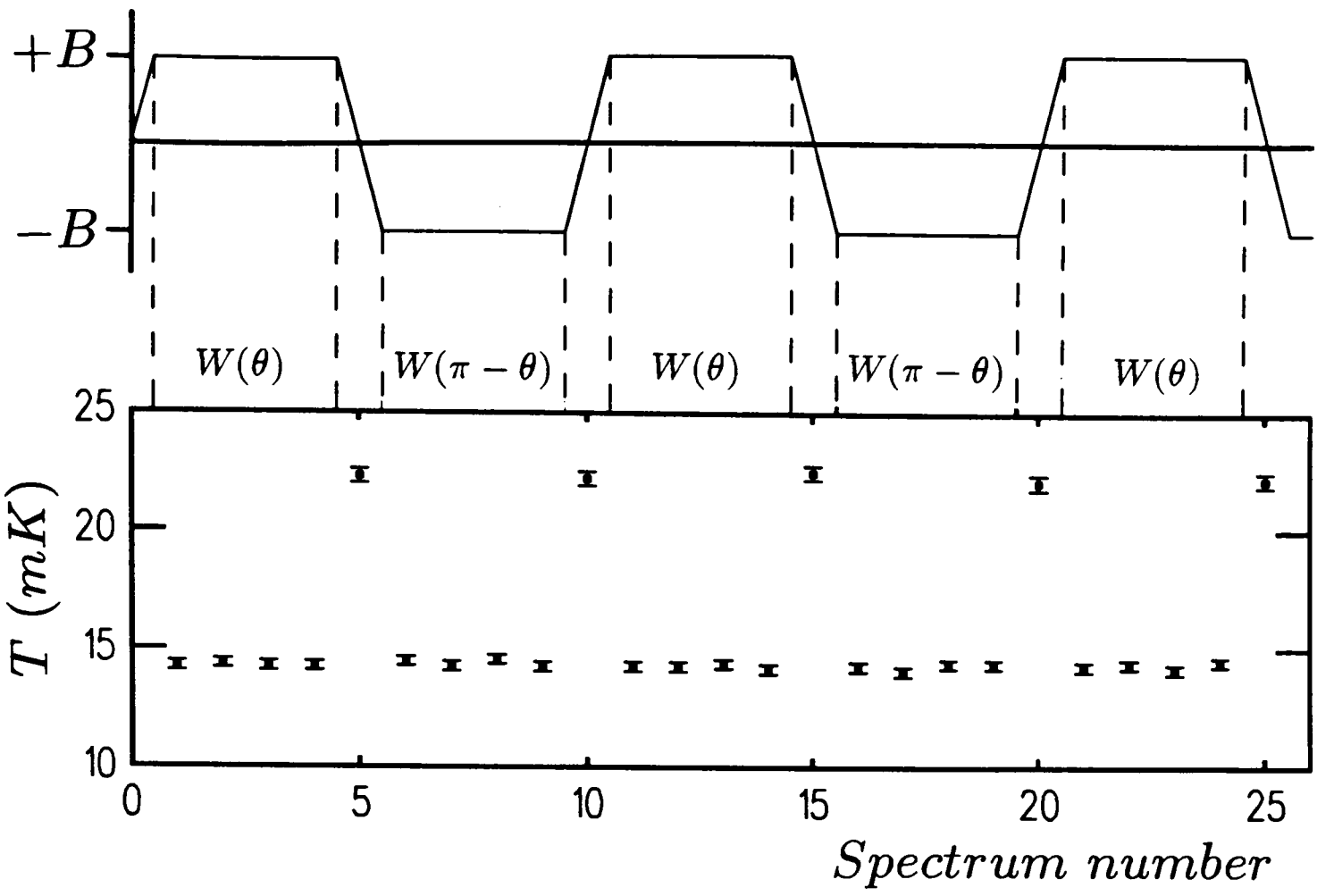

Figure 8.3. A schematic representation of the experimental procedure. The variation in the temperature of the system is also indicated.

are polarized is identical in both field directions. This is an important factor since any disparity in the degree of polarization would lead to systematic differences between $W(+B)$ and $W(-B)$.

The experimental geometry required for the measurement of the time reversal asymmetry is shown schematically in figure 8.4 . The four polarimeter analyzing detectors, labelled $1 \rightarrow 4$, occupy each of the four optimal angles $\phi'_n = n\pi/2 + \pi/4$.

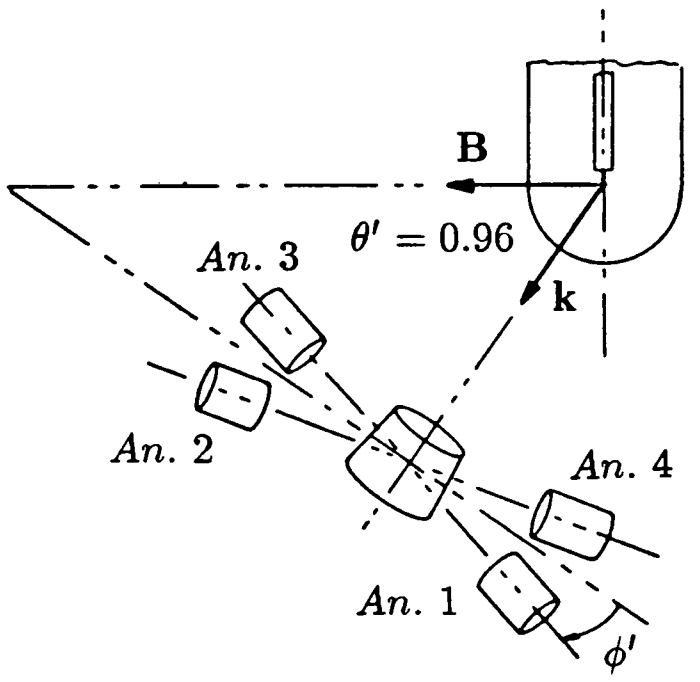

Figure 8.4. A schematic diagram of the Compton polarimeter relative to the source in the time reversal geometry.

At intervals the polarimeter turntable was rotated in $\pi/2$ increments so that each analyzer recorded data at each of the ϕ'_n orientations. In this way systematic errors in the observed asymmetry, such as minor geometrical misalignments, can be removed to first order. The ϕ'_n angle of observation for each analyzer in the four turntable positions is tabulated below. The phase factors $\sin(2\phi'_n)$ which reverse the sign of K (8.9) are enclosed in brackets.

Turntable Position	Analyzer Angle ($\sin 2\phi'_n$) An. 1	An. 2	An. 3	An. 4
1	$5\pi/4(+)$	$7\pi/4(-)$	$\pi/4(+)$	$3\pi/4(-)$
2	$7\pi/4(-)$	$\pi/4(+)$	$3\pi/4(-)$	$5\pi/4(+)$
3	$\pi/4(+)$	$3\pi/4(-)$	$5\pi/4(+)$	$7\pi/4(-)$
4	$3\pi/4(-)$	$5\pi/4(+)$	$7\pi/4(-)$	$\pi/4(+)$

In all approximately 55 spectra, each of 40 minute duration, were acquired per analyzer per turntable position per field direction both "cold" and "warm" ($\sim$ 1 K). The warm spectra serve as an experimental control. An example of the coincidence spectra observed in the analyzers is given in figure 8.5 . The 468 keV singlet and the 589, 604 and 612 keV triplet are shown in more detail in figures 3.1 and 3.2 respectively. Due to a number of disturbances to the system as a result of major technical difficulties with the dilution refrigerator, the resolution, although excellent in the example, deteriorated on occasions and was compounded by small gain shifts in the amplification system. As a result the peak areas were not determined by the peak fitting routine FIT (see section 3.2) since the peak shape variation would lead to erroneous variations in the fitted areas. Instead the 296, 308, 316 and 589, 604, 612 keV triplets were analysed as if single peaks using the CEN routine, thus avoiding any systematic errors due to random peak shape variations. The seven dominant lines in the decay are thus included into three groups

Window 1: 296, 308 and 316 keV triplet

Window 2: 468 keV singlet

Window 3: 589, 604 and 612 keV triplet.

The 468 peak thus remains as the only uncontaminated pure E2 line. Being unmixed and therefore without time reversal asymmetry this also acts as an experimental control.

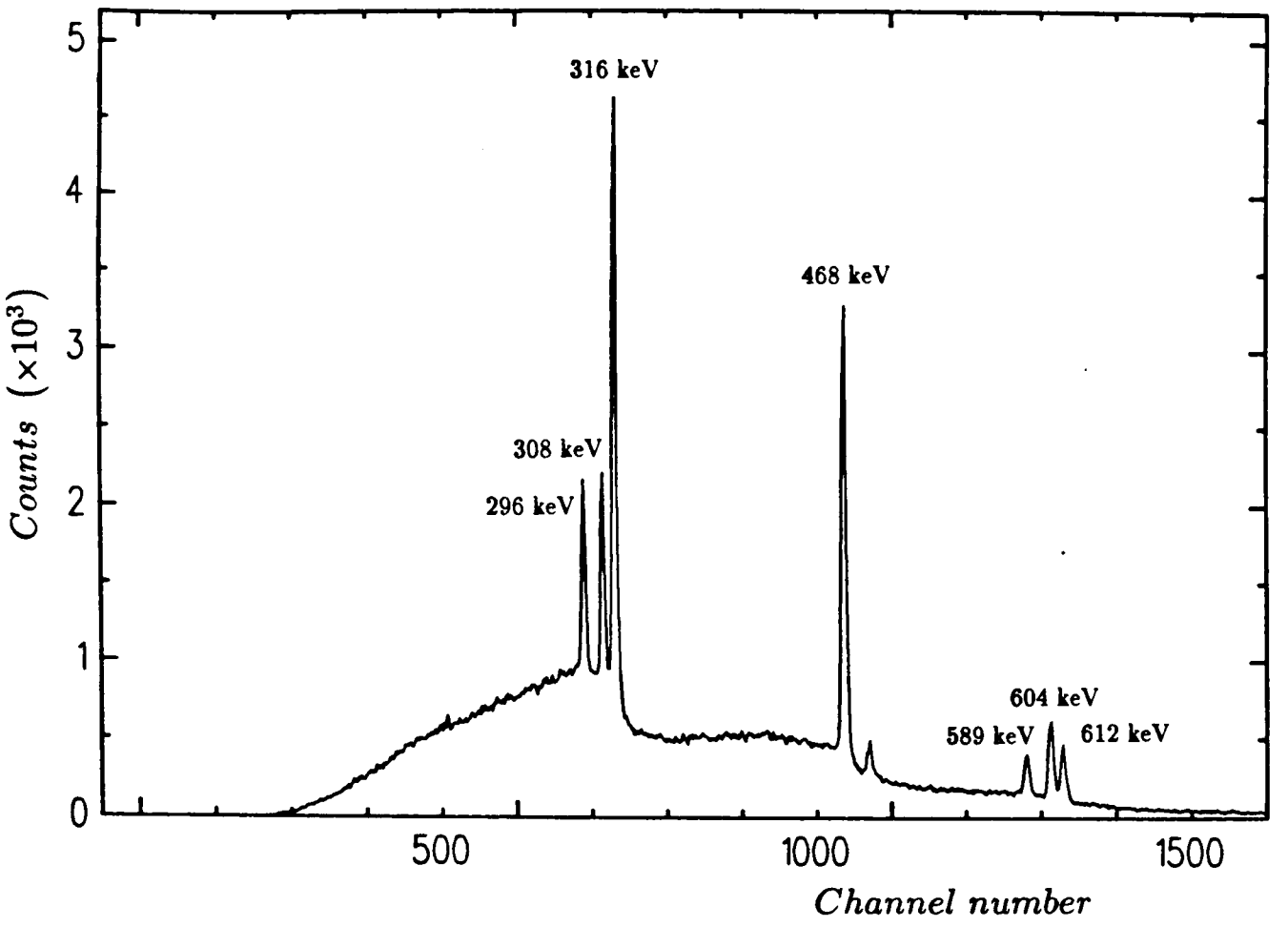

Figure 8.5. A coincidence spectrum of ^{192}Ir acquired over a 40 minute period.

8.7 Results

8.7.1 The raw experimental asymmetries

The experimental asymmetries are calculated separately for consecutive pairs of $W(+B)$ and $W(-B)$ data sets. Odd spectra at the end of a run which did not constitute a complete data set of four spectra were included into the preceeding group. In general, therefore, each asymmetry datum corresponds to eight 40 minute (30 minute live time) spectra. The data were adjusted to account for the small half life decay correction (3.4).

These asymmetry points are shown in figures 8.6, 8.7 and 8.8 for windows 1, 2 and 3 respectively. *No systematic effects* are apparent. In fact generally the stability of the system was excellent, despite the frequent upheavals required to affect repairs to the refrigerator. Only the last few points in analyzer 2, "cold" position 2 were erroneous as a result of a noise introduced by a faulty contact. These have been excluded from the subsequent analysis. Due to an unresolved problem with the electronic equipment the net count rate in analyzer 3 was lower by an order of magnitude than the other three analyzers and so statistically contributes little to the final result. Since this was combined with poor resolution it is not included in this analysis.

The summed asymmetries at each position are given in tables 8.1, 8.2 and 8.3 for windows 1, 2 and 3 respectively. The resulting standard errors were found to be similar to the weighted errors indicating the distribution of data points is largely governed by statistics. Also tabulated are the mean asymmetries summed over all four turntable positions. The phase factors $\sin(2\phi'_n)$ were included at this point.

Table 8.1. The average asymmetries of the 296, 308 and 316 keV triplet (window 1).

Analyzer	Turntable Position 1	2	3	4	Mean ($\times 10^{-3}$)
1 (Cold)	+0.18(0.71)	+0.33(1.29)	−0.58(1.35)	+0.84(0.99)	−0.24(0.49)
(Warm)	+0.08(0.90)	−1.04(1.17)	−0.12(0.99)	+0.79(0.86)	−0.08(0.48)
2 (Cold)	−0.14(0.84)	−0.20(0.61)	−1.63(1.15)	−0.58(0.96)	+0.04(0.41)
(Warm)	+0.50(1.02)	+0.56(0.72)	−0.34(0.88)	−0.52(0.84)	+0.05(0.42)
4 (Cold)	−0.35(0.70)	+0.23(0.82)	−1.07(1.07)	+0.25(1.02)	+0.43(0.46)
(Warm)	+1.21(0.87)	+0.25(0.82)	+0.66(0.78)	−0.63(0.88)	−0.54(0.42)

Table 8.2. The average asymmetries of the 468 keV singlet (window 2).

Analyzer	Turntable Position 1	2	3	4	Mean ($\times 10^{-3}$)
1 (Cold)	−0.42(0.86)	−1.98(1.50)	+0.86(1.56)	−0.76(1.17)	+0.42(0.58)
(Warm)	+1.87(1.03)	−1.56(1.41)	−0.13(1.18)	+1.38(1.06)	+0.40(0.57)
2 (Cold)	+0.74(0.99)	+1.72(1.22)	+0.34(1.46)	+0.39(1.17)	+0.18(0.59)
(Warm)	−0.00(1.08)	−1.05(1.00)	+1.68(1.15)	−0.56(1.01)	−0.80(0.53)
4 (Cold)	−0.75(0.85)	+1.90(1.00)	+0.50(1.28)	−1.00(1.24)	+0.54(0.52)
(Warm)	−0.64(1.02)	+0.87(1.04)	+0.71(0.96)	+0.75(1.14)	+0.33(0.51)

Table 8.3. The average asymmetries of the 589, 604 and 612 keV triplet (window 3).

Analyzer	Turntable Position 1	2	3	4	Mean ($\times 10^{-3}$)
1 (Cold)	−1.19(1.77)	+0.70(2.92)	+3.94(3.13)	−1.48(2.45)	+0.26(1.19)
(Warm)	−1.61(1.95)	−3.29(2.71)	−0.91(2.34)	−0.14(2.07)	−0.13(1.11)
2 (Cold)	+0.83(1.78)	−0.69(1.60)	−2.24(2.65)	+1.73(2.16)	+0.15(0.97)
(Warm)	+1.61(1.83)	+1.44(1.73)	+0.25(2.00)	+2.36(1.78)	+0.57(0.91)
4 (Cold)	−2.97(1.65)	+0.41(1.84)	+1.34(2.30)	+0.84(2.21)	+1.07(0.97)
(Warm)	+0.87(1.71)	−0.60(1.80)	−0.48(1.74)	+1.00(1.88)	−0.03(0.89)

The final results, averaged over all three analyzers, are thus

Window	Total asymmetry ($\times 10^{-3}$)
1 (Cold)	+0.09(0.26)
(Warm)	−0.20(0.25)
2 (Cold)	+0.39(0.32)
(Warm)	−0.03(0.31)
3 (Cold)	+0.52(0.59)
(Warm)	+0.17(0.55)

From these results it is clear that *no statistically significant* asymmetries were observed at any time in any of the windows, either "warm" or "cold". Therefore no normalizing subtraction of "warm" data from "cold" data is necessary.

8.7.2 The orientation parameters

It has already been shown in figure 8.3 that the short term temperature stability of the system was excellent. In fact this is also true in the long term, so that to a good approximation the temperature may be taken as constant for the duration of the experiment. As deduced from the axial anisotropy of the 468 keV transition, this average temperature was 14.99(1) mK. (It is assumed that the method of sample preparation leads to a complete occupation of the iridium impurities in good substitutional sites [17]).

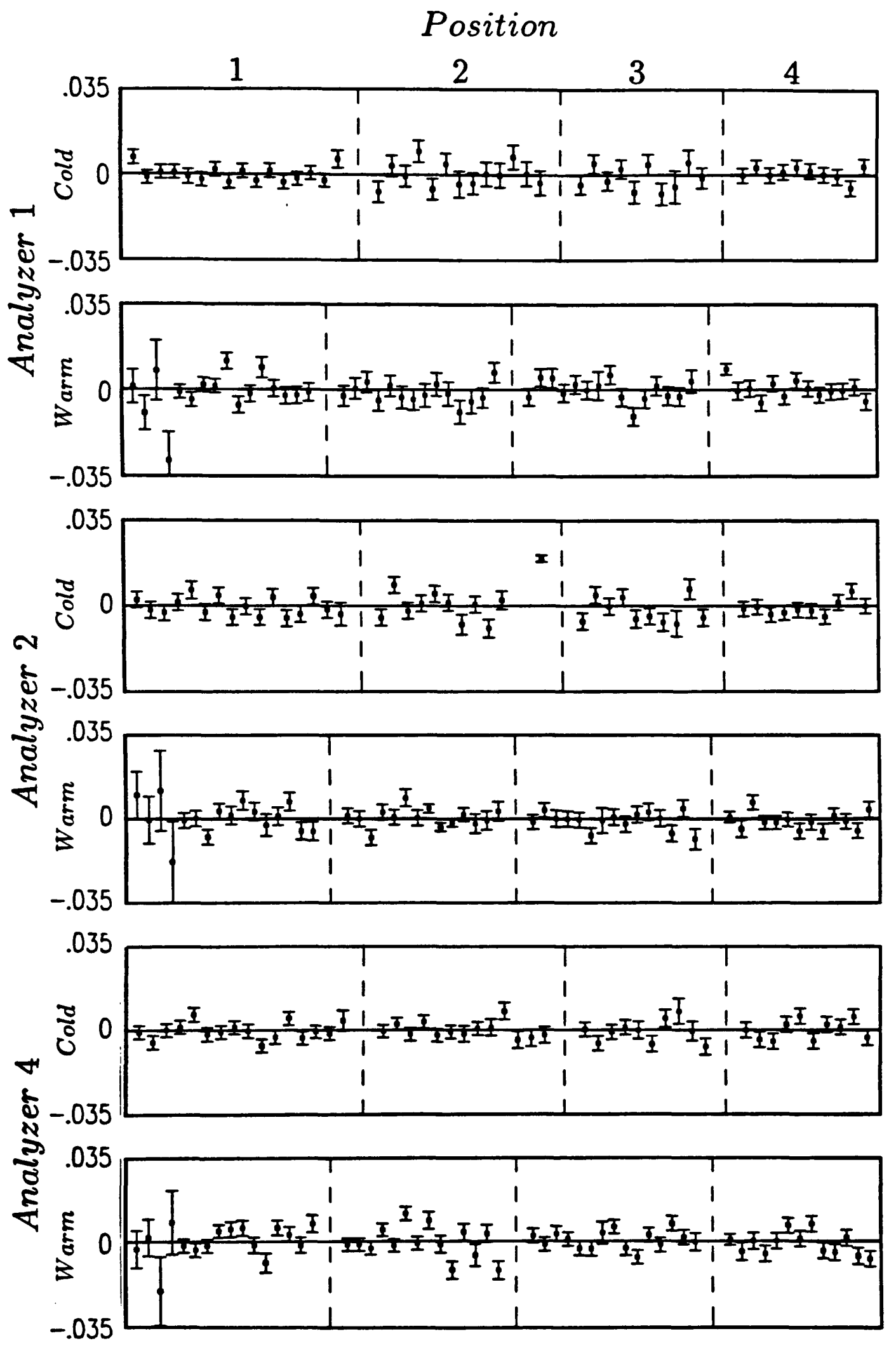

Figure 8.6. The time reversal asymmetries observed in the 296, 308 and 316 keV triplet. Each asymmetry point corresponds to an aquisition period of approximately $5\frac{1}{3}$ hours.

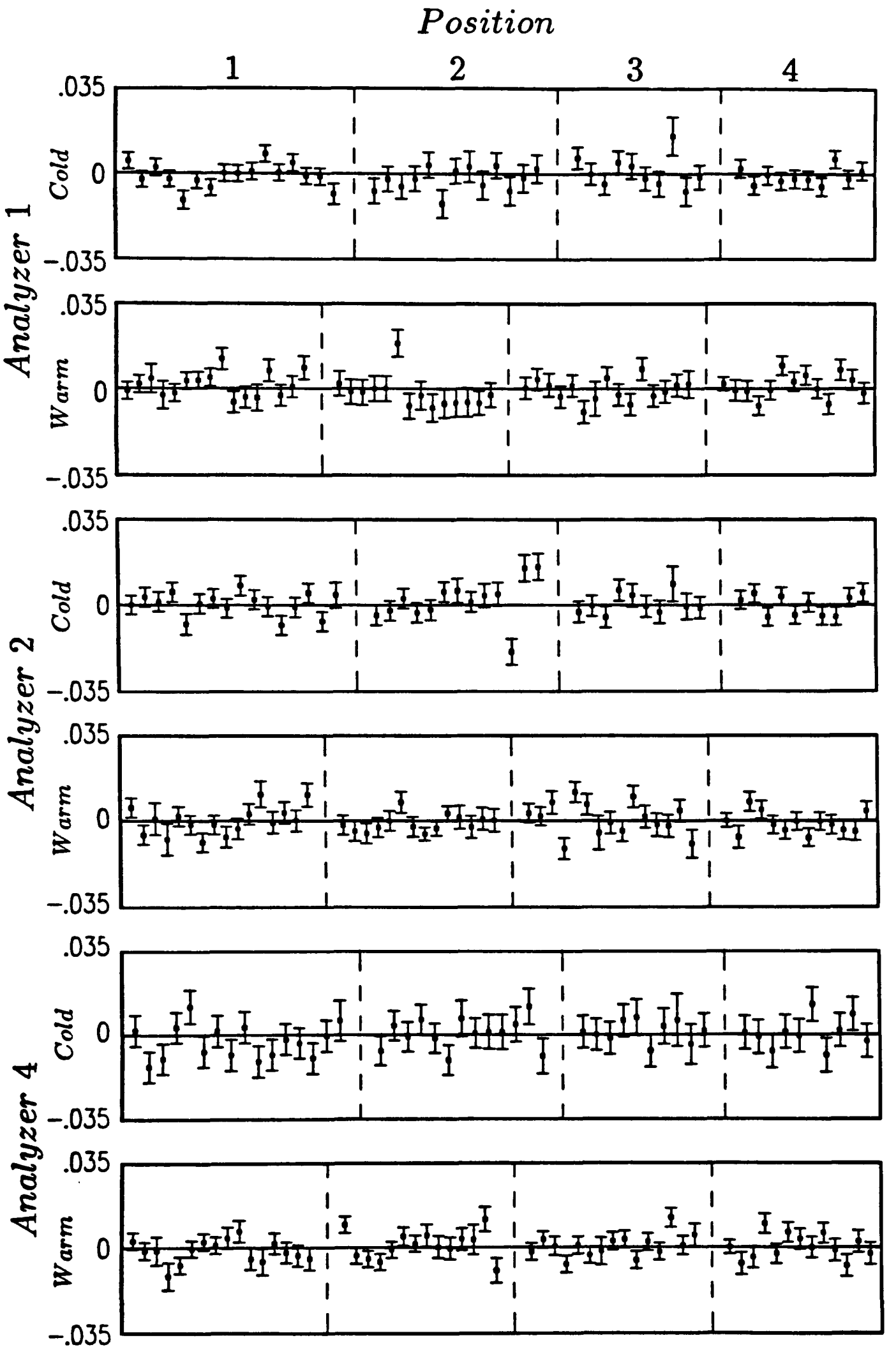

Figure 8.7. The time reversal asymmetries observed in the 468 keV singlet. Each asymmetry point corresponds to an aquisition period of approximately $5\frac{1}{3}$ hours.

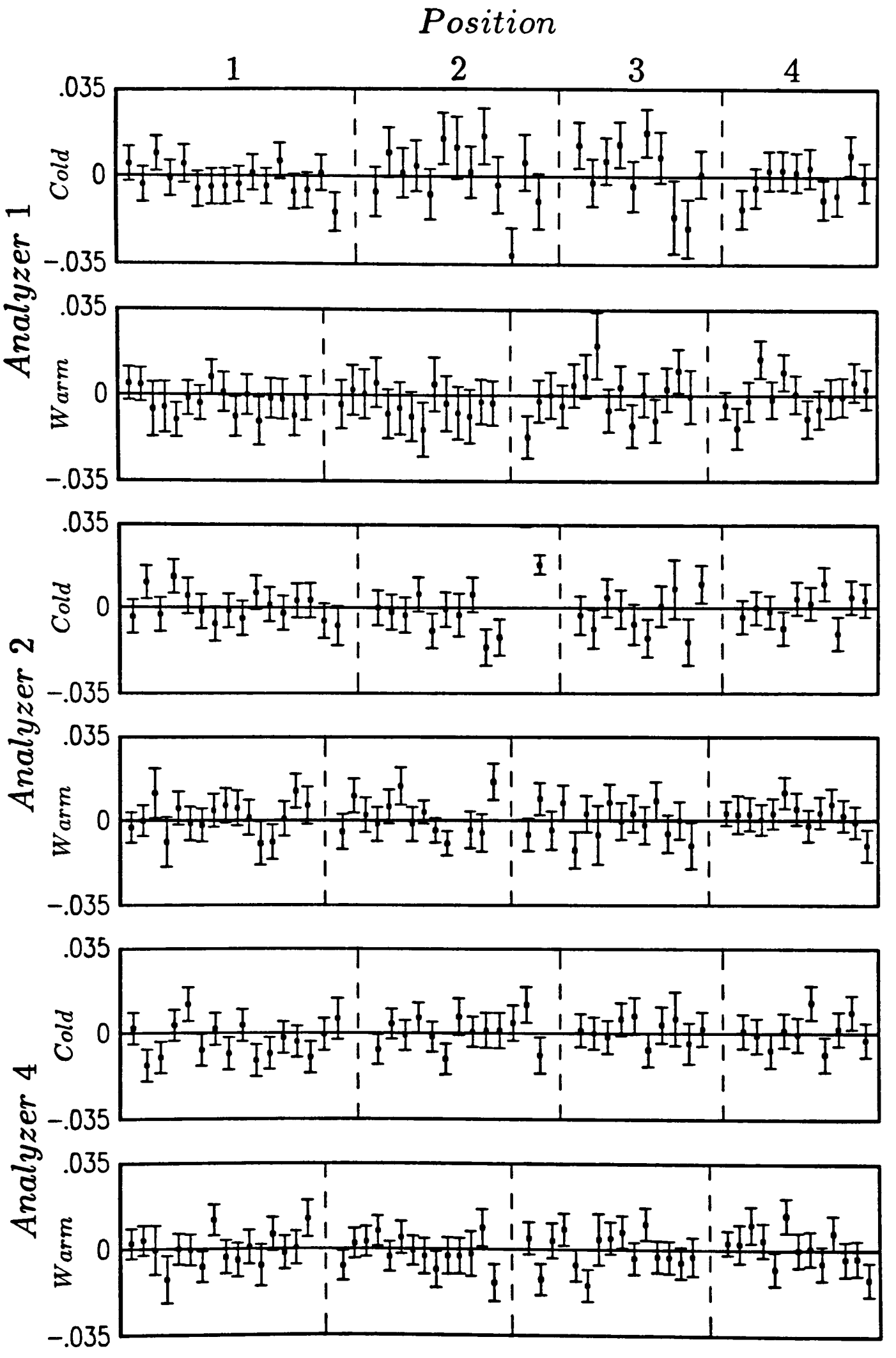

Figure 8.8. The time reversal asymmetries observed in the 589, 604 and 612 keV triplet. Each asymmetry point corresponds to an aquisition period of approximately $5\frac{1}{3}$ hours.

Although the even orders of orientation parameter are always positive, the sign of the odd orders and in particular B_3 is sensitive to that of the Boltzmann parameter (1.27). If this is negative then all the odd orders of orientation parameter are positive and vice versa. Unfortunately, in the case of ^{192}Ir the sign of the magnetic moment is not known and so the phase of B_3 is indeterminate. Therefore, the orientation parameters at this average temperature are

$$\begin{aligned} B_2 &= +1.316(4) \\ B_3 &= \pm 0.914(5) \\ B_4 &= +0.505(4) \end{aligned} \tag{8.18}$$

8.7.3 The polarimeter efficiency

The polarimeter efficiency Q was measured in the geometry ($\theta = \pi/2$, $\phi = 0, \pi/2$) as outlined in section 8.4. Unlike the time reversal case, the peaks were fitted separately since any small systematic errors introduced by gain shifts and resolution changes will not significantly effect the relatively large ordinary linear polarization.

In this way the experimental polarizations (8.11) of the 468 and 589 keV transitions were measured to be $\Delta_{468} = -0.230(3)$ and $\Delta_{589} = -0.199(12)$. Due to large gains shifts the 296, 308, 317 and 604, 612 keV transitions were not well resolved and therefore are not included.

Using the mixing ratios quoted in section 8.5, the corresponding theoretical polarizations (8.10) are calculated to be $P_{468} = -0.666(11)$ and $P_{589} = -0.701(12)$. Thus from (8.14) the polarimeter efficiencies are

$$\begin{aligned} Q_{468} &= 34(1)\% \quad \Gamma = 0.50(1) \\ Q_{589} &= 28(2)\% \quad \Gamma = 0.45(3) \end{aligned}$$

where Γ is defined in (8.16). Taking the mean value, $\Gamma = 0.49(1)$, then the efficiency of the present polarimeter is given as

$$Q = 0.49(1)\frac{\alpha + 1}{\alpha^2 + \alpha + 1}.$$

8.7.4 The sensitivity function K

With the above values for the orientation parameters and polarimeter efficiency, the sensitivity functions K at 15 mK of the three mixed transitions are calculated to be

$$K_{296} = \pm 0.016(4)$$

$$K_{308} = \mp 0.042(7)$$

$$K_{604} = \pm 0.109(8)$$

Where one or more transitions contribute to the same experimental asymmetry an effective sensitivity function K_{eff} can be calculated from

$$K_{eff} \sum_i I_i = \sum_i K_i I_i \tag{8.19}$$

where I_i denotes the gamma intensities. Thus for window 1, where the two mixed transitions have sensitivity functions of opposite sign and are diluted by a much stronger pure transition for which $K = 0$, the effective sensitivity function is as low as ∓ 0.005. This essentially precludes it from contributing to a useful limit on the time reversal phase angle.

In window 3 the mixed 604 keV transition contributes 44(1)% of the total intensity as deduced from a Gaussian fit to the triplet. Thus the effective sensitivity function for this window is $K_{eff} = \pm 0.048(4)$.

8.7.5 The time reversal phase angle

By combining the sensitivity functions with the raw experimental asymmetries according to (8.8) one obtains for the time reversal phase angle of the 604 keV transition in ^{192}Pt

$$\sin(\eta + \xi) = \pm 11(12) \times 10^{-3}.$$

Experimentally one cannot separate the phase shift ξ from the true time reversal effect η. However the magnitude of this unwanted term can be estimated theoretically. There are two main contributors to this term: the Faraday effect and final state interactions. The former, by virtue of the polarization dependence of the refractive index in a magnetized optical medium, causes the polarization vector **e** to rotate as the photons traverse the ferromagnetic iron host lattice. This would be recorded in the polarimeter as an asymmetry. The magnitude of this effect in the time reversal geometry can be estimated from the leading order term of W_2. Thus

$$A \sim QB_2U_2A_{22}2P_2^2(\cos 0.96)\Omega \tag{8.20}$$

where $\Omega = \Omega_0 t \cot(0.96)$, t being the thickness of the iron foil and $\Omega_0 = +3.9(0.3) \times 10^{-3}$ rad cm^{-1} [18]. At 15 mK and with $t \sim 10\mu m$, this corresponds to $A \sim 5 \times 10^{-6}$ and therefore can be safely neglected.

A much more important mimic of the true T-violating effect in angular distributions arises from the atomic final state interaction. In deriving such distributions the electromagnetic matrix elements are calculated in the Born approximation and are therefore Hermitian. However, if higher order terms are considered then the transition operator generally contains an additional skew-Hermitian component. As a result, the interference between direct photon emission and processes involving virtual intermediate states introduces a complex phase angle ξ into the reduced matrix elements.

Henley and Jacobsohn [19] have estimated that the nuclear radiative correction gives a contribution to ξ of only $\sim 10^{-7} \rightarrow 10^{-6}$. Higher order processes involving the atomic electrons are however much more significant. These arise from both virtual internal conversion and elastic photon-electron scattering. From the calculations of Davis *et al.* [20] it is estimated that this correction for the E2/M1 604 keV transition in ^{192}Pt amounts to $\xi = +6.1 \times 10^{-4}$. At the present level of experimental accuracy ξ may therefore be neglected. Thus the final time reversal phase angle is taken to be

$$\sin \eta = \pm 11(12) \times 10^{-3}.$$

8.7.6 Conclusion

Unfortunately the present result has failed to improve upon the previous best limit on the T-violation strength in ^{192}Pt, $\pm 4(5) \times 10^{-3}$ [21]. However it must be emphasized that this experiment was beset by interruptions caused by problems in the refrigeration system. As a result, only 25 out of a total of 100 days were spent acquiring data. Had the full experimental time been available and the full complement of analyzing detectors been operational then a limit in the region of 5×10^{-3} could have been reached.

This is by no means the ultimate precision which can be attained. Firstly, the present experiment has shown that there are no significant systematic asymmetries in the polarimeter. Thus it is possible to dispense with the "warm" data, relying instead on the the 468 keV pure

E2 transition as the sole experimental control, thereby doubling the time available for "cold" data. Secondly, an improved design of the polarimeter is under consideration. By employing a scattering detector with a much narrower crystal, the transmission of scattered radiation to the analyzers can be significantly improved [13]. Also with the present apparatus, the time reversal geometry requires that the gamma rays pass through the thickest and most absorptive part of the polarizing magnet. This reduces the gamma ray intensity by approximately 30% at 604 keV.

With the appropriate modifications it should be possible to attain a precision of $\sim 2 \times 10^{-3}$ in this isotope under favourable experimental conditions.

8.8 Future work

Although interesting in itself, the ^{192}Ir experiment was performed as a preparation for a future experiment on the 501 keV transition in the isomeric decay of $^{180}Hf^{m}$. This is of special interest because of the known P-odd contribution in the initial state of the transition [22]. Thus in addition to the T-odd effect one could also measure the ratio of the P-odd T-odd to P-odd amplitude, potentially providing a much smaller limit on the fundamental coupling constant than a T-violation alone [23].

References

[1] . J.H. Christenson *et al.*, Phys. Rev. Lett. **13** (1964) 138

[2] . R.C. Casella, Phys. Rev. Lett. **22** (1969) 554

[3] . K. Kleinknecht, Ann. Rev. Nucl. Sci. **26** (1976) 1

[4] . I.S. Altarev *et al.*, JETP Lett. **44** (1986) 460

[5] . W.A. Steyert and K.S. Krane, Phys. Lett. **47B** (1973) 294

[6] . R.M. Steffen and K. Alder, in The Electromagnetic Interaction in Nuclear Spectroscopy, ed. W.D. Hamilton (North Holland, 1975)

[7] . F. Boehm, in Hyperfine Structure and Nuclear Radiations, eds. E. Matthias and D.A. Shirley (North Holland, 1968)

[8] . F. Boehm, Hyp. Int. **43** (1988) 95

[9] . N.K. Cheung *et al.*, Phys. Rev. **C16** (1977) 2381

[10] . K.S. Krane, in Low Temperature Nuclear Orientation, eds. N.J. Stone and H. Postma (North Holland, 1987)

[11] . P.A. Butler *et al.*, Nucl. Instr. and Meth. **108** (1973) 497

[12] . J. Rikovska *et al.*, Hyp. Int. **43** (1988) 107

[13] . M. Mejdricky and J. Rikovska, unpublished

[14] . E. Hagn *et al.*, Z. Phys. **A295** (1980) 385

[15] . Nuclear Data Sheets **40** (1983)

[16] . J. Rikovska *et al.*, Hyp. Int. **15/16** (1983) 41

[17] . J. Rikovska, private communication (1989)

[18] . P. Bock and P. Luksh, Z. Phys. **263** (1973) 147

[19] . E.M. Henley and B.A. Jacobsohn, Phys. Rev. Lett. **16** (1966) 706

[20] . B.R. Davis *et al.*, Phys. Rev. **C22** (1980) 1233

[21] . M.J. Holmes *et al.*, Nucl. Phys. **A199** (1973) 401

[22] . K.S. Krane *et al.*, Phys. Rev. Lett. **26** (1971) 1579

[23] . P. Herzceg, Hyp. Int. **43** (1988) 77

Appendix

A.1 The construction of the even-even A VMI Hamiltonian

In the laboratory frame of reference the components of the total angular momentum operator obey the usual commutation rules

$$[R_A, R_B] = i \sum_C \varepsilon_{ABC} R_C \tag{A.1}$$

where ε is the antisymmetric tensor. When the components are taken with respect to the intrinsic axes, upon which they themselves operate, the commutation properties become

$$[R_a, R_b] = -i \sum_c \varepsilon_{abc} R_c. \tag{A.2}$$

As a result of this slight change, the roles of the raising and lowering operators, $R_\pm = R_1 \pm R_2$, are reversed. Thus the non-zero matrix elements required for the even-even VMI Hamiltonian (6.19) and (6.120) are

$$\langle RK|R^2|RK\rangle = \hbar^2 R(R+1) \tag{A.3}$$

$$\langle RK|R_3^2|RK\rangle = \hbar^2 R_3^2 \tag{A.4}$$

and

$$\langle RK|R_1^2 - R_2^2|RK \pm 2\rangle = \frac{1}{2}\langle RK|R_+^2 + R_-^2|RK \pm 2\rangle \tag{A.5}$$

where

$$\begin{aligned}\langle RK|R_+^2|RK+2\rangle &= \langle R-K|R_-^2|R-K-2\rangle \\ &= \hbar^2 \sqrt{\{R(R+1)-(K+1)(K+2)\}\{R(R+1)-K(K+1)\}}.\end{aligned} \tag{A.6}$$

The matrix elements of the constant VMI potential energy term are of course fully diagonal.

A listing of a program which has been written to construct the even-even VMI Hamiltonian is given below, together with a brief correspondence between the program variables and the notation used in the text of chapter 6.

IR $= R$

KUP $= R_3$

L $= \varrho$

STIFF $= C$

AR $= \hbar^2/2\Im_R$

A0 $= \hbar^2/2\Im_0$

A1,A2,A3 $= \left\{\frac{4}{3}\sin^2\left(\gamma - \frac{2\pi}{3}k\right)\right\}^{-1}$

ROTEN $= E_{R\varrho}$

ROTEIG $= A^{R\varrho}_{R_3}$

```
CV##########################################################################CV
CV##########################################################################CV
CV                                                                          CV
CV                  CALCULATION OF CORE STATES                              CV
CV                                                                          CV
CV##########################################################################CV
CV##########################################################################CV
CV
CV    EVEN CORE SPINS
CV
      DO 801 IR=0,(21+ISPIN)/2,2
      CALL INERTIA(IR,A0,STIFF,AR(IR+1))
      IF (VMI .NE. 1) AR(IR+1)=1
      IF (VMI .NE. 1) A0=1
      DO 802 III=0,(IR+2)*(IR+4)/8
      A(III)=0
  802 CONTINUE
      DO 803 KUP=0,IR,2
      DO 803 ICOUNT=0,1
      ANORM=0.25
      IF (KUP .EQ. 0) ANORM=0.35355339
      INDEX=KUP*(IR+3-KUP/2)/4+ICOUNT+1
      IF (ICOUNT .EQ. 0) A(INDEX)=-(AR(IR+1)*(A1+A2)/2.*(IR*(IR+1)
     $-KUP*KUP)+AR(IR+1)*A3*KUP*KUP+STIFF/8.*(1./A0-1./AR(IR+1))**2)
      IF (ICOUNT .EQ. 1 .AND. KUP .LT. IR)
     $A(INDEX)=-AR(IR+1)*ANORM*(A1-A2)*(((IR*(IR+1)-KUP*
     $(KUP+1))*(IR*(IR+1)-(KUP+1)*(KUP+2)))**.5)
  803 CONTINUE
      NN=IR/2+1
      IDIMR=IR/2+1
      CALL BIGMAX(A,VALUE,NN,IDIMR,IDIMR,EIGVEL,MATDIM)
      DO 804 L=1,IDIMR
      VALUE(L) = -VALUE(L)
      ROTEN(L,IR+1)=VALUE(L)
      DO 804 LL=1,NN
      ROTEIG(LL,L,IR+1)=EIGVEL(LL,L)
  804 CONTINUE
  801 CONTINUE
```

```
CV
CV    ODD CORE SPINS
CV
      DO 805 IR=3,(21+ISPIN)/2,2
      CALL INERTIA(IR,AO,STIFF,AR(IR+1))
      IF (VMI .NE. 1) AR(IR+1)=1
      IF (VMI .NE. 1) AO=1
      DO 806 III=0,(IR-1)*(IR+1)/8
      A(III)=0
  806 CONTINUE
      DO 807 KUP=2,IR,2
      DO 807 ICOUNT=0,1
      ANORM=0.250
      INDEX=(KUP-2)*(2*IR+2-KUP)/8+ICOUNT+1
      IF (ICOUNT .EQ. 0) A(INDEX)=-(AR(IR+1)*(A1+A2)/2.*(IR*(IR+1)
     $-KUP*KUP)+AR(IR+1)*A3*KUP*KUP+STIFF/8.*(1./AO-1./AR(IR+1))**2)
      IF (ICOUNT .EQ. 1 .AND. KUP .LT. IR-1)
     $A(INDEX)=-AR(IR+1)*ANORM*(A1-A2)*(((IR*(IR+1)-KUP*
     $(KUP+1))*(IR*(IR+1)-(KUP+1)*(KUP+2)))**.5)
  807 CONTINUE
      NN=(IR-1)/2
      IDIMR=NN
      CALL BIGMAX(A,VALUE,NN,IDIMR,IDIMR,EIGVEL,MATDIM)
      DO 808 L=1,IDIMR
      VALUE(L) = -VALUE(L)
      ROTEN(L,IR+1)=VALUE(L)
      DO 808 LL=1,NN
      ROTEIG(LL+1,L,IR+1)=EIGVEL(LL,L)
  808 CONTINUE
  805 CONTINUE
CV
CV#####################################################################CV
CV
      SUBROUTINE INERTIA(IR,AO,STIFF,AR)
      R=IR*(IR+1)/4./STIFF+1/216./AO**3
      T=R+1./216./AO**3
      T=T*IR*(IR+1)/4./STIFF
      T=T**.5
      AR=(R+T)**(1./3.)+(R-T)**(1./3.)+1./6./AO
      AR=1./2./AR
      RETURN
      END
```

A.2 The calculation of the VMI parameters

The values of the VMI parameters C and $\Im_0$ together with the asymmetry parameter γ may be extracted from the experimental energies of the 2_1^+, 2_2^+ and 4_1^+ levels, denoted E_{21}, E_{22} and E_{41} respectively.

These are given as the simultaneous solutions of the explicit expressions for the energy eigenvalues of the VMI rotor (6.21), (6.23) and (6.121)

$$\left\{\begin{matrix} E_{22} \\ E_{21} \end{matrix}\right\} = \frac{27}{2} A_2 \left(\frac{1 \pm \sqrt{1 - \frac{8}{9}\sin^2(3\gamma)}}{\sin^2(3\gamma)} \right) + \frac{1}{8} C \left(\frac{1}{A_2} - \frac{1}{A_0} \right)^2 \qquad (A.7)$$

$$E_{41} = \frac{3}{2}A_4 E(3\gamma) + \frac{1}{8}C\left(\frac{1}{A_4} - \frac{1}{A_0}\right)^2 \qquad (A.8)$$

where $E(3\gamma)$ is the smallest root of (6.23) and $A_R = \hbar^2/2\Im_R$, together with the equilibrium conditions (6.122)

$$\frac{1}{A_2^2}\left(\frac{1}{A_2} - \frac{1}{A_0}\right) = \frac{4}{C}R(R+1) = \frac{24}{C} \qquad (A.9)$$

$$\frac{1}{A_4^2}\left(\frac{1}{A_4} - \frac{1}{A_0}\right) = \frac{4}{C}R(R+1) = \frac{80}{C}. \qquad (A.10)$$

Owing to the non-linearities of this system of equations the convergence of the solutions in an iterative process is poor. The equations are therefore solved as far as possible by substitution. Thus from (A.9) and (A.10)

$$\frac{1}{A_0} = \frac{10/A_2^3 - 3/A_4^3}{10/A_2^2 - 3/A_4^2} \qquad (A.11)$$

and so with the definition

$$\alpha = \frac{1}{8}C\left(\frac{1}{A_2} - \frac{1}{A_0}\right)^2 \qquad (A.12)$$

one obtains from (A.9)

$$\alpha = 9A_2^2/A_4^2\left\{\frac{1/A_4 - 1/A_2}{10/A_2^2 - 3/A_4^2}\right\} \qquad (A.13)$$

and

$$\frac{1}{8}C\left(\frac{1}{A_4} - \frac{1}{A_0}\right)^2 = \frac{100}{9}\frac{A_4^4}{A_2^4}\alpha. \qquad (A.14)$$

If

$$X = \{E_{22} - \alpha\}/\{E_{21} - \alpha\} \qquad (A.15)$$

then from (A.7) the asymmetry parameter is given as

$$\sin(3\gamma) = \frac{3}{X+1}\sqrt{\frac{X}{2}}. \qquad (A.16)$$

Thus finally the energy eigenvalues may be rewritten as

$$E_{21} = 6A_2\frac{X+1}{X} + \alpha \qquad (A.17)$$

and

$$E_{41} = \frac{3}{2}A_4 E(X) + \frac{100}{9}\frac{A_4^4}{A_2^4}\alpha \qquad (A.18)$$

which, with X given by (A.15) and α by (A.14), are now implicit functions of just the two parameters A_2 and A_4. The convergence properties of the iterative solutions are now found to be excellent with little dependence upon the initial values. From these two values the VMI parameters C and $\Im_o$ and also the γ asymmetry may be calculated explicitly.

The following program employs the NAG library routine C05NBF in order to find the simultaneous roots of (A.17) and (A.18).

```
C######################################################################C
C######################################################################C
C                                                                      C
C     Program VMIPAR: calculates VMI parameters A0 and STIFFNESS       C
C     Input E21,E41 and E22 or Gamma                                   C
C                                                                      C
C######################################################################C
C######################################################################C
      IMPLICIT DOUBLE PRECISION (A-H,O-Z)
      REAL*8 FVEC(2),WA(19),PARAM(2)
      COMMON /INPUT/E21,E22,E41,XSINN,GAMTEST
      COMMON /OUPUT/XSIN
      CHARACTER INPUT,GAMTEST
      EXTERNAL FCN
      IFAIL=1
C
C     INPUT/OUTPUT
C
      WRITE(6,1)
      READ(5,2)GAMTEST
  100 IF (GAMTEST .EQ. 'Y') THEN
      WRITE(6,3)
      READ(5,*)E21,E41,GAMMA
      XSINN=SIND(3*GAMMA)
      IF (GAMMA .EQ. 0) XSINN=0.00005
      ELSE
      WRITE(6,4)
      READ(5,*)E21,E22,E41
      ENDIF
      PARAM(1) =.1
      PARAM(2) =.08
  101 WRITE(6,5)
      CALL C05NBF(FCN,2,PARAM,FVEC,SQRT(X02AAF(0.0)),WA,19,IFAIL)
      WRITE(6,6)F05ABF(FVEC,2)
      IF (GAMTEST .NE. 'Y' .AND. XSIN .GT.1) THEN
      WRITE(6,7)XSIN
      XSIN=1
      ENDIF
      GAMMA=ASIND(XSIN)/3
      A0=(10/PARAM(1)**2-3/PARAM(2)**2)/(10/PARAM(1)**3-3/PARAM(2)**3)
      C=24*PARAM(1)**2/(1/PARAM(1)-1/A0)
      IF (C .LE. 0.0) THEN
      WRITE(6,8)
      READ(5,*)PARAM(1),PARAM(2)
      END IF
      IF (C .LE. 0.0) GOTO 101
```

```
      WRITE(6,9)
      WRITE(6,10)GAMMA,C,4*A0**3/C,A0,PARAM(1),PARAM(2)
      WRITE(6,11)
      READ(5,2)INPUT
      IF (INPUT .NE. 'N') GOTO 100
    1 FORMAT(/,/,X,'Are you inputing Gamma? <CR>=No',/)
    2 FORMAT(A1)
    3 FORMAT(/,/,X,'Input E21,E41 energies (MeV) and Gamma(Deg)',/)
    4 FORMAT(/,/,X,'Input E21,E22,E41 energies (MeV)',/)
    5 FORMAT(/,/,X'FVEC(E21)          FVEC(E41)')
    6 FORMAT(/,/,X,'Norm Of Residuals ',E9.2)
    7 FORMAT(/,/,X,'Warning ...Sine(3*Gamma) = ',F4.2,
     $' Gamma reset to 30',/)
    8 FORMAT(/,/,X,'Warning ...C negative...reset parameters',
     $/,/,X,'Input new A02,A04 start parameters',/)
    9 FORMAT(/,/,X,'Gamma(Deg)    C(MeV**3)      SOFTNESS
     $     A0(MeV)     A02(MeV)     A04(MeV)')
   10 FORMAT(2X,F7.2,X,4X,E10.3,4(4X,F9.4))
   11 FORMAT(/,/,X,'Repeat? <CR>=Yes',/)
      STOP
      END
C
C#####################################################################C
C
      SUBROUTINE FCN(N,PARAM,FVEC,IFLAG)
      IMPLICIT DOUBLE PRECISION (A-H,O-Z)
      COMMON /INPUT/E21,E22,E41,XSINN,GAMTEST
      COMMON /OUPUT/XSIN
      REAL*8 FVEC(2),PARAM(2)
      CHARACTER GAMTEST
      ALPHA=9*(PARAM(1)/PARAM(2))**2*(1/PARAM(2)-1/PARAM(1))
      ALPHA=ALPHA/(10/PARAM(1)**2-3/PARAM(2)**2)
      IF (GAMTEST .EQ. 'Y') THEN
      XSIN=XSINN
      XSIN2=XSIN*XSIN
      XSIN4=XSIN2*XSIN2
      X=8.*XSIN2/9.
      X=2*(1+SQRT(1-X))/X-1
      ELSE
      X=E22-ALPHA
      X=X/(E21-ALPHA)
      XSIN=3/(X+1)*SQRT(X/2)
      XSIN2=XSIN*XSIN
      XSIN4=XSIN2*XSIN2
      ENDIF
C
C     2_1 LEVEL
C
      FVEC(1)=6*PARAM(1)*(X+1)/X+ALPHA-E21
C
C     4_1 LEVEL
C
      A1=48*(27+26*XSIN2)/XSIN4
      A2=-90/XSIN2
      A0=-640*(27+7*XSIN2)/XSIN4
      Q=-A1/3+A2*A2/9
      SQRTQ=SQRT(Q)
      R=(A1*A2-3*A0)/6-A2*A2*A2/27
      PHASE=ACOS(R/SQRTQ/Q)
      E4=-SQRTQ*COS(PHASE/3)-A2/3-1.732050808*SQRTQ*ABS(SIN(PHASE/3))
      FVEC(2)=1.5*PARAM(2)*E4+100/9*ALPHA*(PARAM(2)/PARAM(1))**4-E41
      WRITE(6,1)FVEC(1),FVEC(2)
    1 FORMAT(X,2(E9.2,10X))
      RETURN
      END
```

A.3 The construction of the odd A VMI Hamiltonian

A routine to calculate the transformation brackets (6.136) and construct the matrix elements (6.129) in the strong coupling basis is listed below. The program draws upon the eigenvectors and eigenfunctions of the even-even rotor of appendix A.1 and in the case of axial symmetry (IGAM = 1) the calculations are confined to the ground state rotational band, $\varrho = 1$.

IN = N

IJ = $2j$

IKK = 2Ω

SPCOEFF = $B^{i}_{Nj\Omega}$

IMNT = $2I$

K,KP = $2K$

IR = $2R$

NNN = R_3

I1,I2,ISP = i

IA = ϱ

ROTEN = $E_{R\varrho}$

ROTEIG = $A^{R\varrho}_{R_3}$

OVLP = $\langle IMKi|IMR\varrho j\rangle$

```
CV#########################################################################CV
CV#########################################################################CV
CV                                                                         CV
CV                CALCULATION OF ODD A VMI HAMILTONIAN                     CV
CV                                                                         CV
CV#########################################################################CV
CV#########################################################################CV
CV
CV    CALCULATION OF OVERLAPS
CV
      IF (VMI .EQ. 1) THEN
      ILIMIT1=IDIM
      ILIMIT2=NYIC
      IRSTEP=2
      IF (IGAM .EQ. 1) THEN
      ILIMIT1=NYIC
      ILIMIT2=1
      IRSTEP=4
      ENDIF
      DO 831 IN=INMIN,INMAX
      IJMAX=4*IN-1
      IF (IPAR1 .EQ. '+') IJMAX=4*IN-3
      DO 831 IJ=1,IJMAX,2
      IRMIN=ABS(IMNT-IJ)
      IF (IGAM .EQ. 1 .AND. IRMIN/4*4 .NE. IRMIN) IRMIN=IRMIN+2
      IRMAX=IMNT+IJ
      DO 831 IR=IRMIN,IRMAX,IRSTEP
```

```
      SPINFAC=(((FLOAT(IR)+1)/(FLOAT(IMNT)+1))**.5)/2.0
      DO 810 III=1,ILIMIT1
      IKK=KKMAX-4*(III-1)
      IF (IGAM .EQ. 1) IKK=KAX(III)
      IAMAX=(IR/2-1)/2
      IF( IR/4*4 .EQ. IR) IAMAX=IR/4+1
      IF (IGAM .EQ .1) IAMAX=1
      DO 814 ISP=1,NYIC
      DO 814 IA=1,IAMAX
      SUM(ISP,IA)=0
  814 CONTINUE
      NNNMAX=IR/2
      IF (IGAM .EQ .1) NNNMAX=0
      DO 811 NNN=0,NNNMAX,2
      DELTA=1
      IF( NNN .EQ. 0) DELTA=0.707106781
      IF (ABS(IKK-2*NNN) .LE. IJ) THEN
      CGSUM=DELTA*(CLEBI(IR,IJ,IMNT,2*NNN,IKK-2*NNN,IKK)+
     $CLEBI(IR,IJ,IMNT,-2*NNN,2*NNN-IKK,-IKK)*(-1)**((IR+IMNT-IJ)/2))
      DO 812 IISP=1,ILIMIT2
      ISP=IISP
      IF (IGAM .EQ. 1) ISP = III
      SPC=SPCOEFF(ISP,(IJ+1)/2,(ABS(IKK-2*NNN)+1)/2,IN)
      DO 812 IA=1,IAMAX
      SUM(ISP,IA)=SUM(ISP,IA)+ROTEIG(NNN/2+1,IA,IR/2+1)*SPC*CGSUM
  812 CONTINUE
      ENDIF
      IF (ABS(IKK+2*NNN) .LE. IJ) THEN
      CGSUM=DELTA*(CLEBI(IR,IJ,IMNT,-2*NNN,IKK+2*NNN,IKK)*(-1)**(IR/2)+
     $CLEBI(IR,IJ,IMNT,2*NNN,-2*NNN-IKK,-IKK)*(-1)**((IMNT-IJ)/2))
      DO 813 IISP=1,ILIMIT2
      ISP=IISP
      IF (IGAM .EQ. 1) ISP = III
      SPC=SPCOEFF(ISP,(IJ+1)/2,(ABS(IKK+2*NNN)+1)/2,IN)
      DO 813 IA=1,IAMAX
      SUM(ISP,IA)=SUM(ISP,IA)+ROTEIG(NNN/2+1,IA,IR/2+1)*SPC*CGSUM
  813 CONTINUE
      ENDIF
  811 CONTINUE
      DO 810 IISP=1,ILIMIT2
      ISP=IISP
      IF (IGAM .EQ. 1) ISP = III
      DO 810 IA=1,IAMAX
      OVLP((ABS(IKK)+1)/2,ISP,IA)=SUM(ISP,IA)*SPINFAC
  810 CONTINUE
CV
CV    CONSTRUCT PARTIAL MATRIX ELEMENTS
CV
      DO 831 I1=1,NYIC
      DO 831 I2=1,I1
      I3=IDIM*(I1-1)
      I4=IDIM*(I2-1)
      DO 831 III=1,IDIM
      IF (IGAM .EQ. 1) THEN
      KP=KAX(I1)
      ELSE
      KP=KKMAX-4*(III-1)
      ENDIF
      DO 831 JJJ=1,IDIM
      IF (IGAM .EQ. 1) THEN
      K=KAX(I2)
      ELSE
      K=KKMAX-4*(JJJ-1)
      ENDIF
      K3(JJJ)=K
      I=III+I3
      J=JJJ+I4
      INDEX = (2*IDIM1-J)*(J-1)/2 + I
      IF(J.GT.I) GO TO 831
```

```
      DO 831 IA=1,IAMAX
      A(INDEX)=A(INDEX)+OVLP((ABS(KP)+1)/2,I1,IA)
     $*ROTEN(IA,IR/2+1)*OVLP((ABS(K )+1)/2,I2,IA)
  831 CONTINUE
CV
CV    ADD PAIRING AND S.P. FACTORS
CV
      DO 832 I1=1,NYIC
      DO 832 I2=1,I1
      I3=IDIM*(I1-1)
      I4=IDIM*(I2-1)
      DO 832 III=1,IDIM
      IF (IGAM .EQ. 1) THEN
      KP=KAX(I1)
      ELSE
      KP=KKMAX-4*(III-1)
      ENDIF
      DO 832 JJJ=1,IDIM
      IF (IGAM .EQ. 1) THEN
      K=KAX(I2)
      ELSE
      K=KKMAX-4*(JJJ-1)
      ENDIF
      K3(JJJ)=K
      I=III+I3
      J=JJJ+I4
      INDEX = (2*IDIM1-J)*(J-1)/2 + I
      IF(J.GT.I) GO TO 832
CV
CV    REMOVE SPURIOUS BASIS STATE (K.GT.I): MAY OCCUR FOR IGAM=1
CV
      KTEST=MAXO(IABS(K),IABS(KP))
      IF (KTEST .GT. IMOM .AND. J .EQ. I .AND .I1 .EQ. I2) THEN
      A(INDEX)=50*(A1+A2)*(IMOM*(IMOM+2)+K*K)+SQP(I1)
      A(INDEX)=-A(INDEX)
      ENDIF
      IF (KTEST .GT. IMOM) GO TO 832
      A(INDEX) = A(INDEX)*PUV(I1,I2)
      IF (I1 .NE. I2) A(INDEX) = A(INDEX)*CHSI
      IF (I1 .EQ. I2 .AND. I .EQ. J) A(INDEX) = A(INDEX) + SQP(I1)
      A(INDEX) = - A(INDEX)
  832 CONTINUE
```

A.4 The construction of the odd-odd A VMI Hamiltonian

The overlaps (6.140) and (6.141) and matrix elements (6.138) are calculated in an analogous fashion to the odd A case given in appendix A.3. Again the program truncates the core basis in the case of axial symmetry.

NQP $= N_p$	NQN $= N_n$
IJP $= 2j_p$	IJN $= 2j_n$
IPK $= 2\Omega_p$	IPN $= 2\Omega_n$
IP,IPP $= p$	IN,INP $= n$

JTOT $= J$

SPCOEFF $= B^{p,n}_{(Njl\Omega)_{p,n}}$

ISPIN $= I$

IK,IKP $= K$

IR $= R$

NNN $= R_3$

IAR $= \varrho$

ROTEN $= E_{R\varrho}$

ROTEIG $= A^{R\varrho}_{R_3}$

OVLP $= \langle IMKpn|IMR\varrho Jj_pj_n\rangle$

```
CV#########################################################################CV
CV#########################################################################CV
CV                                                                         CV
CV                CALCULATION OF ODD-ODD A VMI HAMILTONIAN                 CV
CV                                                                         CV
CV#########################################################################CV
CV#########################################################################CV
CV
CV    CALCULATE OVERLAPS
CV
      IF (VMI .EQ. 1) THEN
      ILIMIT1=1
      ILIMIT2=1
      ILIMIT3=NPROT
      ILIMIT4=NNEUT
      IRSTEP=1
      IF (IGAM .EQ. 1) THEN
      ILIMIT1=NPROT
      ILIMIT2=NNEUT
      ILIMIT3=1
      ILIMIT4=1
      IRSTEP=2
      ENDIF
      DO 703 JJJ=1,DIMTRI
      A(JJJ)=0
  703 CONTINUE
      DO 700 NQP=NMIN(1),NMAX(1)
      DO 700 NQN=NMIN(2),NMAX(2)
      IJPMAX=4*NQP-1
      IF (IPAR(1) .EQ. '+') IJPMAX=4*NQP-3
      IJNMAX=4*NQN-1
      IF (IPAR(2) .EQ. '+') IJNMAX=4*NQN-3
      DO 700 IJP=1,IJPMAX,2
      DO 700 IJN=1,IJNMAX,2
      DO 700 JTOT=(ABS(IJP-IJN))/2,(IJP+IJN)/2
      IRMIN=ABS(ISPIN-JTOT)
      IF (IGAM .EQ. 1 .AND. IRMIN/2*2 .NE. IRMIN) IRMIN=IRMIN+1
      IRMAX=ISPIN+JTOT
      DO 700 IR=IRMIN,IRMAX,IRSTEP
      SPINFAC=(((FLOAT(IR)+0.5)/(FLOAT(ISPIN)+0.5))**0.5)/2.0
      IARMAX=(IR-1)/2
      IF (IR/2*2 .EQ. IR) IARMAX=IR/2+1
      IF (IGAM .EQ. 1) IARMAX=1
      DO 702 IIP = 1,ILIMIT1
      IP=IIP
      DO 702 IIN = 1,ILIMIT2
      IN=IIN
```

```
      DO 702 IK = 1,KDIM
      IF (IGAM .EQ. 1) THEN
      K = KPN(IK,IP,IN)
      ELSE
      K = IK-KKMAX-1
      ENDIF
      DO 710 I=1,NPROT
      DO 710 II=1,NNEUT
      DO 710 III=1,IARMAX
      SUM(I,II,III)=0
  710 CONTINUE
      DIMP=(IJP+1)/2
      IPKMAX=IJP
      IF ( (IJP-1)/4*4 .NE. IJP-1) IPKMAX=IJP-2
      DO 701 III=1,DIMP
      IPK=IPKMAX-4*(III-1)
      NNNMAX=IR
      IF (IGAM .EQ. 1) NNNMAX=0
      DO 701 NNN=0,NNNMAX,2
      DELTA=1
      IF (NNN .EQ. 0) DELTA=0.707106781
      IF (K/2*2 .EQ. K) THEN
      IF (ABS(2*NNN-2*K+IPK) .LE. IJN) THEN
      CGSUM=CLEBI(IJP,IJN,2*JTOT,IPK,-2*NNN+2*K-IPK,2*K-2*NNN)*
     $CLEBI(2*JTOT,2*IR,2*ISPIN,2*K-2*NNN,2*NNN,2*K)*
     $(-1)**((IJN-IPK)/2)+
     $CLEBI(IJP,IJN,2*JTOT,-IPK,-2*K+IPK+2*NNN,-2*K+2*NNN)*
     $CLEBI(2*JTOT,2*IR,2*ISPIN,-2*K+2*NNN,-2*NNN,-2*K)*
     $(-1)**(ISPIN+1+IR+(IJP-IPK)/2)
      DO 711 IIIP=1,ILIMIT3
      IF (IGAM .NE. 1) IP=IIIP
      SPCP=SPCOEFF(1,IP,(IJP+1)/2,(ABS(IPK)+1)/2,NQP)*DELTA
      DO 711 IIIN=1,ILIMIT4
      IF (IGAM .NE. 1) IN=IIIN
      SPCN=SPCOEFF(2,IN,(IJN+1)/2,(ABS(2*NNN-2*K+IPK)+1)/2,NQN)
      DO 711 IAR=1,IARMAX
      SUM(IP,IN,IAR)=SUM(IP,IN,IAR)+ROTEIG(NNN/2+1,IAR,IR+1)*
     $SPCP*SPCN*CGSUM
  711 CONTINUE
      ENDIF
      IF (ABS(-2*NNN-2*K+IPK) .LE. IJN) THEN
      CGSUM=CLEBI(IJP,IJN,2*JTOT,IPK,2*NNN+2*K-IPK,2*K+2*NNN)*
     $CLEBI(2*JTOT,2*IR,2*ISPIN,2*K+2*NNN,-2*NNN,2*K)*
     $(-1)**((IJN-IPK)/2+IR)+
     $CLEBI(IJP,IJN,2*JTOT,-IPK,-2*K+IPK-2*NNN,-2*K-2*NNN)*
     $CLEBI(2*JTOT,2*IR,2*ISPIN,-2*K-2*NNN,2*NNN,-2*K)*
     $(-1)**(ISPIN+1+(IJP-IPK)/2)
      DO 712 IIIP=1,ILIMIT3
      IF (IGAM .NE. 1) IP=IIIP
      SPCP=SPCOEFF(1,IP,(IJP+1)/2,(ABS(IPK)+1)/2,NQP)*DELTA
      DO 712 IIIN=1,ILIMIT4
      IF (IGAM .NE. 1) IN=IIIN
      SPCN=SPCOEFF(2,IN,(IJN+1)/2,(ABS(-2*NNN-2*K+IPK)+1)/2,NQN)
      DO 712 IAR=1,IARMAX
      SUM(IP,IN,IAR)=SUM(IP,IN,IAR)+ROTEIG(NNN/2+1,IAR,IR+1)*
     $SPCP*SPCN*CGSUM
  712 CONTINUE
      ENDIF
      ELSE
      IF (ABS(-2*NNN+2*K-IPK) .LE. IJN) THEN
      CGSUM=CLEBI(IJP,IJN,2*JTOT,IPK,-2*NNN+2*K-IPK,2*K-2*NNN)*
     $CLEBI(2*JTOT,2*IR,2*ISPIN,2*K-2*NNN,2*NNN,2*K)+
     $CLEBI(IJP,IJN,2*JTOT,-IPK,-2*K+IPK+2*NNN,-2*K+2*NNN)*
     $CLEBI(2*JTOT,2*IR,2*ISPIN,-2*K+2*NNN,-2*NNN,-2*K)*
     $(-1)**(ISPIN+IR+(IJP+IJN)/2)
      DO 713 IIIP=1,ILIMIT3
      IF (IGAM .NE. 1) IP=IIIP
      SPCP=SPCOEFF(1,IP,(IJP+1)/2,(ABS(IPK)+1)/2,NQP)*DELTA
      DO 713 IIIN=1,ILIMIT4
```

```
      IF (IGAM .NE. 1) IN=IIIN
      SPCN=SPCOEFF(2,IN,(IJN+1)/2,(ABS(-2*NNN+2*K-IPK)+1)/2,NQN)
      DO 713 IAR=1,IARMAX
      SUM(IP,IN,IAR)=SUM(IP,IN,IAR)+ROTEIG(NNN/2+1,IAR,IR+1)*
     $SPCP*SPCN*CGSUM
  713 CONTINUE
      ENDIF
      IF (ABS(2*NNN+2*K-IPK) .LE. IJN) THEN
      CGSUM=CLEBI(IJP,IJN,2*JTOT,IPK,2*NNN+2*K-IPK,2*K+2*NNN)*
     $CLEBI(2*JTOT,2*IR,2*ISPIN,2*K+2*NNN,-2*NNN,2*K)*(-1)**IR+
     $CLEBI(IJP,IJN,2*JTOT,-IPK,-2*K+IPK-2*NNN,-2*K-2*NNN)*
     $CLEBI(2*JTOT,2*IR,2*ISPIN,-2*K-2*NNN,2*NNN,-2*K)*
     $(-1)**(ISPIN+(IJP+IJN)/2)
      DO 714 IIIP=1,ILIMIT3
      IF (IGAM .NE. 1) IP=IIIP
      SPCP=SPCOEFF(1,IP,(IJP+1)/2,(ABS(IPK)+1)/2,NQP)*DELTA
      DO 714 IIIN=1,ILIMIT4
      IF (IGAM .NE. 1) IN=IIIN
      SPCN=SPCOEFF(2,IN,(IJN+1)/2,(ABS(2*NNN+2*K-IPK)+1)/2,NQN)
      DO 714 IAR=1,IARMAX
      SUM(IP,IN,IAR)=SUM(IP,IN,IAR)+ROTEIG(NNN/2+1,IAR,IR+1)*
     $SPCP*SPCN*CGSUM
  714 CONTINUE
      ENDIF
      ENDIF
  701 CONTINUE
      DO 702 IIIP=1,ILIMIT3
      IF (IGAM .NE. 1) IP=IIIP
      DO 702 IIIN=1,ILIMIT4
      IF (IGAM .NE. 1) IN=IIIN
      DO 702 IAR=1,IARMAX
      OVLP(IK,IP,IN,IAR)=SUM(IP,IN,IAR)*SPINFAC
  702 CONTINUE
CV
CV    CONSTRUCT PARTIAL MATRIX ELEMENTS
CV
      DO 704 IP = 1,NPROT
      DO 704 IN = 1,NNEUT
      DO 704 IK = 1,KDIM
      IA = (IP-1)*NNEUT*KDIM + (IN-1)*KDIM + IK
      IF (IGAM .EQ. 1) THEN
      K = KPN(IK,IP,IN)
      ELSE
      K = IK-KKMAX-1
      ENDIF
      DO 704 IPP = 1,NPROT
      DO 704 INP = 1,NNEUT
      DO 704 IKP = 1,KDIM
      IB = (IPP-1)*NNEUT*KDIM + (INP-1)*KDIM + IKP
      IF (IB .GT. IA) GO TO 704
      IF (IGAM .EQ. 1) THEN
      KP = KPN(IKP,IPP,INP)
      ELSE
      KP = IKP-KKMAX-1
      ENDIF
      INDEX = (2*DIM - IB)*(IB-1)/2 + IA
      DO 704 IAR=1,IARMAX
      A(INDEX)=A(INDEX)+OVLP(IK,IP,IN,IAR)*ROTEN(IAR,IR+1)*
     $OVLP(IKP,IPP,INP,IAR)
  704 CONTINUE
  700 CONTINUE
CV
CV    ADD PAIRING FACTORS, S.P. AND Vpn ELEMENTS
CV
      DO 705 IP = 1,NPROT
      DO 705 IN = 1,NNEUT
      DO 705 IK = 1,KDIM
      IA = (IP-1)*NNEUT*KDIM + (IN-1)*KDIM + IK
      IF (IGAM .EQ. 1) THEN
```

```
      K = KPN(IK,IP,IN)
      ELSE
      K = IK-KKMAX-1
      ENDIF
      DO 706 IPP = 1,NPROT
      DO 706 INP = 1,NNEUT
      DO 706 IKP = 1,KDIM
      IB = (IPP-1)*NNEUT*KDIM + (INP-1)*KDIM + IKP
      IF (IB .GT. IA) GO TO 706
      IF (IGAM .EQ. 1) THEN
      KP = KPN(IKP,IPP,INP)
      ELSE
      KP = IKP-KKMAX-1
      ENDIF
      INDEX = (2*DIM - IB)*(IB-1)/2 + IA
CV
CV    REMOVE SPURIOUS BASIS STATE (K.GT.I): MAY OCCUR FOR IGAM=1
CV
      KTEST = MAXO(IABS(K),IABS(KP))
      IF (KTEST .GT. ISPIN .AND. IA .EQ. IB) THEN
      A(INDEX) = 50.*AOR(3)*(A1+A2)*(ISPIN*(ISPIN+1)+IABS(K))
     $+SQP(1,IP)+SQP(2,IN)
      A(INDEX) = -A(INDEX)
      ENDIF
      IF (KTEST .GT. ISPIN) GO TO 706
CV
      A(INDEX) = A(INDEX)*PUV(1,IP,IPP)*PUV(2,IN,INP)
      IF(IP .NE. IPP .OR.  IN .NE. INP) A(INDEX)=A(INDEX)*CHSI
      IF(IP .NE. IPP .AND. IN .NE. INP) A(INDEX)=A(INDEX)*CHSI
      IF (IA .EQ. IB) A(INDEX) = A(INDEX) + SQP(1,IP) + SQP(2,IN)
      IF(IRES .EQ. 0) GO TO 707
      APAIR = UPAIR(1,IP)*UPAIR(1,IPP)*UPAIR(2,IN)*UPAIR(2,INP)
     $+VPAIR(1,IP)*VPAIR(1,IPP)*VPAIR(2,IN)*VPAIR(2,INP)
      BPAIR = UPAIR(1,IP)*UPAIR(1,IPP)*VPAIR(2,IN)*VPAIR(2,INP)
     $+VPAIR(1,IP)*VPAIR(1,IPP)*UPAIR(2,IN)*UPAIR(2,INP)
      M=1
      IF (MOD(K,2) .EQ. 0) M=2
      VRES = 0.0
      IF (KP .EQ. -K) THEN
      VRES = APAIR*VPN(IP,IN,IPP,INP,5-M)
     $+BPAIR*VPN(IP,INP,IPP,IN,5-M)
      VRES=VRES*(-1)**(ISPIN+1)*PHASE
      ENDIF
      IF (KP .EQ. K) THEN
      VRES = VRES + APAIR*VPN(IP,IN,IPP,INP,M)
     $-BPAIR*VPN(IP,INP,IPP,IN,3-M)
      ENDIF
      A(INDEX)=A(INDEX)+CRES*VRES
  707 CONTINUE
      A(INDEX) = -A(INDEX)
  706 CONTINUE
```